Title of Document: AERODYNAMIC MODELING OF A FLAPPING MEMBRANE WING USING MOTION TRACKING EXPERIMENTS

Robyn Lynn Harmon, Masters of Science, 2008

Directed By: Langley Distinguished Professor, Dr. James E. Hubbard Jr., Department of Aerospace Engineering

An analytical model of flapping membrane wing aerodynamics using experimental kinematic data is presented. An alternative to computational fluid dynamics, this experimental method tracks small reflective markers placed on two ornithopter membrane wings. Time varying three dimensional data of the wing kinematics and the corresponding aerodynamic loads were recorded for various flapping frequencies. The wing shape data was used to form an analytical aerodynamic model that uses blade element theory and quasi-steady aerodynamics to account for the local twist, stroke angle, membrane shape, wing velocity and acceleration. Results from the aerodynamic model show adequate correlation between the magnitude of lift and thrust produced but some phase errors exist between the measured and calculated force curves. This analytical model can be improved by comparison with a RANS CFD solver which provides insight into the fluid behavior. Implications on the membrane wing design are also presented.

AERODYNAMIC MODELING OF A FLAPPING MEMBRANE WING USING MOTION TRACKING EXPERIMENTS

By

Robyn Lynn Harmon

Thesis submitted to the Faculty of the Graduate School of the
University of Maryland, College Park, in partial fulfillment
of the requirements for the degree of
Masters of Science
2008

Advisory Committee:
Professor James E. Hubbard Jr., Chair
Dr. James Baeder, Associate Professor
Dr. Inderjit Chopra, Gessow Professor

Acknowledgements

This research is dependent on the support of the University of Maryland, the National Institute of Aerospace and NASA Langley. A special thanks to Joe Conroy at the University of Maryland for providing insight and assistance in operating the Vicon Motion Tracking System.

Table of Contents

List of Tables

List of Figures

Nomenclature

AR	wing aspect ratio
a	location of airfoil pitching access from ½ chord point
b	half chord length defined by quasi-steady thin airfoil theory
B	semispan length
c	chord length at span location r
$\bar{c}$	mean wing chord length
C_a, C_A	2D, 3D axial force coefficients
C_d, C_D	2D, 3D drag force coefficients
C_l, C_L	2D, 3D lift force coefficients
C_n, C_N	2D, 3D normal force coefficients
C_{Dp}	parasite drag coefficient
C_f	flat plate parasite drag coefficient
C_{l_c}	2D circulatory lift coefficient with unsteady effects
$C(k)$	Theodorsen lift deficiency function
dc	blade element chord length
dr	width of blade element (span direction)
f	flapping frequency (Hz)
$\left.\begin{matrix}F'(k)\\G'(k)\end{matrix}\right\}$	Theodorsen function coefficients
$\dot{h}$	vertical velocity of a plunging airfoil
$\ddot{h}$	vertical acceleration of a plunging airfoil
k	reduced frequency $k = c\omega/2U$
l	length of slack in membrane element
N_{nc}	non-circulatory force
r	local span position
$\bar{r}$	span position at mean chord
R	half-span length
Re	Reynolds number
u	longitudinal induced velocity
U	flight velocity
v, w	vertical induced velocity or downwash
V_{rel}	relative inflow velocity
α_{rel}	relative angle of attack including unsteady effects on α
α_{L0}	zero lift angle of attack
β	wing stroke angle with respect to body y-axis (positive up)
$\dot{\beta}$	angular velocity of the flapping wing
$\ddot{\beta}$	angular acceleration of the flapping wing
δ	angle between flapping axis and flight velocity

γ	flight path angle of flight velocity with respect to the ground
ϕ	pitch angle of blade element chord with respect to flapping axis
θ	pitch angle of blade element with respect to flapping axis
ω	flapping frequency

Chapter 1. Introduction

The human desire to duplicate bird flight has existed for hundreds of years. From Leonardo Da Vinci's drawings to Otto Lilienthal's gliders, the first five hundred years of flapping flight research focused on human transport. Today flapping flight research has shifted to a much smaller scale with the goal of an autonomous ornithopter unmanned air vehicle (UAV). Flapping wing vehicles can fill the niche left by traditional fixed and rotary wing vehicles for small, maneuverable and stealthy UAVs in military, civilian and research applications. Ornithopter autonomy has not yet been achieved because the kinematics, aerodynamics and the stability, guidance and navigation of birds are much more complicated than that of a fixed wing aircraft. This challenging problem has sparked a wave of research in dynamic modeling, flapping aerodynamics, structural behavior, and control methods.

While it is unlikely that humans can engineer ornithopters that perform as well as nature's flyers in the near term, improvements can be made by characterizing the behavior and optimizing the design of ornithopter wings for optimum aerodynamic performance and flight control. The goal of this thesis is to provide a predictive aerodynamic model for future autonomous ornithopter control applications. This was accomplished by experimentally determining the dynamic shape change of a flapping membrane wing throughout a complete flapping cycle. A predictive aerodynamic model was generated using membrane wing shape data in combination with unsteady aerodynamic theory applied to a blade element approximation of the wing.

1.1 Introduction to UAVs

Historical insight and motivation for unmanned air vehicle (UAV) technologies are presented in the following sections. The systems required for successful UAV flight and comparisons between fixed wing, rotary wing, and flapping wing platforms are considered. Also included is an examination of low Reynolds number aerodynamics which is important for small, low speed vehicles.

1.1.1 Historical Overview

Unmanned air vehicle development actually began before the first planes flew. As early as 1863 a hot air balloon designed to carry bombs set off by a timer was patented by Charles Perley for use in the Civil War, though it was never deployed by the Union troops. Twenty years later Douglas Archibald developed a kite used to take aerial photography, a practice that would be adopted for the first time by American soldiers in the Spanish-American war to provide crucial surveillance information. The first truly unmanned plane was a converted WWI U.S. Navy Curtiss N-9 trainer aircraft that used a automatic gyroscopic stabilizer and radio control. This plane could carry a 300 pound bomb for 50 miles, but was never used in combat [1].

After World War I UAV development declined until new programs in the 1930's used reusable and returnable UAVs for pilot combat training, all were remotely controlled. The first UAV used to deliver weaponry was the German V-1, which carried a 2000 lb warhead 150 miles to its target, often civilian cities. Countermeasures to the V-1's were soon developed by the Americans to destroy V-1 launch sites. Stealth surveillance became a priority mission for UAVs in the Vietnam War with more than 1,000 AQM-34 Ryan Firebee UAVs flying over 34,000 missions in Southeast Asia. This period showcased the usefulness and reliability of UAVs for military uses. Throughout the 1970's and 1980's many countries developed successful remotely controlled UAV platforms and the need for UAV's to fly above enemy missiles and for extended durations was established.

Modern day UAVs are capable of complete autonomy or remote control. UAV missions have expanded from military tasks to include civilian applications in surveillance, environmental monitoring and communications, and as a test bed for new aerospace technologies. With more applications, the UAV field diversified with increasing desire for small stealthy surveillance air vehicles and larger, high altitude and long endurance UAVs. The following research focuses on small UAV applications for aircraft of 1.25m (4ft) wingspan or less, with the ultimate goal of developing a UAV with the size and maneuverability of a small bird.

1.1.2 UAV Mission Definition and Motivation

UAV uses have broadened significantly since their invention, but all missions require carrying a payload for experimentation, deployment, or reconnaissance purposes. Two typical military UAV applications were established over a hundred years ago: to seek out a target and deploy weapons, or to seek a target and provide surveillance; add communications to these two tasks and the general spectrum of military UAV missions is completed. NASA recently compiled a more specific set of tasks for civilian UAVs which are listed below [2].

- Boarder and Coastal Patrol and Monitoring
- Law Enforcement and Disaster Operations
- Digital Mapping and Planning/Land Management

- Search and Rescue
- Fire Detection and Firefighting Management
- Communications and Broadcast Services
- Ground Transportation Monitoring and Control
- Satellite Augmentation Systems
- Air Traffic Control Support
- Power Transmission Line Monitoring
- Environmental Research and Air Quality Management/Control

These types of civil missions can be categorized into four governing areas in the private and public sectors: Homeland Security, Earth Science, Commercial, and Land Management. Demand in the civil market provides incentive to develop new UAV technology not just for research and tactical missions but also for the civilian sector. To complete these operations UAV's vary in size from a few centimeters to fifty meters in span or larger. Mission parameters such as payload weight, altitude, flight speed and duration, maneuverability and stealth, and the type of launch, control and landing determine the type of UAV to be used. Small UAVs are currently generating great interest as a new frontier of aviation research.

In the following sections operational UAVs from 0.5 to 1.25m span is compared with a remote control flapping wing ornithopter used for this thesis research. This size UAV would typically weigh 0.25 to 1 kg (0.55 to 2.2 lbs), with the weight fractions of its components at 21% for the airframe, 11% for the engine, 30% for the battery, 21% for payload and 17% for avionics [3]. Small and micro air vehicles are desirable for increased maneuverability and stealth on missions which may include urban environments and confined spaces such as disaster zones, where they can provide surveillance and search information as well as monitor air quality for dangerous contaminants. Small UAVs will fly at low altitudes of a few hundred meters or less at speeds under 40 km/h and be capable of obstacle avoidance and waypoint navigation.

Some desirable features of small UAVs are vertical take off and landing (VTOL), hover, and the ability to perch and stare at a target. The UAV should be capable of both human control and full mission autonomy over a limited range, typically a few kilometers based on flight durations averaging one hour or less. Another advantage of small UAVs is that they can be transported and launched by one or two operators for rapid deployment. Their size also corresponds to a reduced radar cross section and a quieter propulsion system through the use of electric motors.

1.1.3 Comparison of Fixed, Rotary, and Flapping Wing UAVs

There are three types of small UAV platforms currently in use or under development; they are the fixed wing, rotary wing and flapping wing. The fixed wing plane is the traditional UAV because it provides a stable, controllable system for a wide range of aircraft sizes and missions. Fixed wing aircraft are challenging to adapt to the low Reynolds number environment of small UAVs because their limited wing span increases the wing loading and decreases lift produced. To avoid this problem the wing chord is extended and the planform takes on a “flying wing” geometric configuration. However, this planform style decreases the aspect ratio and increases induced drag, with the downwash often affecting more than half the wing span adversely. Therefore it is challenging to manufacture a small fixed wing vehicle with good aerodynamic performance. Additionally, most fixed wings cannot perform VTOL or hover over a target without a specialized propulsion system. To acquire the increased mobility and hovering capability desired for the aforementioned missions, rotary wing aircraft such as helicopters and ducted fans have been designed as UAVs at scales of one to two meters or less. While helicopters can provide the necessary maneuverability and payload, they are typically louder and have reduced range in comparison to fixed-wing vehicles. The helicopter rotor system is also complex and unprotected from obstacles which make helicopters prone to maintenance and durability issues. Flapping wing UAVs, or ornithopters, have been proposed as a viable solution to reduce noise, increase stealth, and improve durability over a helicopter while maintaining rotary wing maneuverability. Ornithopters are typically between 0.2 and 2 meters span and are designed using avian flight principles. Flapping wing vehicles with spans under 0.2 m are called emtomopters and are modeled after insect flight. Relative to fixed and rotary wing platforms, ornithopters are still in the experimental research stage. The process of applying experimental and analytical studies of bird and insect flight to the UAV aeromechanical design is a form of biomimetics, or mimicking biology in a synthetic system. Mechanical limitations keep ornithopter systems simpler than birds and insects, and current designs are still working to achieve the maneuverability, controllability and reliability of other UAVs.

Every UAV platform has essential components or systems for successful flight including aerodynamics, propulsion, navigation, communications, and payload integration. The most important of these fundamentals is the production of lift, which is discussed in detail in the following section on low speed aerodynamics. The remaining systems are discussed below for each UAV platform.

To generate thrust small fixed wing platforms use propellers powered by an electric motor and a bank of batteries or a small internal combustion engine that runs on aviation grade fuel. Helicopters generate thrust by changing the angle of the rotor plane to move a component of the lift vector into the path of forward motion; they are also powered by electric motors or internal combustion engines. Some small UAVs use ducted fan engines as an alternative to traditional rotor technology because the fan is guarded to protect both the vehicle and the UAV operator. Ducted fans also combine the hovering or vertical flight of a helicopter with the classical forward flight of a fixed wing when the fan is used as a propeller. The nature of a flapping wing is to produce both lift and thrust by twisting the wing throughout the flapping stroke, for details on this motion see Sections 2.3 and 5.5.1. Circulatory and non-circulatory forces are developed based on the position and acceleration of the wing.

For a specified mission, the communications, power supply, and payload packages are similar for all three UAV platforms. All onboard UAV communication and control systems along with the payload should be capable of operating in the environment on the aircraft including electromagnet interference and inertial loading, which can be in excess of five times the force of gravity for short durations on a flapping wing vehicle [4]. UAVs are controlled by radio frequency transmission from a ground station to the aircraft onboard receiver, with either a pilot in the loop or autonomous control via an autopilot system.

Attitude control is the most important element to achieve maneuverability and autonomy in flight. Fixed wing vehicles control roll, pitch and yaw using ailerons and elevators or just elevons and a rudder; most autopilots assume this control scheme. Flapping wing directional control often mimics bird flight by using a coupled two degree of freedom tail that provides pitching, rolling and yawing control torques; such a mechanism is identified in Section 1.2.2 and Figure 1.9 for the ornithopters used in this thesis research. Characterizing this unconventional navigation system is a challenging segment of ornithopter control research which is being studied in parallel with ornithopter aerodynamics [4]. Unlike fixed and flapping wing vehicles, rotary wing aircraft have no traditional control surfaces for directional control; instead they adjust the angles and position of the swash plate and the tail rotor to maneuver. Each of these navigation solutions is unique and requires a unique solution for implementation of autonomous control.

Fixed wing and rotary wing UAVs have successfully completed missions under piloted and autonomous control. Ornithopters have not advanced to autonomous control because their lift and thrust are generated from the same flapping mechanism which couples the forces, unlike a fixed wing which has separate lifting and propulsions systems. There is also coupling between the rolling and pitching control because they are operated using two servos in series to orientate one control surface. These coupling phenomenon are not accounted for in traditional fixed wing autopilot controls, which is why the aerodynamic modeling presented in this thesis is a prerequisite for developing an ornithopter autopilot control scheme.

1.1.4 Low Reynolds Number Aerodynamics

Maximizing aerodynamic performance is an integral part of UAV design and predicting aerodynamic measures such as the lift, drag, and pitching moment are necessary for autonomous control. Small UAVs are designed to achieve adequate L/D ratios at cruise speeds of 15 to 30 km/h and hover if possible while being stable and easy to maneuver. Aerodynamic efficiency is optimal at the maximum lift-to-drag ratio, $(C_l/C_d)_{\max}$. Lift-to-drag ratio is partially dependent on the local airfoil shape and the total wing shape. The local airfoil camber will determine the lift coefficient produced with respect to the relative angle of attack. Airfoils with large camber have large lift coefficients at small and even negative angles of attack, but they also achieve stall at angles of attack lower than small cambered or symmetric airfoils.

The drag coefficient in the lift-to-drag ratio is the sum of profile and induced drag terms. Finite wings experience induced drag due to lift when an induced velocity is developed due to pressure discontinuities at the wing edges. Induced drag increases with low aspect ratio or “flying wing” designs. Despite the poor induced drag performance associated with flying wings, their implementation using moderate camber, thin airfoils that imitate bird airfoils have shown increased lift-to-drag performance in micro air vehicles [3]. This is because the flying wing is typically flown at high angles of attack like a delta wing so that it can use tip vortices to maximize lift production. The increase in lift counteracts the poor induced drag performance, which can also be alleviated by using flexible wings or winglets at the wing tips. Airfoil camber and flight speed determine the profile drag on an airfoil via boundary layer development; both cambered and symmetric wings can be designed to reduce the profile drag by avoiding laminar separation bubbles at Reynolds numbers below 10^6. Reynolds number is a dimensionless aerodynamic parameter that measures the ratio of inertial forces to viscous forces,

$$\mathrm{Re} = \frac{\rho l_{ref} U_{ref}}{\mu} \tag{1.1}$$

where ρ is the air density, l_{ref} is the reference length (usually the chord length), U_{ref} is the reference velocity, and μ is the fluid viscosity. For an airfoil with a 0.25 m chord length, an average size for the fixed wing UAV with a one meter span, the airfoil would see Reynolds numbers between 75,000 and 200,000 at cruise speeds of 10 to 30 km/hr. This Reynolds number range is a transition region with increasingly poor lift-to-drag ratios for smooth fixed wing airfoils, as identified by Figure 1.1.

At Reynolds numbers below 200,000 the flow is strongly laminar with more significant viscous forces that resist transition. This environment often leads to laminar separation bubbles or complete boundary layer separation on a fixed wing resulting in stall at low angles of attack. Even partial separation increases drag and decreases the maximum lift, leading to the significant drop in the lift-to-drag ratio seen in Figure 1.1. Maintaining an attached boundary layer is critical because it affects the aerodynamic performance and stability and control of the vehicle. The primary means of avoiding boundary layer separation is to encourage turbulent flow over the wing. Turbulent boundary layers have more energy and mixing and therefore resist separation. Birds use the roughness of feathers to induce turbulent transition and maintain attached flow which increases the lift-to-drag ratio. Aircraft also apply rough surfaces as turbulent trips on airfoils just before the start of the adverse pressure gradient to reduce the risk of separation. The improved performance of a rough, turbulent flow airfoil over a smooth, laminar flow airfoil at low Reynolds numbers can be seen in Figure 1.1c.

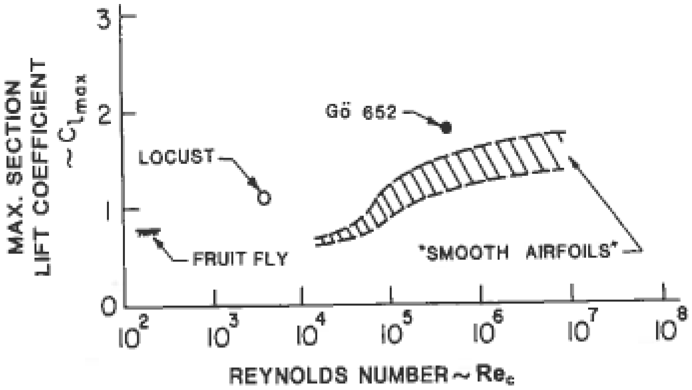

a) Maximum lift coefficient

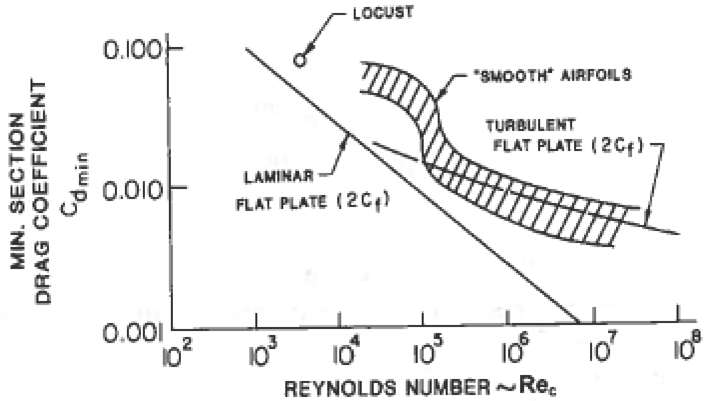

b) Minimum drag coefficient

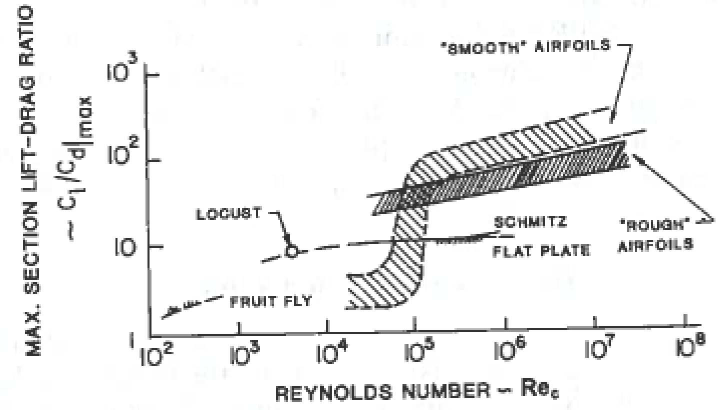

c) Maximum lift-to-drag ratio

Figure 1.1: Lift and drag performance with Reynolds number, [3].

Flapping wing fliers find an additional source of lift and thrust at the very low Reynolds number regime by utilizing the unsteady flow phenomena generated by pitching, bending, and flapping motions of a wing. The added velocity generated from the flapping motion increases the local Reynolds number of the wing, allowing birds to fly at slower speeds. Flapping flight also utilizes dynamic twisting of the wing to maintain a local angle of attack where lift is produced and stall is avoided. The degrees of freedom in the "elbow" and "wrist" of birds articulate the shortening and lengthening of the chord and span. Decreasing span during upstroke or at high speeds reduces parasitic drag by decreasing the wetted area of the wing. Additionally, the spanwise twisting and bendng of the wing help to maintain attached flow and reduce induced drag at the wing tip. Varying the kinematics between the two wings is also a tool used to induce a rolling moment that improves bird mobility. Avian wing kinematics, wing structure, flying techniques, and research in avian aerodynamics are discussed further in Ch. 2.

Rotary wing vehicles can also experience low Reynolds numbers, especially during hover. Techniques for analyzing and optimizing low Reynolds number rotor airfoil and blade designs have been explored by Hein and Chopra [5] and Bohorquez and Pines [6]. Low Reynolds number aerodynamics is an area of growing research and experimentation in aircraft design with many questions yet to be answered; much of what has been learned was gleaned from biological flight [6-11].

1.2 The Ornithopter Research Platform

To date, there are no known studies that track a membrane wing's shape and motion in three-dimensional space and use the experimental information for aerodynamic analysis. In order to complete this research two ornithopters from the University of Maryland's Morpheus Laboratory [12] were selected for analysis, hereafter they are designated the blue and white ornithopters as shown in Figure 1.2. These ornithopters are commercially available and have spans of 1.07m (42") and 1.20m (48"), for the blue and white ornithopter respectively. They were chosen because of their stable and controllable flight behavior and because they have a relatively large payload capacity, with a typical flight sensor suite of 30 grams. The ornithopters are operated via remote control with hand launched take-off and a belly landing upon flight completion.

Figure 1.2: Blue ornithopter with 1.07m (42") span and white ornithopter with 1.22m (48") span.

Additional specifications for ornithopter size, weight and flight performance can be found in Table 1.1. The vehicle mass without payload typically varies between 425g and 450g, with an average payload capacity adding 7% to 10% to this mass. Also of great importance is the flapping rate of the ornithopter, which varies from depending on steady, climbing, turning flight and wind conditions. For the majority of the aerodynamic analysis developed in Ch. 4 and Ch. 5, the flapping rate is assumed at an optimal 5 Hz and 4.5 Hz for the blue and white ornithopter respectively. These two frequencies are typical of steady flight conditions.

Table 1.1: Ornithopter geometry, weight and flight specifications.

Bird	Mass	Span	Max. Chord	Flapping Rate	Speed	Range
Blue	425g	1.07m/42”	0.28m/11”	4.0 – 6 Hz	10-30 km/h	0.8km
White	452g	1.21m/48”	0.36m/14”	3.5 – 5 Hz	10-30 km/h	0.8km

1.2.1 Ornithopter Wing Design and Dynamic Behavior

For steady level flight conditions the ornithopters flap their wings three to six times per second and can reach speeds of thirty kilometers per hour. Wing construction consists of nylon stretched over a network of carbon fiber spars and fingers. The blue and white ornithopter wings are shown in Figure 1.3 and Figure 1.4 respectively. There are two spars, one at the leading edge and another placed diagonally from the leading edge to the rear of the fuselage. Each spar is held in place by a Dacron tape pocket to add stiffness and durability. This spar arrangement creates two regions in the wing, the triangular “luff” region, which is a loose membrane, and the “flap” region which is kept taught by a series of fingers that run from the diagonal spar to the trailing edge.

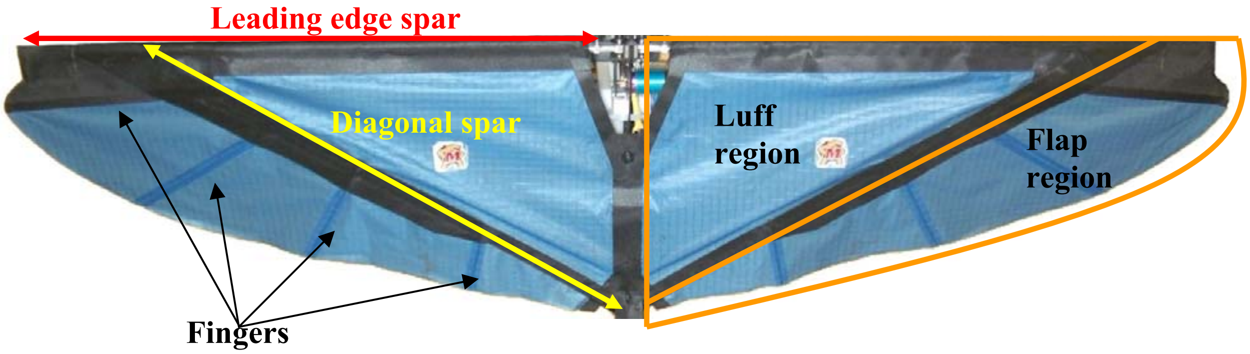

Figure 1.3: Blue wing structure with leading edge and diagonal spars and trailing edge fingers.

Figure 1.4: White wing has a similar structure to the blue wing.

This skeletal and membrane wing structure is more reminiscent of a bat than a bird and the wing behavior exhibits this fact. The flexible skeleton-membrane structure allows for highly dynamic passive shape change as the wing moves through the air, as demonstrated by the high speed photo sequence of Figure 1.5. This flapping sequence shows the downstroke on the left and the upstroke on the right in a counterclockwise circle.

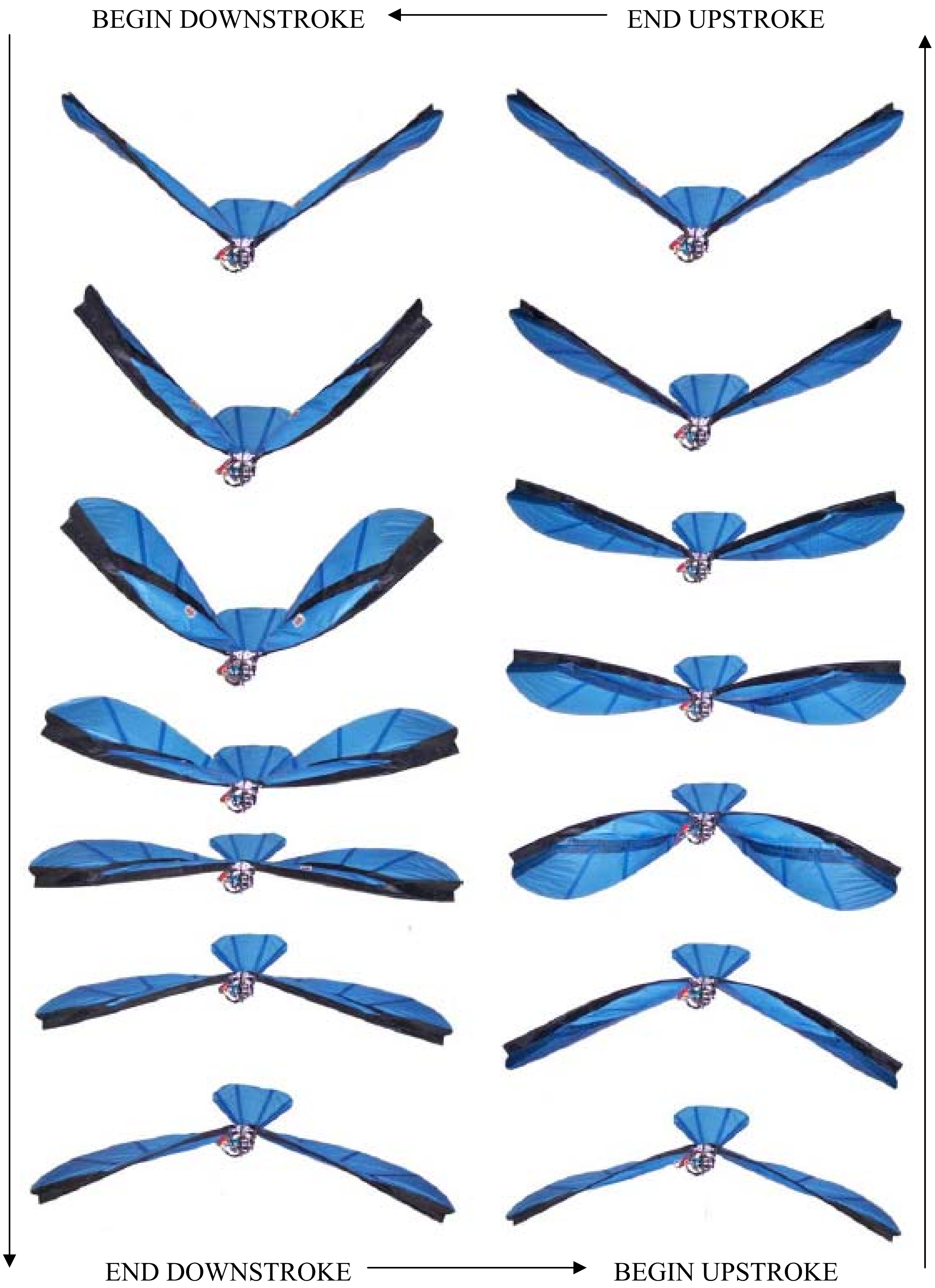

Figure 1.5: High speed photography of the stroke cycle of the blue ornithopter. Down stroke is presented on the left column, starting at the top of the figure and ending at the bottom. Upstroke begins at the bottom of the right column and continues to the top of the right column.

The large degree of bending and twisting visible in the wing is a result of the membrane adjusting its camber and pitch to maintain tension equilibrium throughout its surface when the relative inflow speed and inflow angle change throughout the stroke. At the beginning of downstroke and upstroke the inertial acceleration of the wing causes the leading edge spar to bend significantly around one-quarter and three-quarters of the semi span length. This results in a variation of the local stroke angle along the span and therefore a phase-lag between the wing root and wing tip during the stroke period. Additionally, since the flap region is essentially hinged about the diagonal spar, it experiences a large rotational deflection which acts like a passive flap on an aircraft. The flap deflection, which is the most significant near the wing tip, is also a response to the wing inertia. A consequence of the flap deflection is that the flap's force loading exerts a moment on the wing that increases the pitch into the flapping motion, so if the wing is in downstroke, it will have downward or negative pitch. This pitch adjustment is important to maintain a relative angle of attack with minimual stall, whereas an untwisted rigid wing would experience accelerated flow separation due to the large inflow angles.

The passive morphing behavior of the wing displays the importantance of tracking the wing shape and quantizing the membrane airfoil profile and the local bending and twisting angles. Including the structural behavior in any aerodynamic model is imperitive for accurate results. Membrane aerodynamics and blade element theory can be utilized to capture the structural behavior of the wing and provide improved results over approaches that apply rigid wing and thin airfoil theory methods. Wing tracking and modeling techniques are detailed in Ch. 4 and Ch. 5.

1.2.2 Ornithopter Flight Systems

The flight systems on the ornithopters consist of a drive mechanism and power assembly, remote control receiver, servo operated directional control of the tail, and electronic payload such as an inertial measurement unit or small camera. A unique gear train, shown in Figure 1.6 through Figure 1.8, drives the flapping motion of the wing with the gears varying in size, depending on the desired flapping rate. Unlike most drive mechanisms the gears are integrated parallel to the fuselage rather than perpendicular which reduces the vehicle profile. The crank arm designated in Figure 1.6 provides a slightly asymmetric flapping angle at the wing root which averages five degrees higher at the maximum stroke angle (30˚) than the minimum stroke angle (-25˚). Section 4.4 of this thesis provides a detailed discussion of the measured wing kinematics, including how the local stroke angles and twist angles vary with wing span position.

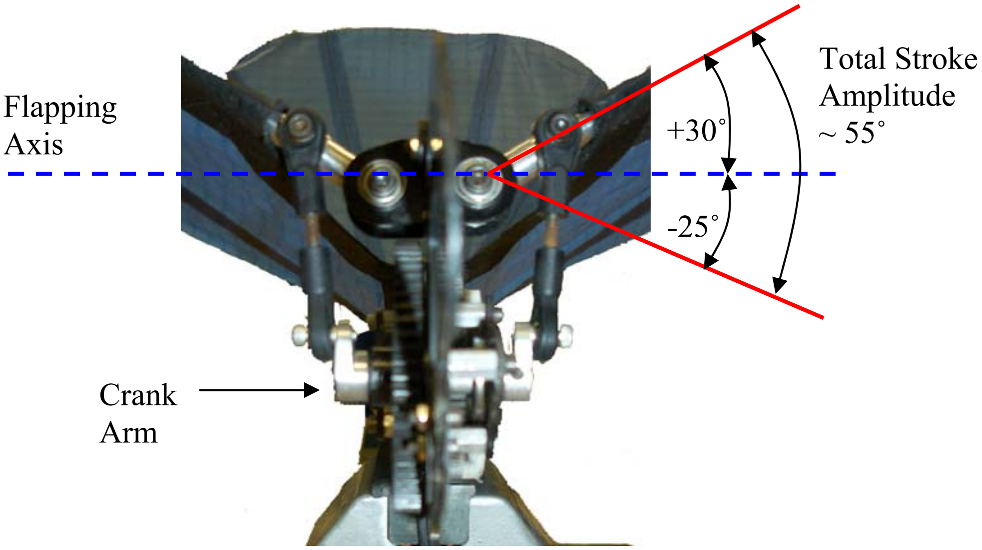

Figure 1.6: Front view of ornithopter shows drive gear and crank arms that flap the wing.

The gear train is powered by a 2 or 3 cell lithium polymer battery with operation between 7.4 and 11.1 volts and durations of ten to twenty minutes depending on battery age, steady or climbing flight requirements, and wind speed. The battery powers a speed controller which takes input from the receiver for voltage regulation to control the electric motor speed and therefore the flapping frequency. These components are identified in Figure 1.7 and Figure 1.8.

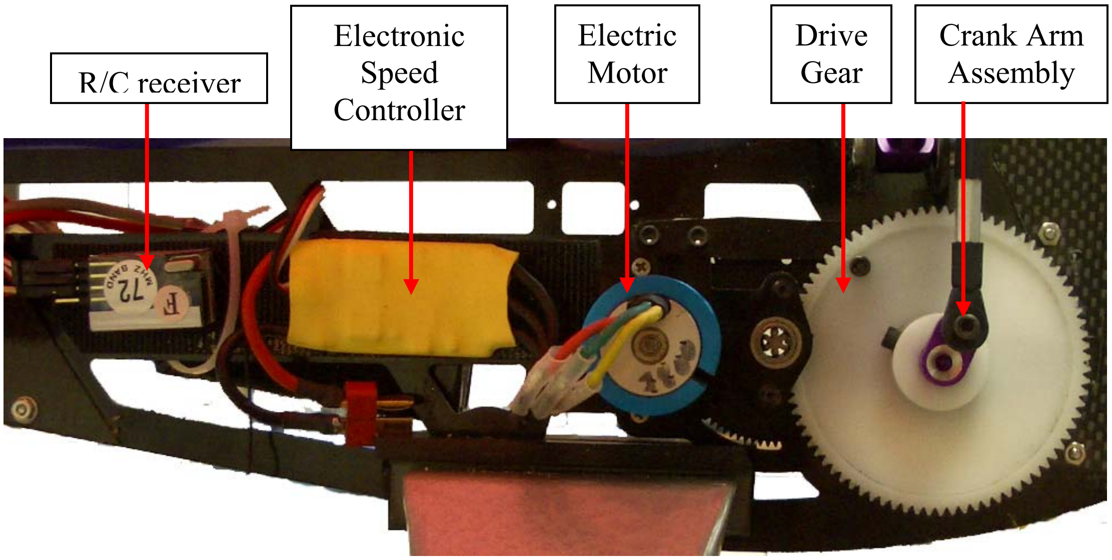

Figure 1.7: Right hand side of ornithopter. Components from left to right include RC receiver, speed controller, electric motor, drive gear and crank arm.

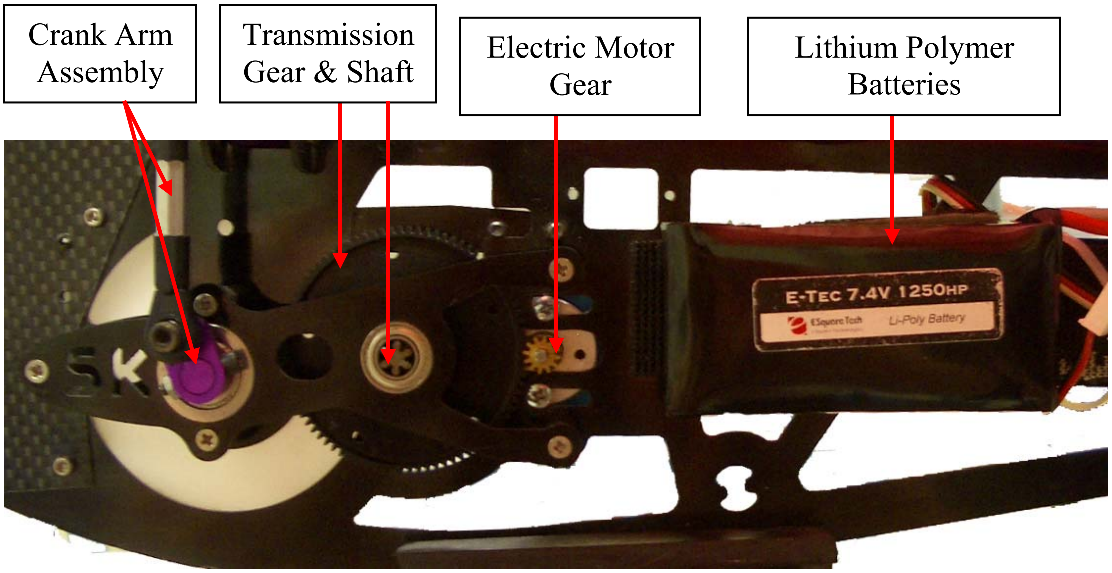

Figure 1.8: Left side of ornithopter. Components from right to left include lithium polymer battery, pinion gear from electric motor, transmission gear and shaft, and crank arm assembly.

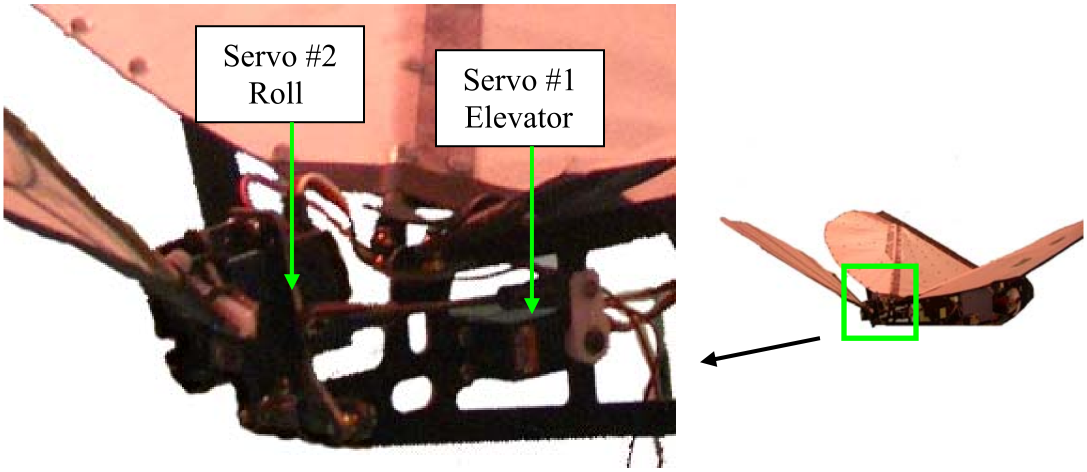

Figure 1.9: Ornithopter tail assembly, right servo controls elevator, left servo controls roll.

The tail assembly shown in Figure 1.9 is operated by two servos, one that provides elevator control and another that provides roll control; their combined action generates drag to develop a torque which induces a turn. The coupling of the elevator and roll motion is another complication in the autonomous control of the ornithopter. This is currently is being examined during the development of a stability and control mechanism for these test vehicles. Now that the research objective, to create a flapping wing aerodynamic model using the wing's structural behavior information, has been established, a study of previous work can be completed.

1.3 Previous Work

Two areas of research are discussed in this section. First, the successful autonomous small UAV designs of industrial and government programs are presented, including fixed and rotary wing platforms. Following this, an overview is provided of the analytical, numerical and experimental research on the aerodynamics of flapping flight. A more detailed discussion of relevant theories and analysis methods are provided in Ch. 2 and Ch. 3, which discuss avian flight and aerodynamic theories, respectively.

1.3.1 Operational UAVs

There are several companies and government programs which produce small autonomous UAVs; one of the most notable is Aerovironment. Three of the smallest successful fixed wing UAVs currently in use for low altitude military surveillance missions are Aerovironment's Raven, Dragon Eye, and Wasp, identified in Figure 1.10. Another small fixed wing UAV platform is the MITE (Figure 1.11), or Micro-Tactical Expendable UAV, which was developed by the US Navy Research Laboratory to explore several different wingspans to optimize performance and payload capabilities. Small companies are abundant in the UAV business, with products such as Theiss Aviation's backpackable Ferret UAV of Figure 1.12, Mission Technologies' gas powered "twinwing" Buster UAV shown in Figure 1.13 and Applied Research Associates foldable Night Hawk vehicle of Figure 1.14. All of these vehicles can be carried to the field and operated by two or three personnel for tactical missions utilizing hand launch, catapult systems or missile type launch from a tube. Vehicle size, weight, speed, and range specifications are given in Table 1.2.

Table 1.2: Operational Fixed Wing UAV Specifications

UAV System	Span (m)	Length (m)	Wt (kg)	Altitude (m)	Speed (km/h)	Endurance (minutes)	Range (km)
AV Raven	1.4	0.9	1.9	30-150	20-57	60-110	10
AV Dragon Eye	1.1	0.9	2.7	30-150	35	45-60	5
AV Wasp II	0.41	0.15	0.28	15-300	40-60	45-60	2-4
AV Wasp III	0.72	0.38	0.43	15-300	40-65	45	5
NRL MITE	0.3-0.5	0.23	0.13-0.35	15-300	16-32	30	1-2
Theiss Ferret	1.0	0.94	2.5-3.2	< 2400	65	unknown	1.5
MiTex Buster	1.25	1.04	6.3-7.8	< 3000	65	4 hours	40
Nighthawk	0.66	0.5	0.7	60-150	33-74	70-90	2-10

Figure 1.10: (Clockwise from top left) Aerovironment’s Raven, Dragon Eye, Wasp 3 and Wasp 2.

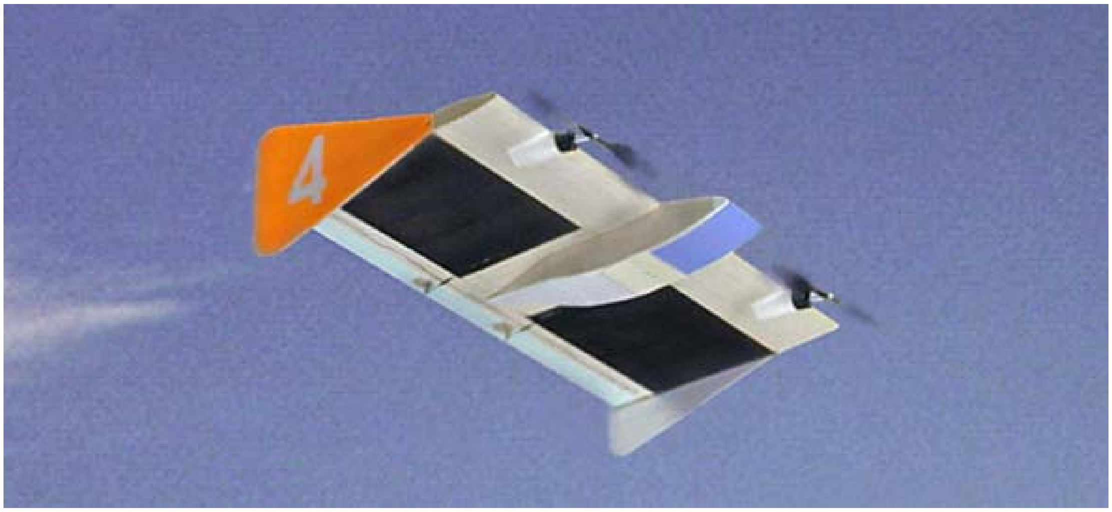

Figure 1.11: Naval Research Laboratory's Micro-Tactical Expendable UAV (MITE).

Figure 1.12: Theiss Aviation Ferret UAV.

Figure 1.13: Buster UAV from Mission Technologies Inc (MiTex).

Figure 1.14: Applied Research Associates Nighthawk Micro Air Vehicle.

The Wasp, MITE and Nighthawk are the smallest vehicles, and therefore experience the lowest Reynolds numbers. Both the Wasp and MITE are “flying wing” low aspect ratio designs with relatively thin and high camber wing airfoils. The Nighthawk’s wings are larger aspect ratio but are also flexible and foldable, with a membrane-like covering over the supporting structure that resembles a bird or bat wing. A very similar in design is shared by the Dragon Eye and Ferret which have equal size and payload capacity. Their wings are a more conventional low Reynolds number airfoil such as those used by hobby vehicles, the chord is large to increase the payload capacity and reduce the wing loading. The Raven has the lowest wing loading, with a large span and low weight it is easily hand launched, can fly at low and high speeds and has larger range and endurance than most of its counterparts. The Buster “twinwing” design is very unique and allows three times the vehicle weight of the Ferret and Dragon Eye by providing more wing surface area. However, the rugged design of the Buster makes it challenging to carry in the field with more equipment required for take-off. Buster also uses a gasoline motor which makes it much louder than its electric competition, but also increases its range and endurance.

Most rotary vehicles also use gasoline powered engines and are heavier than similar sized fixed wing UAVs because they use gas based engines. Rotary wing UAVs are also less common, the most recognized is the Fire Scout, a full size helicopter operated by the US Navy. At the small UAV level it is harder to find helicopter style UAVs, but one example is from a small company called Nascent Technologies which sells complete helicopter setups with the option for multi-vehicle coordinated missions. This complete vehicle system is shown in Figure 1.15.

Figure 1.15: Nascent Technologies Helicopter UAV.

There are alternative rotary solutions to the VTOL problem, and many companies are developing ducted fan technologies. At the mini-UAV level Honeywell has a promising new ducted fan VTOL UAV which just entered mass production for military deployment. This UAV, shown in Figure 1.16, is compact and backpackable at 6.5kg and requires minimal assembly and training to fly missions. The vehicle provides excellent maneuverability in urban environments, but is gas powered and quite loud. This UAV is already being used in military missions to detect IED weapons and provide hover and stare surveillance capabilities.

Figure 1.16: Honeywell Ducted Fan UAV model and demonstrated in active flight tests.

Another successful ducted fan VTOL design is Aurora Flight Sciences GoldenEye 50, shown in Figure 1.17, which can morph into a fixed wing flyer outside of hover, take-off, and landing operations. The GoldenEye's combination of fixed and rotary wing reduces its noise profile and increases its cruise speed and range. Another advantage of these ducted fan designs is safety and ease of operation. There is a significant niche for these vehicles in both civilian and military markets.

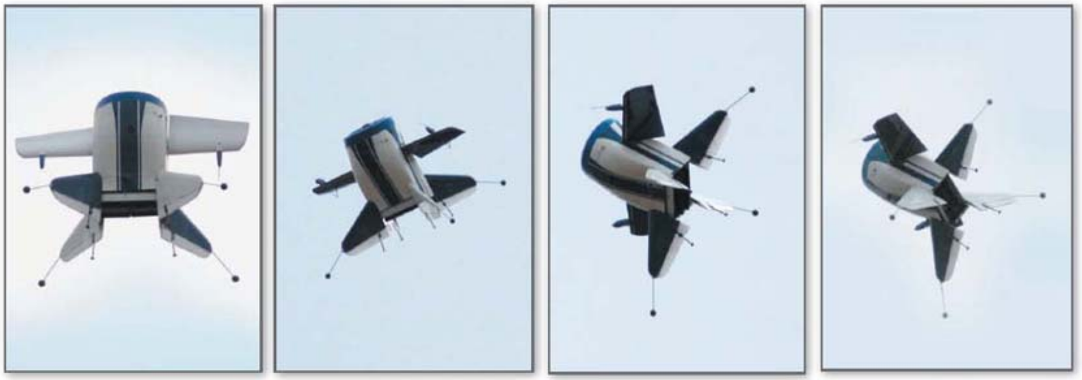

Figure 1.17: Aurora Flight Sciences GoldenEye 50 transitions from vertical to forward flight.

A performance metric of the rotary UAV platforms is provided in Table 1.3. As a whole, the rotary wing systems are much heavier due to their large engines and fuel systems, but this also increases their payload over fixed wing designs. The speed, endurance and range of these vehicles are on par with small fixed-wing UAVs, but they also have VTOL technology which increases mission capability.

Table 1.3: Rotary UAV System Specifications.

UAV System	Span (m)	Length (m)	Wt (kg)	Altitude (m)	Speed (km/h)	Endurance (minutes)	Range (km)
Honeywell	0.33	N/A	8	30-150	N/A	55	N/A
GoldenEye 50	1.37	N/A	9	1500	185	60	N/A
Nascent Tech	1.37	1.5	7-10	1500	65	60-180	4.8

Micro sized flapping wing vehicles are currently in development at several universities and companies for research as well as constructions by individual hobbyists. Though only limited autonomy has beed achieved, many ornithopters carry electronics packages and cameras and can be controlled from a computer rather than a traditional R/C transmitter. These ornithopter and entomopter designs with spans less than 25 cm utilize insect based unsteady aerodynamics to produce lift, including delayed stall, rotational circulation, wake capture, and clap-fling wing motion [13]. Some examples of micro sized ornithopters are shown in Figure 1.18, including Aerovironment and CalTec's Microbat, University of Florida's MAV, University of Toronto's Mentor, the Delfly by the Technical University of Delft, Nathan Chronister's Hummingbird, and the smallest flying ornithopter developed by Petter Muren [7]. The Mentor, Delfly and Hummingbird all have hovering flight capabilities and the Delfly carries a camera for surveillance. Incentive to build Micro ornithopters is strong, generated by government sponsored programs and the International Micro Air Vehicle Competition, which acts to achieve autonomy in flapping flight and act as a technology exchange.

Figure 1.18: Micro sized ornithopters. Top row left to right: Aerovironment/Caltec's Microbat, University of Florida MAV, University of Toronto Mentor. Bottom row left to right: Technical University of Delft's Delfly, Nathan Chronister's Hummingbird and Petter Muren's MAV.

Larger ornithopters with spans of one to two meters are also being produced commercially by hobbyists and experimentally by researchers. These ornithopters have much higher payloads and are more durable than the micro air vehicle designs. Their size also makes these larger vehicles less suceptable to wind gusts which makes them easier to fly outdoors in diverse flight conditions. Two successful commercial ornithopters include the Cybird and Kinkade models shown in Figure 1.19. As discussed earlier in Section 1.2, the Kinkade Parkhawk series of ornithopters was chosen for analysis in this thesis because they are proven reliable flapping wing fliers. The following subsections will provide an overview of technical research in flapping wing and membrane aerodynamics.

Figure 1.19: Cybird (left), Kinkade Parkhawk (right).

1.3.2 Flapping and Membrane Wing Research

The founders of modern flapping flight research are Lilienthal, Lighthill, Ellington, Penneycuick, Rayner, Tucker, Dial, and Weis-Fogh. These aerodynamicists and biologists produced the greatest advancements in flapping flight during the 1970’s and 1980’s, paving the way for current day research. A broad overview of flapping and low Reynolds number flight research is presented in several texts including: *Fixed and Flapping Wing Aerodynamics for Micro Air Vehicle Applications* [3], *Avian Flight* [8], *Aerodynamics of Low Reynolds Number Flyers* [9], *The Biokinetics of Flying and Swimming* [10], and *Biophysical Aerodynamics and the Natural Environment* [11]. Research progress is also summarized in Anders' "Biomimetic Flow Control" [13] and Shyy et al's "Flapping and flexible wings for biological and micro air vehicles" [14]. Additional analytical, experimental and computational studies are summarized in the following sections with further discussion of relevant theories to be presented in Ch. 2 and Ch. 3.

1.3.2.1 Analytical Methods

Analytical approaches to the flapping wing aerodynamic problem can be separated into two realms, quasi-steady models and unsteady models. The quasi-steady model assumes that flapping frequencies are slow enough that shed wake effects are negligible, while the unsteady approach attempts to model the wake. There are six techniques generally used to solve the quasi-steady problem, they include: momentum theory, blade element theory, hybrid momentum theory, lifting-line theory, thin-airfoil theory and lifting-surface theory [16].

Momentum theory provides simple but imprecise measurements of aerodynamic forces and power requirements and requires little aerodynamic background; it is therefore a popular estimation method for biologists. Blade element theory separates the wing into chord-wise sections and applies a two dimensional aerodynamic analysis to each section, such as thin airfoil theory. Each section's aerodynamic forces and moments are then combined to solve the three dimensional problem. Blade element theory is commonly used to solve rotary wing problems and is now being utilized for flapping wing analysis by DeLaurier [17], whose methods are used in part in this thesis. Blade element approaches are also introduced by Shyy

[9], Azuma [10], and Singh and Chopra [18], and can be found in most rotary wing aerodynamics texts. Lifting-line theory is very popular in the flapping wing field, with early application by Betteridge and Archer [19] who combined it with actuator disc theory to predict induced flows, aerodynamic loading and to optimize lift distributions.

Lifting line theory can also be applied to an unsteady wing with wake modeling. A discrete nonplanar vortex element method is utilized by Phlips, East and Pratt [22] assuming a rigid, non-twisting wing. Rayner produced a model that assumes the wing is aerodynamically active only during downstroke, therefore forming a vortex wake of closed rings [23]. Lighthill amended Rayner's model by assuming the upstroke produced the net thrust, and the vortex can be a continuous "concertina" wake rather than requiring starting and stopping vortices at the peaks of a wing stroke [24]. Azuma recently developed an unsteady method for two-dimensional, thin and angular airfoils that utilizes potential theory and Polhamus's leading edge suction analogy; it is especially useful for insect wing airfoils [25].

Many analytical studies of flapping wing flight assume sinusoidal plunging and pitching of the wing. This approach lends itself to the application of Theodorsen's [20] and Garrick's [21] lift deficiency function which accounts for the reduction in lift caused by the sinusoidal wing motion. Additional unsteady affects that can be accounted for include spanwise bending and twisting of the wing, leading edge suction, camber drag and post stall behavior [17].

Membrane wing aerodynamics is another important area of research where many of the same methods can be applied with slight variations to account for the structural/aerodynamic interactions of the membrane. Early research was completed by Thwaites [27], who analyzed the nonlinear membrane equation. Newman presents an excellent overview of linear membrane aerodynamics and solution methods [28]. Current membrane research focuses on nonlinear solutions, computational methods and applications; a summary is provided in Shyy et al's "Membrane wing aerodynamics for micro air vehicles" [15].

1.3.2.2 Numerical Methods

Numerical methods are typically employed to resolve the complex unsteady aerodynamics associated with flapping wings. A thorough investigation of various numerical and experimental methods for the analysis of flapping wing propulsion is presented by Jones et al [29]. A simpler approach is given by Neef and Hummel who formed an inviscid solution to the 2D and 3D Euler equations on a plunging and pitching rectangular wing [30]. Vest and Katz produced an unsteady aerodynamic model and created an experimental test platform to verify their results [31, 32]. Lian et al studies the performance, including stall behavior, of a pitching and plunging airfoil at a transitional Reynolds number of 60,000 by comparing experimental PIV measurements with a variety of computational simulations [33]. A comparison of potential flow methods and high fidelity methods is presented by Willis et al, including the application of wake only, panel and Arbitrary-Lagrangian-Eulerian (ALE) schemes to a flapping wing problem [34].

Membrane aerodynamics problems are extensively solved using numerical methods. Smith and Shyy produced a several articles on computational fluid dynamics and structural solvers for membrane problems [35-37], these are summarized for UAV applications in [15]. An inviscid solution for a nonlinear two-dimensional membrane is given by Vanden-Broeck [38], while de Matteis and de Socio solves the viscid problem with boundary layer separation considerations [39]. A computational fluid dynamics analysis is currently being completed by staff scientists at NASA Langley for the membrane wing examined in this thesis research. Preliminary results are compared with the analytical model in Ch. 5.

1.3.2.3 Experimental Methods

Experimental design, testing, and analysis provide the most important information to the flapping flight field of research because experiments measure actual aerodynamic performance and describe the motion of the wing and the fluid dynamic response to the motion. The aerodynamic design and testing of an ornithopter focuses on the wing and the mechanism driving the flapping process. DeLaurier produced two large scale ornithopters, one model with a span of approximately nine feet and another large enough for a human passenger [40, 41]. His work focused on the wing design, including analysis of structural flexibility, aerodynamic performance and stability and control with documented wind tunnel and flight tests. Raney et al. provides an overview of biologically inspired micro air vehicles and the experimental design of a hummingbird style wing and flapping mechanism that is tuned to the resonance of the structure like an insect [42]. Flapping mechanisms and wing planform design are examined by Malolan et al. who measured lift using strain gauge instrumentation to find the optimal membrane wing design for various free stream velocities [43]. Additional wind tunnel research by this group explored the lift, thrust and unsteady aerodynamic effects on the wing by changing parameters such as aspect ratio, reduced frequency, advance ratio and planform shape [44]. The effect of Strouhal number on the performance of a flapping membrane wing design optimized by Malolan is explored by Aditya, with important results relating to optimal thrust [45]. Another detailed flexible wing design and aeroelastic analysis is given by Unger et al with performance comparisons to a rigid airfoil [46]. DeLuca et al. used wind tunnel tests and XFOIL predictive code to show that flexible membrane wings further delayed stall and increased lift-to drag ratios by 30 percent over rigid fixed wings [47].

Experimental analysis of membrane aerodynamics at low Reynolds numbers is presented by Tamai et al. with research inspiration from bat flight [48]. Particle Image Velocimetry was utilized by Rojratsirikul et al. to study the unsteady aerodynamics of a two dimensional membrane airfoil. This study also includes measurements of the membrane shape, dynamic analysis of membrane vibration modes, and flow visualization as the angle of attack and velocity change to understand the effects of separation on membrane oscillations [49].

There are many more technical papers involving experimental designs and aerodynamic analysis than those provided above. The field of aerodynamic and kinematic research on birds, bats, and insects is examined in Ch. 2 and relevant aerodynamics theories and tools are discussed in Ch. 3.

1.4 Thesis Outline

This thesis is composed of seven chapters; a brief description of each is given below.

Chapter 1: Introduction:

Chapter one provides an overview of UAV history, mission definition and the challenges associated with small UAV's while examining successful small UAV platforms. Flapping wing vehicle designs and related aerodynamic research are explored and the thesis research ornithopters are introduced.

Chapter 2: Avian Flight and Biomimetics:

Chapter two begins with a historical overview of avian flight studies and their influence in the aerodynamic field. An introduction to avian wing structure, kinematics and flight modes is given, followed by a summary of experimental and analytical research of avian flight mechanisms and aerodynamics.

Chapter 3: Aerodynamic Theory:

Chapter three examines relevant aerodynamic theory and its application to flapping flight, including traditional fixed wing aerodynamics, blade element theory, membrane aerodynamics and unsteady aerodynamic affects.

Chapter 4: Wing Tracking Experiments:

Chapter four details the dynamic wing shape visualization and quantization experiments completed on the Morpheus Laboratory research ornithopters as well as lift and thrust force measurements recorded during the testing. These experiments provide vital information about the membrane shape, local wing pitch and bending angles which were used in the aerodynamic modeling.

Chapter 5: Aerodynamic Modeling Theory

Chapter five details the aerodynamic modeling theory starting with the modeling algorithm. Blade element definition and wing geometry are addressed along with quasi-steady wing kinematics. Reference quantities and aerodynamic parameters such as Reynolds number and reduced frequency are analyzed. Drag and power requirements are estimated to establish an optimimum flight condition. Finally, the aerodynamic equations used by the predictive model are presented.

Chapter 6: Aerodynamic Modeling Results:

Chapter six presents results of the aerodynamic model when applied to both ornithopters at their optimal flapping rate and flight speeds. Comparisons are drawn between the vertical and horizontal forces predicted by the model and those measured during motion tracking experiments. The forces predicted by the model are separated into circulatory and noncirculatory components and the contribution of the luff and flap region of the wing is examined. Model results are also compared to computational fluid dynamics predictions for the hovering case. Conclusions are drawn about the models predictive capability and reasons for disagreement with measurements are presented.

Chapter 7: Conclusions:

Chapter seven provides a summary of the thesis and presents conclusions from the research with suggestions for future work in the field.

Chapter 2. Avian Flight and Biomimetics

Bird flight has fascinated humans for millennia, with scientific studies of bird flight starting during the Renaissance and expanding to the current day with the discovery of the laws of fluid mechanics and modern computational capabilities. There are two fields of science that study bird flight: the biomimetic engineers and physicists who wish to develop theories that explain bird flight and use the information to build new flying vehicles, and the experimental biologists who directly analyze birds to obtain an improved understanding of their biological systems. A history of pre-modern avian flight study including its relevance in the development of aerodynamic theory and engineering is discussed in the following section. Later sections provide a detailed description of avian wing geometry and kinematics, followed by a summary of current day avian flight research.

2.1 Historical Influence of Avian Flight Research

Leonardo da Vinci's (1452-1519) dream of engineering a human flying machine provided the first significant insight into fluid mechanics through the study of flying and swimming animals and fluid flow over objects. Da Vinci's experiments, recorded by sketches and notes not deciphered until the nineteenth century, conceptualized the concept of continuity of a fluid as well as the lift and pressure drag forces over a bird wing [8]. His sketches showed the shape of fluid flow over an object and postulated that both the surface area and shape of a body determines the drag it experiences. Da Vinci designed many flying contraptions including a human powered flapping wing vehicle which is sketched in Figure 2.1.

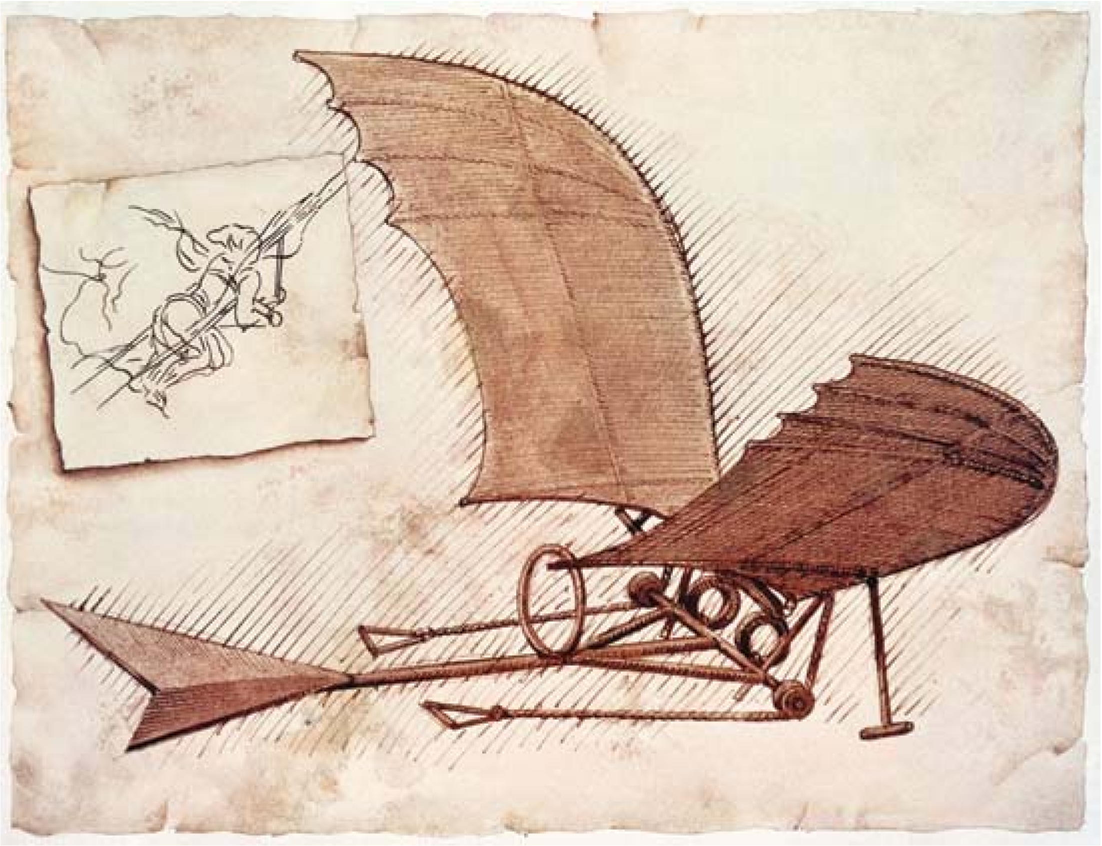

Figure 2.1: Leonardo da Vinci's human powered ornithopter design.

After the Renaissance, a scientific age was born. The modern laws of physics and the principle of conservation of energy arose in the seventeenth century with Newton (1642-1727), Huygens (1629-1695), and Leibniz (1646-1716). Bernoulli (1700-1782) and Euler (1707-1783) used these laws to quantitatively explain the relationship between pressure and velocity in inviscid fluids. Navier (1785-1836) and Stokes (1819-1903) introduced viscosity to Euler's equations and produced the modern day fluid equations which are now solved using computers [8].

Bird flight was also used during the nineteenth century to aid the design of aircraft. Sir George Cayley (1773-1857) studied avian flight and recognized the lift and thrust forces. Cayley produced the first quantitative kinematic data on flapping flight, recording the forward flight speed of birds and the flapping rate and vertical velocity of the wing. His studies of birds and fish led to the design of streamlined bodies including the first airfoil designs which were used to build and test the first flapping manned airplane, which was also unsuccessful.

Cayley was followed by Otto Lilienthal (1848-1896), a German engineer who studied bird wings and kinematics and was the first to measure the lift force generated by a cambered wing using a force balance. He proposed that the outer portion of the wing generated thrust while the interior produced lift and he identified the three types of flight: hover, flapping forward flight and gliding forward flight. Lilienthal built large gliders and flew successfully (Figure 2.2), but later died from injuries sustained while testing a glider. The most significant problem of glider flight at this time was achieving stability and control in an aircraft; the Wright brothers would solve this problem by using a wing twisting mechanism to adjust lift on each wing and induce a turn. This technique which is adapted from avian flight is also used by Abdulrahim et al. on a modern flexible membrane fixed wing UAV [51].

Figure 2.2: Otto Lilienthal's successful gliding attempt.

With the invention of the camera, the first high speed photographs of flying birds were taken in the 1890's by Marey (1830-1904), shown in Figure 2.3. Marey used the photographs to analyze the kinematics of the flapping motion. From the photographic studies Marey postulated eight kinematic rules of avian flight which can be partially identified in Figure 2.3, [8]. While modern research has found these rules to be sometimes inaccurate, they do note trends in kinematic behavior:

1. The downstroke lifts the body and increases the speed; the upstroke also generates lift but decreases the velocity.
2. The wing tip describes an elliptic trajectory
3. The direction of the movement of the trajectory is such that the wing tip goes forward and downward, and upward on the way back.
4. The wing is extended and almost flat during the downstroke.
5. During the upstroke the surface of the wing is inclined with respect to the flight direction, the underside faces forward.
6. The duration of the downstroke is generally longer than that of the upstroke.
7. In flight the wing is only rigid during the downstroke and partly folded during the upstroke.
8. During the upstroke the primary feathers (tip feathers) rotate around their longitudinal axis. These feathers leave slits to let the air pass freely.

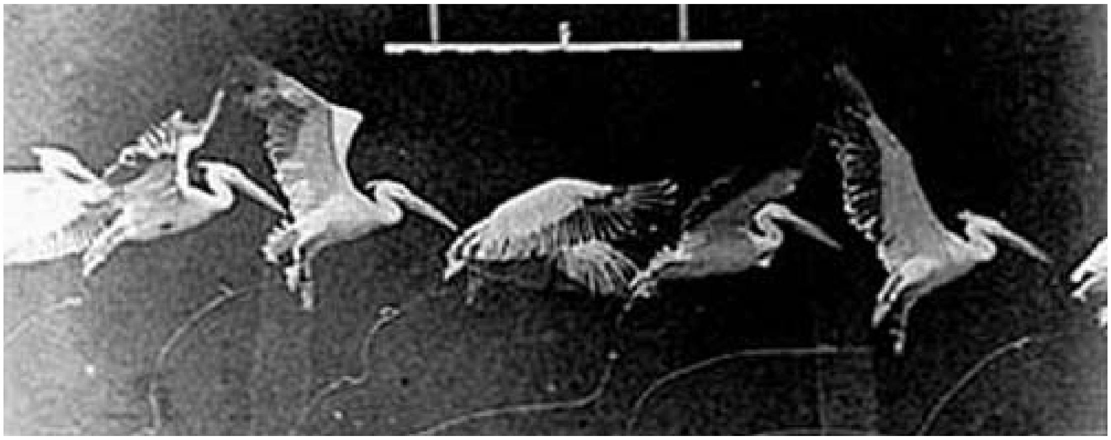

Figure 2.3: First high speed photographs of bird flight, a stork, taken by Marey, [8].

Marey also designed and completed experiments that monitored the flight muscles and wing beat of flying birds as shown in Figure 2.4. To understand the lift forces during the flapping motion Marey built mechanical models and complex test equipment to measure the pressure changes around the wing. These tests revealed the need for a drag coefficient in addition to measuring drag based on surface area.

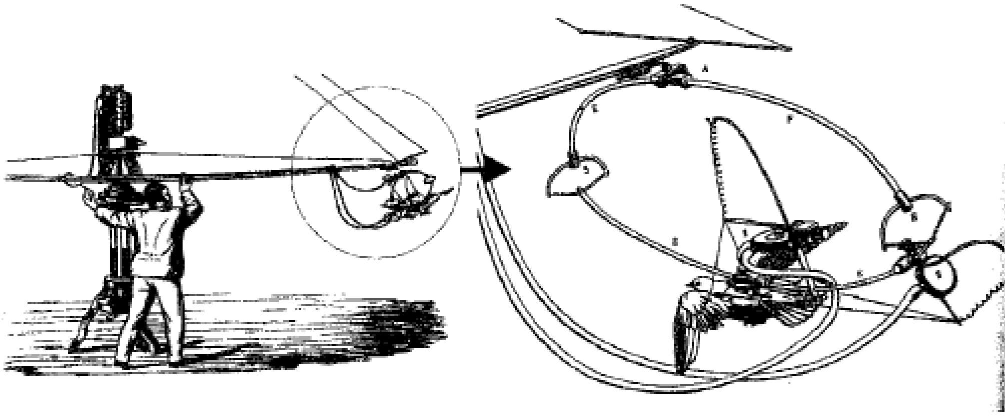

Figure 2.4: Marey's experiment setup to examine birds in flight, [8]

By the turn of the twentieth century engine powered airplanes were being constructed and avian inspired flight was put to the side as a source for human transport. Wind tunnels were soon in use and experimental and theoretical knowledge grew dramatically leading to Prandtl's discovery of the boundary layer and commercialization of fixed and rotary wing aviation. Research into avian flight and wing structures was pursued primarily by biologists during the first two-thirds of the twentieth century as fixed wing aviation grew. Unmanned air vehicles brought back the fervor for flapping flight as small biomimetic UAVs became desirable in the 1980's with advancements in low Reynolds number flows and unsteady aerodynamic theory. Today engineers and biologists are working together to solve the small and micro UAV challenge using avian and insect flight techniques.

2.2 Wing Structure

In addition to the forward motion that a fixed wing experiences, a bird wing also flaps up and down, sweeps forward and back, twists along the span, and folds to adjust the wing wetted area. The bone, joint and feather structure of birds and bats is integral to understanding the kinematics of the wing. Compared to the human arm in Figure 2.5, the bird skeleton has a shortened humerus bone in proportion to the radius and ulna, and the wrist and fingers, or "hand wing", are fused to support the weight of the primary feathers and provide strength to the wing tip [8]. A bat on the other hand has long rib-like fingers which support the membrane covering and provide the ability to alter camber and tension in the membrane for lift adjustments and dynamic control. The bat wing also has a membrane section forward of the arm bones that behaves like a leading edge flap to help maintain attached flow for a wide range of angle of attack; future ornithopter design may emulate this wing structure.

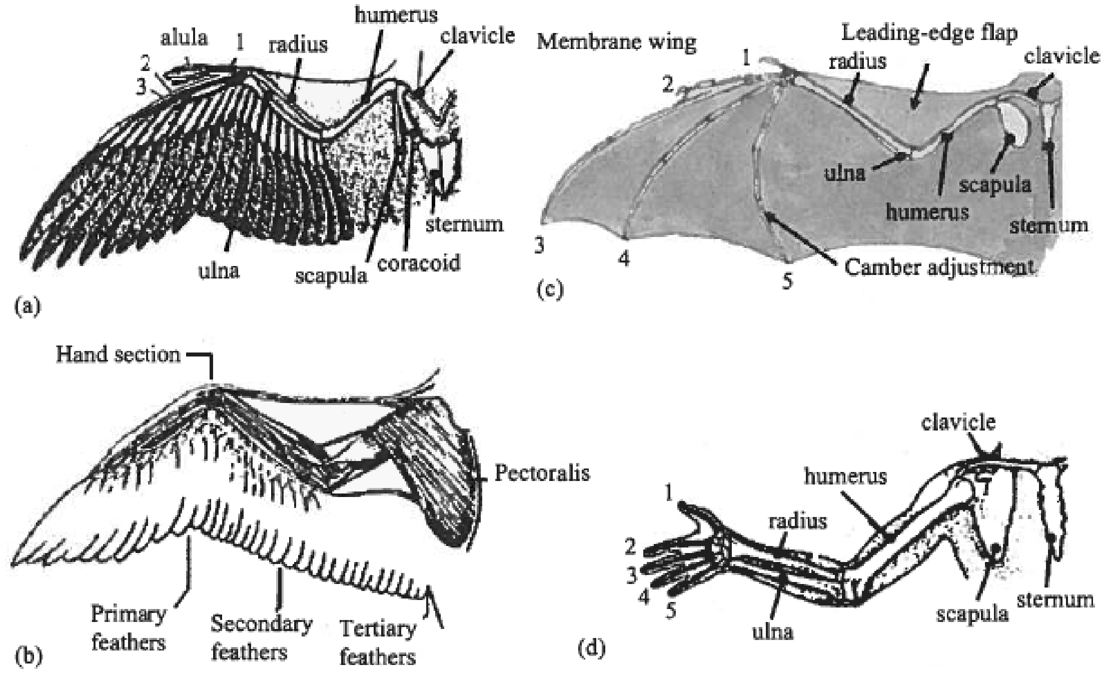

Figure 2.5: Schematics for (a), (b) a bird wing, (c) bat wing, (d) human arm, [9].

Every bird species has different proportions in the arm and hand bones which are optimized for its dominant flight mode, some scaled examples of avian wing skeletons are shown in Figure 2.6. The hand wing, shown between the two vertical lines in Figure 2.6, provides the dynamic control for the bird and can comprise as much as eighty percent of the wing length for small birds which fly in highly unsteady flight conditions, such as hover [8]. Arm bones in larger birds compose 40% to 60% of the total wing length because they fly at higher Reynolds numbers in quasi-steady flows and use prolonged gliding. Slow flapping or gliding flight modes benefit from a larger region of secondary and tertiary feathers that can act like a fixed wing. The longer arm wing also allows for more bending and spanning to reduce drag on upstroke and vary the wing area. To demonstrate the influence that bone proportion has on flight, a hummingbird is compared to a hawk in Figure 2.7 and Figure 2.8.

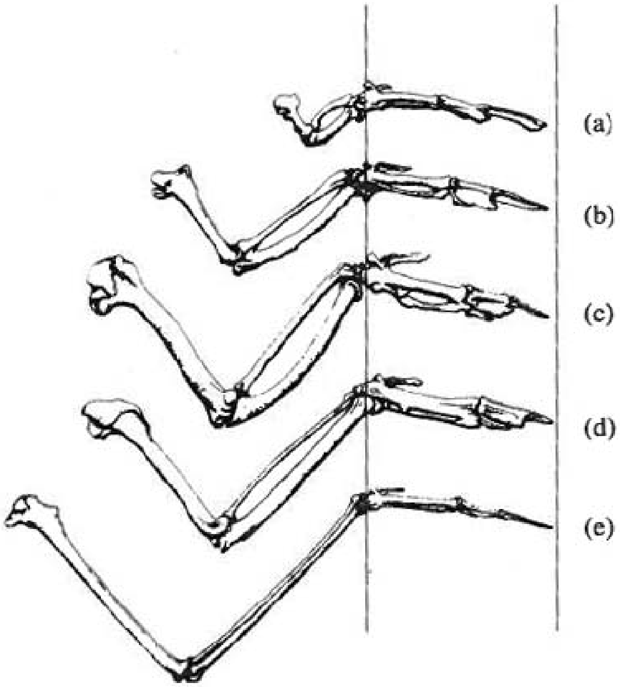

Figure 2.6: Proportion of hand wing to arm wing, for (a) Calliope hummingbird; (b) Rock dove; (c) Blue grouse; (d) Starling; (e) Albatross, [8].

Figure 2.7: Hummingbird in hover mode.

Figure 2.8: Soaring flight of a red tailed hawk with separated primary feathers.

The behavior of the wing covering material is also essential to achieving flight. Bird wings utilize feathers to support themselves in the air, while bats and insects use a membrane reinforced by the skeletal structure of the wing. Both feathered wings and membrane wings provide a thin, highly cambered lifting surface that varies in shape along the span.

Early structural and aerodynamic analysis of bird wings as fixed airfoils was completed by Withers in 1980, [52]. Recently, Liu et al. used non-contact surface measurements to create three dimensional computer models of bird wings and develop equations to characterize the wing planform, camber and thickness along the span [53]. The modeled airfoil shapes of the avian wings are then compared aerodynamically using XFOIL with the high lift low Reynolds number S1223 airfoil for a range of angle of attack. Liu also developed a two joint kinematic model of the wing by simulating the shoulder and elbow motions of the birds as they were captured on high speed video. Shyy also examines the similarities and differences between avian and fixed wing airfoil sections along the wing span as shown in Figure 2.9 [9].

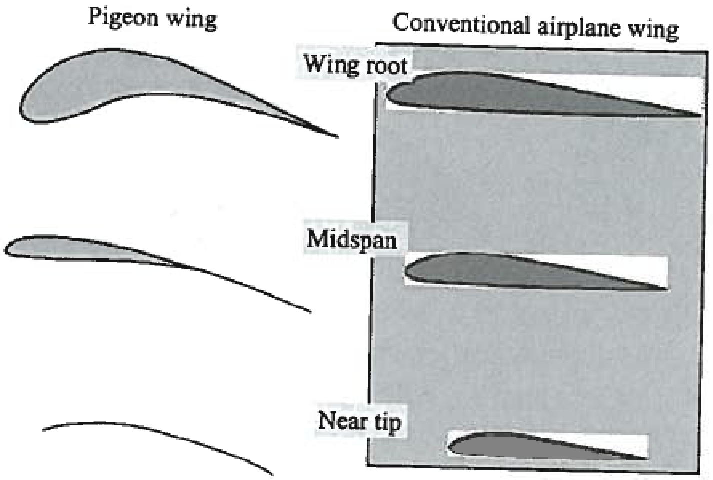

Figure 2.9: A pigeon airfoil versus a conventional wing at the root, midspan and wing tip, [9].

Note the thick, high camber leading edge near the root of the avian wing which provides large lift values. The wing airfoil quickly thins to a very sharp trialing edge because it is composed of feathers with no bone structure, making it highly flexible and very structurally responsive to aerodynamic loads. This flexibility allows the feathers near the trailing edge to morph the airfoil shape by lifting up and reducing the adverse pressure gradient to reattach flow as stall is breached.

The avian airfoil shape improves the low Reynolds number aerodynamic performance over a traditional low-speed fixed wing which is prone to stall at low speeds and high angles of attack. Birds avoid stall at these conditions in part because the leading edge roughness or “leading edge comb” which provides a turbulent trip to encourage attached flow and alleviate laminar separation bubbles from forming. Leading edge comb in owls has also been shown to create a stationary spanwise vortex sheet over the primary feather region which prevented flow separation and alleviated laminar separation bubbles on the outer portion of the wing [10].

Leading edge comb is one of many unique evolutionary developments in feathers and wings to improve flight performance and stealth. When combined with a jagged leading edge, the wooly leading edge comb of owls reduces the sound generated by the wing motion and makes the owl a very successful stealth hunter. The alula or “bastard wing” which is shown in Figure 2.5a acts like a leading edge flap to maintain attached flow on the outer wing at high angles of attack. The tail can also be used as a high lift device when operated as a slotted trailing edge flap to increase the wing camber. Many birds that utilize soaring to minimize power requirements also have slotted primary feathers under full wing extension, such as the hawk in Figure

2.8. Much like a winglet on a plane, slotted primary feathers increase the spreading of the vortex wake which reduces kinetic energy in the wake and therefore decreases the induced drag [54]. The reduction of induced drag also extends the operating range of the wing to higher angles of attack before the onset of stall. This practice can lead to a significant increase in lift to drag ratios and simulate an increase in span and aspect ratio. Adapting these high performance techniques to UAV design could provide significant improvements in performance.

2.3 Wing Kinematics

In addition to bone proportion and structure the rotational mobility in the wing joints, particularly the shoulder, define a wing's motion. Rotation about the "universal" shoulder joint is powered by the pectoralis muscles and includes three types of motion: flapping, feathering, and lead-lag; each is described below.

- *Flapping*: The up and down plunging motion of the wing. Flapping produces the majority of the bird's power and has the largest degree of freedom with a typical range of motion between forty degrees down and ninety degrees up. The flapping cycle of the wing is broken down into two components, *1) downstroke* or *power stroke*, when the wing moves from its uppermost to its lowermost position, *2) upstroke* or *recovery stroke*, when the wing moves from its lowermost to its uppermost position.
- *Feathering*: The pitching angle of the wing. It can vary along the span due to rotation in the shoulder, elbow and hand joints and also from the flexibility of the feathers and bone structure. Positive or pitch up motion of the wing is called *supination* while downward pitch is referred to as

pronation. Birds can vary pitch angles between the left and right wings to induce a rolling moment for directional control.

- *Lead-lag*: An in-plane lateral rotation of the wing about the bird's vertical axis, it is positive for forward or leading motion.

These three rotations can be idealized as Euler angles about the bird's body axis system as shown in Figure 2.10. The elbow and hand joints of the wing are also instrumental in adjusting the twist, bending and spanning or folding of the wing to optimize flight performance and maneuverability. When combined with the bending and spanning motion of the elbow and hand wing, the three rotational motions of the shoulder result in an adaptive structure capable of producing lift, thrust and directional control for all flight modes.

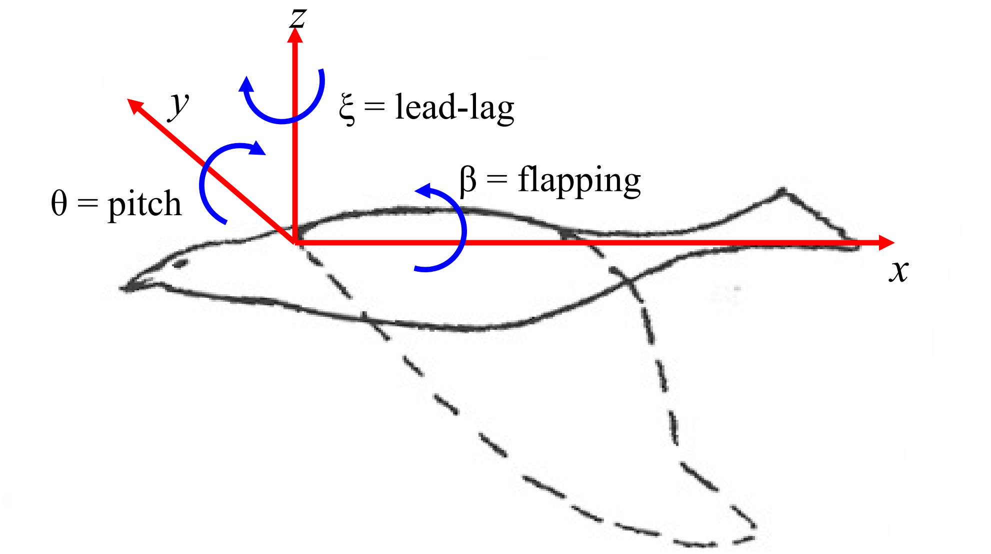

Figure 2.10: Three angular motions of the wing: flapping β, pitching θ, lead-lag ξ.

The flapping motion is of primary importance because it generates the lift and thrust forces that enable flight. Near the wing tips where the vertical induced flow from flapping motion is large the leading edge of the wing must pitch into the flapping direction to maintain attached flow. Therefore the pitching motion is also critical to achieve flight. The forces generated by a positively cambered flapping wing during upstroke and downstroke are shown in Figure 2.11. Maintaining positive angle of attack during upstroke requires significant upward twist because the downward inflow angle due to the flapping motion increases with increasing span position. If a positive angle of attack is achieved, the lifting force will be upwards and backward, increasing the drag on the wing. However, if the angle of attack on upstroke is negative, the lift vector will be negative and forward, creating thrust but also causing negative lift. During downstroke, the wing is always at a positive angle of attack with significant upward inflow near the wing tip. The relative inflow tilts the lift vector forward so that it produces thrust, especially near the wing tip. This reasoning shows how the motion of the wing tip is instrumental in increasing thrust and decreasing drag, while the interior of the wing primarily produces lift.

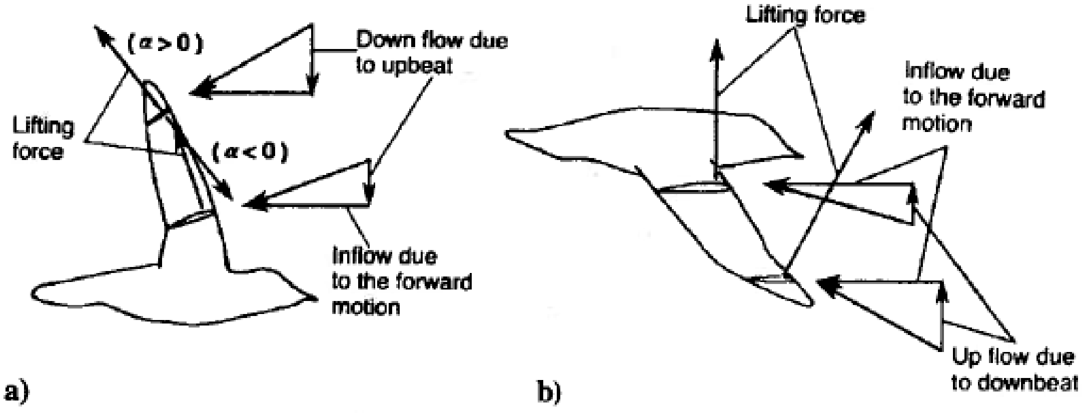

Figure 2.11: Forces generated by a flapping wing during a) upstroke and b) downstroke, [10].

Each bird, bat or insect uses a different type of wing motion to fly, and they are generally categorized by the path of the wing tip during one beating cycle, as shown in Figure 2.12. Wing tip paths also vary based on flight modes including taking off and landing or flight speeds. Two common tip path shapes are ovals and figure eights. The line connecting the top and bottom of the tip path is called the stroke plane; it varies from vertical for forward flight to horizontal for hovering.

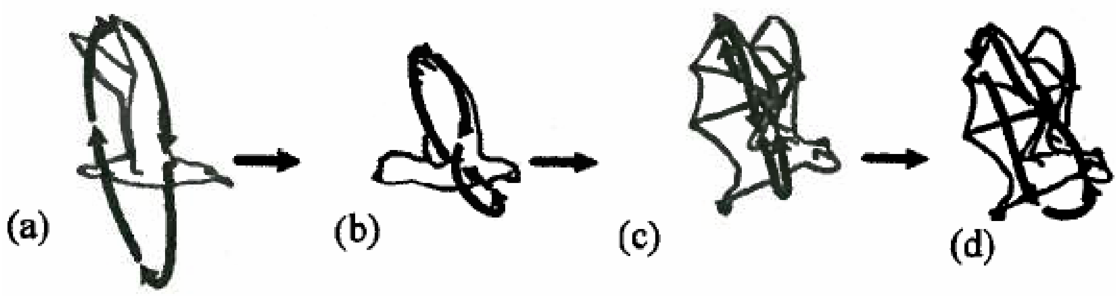

Figure 2.12: Tip paths for (a) albatross, fast gate; (b) pigeon, slow gate; (c) horseshoe bat, fast gate; (d) horseshoe bat, slow gate, [9].

Experiments similar to the reflective marker motion tracking experiments of this thesis (Ch. 4) were completed by Tian et al. on bats to identify the exact kinematic motion of the membrane wing in conjunction with PIV measurements of the wing wake velocities [55]. This work from Tian et al. provides a source of comparison for the thesis because it identifies the behavior of a membrane wing in a successful natural flyer. Findings of the bat flight research included characterizing the wing tip motion, which shows an elliptical tip path with wing extension during the downstroke and a wing contraction during the upstroke. Tian et al. also modeled the wing beat frequency and amplitude at the wing tip using a Fourier series, a method that can be utilized to reduce data to an accurate kinematic model.

2.4 Flight Modes

Flapping flight is the traditional cyclic power source utilized to gain or maintain altitude and speed, hover, or act as a tool for take-off, landing and maneuverability [10]. Forward flapping flight or cruising flight is typified by slow to moderate flapping rates of two to four Hertz for large birds with high aspect ratio wings and faster rates of four to ten Hertz for small birds such as sparrows. As explained in the previous section, large birds in flapping flight utilize the inner portion of the wing for lift and the outer portion of the wing for thrust, this helps to maximize their cruising flight efficiency. Analysis of steady cruising flapping flight presents the simplest, quasi-steady aerodynamic case and therefore is the primary focus of the aerodynamic model in this thesis.

Both take-off and landing are accomplished at high angles of attack with typical push off and landing angles of seventy degrees [8]. The take off requires the bird to push off with it legs at a force of one to four times its weight in order to gain altitude as it begins to flap. Landings are generally approached from a glide and use a few cycles of flapping at the end of an approach to maneuver and reverse the thrust and momentum of the bird so that it can land safely.

Maneuverability is a measure of the speed and radius of a turn that can be achieved in flight. Turning results from a rolling moment caused by variations in lift produced by the right and left wings. Three methods commonly used by birds and bats to achieve this rolling moment are downstroke velocity asymmetries, angle of attack asymmetries or surface area asymmetries between the wings. Warrick and Dial studied the kinematic mechanisms used in the maneuvering flight of pigeons and discovered they utilize variations in downstroke velocities between the wings to induce a banking angle, with counteracting motions active in the upstroke [56]. Norberg and Rayner studied the wing morphology in bats via the aspect ratio and its effect on optimal flight speed, power requirements and maneuverability. They found the turning radius of a flapping bird or bat is limited by the wing loading and flight speed, with lower wing loading and low speeds producing the smallest turns [57].

Whether a bird utilizes forward flapping flight, gliding or hovering is largely determined by wing size, structural proportion and the flight path to be covered. Long duration hovering is achieved only by the smallest birds and insects which utilize highly unsteady aerodynamics to fly. Birds achieve hovering by bringing their body to a vertical position so the wings can track a horizontal figure eight motion, much like treading water; a hummingbird's hover stroke is identified in Figure 2.13.

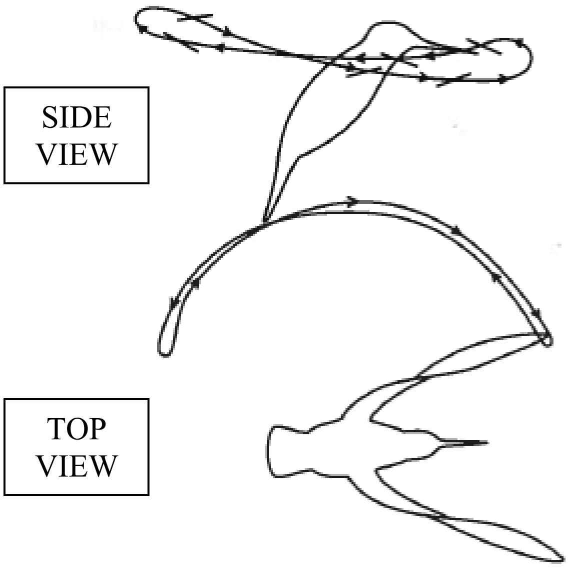

Figure 2.13: Tip path's of a hovering hummingbird, [8].

The kinematics for hovering flight at flapping rates up to seventy times per second requires very low inertia wings with large degrees of freedom. Hummingbirds attain this motion by maximizing the hand wing dimension and minimizing size and motion of the arm wing. Larger birds can hover briefly but generally lack the ability to quickly rotate the angle of attack between forward and backward strokes; instead they fold the wing on upstroke to reduce drag. Hovering in large birds is used temporarily for maneuvering and landing. “Windhovering” matches the forward speed to the oncoming wind speed to achieve a hover condition; this technique is used by birds to isolate prey and could be utilized on a UAV for point and stare purposes.

Gliding and soaring flight is very common among medium and large birds and bats which have a large wing surface area. While any air vehicle can glide, those that maximize their glide ratio, a measure of how far a vehicle flies horizontally to the amount of altitude it loses, are the most effective. Many birds have glide ratios in the 10:1 to 20:1 range, and sailplanes can achieve glide ratios up to 60:1. There are many techniques to supplement a glide such as thermal, gust and dynamic soaring which extract energy from the air to gain altitude and speed. Small birds often fly sinusoidal paths in altitude, with flapping flight to increase speed over the lower part of the cycle and closely folded wings over the top of the path. This intermittent flap-bounding method minimizes energy expenditure for birds that cannot achieve prolonged glides.

2.5 Aerodynamic Parameters

As with fixed wing flight, there are important non-dimensional parameters that provide insight into flapping flight aerodynamics and performance. The flapping kinematics are essential to developing and understanding these parameters.

2.5.1 Reduced Frequency

An important non-dimensional parameter of forward flapping flight is the reduced frequency *k*, a ratio of the flapping velocity to the reference velocity

$$k = \frac{\omega c_{ref}}{2U_{ref}} \tag{2.1}$$

In Eq. (2.1) ω is the angular velocity of the flapping wing, c_{ref} is the wing's reference chord length and U_{ref} is the reference velocity which is the forward flight velocity. Reduced frequency indicates the degree to which unsteady aerodynamic effects are present. As k approaches zero the wing tends toward a quasi-steady state while slow forward flight with large flapping frequencies result in unsteady flows [9].

2.5.2 Strouhal Number

Another non-dimensional parameter that describes kinematics of flapping flight is the Strouhal number, which divides flapping frequency f and vertical wing tip amplitude A by the forward vehicle speed U.

$$St = \frac{fA}{U} \tag{2.2}$$

Strouhal number has been shown to indicate propulsive efficiency, a measure of mechanical power input to mechanical power output. Efficiencies as high as 70% have been achieved within the optimal Strouhal number range of $0.2 < St < 0.4$ with a peak efficiency at St ~ 0.3. Taylor et al. summarized this phenomenon, noting that peak efficiency occurs "when the kinematics cause maximum amplification of the shed vortices in the wake and an average velocity profile equivalent to a jet" [58]. Clearly Strouhal number is an important parameter that should be considered when optimizing a flapping wing design. Aditya and Malolan completed experiments on a flapping membrane wing utilizing Strouhal number to optimize thrust [45].

2.6 Experimental Research in Avian Flight Theory

Biological avian flight research since the 1950's has focused on establishing empirical formulas to understand wing sizing, flapping frequency and forward velocity. These findings, as well as studies of aerodynamics and muscle use are often utilized in calculating the power requirements for various flight modes. Power calculations are very important when understanding flight patterns that optimize range, endurance or speed; this is often the goal of avian flight research. The pioneers of this spectrum of avian flight research include Pennycuick [59, 60], Tucker [54, 61], Rayner [23, 57], Spedding [62], and Lighthill [24, 63]. Relevant empirical results and aerodynamic modeling methods of these and other researchers are now examined.

2.6.1 Empirical Results

Several empirical results have been established relating avian sizing, such as wing area S, bird mass m or weight W, to the optimal flapping frequency, flight speed, power available and power required for flight. The geometry of the wing is generally determined by the mass, with the span b and area S given by Eqs. (2.3), with wing area and wing loading relations varying based on the type of bird.

$$\begin{gathered} b = 1.704 m^{1/3} \\ S \sim m^{0.71} \quad or \quad S \sim m^{0.78} \end{gathered} \tag{2.3}$$

It is also possible to relate the airspeed U of the bird to its wing geometry or mass by examining airspeed versus lift coefficient or airspeed versus wing loading [9].

$$U = \sqrt{\frac{(W/S)}{0.5\rho C_L}} \propto \sqrt{l} \propto m^{1/6} \cong S^{1/4}$$

$$U \propto \left(\frac{W}{b^2}\right)^{0.55} \tag{2.4}$$

The wing beat frequency range for birds can also be related back to the mass through the use of the aerodynamic power, P_A, which is proportional to the product of the wing area and the cube of the tip speed, by the relation $P_A \propto m^{5/3} f^3$. Flapping frequency is also related to the power generated during flapping via $P_A \propto m^{2/3} f$. Combining the two power relations gives the final relation for maximum flapping frequency f_{max} given in Eq. (2.5). Some texts also limit the maximum flapping rate based on how much heat the body can sustain.

$$f_{\max} \propto m^{-1/3} \tag{2.5}$$

The lower flapping rate boundary is determined by the induced velocity at low speeds which must still support the lift of the bird as shown in Eq. (2.6), [9].

$$f_{\min} \sim \frac{w_i}{l} \propto l^{-1/2} \sim m^{-1/6} \tag{2.6}$$

An exact relation for the flapping frequency given in Eq. (2.7) was developed by Pennycuick in the examination of fourty-five different bird species; it includes a dependence on weight, wingspan, wing area, wing inertia and air density.

$$f = (mg)^{-1/2} b^{-17/24} S^{-1/3} I^{-1/8} \rho^{3/8} \tag{2.7}$$

2.6.2 Aerodynamic Models

Many methods have been utilized to study flapping wing aerodynamics, from momentum theory to blade element analysis to vortex wake studies and computational fluid dynamics. The following sections will introduce the techniques and important findings from momentum theory and vortex wake analysis, a more thorough discussion of aerodynamics is presented in Ch. 3.

2.6.2.1 Momentum Theory

Momentum theory is often used to generate a “back of the envelope” estimate of induced aerodynamic forces and power requirements, as well as the vertical and horizontal induced velocities. The theory models the circular swept area of the flapping wing as an actuator disk which accelerates the surrounding air, increasing its momentum. All momentum changes must act via an induced velocity whose energy balances the thrust and lift or equivalently the vehicle drag and weight in steady flight. Momentum theory requires that the induced velocity field across the span be uniform. While this approximation is not realistic, it may only vary by 10% from the actual distribution, which is highly non-uniform and challenging to calculate.

The following presentation of momentum theory is adapted from Azuma’s *Biokinetics of Flying and Swimming*. Figure 2.14 pictures a bird at a flight path angle γ, angle of attack α, and flight speed U. The total induced velocity w has parallel and normal components u and v respectively. The mass flow must be constant for momentum theory; therefore the mass per unit length is given by Eq. (2.8).

$$m = \frac{\pi b^2}{4} \rho U \tag{2.8}$$

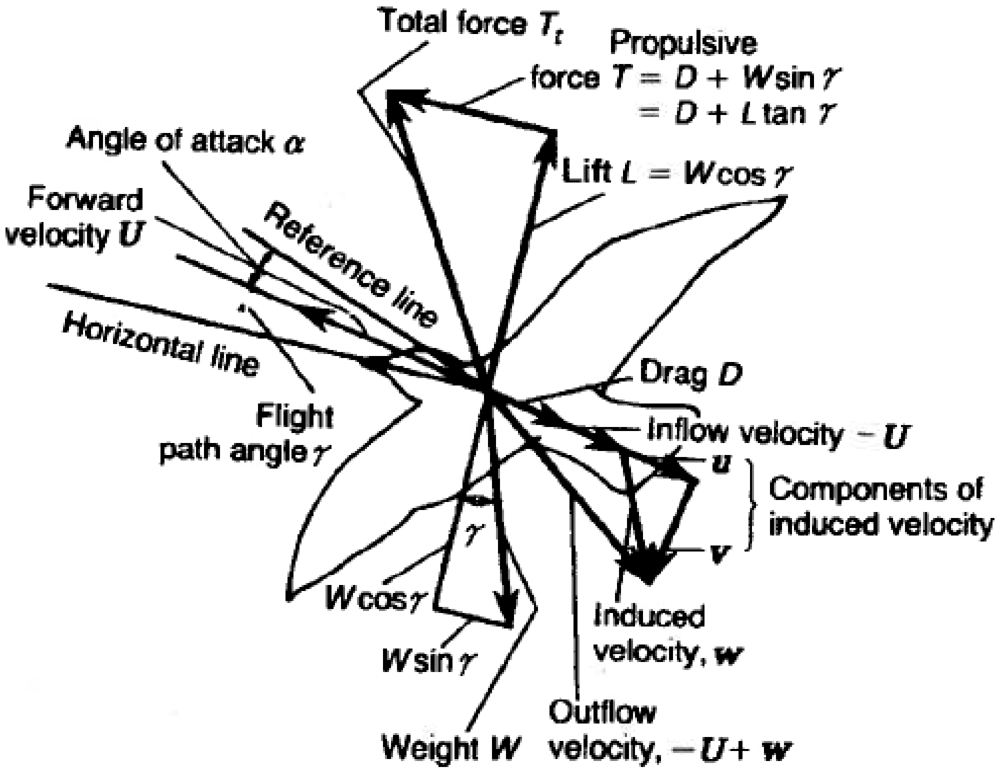

Figure 2.14: Representation of induced velocities and forces, [10].

Lift equilibrium is established by setting the weight component equal to the lift and the downward momentum as shown in Eq. (2.9), where the factor of two comes from the fact that the induced flow is doubled far downstream.

$$W\cos\gamma = L = 2mv \quad \rightarrow \quad v = \frac{2L}{\pi b^2 \rho U} = \frac{2W\cos\gamma}{\pi b^2 \rho U} \approx \frac{UC_L}{\pi AR} \tag{2.9}$$

Likewise, the thrust and the induced momentum are set equal to the drag and weight component in the horizontal direction as shown in Eq. (2.10), where e is the deficiency factor for non-elliptical wings ($e < 1$).

$$W\sin\gamma + D = T = 2mu \quad \rightarrow \quad u = \frac{2T}{\pi b^2 \rho U e} = \frac{2(W\sin\gamma + D)}{\pi b^2 \rho U e} \tag{2.10}$$

The induced power required is the sum of the components for lift and thrust and is given by Eq. (2.11) for small flight angle γ. This equation can be converted to a form that uses only the lift to drag ratio and flight angle if required. More accurate approximations can also be made if the actuator disk area is reduced to the actual swept area of the wing, which will likely be 70% of the larger disk area.

$$P_i = Lv + Tu = \frac{2\left(L^2 + T^2\right)}{\pi b^2 \rho U e} \tag{2.11}$$

If the bird is in a hovering condition, only the weight must be equalized and only the vertical induced velocity is generated as identified in Eq. (2.12).

$$v_{hover} = \sqrt{\frac{W}{2\rho A}} \tag{2.12}$$

Note that the induced velocities decrease as forward flight speed increases and therefore the power required to overcome induced effects reduces with increasing forward velocity. The normal induced velocity effects can also be alleviated by an increase in the wing aspect ratio or the use of winglets to reduce tip vortices. While this uniform flow result does not capture the variation of u across the span, it only underestimates the longitudinal induced power loss by 5-10%, making momentum theory a common tool in estimations of aerodynamic performance.

2.6.2.2 Vortex Wake Theory

Many biologists wished to find a more accurate method for modeling bird flight than momentum theory. The result was vortex wake theory applied to flapping flight, with extensive experimental research completed by Pennycuick, Rayner and Spedding to determine the wake behavior in different flight modes. A shed vortex wake analysis calculates lift by measuring the production of new downward momentum in the wake, while the induced drag must equal the wake's kinetic energy per unit length. The accuracy of the lift and drag measurements proved the worth of vortex wake aerodynamic models. Several attempts were made to describe the wake behavior before the correct models were found; the final result included two types of wake, one each for low and high speeds. At low speeds and in intermittent flight the vortex ring gate, first proposed by Rayner, may be used; while at high speeds a continuous and constant circulation or "concertina" wake is established.

Vortex ring theory was the first to gain ground in scientific circles in the 1970's, but later research found its application limited to low speed fliers, birds that fold the wing extensively on upstroke and intermittent flight modes. The vortex ring gate, shown in Figure 2.15, proposes that the steady flapping flight vortex wake can be modeled by a chain of elliptical vortex rings, each of which is generated by a single downstroke. Under vortex ring theory the upstroke is inactive and does not contribute any force. This inactivity causes the discontinuous rings because of the abrupt shed of circulation at the end of downstroke.

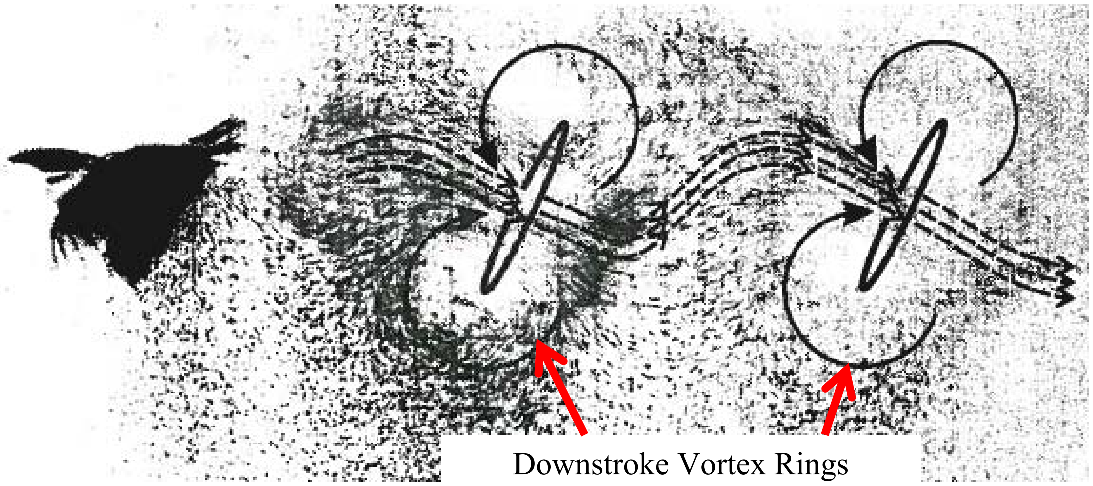

Figure 2.15: Vortex ring gate of a chaffinch flying through a cloud of dust.

A vortex ring is started by both wings at the top of the downstroke. As each wing sweeps down it forms a side of the ring until the sides reattach at the bottom of the downstroke and the ring is completed. The vortex ring's shape and orientation depend on the motion of the downstroke, while the ring size is determined by the circulation the wing produces. Researchers found that vortex rings for finches and pigeons were positioned at oblique angles of about ten degrees from the horizontal [8, 23]. Further experimental study of the vortex ring gate showed that the momentum measured in the wake was one-third to one-half the amount required to support the weight of the bird. This discrepancy is significant and shows that the vortex ring model is too simplistic to capture the unsteady aerodynamic behavior used by birds in the vortex ring gate flight mode.

While the vortex ring discrepancy was being explored a new vortex behavior was discovered by Spedding that consisted of two continuous trailing vortices with constant circulation; Lighthill named this the "concertina" wake [24, 62]. This wake behavior is produced by a wing with active downstroke and upstroke, with the upstroke wake shedding from the beginning of the primary feathers which are folded to reduce drag. The inner secondary and tertiary feathers remain in the flow and actively produce lift and therefore circulation in a concertina wake. Spedding's flow visualization of the vortices from experiments with kestrels are shown in Figure 2.16.

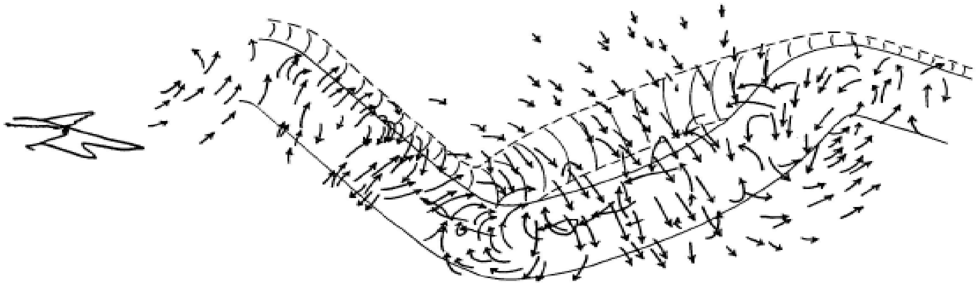

Figure 2.16: Two trailing vortices of constant circulation from a kestrel in flight, [62].

Spedding characterized the concertina wake via the diagram of Figure 2.17. During the upstroke the two trailing vortices are held parallel at a distance $2b_2'$ apart and move diagonally upward at an angle ψ_2 for a distance L_2. Through the downstroke the vortices arc out and back in the circular motion of the wingtip with a maximum span of $2b_1'$. The downstroke vortices follow a diagonally downward path at angle ψ_1 for a distance L_1. The maximum height of the vortices is h which is partially defined by the stroke amplitude ϕ.

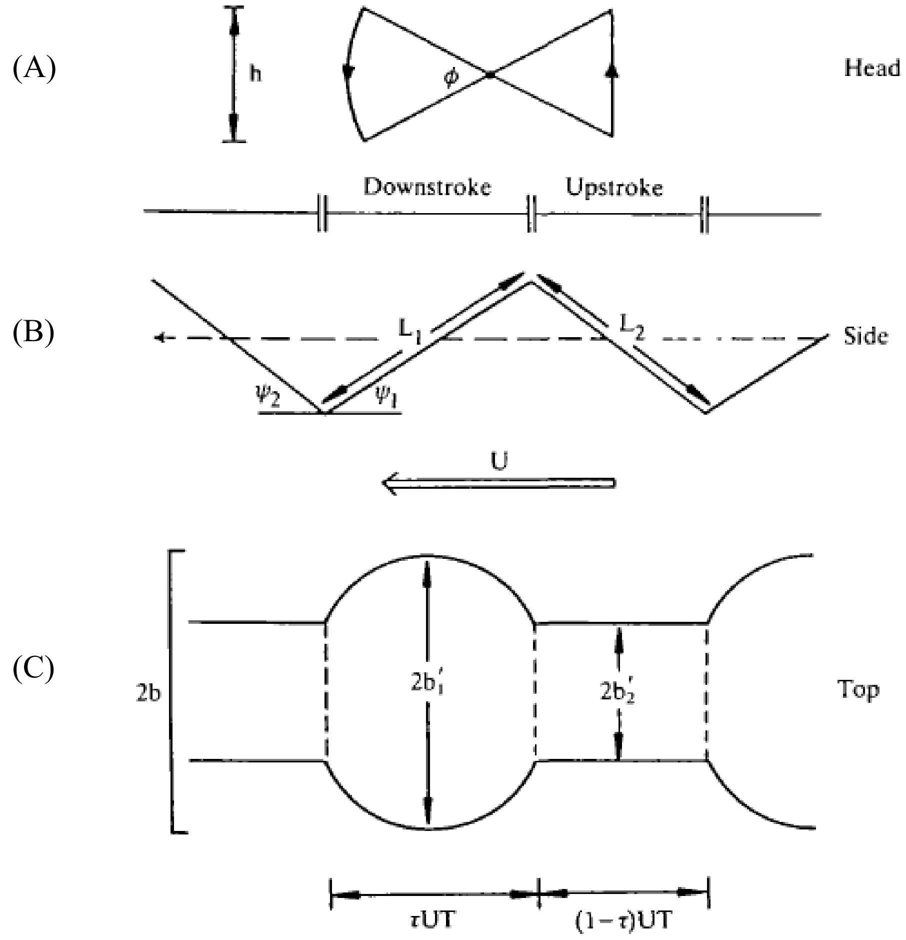

Figure 2.17: Spedding's model of the concertina wake, [62]. Part A shows the amplitude *h* of the wake which matches the stroke amplitude ϕ. Part B, the side view, shows the length and angles of the vortex during downstroke (L_1 and ψ_1) and upstroke (L_2 and ψ_2). Part C shows the top view and indicates the lateral separation of the vortices with $2b_1$ for downstroke and $2b_2$ for upstroke, where the bird's wingspan is *2b*. Also U is the velocity, *T* is the stroke period, and τ is the ratio of time spent during downstroke over the total stroke period.

If one assumes the simple description of the concertina wake provided by Spedding in Figure 2.17 then the analysis of the wake becomes quite simple. First Spedding provides an estimate for the two distances between the trailing vortices by defining a dimensionless wake spacing *R*. For gliding flight *R* is about 0.76, while flapping flight values average 0.9. Using this dimensionless wake spacing the upstroke and downstroke spacing are defined in Eqs. (2.13), where $2b$ is the total wing span, and $2b_2$ is the wing span with the primary feathers folded down. The difference between the maximum widths of the vortices is given by *B*:

$$\begin{aligned} 2b_1' &= R \cdot 2b \\ 2b_2' &= R \cdot 2b_2 \\ B &= 2b_1' - 2b_2' \end{aligned} \tag{2.13}$$

If the time period of one complete wing stroke is given by *T* and the downstroke ratio, or fraction of a period spent in downstroke, is given by τ, then the incidence angles of the vortices can be calculated using the maximum vortex height *h*. The vortex height and incidence angles are presented in Eqs. (2.14) and the lengths of the vortices during upstroke and downstroke are defined in Eqs. (2.15).

$$\begin{aligned} h &= 2b_1' \tan(\phi/2) \\ \psi_1 &= \tan^{-1}\left[h/(\tau UT)\right] \\ \psi_2 &= \tan^{-1}\left[h/((1-\tau)UT)\right] \end{aligned} \tag{2.14}$$

$$\begin{aligned} L_1 &= \sqrt{h^2 + (\tau UT)^2} \\ L_2 &= \sqrt{h^2 + [(1-\tau)UT]^2} \end{aligned} \tag{2.15}$$

Finally, the planar areas of the downstroke and upstroke wakes, A_1 and A_2, are determined by assuming $l = L_1/2$.

$$A_1 = 2b_2^{'} \cdot L_1 + \sqrt{\left[\tan^{-1}\left(\frac{2Bl}{l^2 - B^2}\right)\right]\left[\frac{l^2 - B^2}{2B}\right]^2 - l \cdot \left[\left(\frac{l^2 + B^2}{2B}\right)^2 - l^2\right]}$$

$$A_2 = 2b_2^{'} \cdot L_2 \tag{2.16}$$

Using the planar areas, the total lift and drag are calculated as a function of the circulation in Eqs. (2.17). If the lift is assumed to equal the bird's weight or the drag can be estimated by profile and parasite values, then the total circulation can be determined by these equations.

$$\begin{aligned} L &= \rho\Gamma\left(A_1 \cos\psi_1 + A_2 \cos\psi_2\right)/T \\ D &= \rho\Gamma\left(A_1 \sin\psi_1 + A_2 \sin\psi_2\right)/T \end{aligned} \tag{2.17}$$

Spedding also examines the induced drag value by using a quasi-steady aerodynamic analysis which is applicable because of the constant circulation wake. The induced drag is calculated by assuming a fixed wing, elliptical circulation distribution where the peak circulation is given by Γ.

$$D_i = \frac{1}{8}\pi\rho\Gamma^2 \tag{2.18}$$

The concertina wake solution is accurate at predicting the lift and induced drag for birds in cruising flight at medium or fast speeds with active lift production on the upstroke. This solution is elegant because the circulation is constant while the change in wake width adjusts the momentum of the flow. During downstroke the wake widens to carry greater momentum and therefore a heavier load, while the narrow wake of the upstroke contributes a small momentum and less lift loading. Additionally, the concertina wake is simple to model analytically. All that is required to use Speddings method is knowledge of the full and adjusted wing spans for downstroke and upstroke, and a measure of the stroke amplitude, downstroke time ratio and total stroke time. These quantities are readily measured experimentally which makes the concertina wake a useful model.

2.6.3 The Power Curve

Steady forward flapping flight of birds requires equalizing the thrust and drag forces as well as the lift to the bird's weight. There are three types of drag which must be accounted for when estimating power, they include form drag due to pressure, skin friction drag, and wake induced drag. The sum of the form drag and skin friction drag is refered to a profile drag for two dimensional airfoils and as parasite drag for three dimensional airfoils. The parasite drag increases with flight speed, while induced drag decreases with flight speed. Section 2.6.2.1 provided equations to calculate the induced power using momentum theory [10]. A similar approach can be used to calculate power requirements using vortex wake theory.

A graphical presentation of the power curve for a bat is given by Norberg and Rayner in Figure 2.18. In this case Norberg and Rayner assumed that parasite power is caused by skin friction and that profile power is caused by the pressure distribution on the wing. Rayner's method utilizes his vortex ring theory to calculate the induced power with the other power terms determined experimentally or empirically. At low speeds, the induced power dominates because induced velocities have a greater effect on the angle of attack, while high speeds are dominated by the parasite or profile power terms. Also note the minimum power (mp) speed is less than the maximum range speed (mr), though the optimal speed often depends on more than power or range requirements.

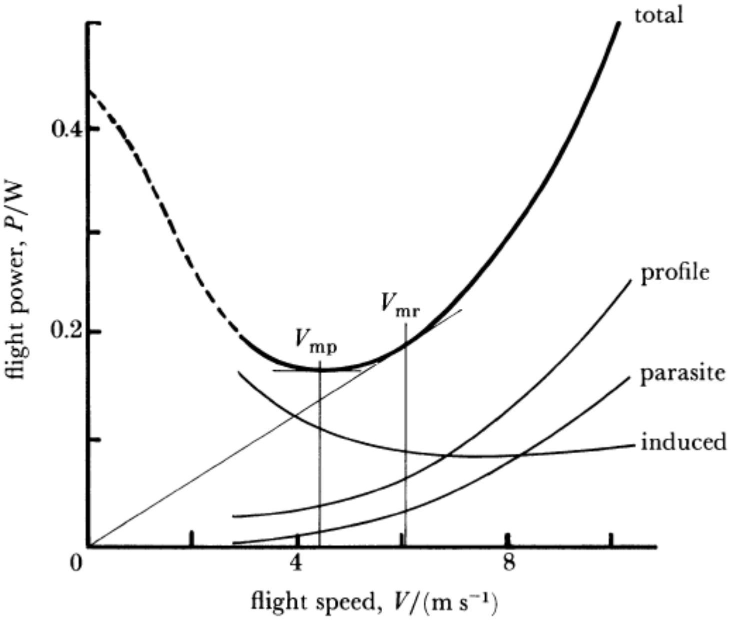

Figure 2.18: Power required for flight, [57].

Rayner’s interpretation of the total power required is given by Eq. (2.19) which uses non-dimensional coefficients for the induced, parasite and profile power terms: p_i , p_{par} , p_{pro} . In this equation *m* is the body mass, *g* is gravity, *b* is the wingspan, *S* is the wing area, and *V* is velocity.

$$P(V) = \frac{p_i m^2 g^2}{b^2 V} + \frac{1}{2}\rho\left(p_{par} + p_{pro}\right) S V^2 \tag{2.19}$$

The power curve is a very important performance measure that will define the active flight envelope and optimal operating conditions for a bird or aircraft; it also demonstrates the importance of minimizing induced drag at low speeds. In summary, this chapter provides a necessary introduction to flapping flight kinematics and aerodynamics that can be utilized in the design and analysis of flapping vehicles.

Chapter 3. Review of Aerodynamic Theory

This chapter reviews relevant aerodynamic theories, methods of analysis and empirical results that are necessary to understand or develop the analysis tools that are applied to generate an aerodynamic model of the research ornithopter. A review of two and three dimensional fixed wing aerodynamics is presented first, followed by a discussion of membrane aerodynamics with important empirical results. Finally the blade element method of analysis is introduced along with methods to model the unsteady aerodynamics experienced by the wing.

3.1 Fundamentals of Fixed Wing Aerodynamics

Fixed wing aerodynamic theories provide essential concepts for solving the flapping wing problem such as lift and drag coefficients, angle of attack (AOA), and the effect of induced flows. Aircraft aerodynamics are typically explored first from a two dimensional perspective to simplify the problem and develop fundamental ideas such as circulation and vortex representations of a flow, which are then used to characterize the aerodynamic performance of an airfoil. The expansion to three dimensional finite wings introduces the concept of downwash and induced drag with vortex analysis methods such as lifting-line and lifting-surface theories as well as numerical vortex lattice methods. Important concepts from these theories are discussed in the following sections; for a thorough review see Anderson [64].

3.1.1 Aerodynamic Coefficients

Aerodynamic coefficients provide a method to calculate the lift and drag forces and the pitching moment of an airfoil or finite wing. The coefficients also relate to the aerodynamic performance of the airfoil or wing through measures such as lift-to-drag ratio and stability derivatives. An essential quantity in these dimensionless equations is the dynamic pressure, q_∞, identified in Eq. (3.1) where ρ_∞ and V_∞ are the free stream density and velocity respectively.

$$q_\infty = \frac{1}{2}\rho_\infty V_\infty^2 \tag{3.1}$$

Utilizing the dynamic pressure the dimensionless force and moment coefficients are given in Table 3.1. The three-dimensional (3D) equations are for finite bodies where *S* indicates the wing area and *c* is the chord length. For the two-dimensional (2D) bodies, the coefficients are lowercase and the apostrophe after the force or moment indicates a per unit length quantity; likewise the surface area assumes a unit length and reduces to the chord length, *c*.

Table 3.1: Aerodynamic coefficients for 2D and 3D bodies.

	2D (per unit length)	3D
Lift Coefficient	$C_l = \frac{L'}{q_\infty c}$	$C_L = \frac{L}{q_\infty S}$
Drag Coefficient	$C_d = \frac{D'}{q_\infty c}$	$C_D = \frac{D}{q_\infty S}$
Normal Force Coefficient	$C_n = \frac{N'}{q_\infty c}$	$C_N = \frac{N}{q_\infty S}$
Axial Force Coefficient	$C_a = \frac{A'}{q_\infty c}$	$C_A = \frac{A}{q_\infty S}$
Pitching Moment Coefficient	$C_m = \frac{M'}{q_\infty c^2}$	$C_M = \frac{M}{q_\infty Sc}$

The aerodynamic forces are indicated in Figure 3.1. Lift, *L*, and drag, *D*, measure the force components that are vertical and horizontal to the free stream velocity, respectively. The normal force, *N*, and axial force, *A*, are aligned perpendicular and parallel to the airfoil chord, respectively.

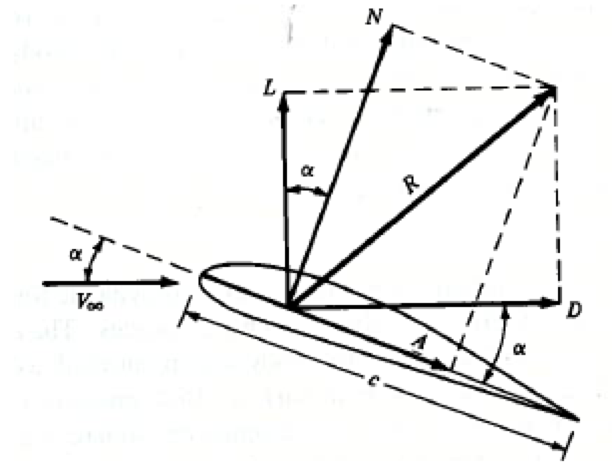

Figure 3.1: Direction of aerodynamic forces, [64].

3.1.2 Two-Dimensional Airfoil Theory

Thin airfoil theory applies a vortex sheet to a two dimensional airfoils chord line to determine the circulation, and therefore the lift, generated by the airfoil at a specific AOA. While thin airfoil theory is restricted to airfoils at small AOA in steady inviscid flows, it provides an accepted and accurate baseline for the two dimensional lift coefficient C_l of airfoils as well as pitching moment C_m. While the details of thin airfoil theory are left to aerodynamic texts, the important elements are presented now for the general cambered airfoil solution [64].

For an airfoil at an angle of attack α whose camber line is described by dz/dx, the vortex distribution $\gamma(\theta)$ along the chord is given by Eq. (3.2).

$$\gamma(\theta) = 2V_\infty \left(A_0 \frac{1+\cos\theta}{\sin\theta} + \sum_{n=1}^{\infty} A_n \sin n\theta \right) \qquad (3.2)$$

Where the x variable has been transformed by $x = \frac{c}{2}\left(1 - \cos\theta_0\right)$ and θ_0 varies between zero and 2π. The vortex distribution takes the form of a cosine Fourier expansion of dz/dx where the solutions for the Fourier coefficients are determined by the slope of the camber line and the angle of attack as shown in Eqs. (3.3).

$$A_0 = \alpha - \frac{1}{\pi}\int_0^{\pi} \frac{dz}{dx} d\theta_0$$

$$A_n = \frac{2}{\pi}\int_0^{\pi} \frac{dz}{dx} \cos n\theta_0 \, d\theta_0 \tag{3.3}$$

These coefficients can be solved for using the known airfoil shape. Then the vortex distributions and circulation can be found. The lift is determined based on the circulation, and can be calculated directly from the Fourier coefficients as shown in Eq. (3.4). This solution can be rewritten in terms of the effective angle of attack and the zero lift angle of attack, which is provided in Eq. (3.5). Likewise, the pitching moment coefficient at the quarter chord and the center of pressure location are given in Eq. (3.6) and Eq. (3.7) respectively.

$$C_l = \pi\left(2A_0 + A_1\right) \tag{3.4}$$

$$C_l = 2\pi\left(\alpha - \alpha_0\right) \tag{3.5}$$

$$C_{m,c/4} = \frac{\pi}{4}\left(A_2 - A_1\right) \tag{3.6}$$

$$x_{cp} = \frac{c}{4}\left[1 + \frac{\pi}{C_l}\left(A_1 - A_2\right)\right] \tag{3.7}$$

The lift coefficient equation is valid for any thin airfoil, and reduces to $2\pi\alpha$ for symmetric airfoils, where the zero lift angle of attack α_0 is zero. For most airfoils the lift slope is approximately proportional to the AOA and is equal to 2π until stall is breached, typically between ten and twenty degrees as shown in Figure 3.2.

$$Lift\ Slope = C_{l\alpha} = \frac{\partial C_l}{\partial \alpha} = 2\pi \tag{3.8}$$

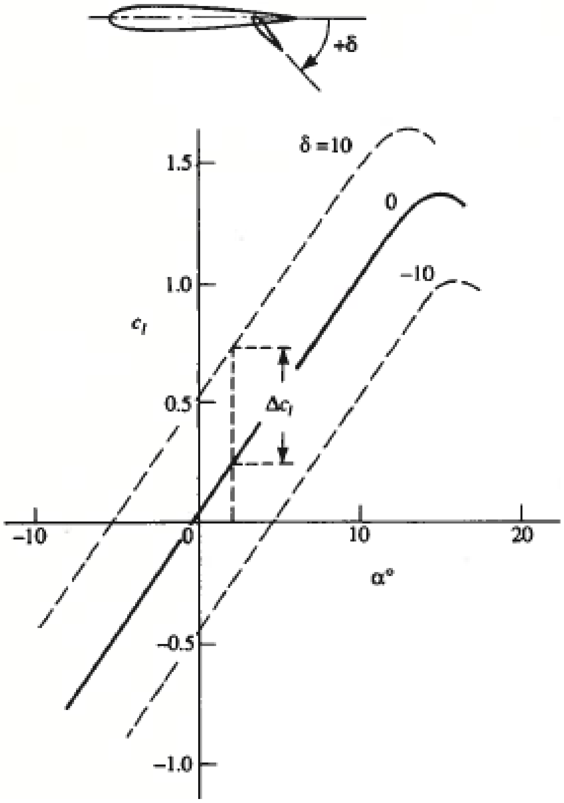

Figure 3.2: Effect of camber from trailing edge flap on lift curve, [64]

Figure 3.2 also shows the effect of positive camber through the use of a trailing edge flap. Increasing camber causes an increase in lift over a symmetric airfoil at lower AOA as indicated by a leftward shift of the lift curve to intersect with the airfoil α_0 value. Adjusting the camber of an airfoil is possible by changing the design or adding flaps to the trailing edge which can shift the lift curve to improve performance at a specific AOA, such as high angle of attack landings. Leading edge devices, such as flaps or slats, can also be utilized to extend the lift coefficient to higher values at higher AOA by delaying stall as in Figure 3.3.

Leading and trailing edge devices are simple ways to manipulate the flow over an airfoil for improved performance, and birds use similar techniques in flight to delay stall and boost lift. Thin airfoil theory provides a simple and accurate tool for analyzing both symmetric and cambered airfoils and the effect of leading and trailing edge devices in the two dimensional realm. However, to understand the true behavior of a wing, the theory must be expanded to three dimensions.

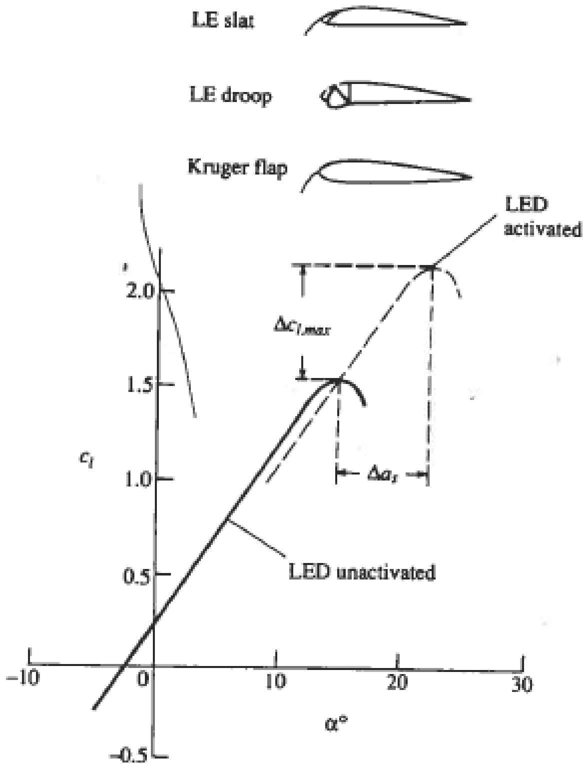

Figure 3.3: Delayed stall effect of leading edge device, such as a flap, on lift curve; [64].

3.1.3 Finite Wing Aerodynamics

Finite wings experience flow in three dimensions because of the sudden pressure difference at the wing tips. The pressure differential causes the high pressure flow on the bottom surface to wrap around the wing tip to the low pressure of the upper surface and produce a spanwise flow component that moves outward on the bottom surface and inward on the upper surface. Another effect of this circular motion is to generate wing tip vortices that trail downstream as the wing moves forward. The downstream wing tip vortices generate a vertical induced flow at the wing called downwash, *w*, which effectively reduces the local geometric angle of attack, α , by an amount called the induced angle of attack, α_i . The effective angle of attack, α_{eff} , is then given by Eq. (3.9) and is illustrated in Figure 3.4.

$$\alpha_{eff} = \alpha - \alpha_i \tag{3.9}$$

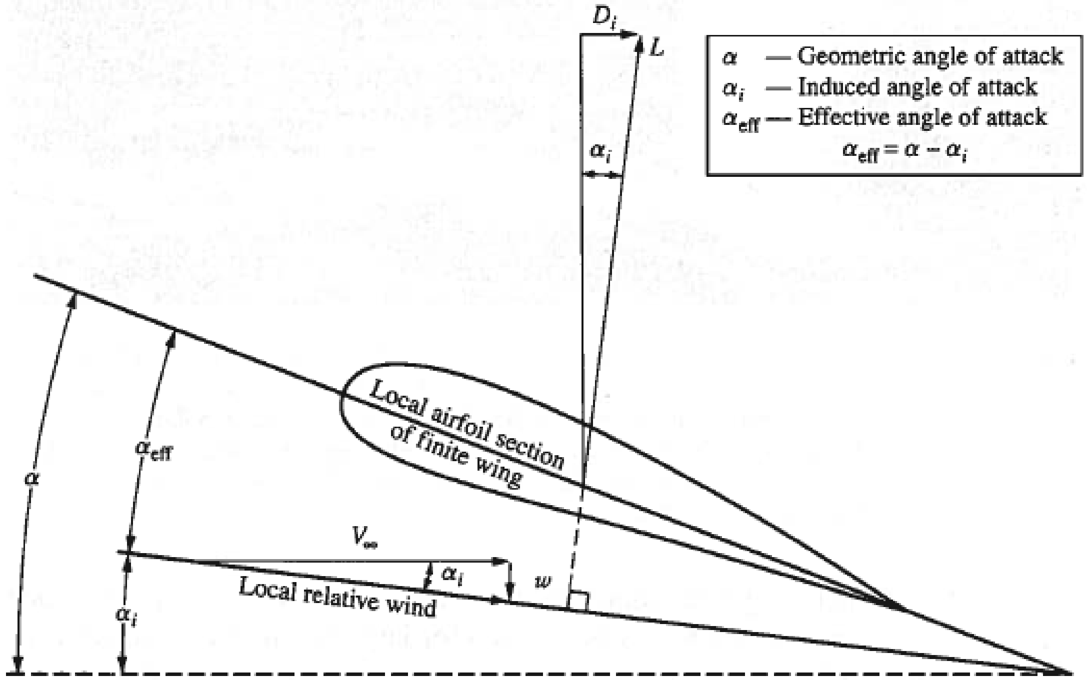

Figure 3.4: Representation of downwash, *w*, with induced AOA and induced drag indicated, [64].

Figure 3.4 shows the effects of downwash on the relative velocity and relative AOA, including the tilting of the lift vector back by the induced AOA, α_i. The new horizontal component of lift is called the induced drag, D_i, which is a measure of the kinetic energy lost by the vehicle engine to generate the wing tip vortices.

Induced drag for a fixed wing is estimated by Eq. (3.10), where e has a maximum value of one for elliptical circulation distributions which have minimum induced drag. The value of e reduces as the wing takes alternate load shapes with average values ranging between 0.8 and 1.0. Note that the induced drag is proportional to the lift coefficient squared; therefore induced drag is a large factor at high angle of attack.

$$C_{Di} = \frac{C_L^2}{e\pi AR} \tag{3.10}$$

Downwash velocities vary along the span and therefore each part of the span should be considered locally. Techniques for solving for the nonuniform downwash must be able to account for variations in wing geometry as well. Most methods for determining the downwash, circulation and aerodynamic forces and moments on a finite wing are extensions of the vortex theories from the two dimensional cases.

Prandtl’s lifting-line theory is often used as an alternative to more complex numerical methods. Lifting-line theory utilizes a superposition of horseshoe vortices attached as a bound vortex of varying length to the leading edge, or “lifting-line”. The vortices then extend downstream as two free-trailing vortices at symmetrical locations along each half-span. Figure 3.5 shows the change in circulation that occurs between each pair of bound vortices as indicated by the strength of each trailing vortex.

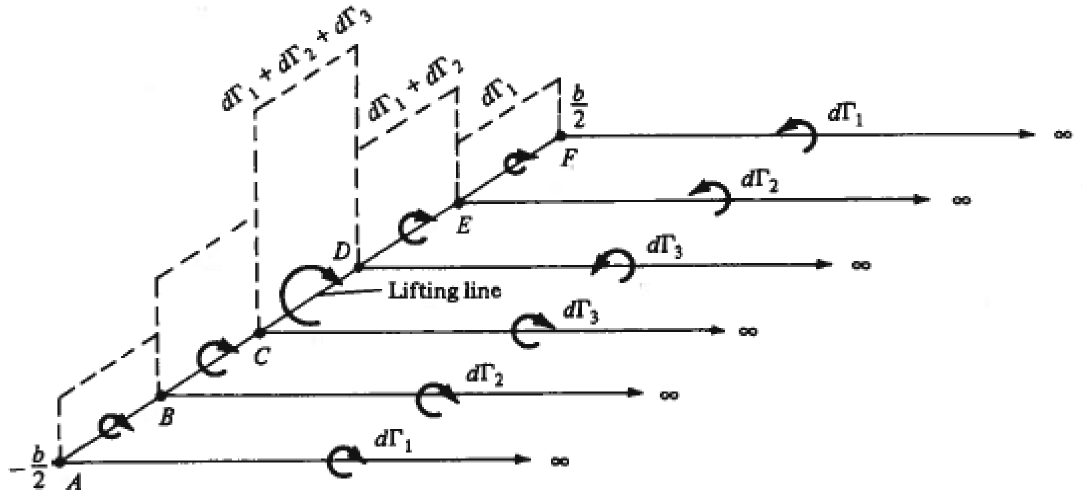

Figure 3.5: Lifting line with three horseshoe vortices showing superposition of circulation, [64].

Using the Biot-Savart law, the downwash due to all vortices at a location y_0 along the lifting line can be calculated if the circulation, Γ, of each vortex is known. This method is described by Eq. (3.11) and can be explored visually in Figure 3.6.

$$w(y_0) = -\frac{1}{4\pi}\int_{-b/2}^{b/2} \frac{(d\Gamma/dy)}{y_0 - y}dy \tag{3.11}$$

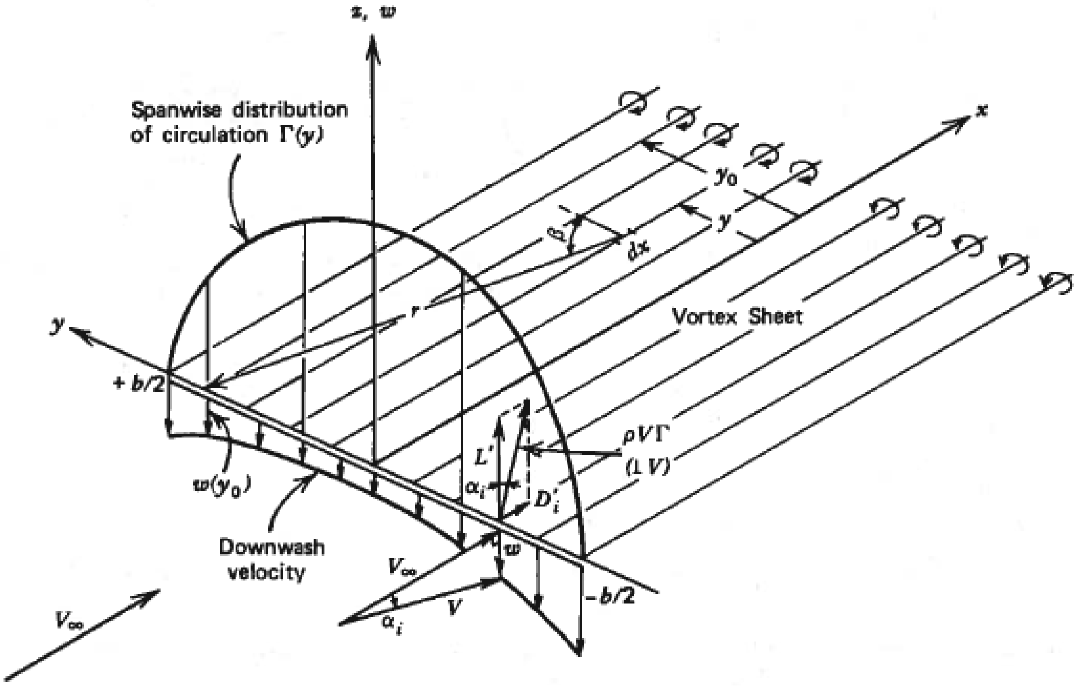

Figure 3.6: Representation of the downwash solution for lifting-line theory, [65].

The induced angle of attack α_i is formed in Eq. (3.12) by assuming the downwash is much slower than the free stream so small angle approximations apply.

$$\alpha_i(y_0) = -\frac{1}{4\pi V_\infty}\int_{-b/2}^{b/2}\frac{(d\Gamma/dy)}{y_0 - y}dy \tag{3.12}$$

To determine the circulation distribution, the lift slope result from thin airfoil theory must be used along with the local airfoil properties at y_0, including α, $\alpha_{L=0}$ and the chord length. The fundamental lifting-line solution of is then formed.

$$\alpha(y_0) = \frac{\Gamma(y_0)}{\pi V_\infty c(y_0)} + \alpha_{L=0}(y_0) + \frac{1}{4\pi V_\infty}\int_{-b/2}^{b/2}\frac{(d\Gamma/dy)}{y_0 - y}dy \tag{3.13}$$

Equation (3.13) simply restates the angle of attack relation from Eq. (3.9) with the circulation as the only unknown. If the lift distribution is known, the lifting line equations can be solved directly, however this is not usually the case. Kuethe and Chow present a solution method to the lifting-line equation for an arbitrary circulation distribution on an arbitrary wing in *Foundations of Aerodynamics* [65]. The solution assumes that the circulation distribution is symmetric and can be expressed as a Fourier series in terms of spanwise location. The lifting-line equation is then solved by segmenting the wing and forming a system of equations based on the known geometric angle of attack values for each wing section. Results can be achieved even for twisted wings and provide an estimate of the local induced angle of attack or downwash for each section as well as the circulation and lift distribution on the wing. Beyond lifting-line theory, computational techniques that include viscosity and turbulence models can provide more accurate results to the finite wing problem.

3.2 Membrane Aerodynamics

Recall that the Morpheus Laboratory's research ornithopters use membrane wings. The luff region of the membrane wing, defined as the region between the leading edge spar and diagonal spar of the ornithopter wing, is analyzed using the linear results of the following sail theory analysis. The study of membrane aerodynamics was first explored to improve sail design, a field of research which is dominated by experimental innovation and sailors' intuition. Sail theory was introduced by Thwaites, whose discourse on sail aerodynamics provided a basis for later research [27]. Two dimensional sail theory is presented in detail along with a discussion of modern membrane aerodynamics research.

3.2.1 Thwaites Two-Dimensional Sail Theory

While sails or membranes could be idealized as high incidence, thin airfoils, their behavior is quite different, especially in their response to dynamic flows. This is because pressure or load differences on the sail from a change in velocity or angle of attack will cause the sail curvature to adjust and turn the luff, or the slack portion of the sail, into the wind to counteract pressure changes. In light of this behavior, Thwaites describes why rigid wing aerodynamic theory cannot be applied directly to sails and membranes [27]:

> *"In flow past wings, either the shape of the wing or the aerodynamic pressures on it may be prescribed in advance; so the purpose of a theory is to determine the one given the other. But for a sail which is flexible, it is a manifest reality that its shape cannot be arbitrarily assigned; this arises from the necessity for each element of sail to be in static equilibrium – or, in other words, for the curvature of the sail to be such that the tension exactly counterbalances the aerodynamic load. Thus both dynamic and static conditions have to be satisfied, and as a result, the analysis for sails is different from that for rigid wings."*

The following sections present the two-dimensional sail problem and the derivation of the fundamental sail equation. Solutions to the sail problem and important conclusions are summarized.

3.2.1.1 Derivation of the Fundamental Sail Equation

The fundamental equation for two dimensional sails is similar to Prandtl's wing equation, but differs in two primary ways. First, there are additional conditions applied to the integral and the lack of geometric symmetry makes conventional wing theory inapplicable. Second, the sail equation includes a parameter λ which is inversely proportional to the membrane tension. The eigenvalues of λ indicate whether the flow is smoothly attached at the leading edge; such a condition requires a wavy sail with zero lift. Likewise, inviscid theory dictates that a wholly concave sail has a sharp leading edge that experiences a theoretical infinite velocity; only this type of sail formation produces lift.

The task at hand is to develop an aerodynamic equation connecting the shape of the sail to the pressure distribution on it. The first step towards this sail equation is to simplify the problem to the two-dimensional flow of an inviscid, incompressible fluid past an infinitely long, inelastic, non-porous sail. Assuming the sail is fixed at the leading and trailing edge, the chord length is given by c and the total length of the sail is $c+l$ where l is a measure of the slack, as identified in Figure 3.7. The sail is positioned along the x-axis with its camber in the z-axis; the leading edge is located at the origin and the trailing edge at $(c,0)$.

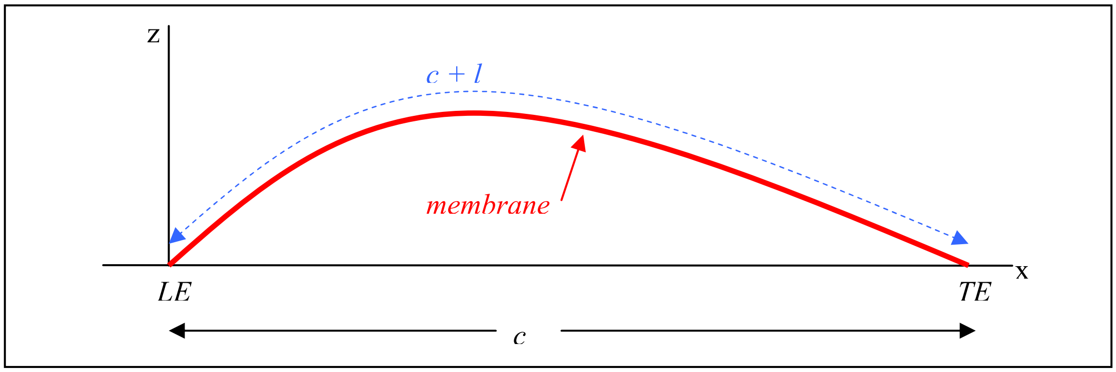

Figure 3.7: Example of a membrane with chord length c and slack length l

To further define the problem shape and notation a free stream velocity U is applied to the sail at an angle of attack α. At any location $0 \le x \le c$ the slope of the sail is given by $\psi(x)$ and the vortex sheet strength per unit length on the z-axis is given by $\gamma(x)$. The x-axis variable of integration for the vortex is ξ, with an infinitesimal element $d\xi$. This notation is shown in Figure 3.8.

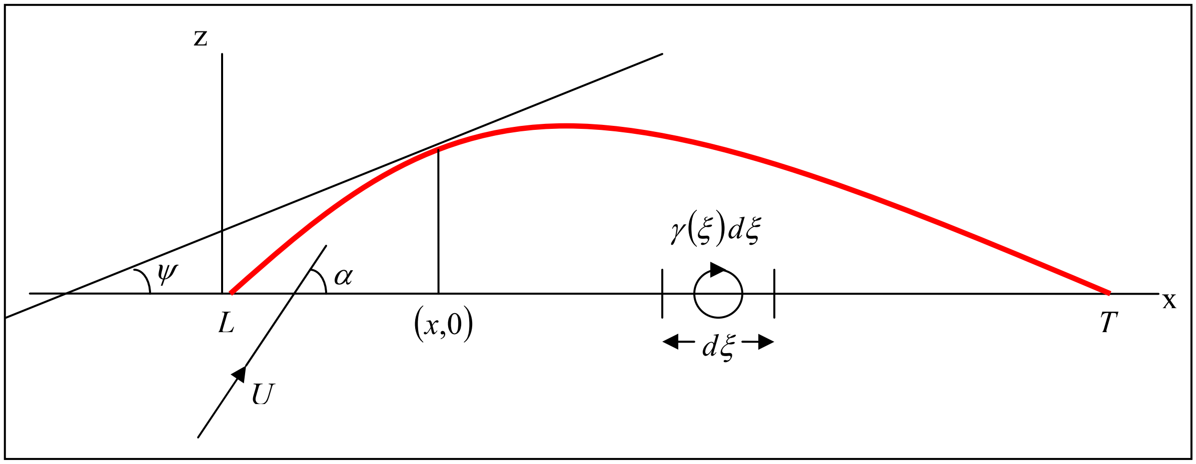

Figure 3.8: Sail theory notation, including integration element $d\xi$.

Equilibrium is enforced to relate the sail aerodynamics to the sail shape. The slope $\psi(x)$ of the sail at a location x must equal its local velocity inflow angle, which is a combination of the free stream angle of attack and the induced flow or downwash angle from the vortex sheet. The induced flow angle is given by thin airfoil theory.

$$\alpha_i(\xi) = \frac{1}{2\pi U}\int_0^c \frac{\gamma(\xi)}{\xi - x}d\xi \tag{3.14}$$

Equating the inclination angle of the combined velocities with the slope at x gives:

$$\frac{dz}{dx} = \psi(x) = \alpha + \frac{1}{2\pi U}\int_0^c \frac{\gamma(\xi)d\xi}{\xi - x} \tag{3.15}$$

Rewriting Eq. (3.15) gives the aerodynamic equilibrium in Eq. (3.16).

$$-\frac{1}{\pi}\int_0^c \frac{\gamma(\xi)d\xi}{\xi - x} = 2\{U\alpha - U\psi(x)\} \tag{3.16}$$

Continuing the discussion of static equilibrium, one can analyze the pressure and tension on the sail element shown in Figure 3.9. As with thin airfoil theory, the lift on the sail element dx due to the vortex is $\rho U\gamma(x)dx$, where ρ is the free stream fluid density. The pressure difference between the upper and lower sail surfaces is then given by Eq. (3.17).

$$\Delta p = \rho U\gamma(x) \tag{3.17}$$

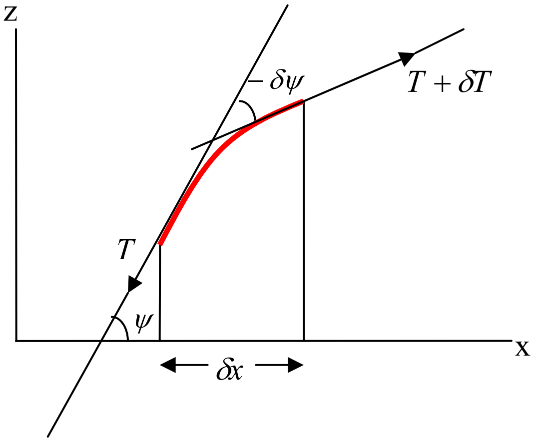

Figure 3.9: Equilibrium of a sail segment dx.

Since the flow is assumed to be inviscid, there can be no viscous shearing forces acting on the sail and therefore the tension must be constant. Equating the normal forces on the sail element due to pressure and tension results in Eq. (3.18).

$$\Delta p\, dx = -T\, d\psi \quad \rightarrow \quad \rho U \gamma(x) = -T\, d\psi / dx \tag{3.18}$$

Equation (3.16) and Eq. (3.18) provide two simultaneous equations to solve for the sail slope $\psi(x)$ and vortex distribution $\gamma(x)$. These equations are constrained by the Kutta condition and the slope condition that the leading and trailing edges must lie on the x-axis, these constraints are summarized by Eq. (3.19) and Eq. (3.20).

Constraints

Kutta Condition: $$\gamma(c) = 0 \tag{3.19}$$

Slope Condition: $$\int_0^c \psi(x)\, dx = 0 \tag{3.20}$$

Since Eq. (3.16) cannot be solved directly Thwaites inverts the aerodynamic equilibrium equation using the Muskheishvili method while incorporating the constraints; this results in the aerodynamic equilibrium of Eq. (3.21).

$$\gamma(x) = \frac{2}{\pi}\left(\frac{c-x}{x}\right)^{\frac{1}{2}} \int_0^c \left(\frac{\xi}{c-\xi}\right)^{\frac{1}{2}} \frac{U\alpha - U\psi(\xi)}{\xi - x}\, d\xi \tag{3.21}$$

The transformations of Eqs. (3.22) are made to simplify Eq. (3.21). The two geometric quantities x and ξ are transformed into angular representations in a manner similar to thin airfoil theory. Also, the tension parameter λ is defined and the slope and vortex strength are established as functions of angle of attack and airspeed. All further equations are solved for $\Psi(x)$, which is a dimensionless ratio of the local slope to the angle of attack of the incoming velocity.

$$\begin{aligned} &\left.\begin{aligned} x &= 0.5c(1-\cos\theta) \\ \xi &= 0.5c(1-\cos\phi) \end{aligned}\right\} \quad (0 \le \theta, \phi \le \pi) \\ &\lambda = 2\rho U^2 c/T \\ &\gamma(x) = 4U\alpha\,\Delta(\theta)\operatorname{cosec}\theta \\ &\psi(x) = \alpha\Psi(x) \end{aligned} \tag{3.22}$$

Using these transformations, Eq. (3.18) and Eq. (3.21) are simplified to:

$$\Delta(\theta) = -\frac{1}{\lambda}\frac{d\Psi(\theta)}{d\theta} \tag{3.23}$$

$$\Delta(\theta) = \frac{\cos^2(\theta/2)}{\pi}\int_0^\pi \frac{(1-\cos\phi)(1-\Psi(\theta))d\phi}{\cos\theta-\cos\phi} \tag{3.24}$$

Equations (3.23) and (3.24) can now be combined to form Eq. (3.25) which is constrained by the transformed slope boundary condition of Eq. (3.26).

$$-\frac{1}{\lambda}\frac{d\Psi(\theta)}{d\theta} = \left[1-\frac{1}{\pi}\int_0^\pi \Psi(\theta)d\theta\right]\cos^2(\theta/2) - \frac{\sin^2\theta}{2\pi}\int_0^\pi \frac{\Psi(\phi)d\phi}{\cos\theta-\cos\phi} \tag{3.25}$$

$$\int_0^\pi \Psi(\theta)\sin\theta d\theta = 0 \tag{3.26}$$

Thwaites finally forms the fundamental sail equation of Eq. (3.27) by integrating Eq. (3.25) while satisfying the boundary equation in Eq. (3.26).

$$\boxed{\begin{aligned} &\Psi(\theta) + \lambda\left\{-\frac{1}{2\pi}\int_0^\theta \sin^2\theta\int_0^\pi \frac{\Psi(\phi)d\phi}{\cos\theta-\cos\phi}d\theta + \frac{1}{4\pi}\int_0^\pi \sin\theta\int_0^\theta \sin^2\theta\int_0^\pi \frac{\Psi(\phi)d\phi}{\cos\theta-\cos\phi}d\theta\,d\theta\right\} \\ &\quad + \lambda\left(\frac{3}{8}\pi - \frac{1}{2}\theta - \frac{1}{2}\sin\theta\right)\left[\frac{1}{\pi}\int_0^\pi \Psi(\theta)d\theta\right] = \lambda\left(\frac{3}{8}\pi - \frac{1}{2}\theta - \frac{1}{2}\sin\theta\right) \qquad (3.27) \end{aligned}}$$

The sail equation cannot be solved analytically, but solutions can be determined iteratively if the tension parameter λ is set. As λ approaches zero the tension in the sail approaches infinity and the sail is forced to a flat condition where $\Psi(\theta)=0$. For increasing λ the slack l in the sail increases and purely concave shapes are achieved for $0<\lambda<2.316$. The sail geometry is defined by the slack ratio l/c and height coordinates $z(\theta)$ which are determined by the sail slope ratio $\Psi(\theta)$ in Eq. (3.28) and Eq. (3.29) respectively. The lift and pressure coefficients as well as fluid speeds along the sail can also be calculated based on the tension parameter and slope function. These results are provided in Eq. (3.30) through Eq. (3.32) respectively.

$$\frac{l}{c\alpha^2}=\frac{1}{4}\int_0^{\pi}\Psi^2(\theta)\sin\theta d\theta \tag{3.28}$$

$$\frac{z}{\sqrt{lc}}=\frac{\int_0^{\theta}\Psi(\theta)\sin\theta d\theta}{\left[\int_0^{\pi}\Psi^2(\theta)\sin\theta d\theta\right]^{1/2}} \tag{3.29}$$

$$c_l=\frac{4\alpha}{\lambda}\left[\Psi(0)-\Psi(\pi)\right] \tag{3.30}$$

$$C_p(\theta)=-8\frac{\lambda}{\alpha}\frac{d\psi}{\sin\theta d\theta} \tag{3.31}$$

$$\frac{u}{U}=1\mp2\frac{\alpha}{\lambda}\frac{d\psi}{\sin\theta d\theta} \tag{3.32}$$

3.2.1.2 Sail Equation Solutions: Large Tension

Sails of very large tension behave like a flat plate. These results are applied to the trailing edge flap region of the ornithopter wing, which is stretched taught with a neglible slack length. In large tension cases the tension parameter is constrained to $\lambda < 0.5$ and the sail has very little slack with $l/c \approx 0.001$. The concaveity of the sail is so small that it is not sensitive to the aerodynamic forces and therefore the sail shape $z(\theta)$ is independent of the angle of attack α. Also, the lift coefficient, center of pressure and velocity over the sail are reduced to the flat plate solutions below.

$$c_l = 2\pi\alpha \tag{3.33}$$

$$C_p(x) = 4\alpha\left[\frac{(c-x)}{x}\right]^{1/2} \tag{3.34}$$

$$\frac{u}{U} = 1 \pm 2\alpha\left[\frac{(c-x)}{x}\right]^{1/2} \tag{3.35}$$

3.2.1.3 Sail Equation Solutions: Critical Incidence Angle

Critical incidence angle α_c is defined as the angle of attack where the flow attaches smoothly to the leading edge and therefore produces no load at the leading edge of the sail. For a rigid airfoil if the angle of attack is higher than the critical incidence, $\alpha > \alpha_c$, then the sail will have a stagnation point on it lower surface; likewise if $\alpha < \alpha_c$ the stagnation point will move to the upper surface. On a sail, these incidence changes would cause curvature adjustments, especially at the leading and trailing edges, which then readjust the incidence and stagnation point to maintain concave curvature. Thwaites therefore proposed and later proved that critical incidence angles cannot be achieved on sails of purely concave curvature, but only exist for sails of more complex shapes. Solving for these complex shapes requires constraining the fundamental sail equation to reduce it to an eigenvalue problem. The solutions of the eigenvalue problem are given in terms of λ, with only sail shapes symmetric about $\theta = 0.5\pi$ satisfying the critical condition. Due to their symmetry, these solutions require that their lift coefficients be zero and therefore all critical flows produce zero lift. The first three critical shapes are shown in Figure 3.10.

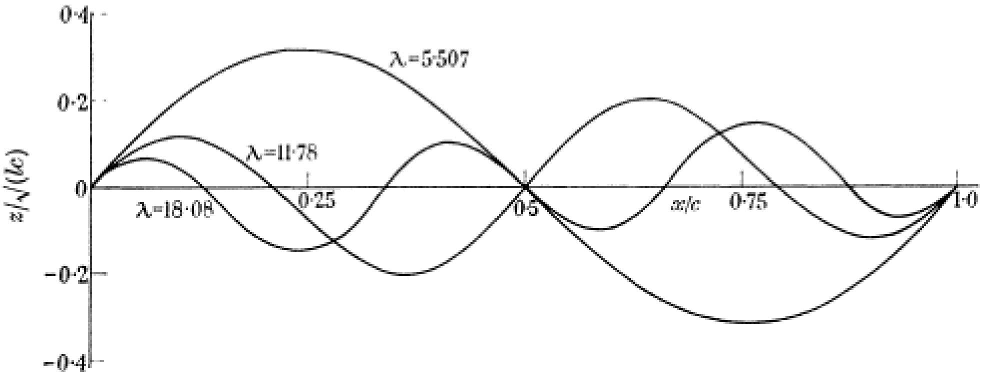

Figure 3.10: The first three critical shapes, $\lambda_2 = 5.507, \lambda_4 = 11.78, \lambda_6 = 18.08$**, [27].**

3.2.1.4 Sail Equation Solutions: General Case

Thwaites presents an eigenvalue method to solve the fundamental sail equation numerically. This method can be reviewed in his publications and only the important results are presented here. The critical cases described above represent the limits of each shape of the sail, with the eigenvalue number describing the number of sail inflexion points, or locations where the camber changes sign. If a solution falls between two critical eigenvalues, it will have the same number of inflexion points as the critical solution below it. Examples of sail shape solutions for $3 < \lambda < 8$ are given in Figure 3.11

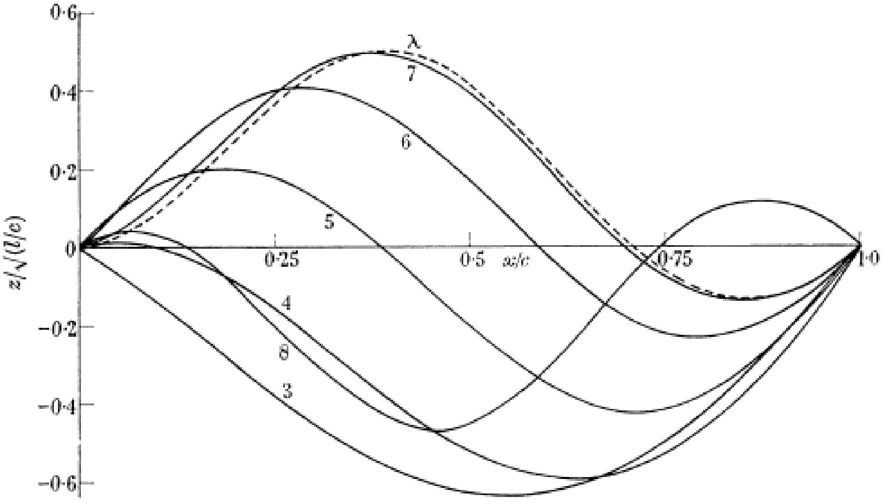

Figure 3.11: Sail shape solutions for $3 < \lambda < 8$, [27].

The number of mode shapes a sail can take on depends on the values of α and l/c, which determine the tension parameter λ. Solutions for specified $\alpha\sqrt{c/l}$ are shown in Figure 3.12, which indicates there is only one solution for $\alpha\sqrt{c/l} > 0.99$, but there are three possible solutions for $0.4 < \alpha\sqrt{c/l} < 0.99$ and so on. The sign of the lift coefficient for each solution is indicated by the sign at the apex of each curve.

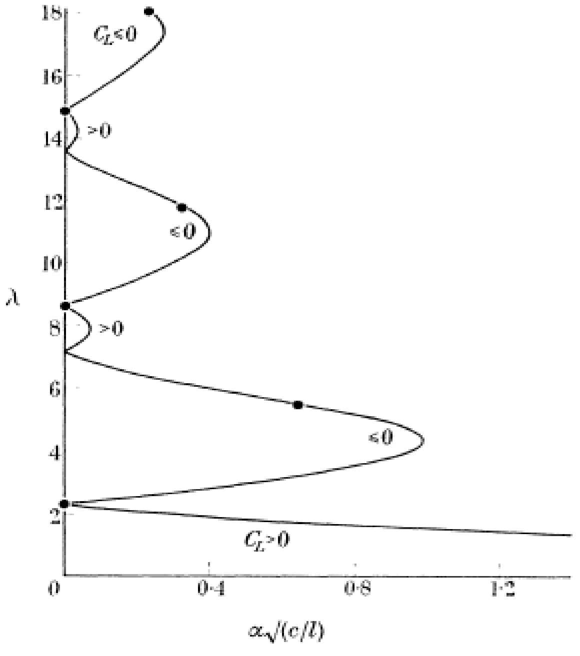

Figure 3.12: Solution curve for varying $\alpha\sqrt{c/l}$, [27].

3.2.1.5 Sail Equation Solutions: Concave Sails

Recall that purely concave sails are only present when $0 < \lambda < 2.316$, and most sails follow this behavior. This concave sail result is applied to the luff region of the ornithopter membrane wing. The relationship between $\alpha\lambda\sqrt{c/l}$ and λ is nearly linear for concave sails as identified in Figure 3.13; this leads to the evaluation of λ based on known values for known values of α and l/c.

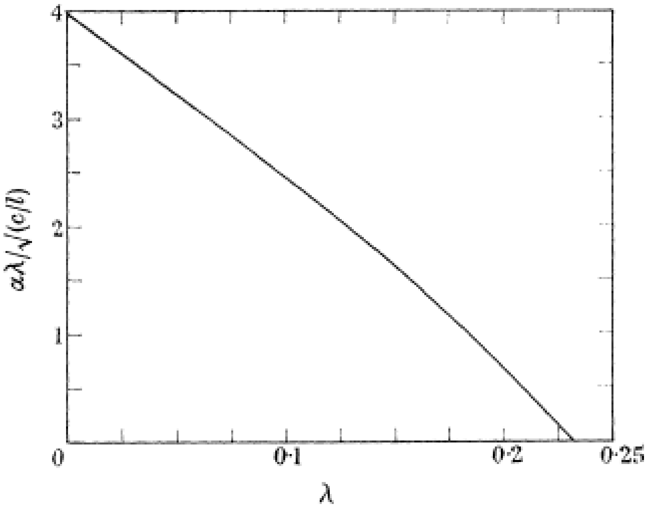

Figure 3.13: Relationship between $\alpha\lambda\sqrt{c/l}$ and λ, [27].

The shapes of a concave sail vary little as shown in Figure 3.14, with the point of maximum camber shifting rearward for increasing λ and forward for decreasing λ.

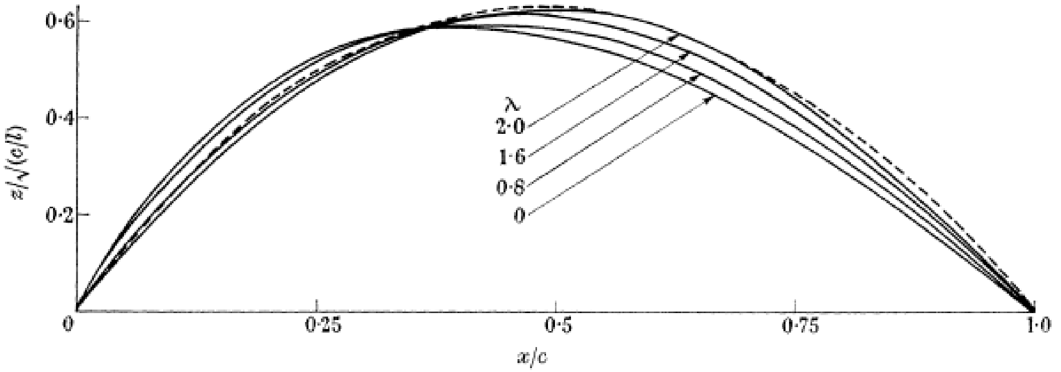

Figure 3.14: Concave sail shapes showing shift of maximum camber, [27].

Changes in shape are so small for purely concave sails that they can be approximated as an average shape. The resulting variations in the sail aerodynamics are small and behave linearly with the slack ratio l/c and angle of attack α. Thwaites concludes that the lift coefficient for a concave sail can be represented by the flat plate lift coefficient equation with the addition of a term dependent on the square root of the slack ratio. The result is an empirical solution for the sal lift coefficient:

$$c_l = 2\pi\alpha + 0.636\sqrt{l/c} \tag{3.36}$$

This lift coefficient is utilized in the aerodynamic model in Ch. 5 to accurately capture the behavior of the luff region of the flapping membrane wing.

3.2.2 Modern Membrane Aerodynamics

Thwaites introduction of two-dimensional sail theory provided a basis for future research which would include a variety of theoretical, experimental and numerical approaches to membrane aerodynamics. Some researchers simplified the membrane problem while others tackled its complexities by moving to three dimensions and including viscous flows and nonlinearities in the problem. The elements of these studies relevant to the flapping wing problem are presented now.

3.2.2.1 Simplified Theoretical Approaches

Newman provides the essential overview of progress in membrane aerodynamics through 1986, when numerical solutions were becoming attainable. This review reexamines two dimensional sails and compares experimental results for the lift and thrust coefficient to theory. Newman also explains the loss of lift at the trailing edge and the presence of leading edge suction due to thick boundary layers and separation bubbles [28]. Leading edge suction forces occur because of the vortex flows at the leading edge and can provide thrust on the order of 1/10th the amount of lift if utilized effectively. Newman also examines oscillating sails, double membrane airfoils, bluff membranes, and introduces three-dimensional membrane wings and the complications they present.

A very simple and relatively accurate two-dimensional sail model was developed by Jackson in 1983 [67]. Rather than determining the sail length via a complex numerical solution, Jackson assumed the concave sail shape could be closely represented by a cubic shape. If the sail's leading and trailing edges were fixed at $(0,b)$ and $(0,-b)$ respectively then the cubic sail shape is given by Eq. (3.37) where x and y are the chord and camber height coordinates, respectively.

$$\frac{y}{b} = \frac{1}{4}\left(1 - \frac{x^2}{b^2}\right)\left(A + \frac{Bx}{b}\right) \tag{3.37}$$

The two cubic parameters A and B can be formulated from the geometry of the membrane as $A = \theta_1 + \theta_2$ and $B = \theta_2 - \theta_1$, where θ_1 and θ_2 are the slope angles of the leading and trailing edges respectively. The lift and leading edge moment coefficients can be determined by the angle of attack and the cubic parameters A and B as shown in Eq. (3.38) and Eq. (3.39). The center of pressure location x_c is also set by the membrane shape in Eq. (3.40).

$$c_l = 2\pi\left(\alpha + \frac{A}{4} + \frac{B}{8}\right) \tag{3.38}$$

$$c_m = \pi\left(\frac{\alpha}{2} + \frac{A}{4} + \frac{5B}{32}\right) \tag{3.39}$$

$$\frac{x_c}{2b} = \frac{1}{2} + \frac{B}{2A} \tag{3.40}$$

The results of Jackson's analysis compare well with historical membrane theory results and are very simple to solve for concave sails. These simple two-dimensional models provide useful estimations of the local behavior of a sail and can be improved with more complex models as increased accuracy becomes necessary.

3.2.2.2 Sail and Membrane Experiments

Experiments on both two and three dimensional sails provide an essential point of comparison for theoretical and numerical results as well as reasoning for discrepancies between them. Greenhalgh et al. examined the effectiveness of two dimensional sail theory to predict the behavior of inextensible flexible airfoils in a wind tunnel [68]. Greenhalgh's experiments measured lift and drag of flexible airfoils with up to 5.6% slack operating at positive and negative AOA. Results proved that the operating range of a membrane airfoil is limited by the slack percentage which determines the stall due to separation at high AOA and when the airfoil reverses camber at negative AOA. The lift curve experiences hysteresis from the onset of stall stall through the negative AOA values as shown in Figure 3.15 where the sign of the lift coefficient indicates positive or negative camber. Membrane camber will be posive for positive angles of attack and negative at negative angles of attack.

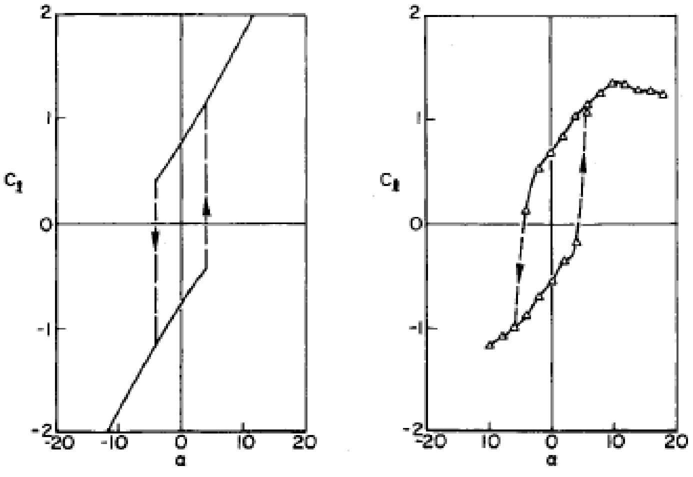

a) Theory b) Experiment.

Figure 3.15: Example of lift hysteresis of a flexible airfoil with 1.4% slack, [68].

Positive lift was achievable for all slack values at negative angles of attack provided the camber reversal has not occurred. As slack values increased the maximum lift increased but the operating range decreased due to earlier onset of stall; the lift slope was also reduced. As a whole, flexible airfoils display an advantage over fixed airfoils because their camber adjusts to alleviate adverse pressure gradients and extend the operating range to higher angles of attack before stall is reached [48]. Greenhalgh found the same relation between the slack ratio and the lift coefficients for the airfoils as Thwaites, with a slight variation of the empirical coefficient B depending on the test case. The empirical lift coefficient is given by Eq. (3.41), where B is 6.36 for Thwaites and 7.0 for Greenhalgh.

$$c_l = 2\pi\alpha + 0.1B\sqrt{l/c} \tag{3.41}$$

The aerodynamic and structural dynamic behavior of elastic membrane wings is discussed by Song et al. [50]. This research examined the influence of the Weber number, a ratio of the aerodynamic load to the membrane elasticity, as well as aspect ratio and membrane thickness or compliancy on the aerodynamic performance. Song et al. found that compliant wings had a higher lift slope and maximum lift coefficient, but also suffered from increased drag. Stall was delayed by up to ten additional degrees over a rigid wing and the onset of stall was milder with a more gradual reduction of lift. The unsteady membrane motions were also measured, with vibration frequencies that correlate to the natural frequency and modal shapes of the membrane at a specific tension, as could be expected.

The influence of structural behavior on performance is important to consider near stall and camber reversal. Rojratsirikul et al. conducted experiments on the unsteady aerodynamics of two-dimensional membrane airfoils using high speed cameras, particle image velocimetry (PIV) and flow visualization [49]. The effect of angle of attack and velocity on membrane vibrations and mode shapes was examined. Findings indicated the membrane shape was only slightly sensitive to angle of attack and that the vibrations depended on the unsteadiness of the separated shear layer, with coupling between the membrane oscillations and the vortex shedding in the wake at post-stall incidences. Again, membrane airfoils were shown to delay stall at high α.

3.2.3 Nonlinear and Computational Membrane Models

Analysis of membrane behavior advanced dramatically with numerical methods that solve the nonlinear structural and aerodynamic equations in parallel. Early numerical approaches, such as that of de Matteis and DeSocio, divided the two-dimensional sail into panels based on an initial guess of the sail shape [39]. The panels are then evaluated aerodynamically under the static equilibrium tension constraints and the panel positions are adjusted based on results; the process iterates until a solution is found. Matteis and DeSocio's process can be used for both attached and partially separated flow with results that compare well to experiment and improve linearized analytical solutions.

Significant strides have also been made in solving the viscous flow, finite membrane wing problem. A series of articles by Smith and Shyy provide a detailed approach to the problem by combining an incremental, continuum based, finite element formulation of the membrane structural problem with a control volume formulation of the Navier-Stokes equations [35-37]. This approach simultaneously solves for the membrane shape, stress and the viscous flow field variables. Several cases are examined using this solver, including elastic wings with no pretension, the constant tension case, and the inextensible wing case. The response of the constant tension test case to harmonically varying free streams is examined using an arbitrary Lagrangian-Eulerian method for the Navier-Stokes solver with a Runge-Kutta time step. Results show periodic separation and reattachment which indicate the importance of the viscosity in the calculations. Also, the membrane shape continuously adjusts in aeroelastic response to the free stream variations. However, the membrane oscillations are not necessarily determined by the flow frequency. Using these results and computational techniques, Lian et al. and Levin et al. produced optimization schemes for low Reynolds number membrane airfoils and applied them experimentally to micro air vehicles [69, 70]. Similar techniques could be used to optimize ornithopter wing design to maximize desired performance specifications.

3.3 Blade Element Theory

Blade element theory is a tool developed to calculate the aerodynamic forces of a moving wing or blade such as a helicopter rotor, but it can be easily applied to a flapping wing as well. In helicopter analysis, blade element theory is the application of lifting-line theory to the rotating wing. For more general applications, blade element theory is the aerodynamic analysis of a wing segmented into sections that are idealized as two-dimensional airfoils or membranes, as shown in Figure 3.16. Each segment has an individual airfoil shape and a specific inflow velocity and angle of attack that depend on the segments' local motion and the induced flows generated by the entire wing at that location. The aerodynamics of each blade section are analyzed individually, and then integrating over the sections to accumulate the total forces and moments experienced by the moving wing. Blade element theory is a simple tool that can provide adequate results without the complexity of computational methods.

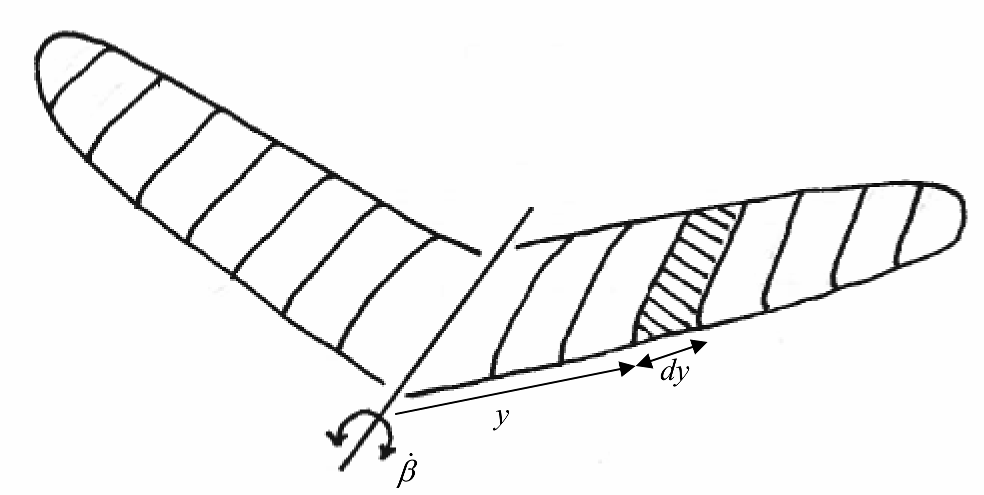

Figure 3.16: Blade element diagram of a flapping wing with eight sections per semi-span.

3.4 Unsteady Aerodynamics

One challenge in modeling flapping wing aerodynamics is accounting for the effects of oscillatory wing motion which causes unsteady flow behavior. The degree of unsteadiness is determined by the reduced frequency shown in Eq. (3.42), which is a ratio of the oscillatory velocity to the flight velocity

$$k = \frac{\omega c}{2U} \tag{3.42}$$

Reduced frequency can be used to measure the influence of any oscillatory motion experienced by a wing, but it focuses on the flapping frequency for an ornithopter. The value of the reduced frequency determines whether the flow is considered steady, quasi-steady or unsteady, these ranges are given in Table 3.2. When the reduced frequency reaches 0.2 or higher the flow becomes highly unsteady and acceleration effects become large. An accurate model must account for the unsteady effects which introduce changes in the amplitude and phase of the aerodynamic loads.

Table 3.2: Flow unsteadiness level based on reduced frequency.

Degree of Unsteadiness	*Reduced Frequency Value*
Steady	$k = 0$
Quasi-Steady	$0 < k < 0.05$
Unsteady	$0.05 \leq k < 0.2$
Highly Unsteady	$k \geq 0.2$

This section will provide equations for the quasi-steady flow and explain the types of unsteady flow phenomenon associated with large flapping wing vehicles such as lift deficiency, apparent mass, induced flows and dynamic stall. Methods are presented to account for these unsteady effects in the aerodynamic model.

3.4.1 Quasi-Steady Thin Airfoil Theory

Unsteady flow can be characterized by the existence of a normal perturbation velocity across the chord. This normal velocity can be accounted for in the solution of the vortex sheet strength in classical thin-airfoil theory which requires flow tangency at the chordline. There are three types of airfoil positions or motion that produce perturbations normal to the chord, they include an angle of attack, α, a plunge velocity, $\dot{h}$, and a pitch rate $\dot{\alpha}$ about location a on the airfoil. The plunging (flapping) and pitching motions are captured by Leishman in Figure 3.17A, with the velocity acting normal to the airfoil chord due to the motion given by *w(x)* Figure 3.17B. Finally, the equivalent angle of attack at the quarter chord due to the wing motion α_{eq}, is shown in Figure 3.17C, [71].

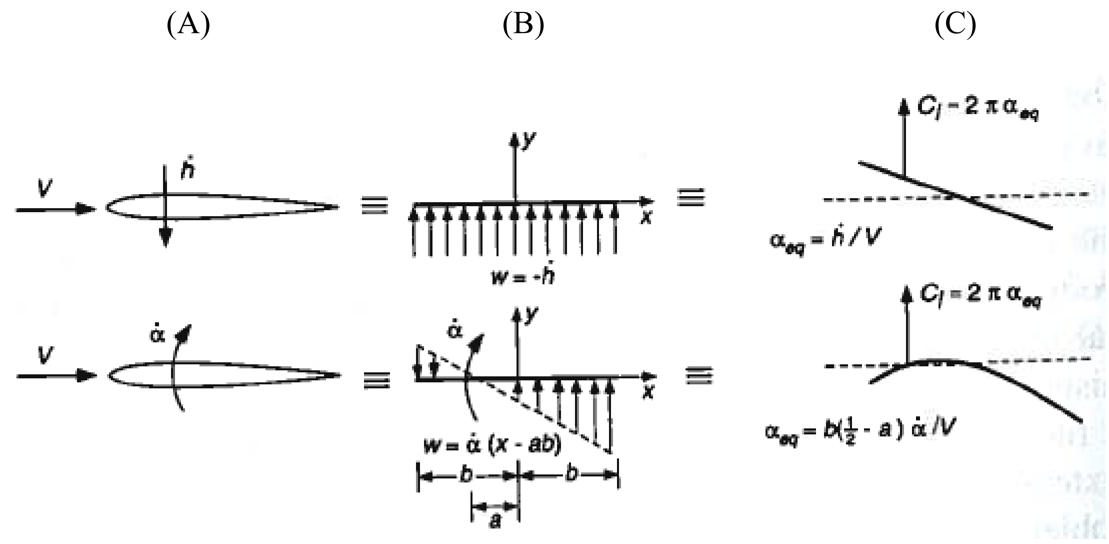

Figure 3.17: (A) – The plunging and pitching motion of an airfoil, (B) – The resulting vertical velocity, w(x), acting on the airfoil due to its motion, (C) – The equivalent angle of attack.

The Fourier coefficients from thin airfoil theory can be rewritten using the ratio of normal velocity to the free stream velocity, doing so gives Eqs. (3.43):

$$A_0 = \alpha - \frac{1}{\pi}\int_0^{\pi} \frac{w}{V}\,d\theta$$
$$A_n = \frac{2}{\pi}\int_0^{\pi} \frac{w}{V}\cos(n\theta)\,d\theta \tag{3.43}$$

Utilizing the normal velocity distributions of the three quasi-steady motions Fourier coefficients A_0 through A_2 can be calculated as shown in Table 3.3.

Table 3.3: Fourier coefficients for AOA, plunging and pitching airfoils.

Velocity Term	A_0	A_1	A_2
α	α	0	0
$\dot{h}$	$\dot{h}/V$	0	0
$\dot{\alpha}$	$-\dot{\alpha}ab/V$	$-\dot{\alpha}b/V$	0

The values of the Fourier coefficients are substituted into the lift and pitching moment from Eq. (3.5) and Eq. (3.6) where the effects of angle of attack, plunging and pitching are summed to produce the total quasi-steady lift and pitching moment coefficients of Eq. (3.44) and Eq. (3.45). Note that the pitching moment at the quarter chord is independent of the pitching axis location *a*. Also, if the pitching axis is assume to act at the quarter chord so that $a = -1/2$, the term inside the brackets for lift coefficient is the effective angle of attack at the ¾-chord or rear neutral point.

$$C_l = 2\pi\left[\alpha + \frac{\dot{h}}{V} + b\left(\frac{1}{2} - a\right)\frac{\dot{\alpha}}{V}\right] \tag{3.44}$$

$$C_{m,c/4} = -\frac{\pi}{4}\frac{\dot{\alpha}b}{V}; \quad C_{m,c/2} = \left[-\frac{\pi}{4} + \frac{1}{2}\left(\frac{1}{2} - a\right)\right]\frac{\dot{\alpha}b}{V} \tag{3.45}$$

3.4.2 Lift Deficiency Function

The quasi-steady solution provides a necessary start in accounting for unsteadiness, but additional adjustments are needed which use the reduced frequency to account for the degree of unsteadiness in the problem. The lift deficiency function provides a method to account for wake-induced lift loss caused by transverse or rotational changes in an airfoil position. This lift loss can be visualized as the energy used when changing the circulation around an airfoil as its position changes; the variation in the vortex wake circulation causes variation in downwash at the airfoil.

Theodorsen developed the lift deficiency function to quantize these wake loses due to oscillations such as pitching and plunging of airfoil and airfoil-aileron combinations [20]. The analysis assumes a simple harmonic motion of a thin airfoil in a uniform flow so the wake is harmonic with one time period. Potential flow theory and the Kutta condition are then applied to arrive at a numerical solution for the adjustment to the quasi-steady circulatory lift described in the previous section. The resulting lift deficiency function $C(k)$ is a complex equation resulting from the evaluation of multiple Bessel functions at the reduced frequency. The real and imaginary parts of the Bessel function evaluations are represented by the F and G functions respectively, to give $C(k)$ in Eq. (3.46).

$$C(k) = F(k) + i\,G(k) \tag{3.46}$$

The relation between $C(k)$ and its real and imaginary parts is plotted in Figure 3.18. Note that the phase shift increases as $k \rightarrow 0.2$ and then falls again as k increases. Lift magnitudes are reduced by up to 10% for quasi-steady flows and by

10-30% for unsteady flows. Highly unsteady flows, especially for $k > 1$, reach the maximum 50% loss of circulatory lift.

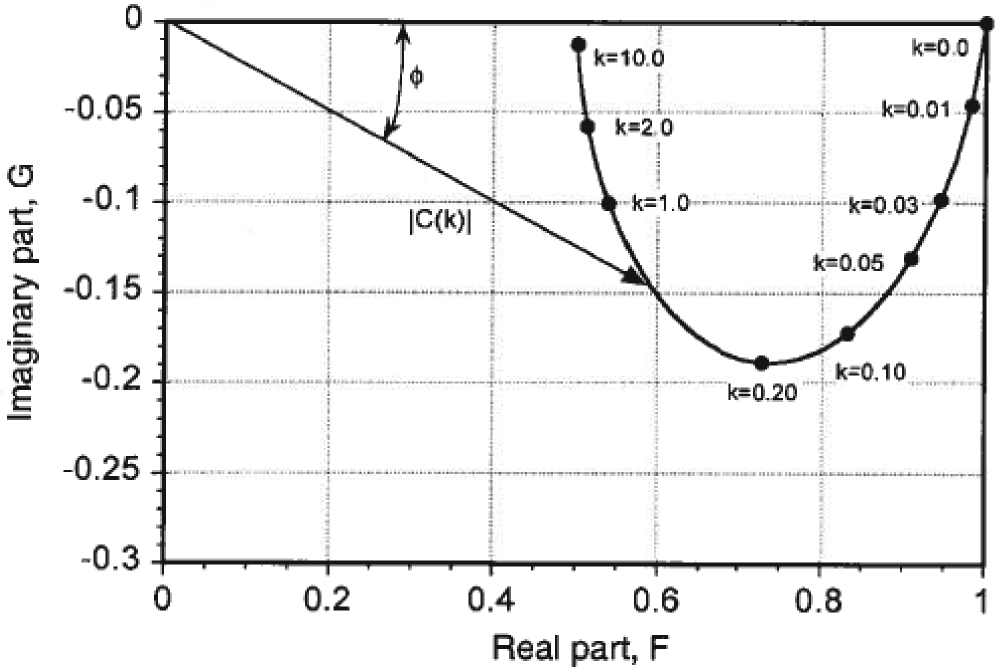

Figure 3.18: The lift deficiency function C(k) versus F and G, [71].

Values for $C(k)$ are generally evaluated using tables or graphs found in most aerodynamics texts. The lift deficiency function is applied by multiplying it with the quasi-steady circulation lift; however circulation lift is not the only lift force acting on an oscillating wing. For flows that are not uniform, as is the case with flapping wings and helicopters, it has been found that the lift deficiency correction remains appropriate for flow oscillation amplitudes up to 70% of the mean velocity and additional unsteady free-stream effects can be ignored [71].

3.4.3 Apparent Mass Effect

Apparent mass effect is the force generated when a flapping wing pushes the surrounding air perpendicular to the wing surface. This acceleration of air is the primary non-circulatory force experienced by a flapping wing vehicle and can be utilized to generate lift even when there is no forward motion of flying vehicle. The amount of air accelerated by the wing is estimated as the mass of air within a circular cylinder whose diameter is the chord and whose length is the local section or span length of the wing. This mass of air is multiplied by the acceleration of the wing section normal to the chord to calculate the apparent mass force shown as shown in Eq. (3.47). The apparent mass force acts normal to the wing section and is 180° out of phase with the wing displacement.

$$N'_{apparent} = \frac{\pi c^2}{4}\rho \cdot acceleration \tag{3.47}$$

Theodorsen took into account the apparent mass force when he was solving the two-dimensional unsteady aerodynamics problem with lift deficiency. The final Theodorsen equations for the lift and moment coefficients including both circulatory and non-circulatory terms are summarized in Eq. (3.48) and Eq. (3.49).

$$C_l = \underbrace{\pi b\left[\frac{\dot{\alpha}}{V} - \frac{\ddot{h}}{V^2} + \frac{ba\ddot{\alpha}}{V^2}\right]}_{Apparent\ Mass\ Lift} + \underbrace{2\pi C(k)\left[\alpha + \frac{\dot{h}}{V} + b\left(\frac{1}{2} - a\right)\frac{\dot{\alpha}}{V}\right]}_{Circulation\ lift\ adjusted\ by\ C(k)} \tag{3.48}$$

$$C_{m,c/2} = \underbrace{\frac{\pi}{2}\left[\frac{ba\ddot{h}}{V^2} - + \frac{b^2}{V^2}\left(\frac{1}{8} + a^2\right)\ddot{\alpha}\right]}_{Apparent\ Mass\ Lift} + \underbrace{\pi C(k)\left(a + \frac{1}{2}\right)\left[\alpha + \frac{\dot{h}}{V} + b\left(\frac{1}{2} - a\right)\frac{\dot{\alpha}}{V}\right] - \frac{\pi}{2}\left[\left(\frac{1}{2} - a\right)\right]\frac{\dot{\alpha}b}{V}}_{Circulation\ lift\ adjusted\ by\ C(k)} \tag{3.49}$$

As the reduced frequency increases, the accelerations of the airfoil become more important and the non-circulatory or apparent mass forces will become more relevant in the total loading on the wing. The strength of the apparent mass effect will also shift the phase angle of the total loading because it acts ninety degrees out of phase with the circulation force. The apparent mass effect is very important for flapping wing vehicles especially in hover or at very low speeds when circulation forces are only induced by the wing motion instead of fast forward flight.

3.4.4 Induced Flows

The total inflow or relative velocity at each segment of a flapping or rotating wing is a combination of the free stream flight speed, the rotational velocity of the wing and induced flow components from the vortex wakes that form as the wing moves through the air. Induced velocities have components in the longitudinal, lateral and vertical plane of the wing as shown in Figure 3.19; each of these flow components is discussed in the following subsections.

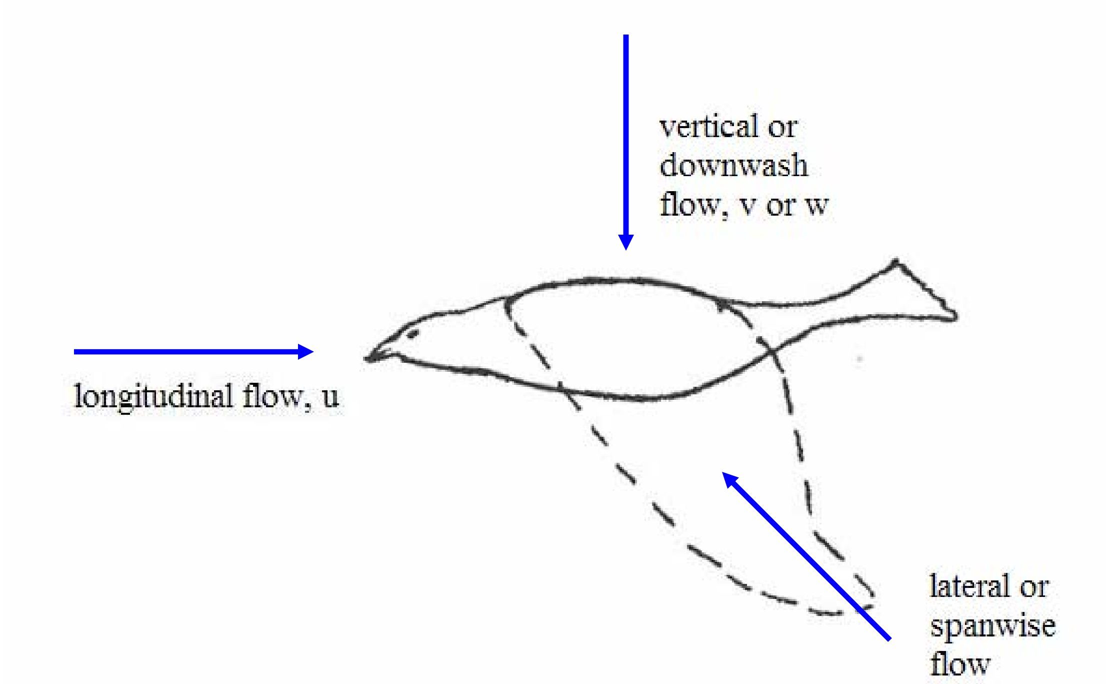

Figure 3.19: Depiction of induced flow directions.

3.4.4.1 Uniform Induced Flow

The longitudinal and vertical induced velocities *u* and *v* are the primary induced flows. As discussed in Section 2.6.2.1 the simplest technique for their analysis is to assume a uniform variation of the flow across the span so that momentum theory can be applied. The uniform induced flow results are calculated using known values for required lift (weight) and thrust (drag) to maintain flight. These inflow relations are restated below in Eq. (2.9) and Eq. (2.10) for a vehicle with flight speed U at a flight path angle γ.

$$u = \frac{2T}{\pi b^2 \rho U e} = \frac{2(W \sin\gamma + D)}{\pi b^2 \rho U} \tag{2.9}$$

$$v = \frac{2L}{\pi b^2 \rho U} = \frac{2W \cos\gamma}{\pi b^2 \rho U} \approx \frac{U C_L}{\pi AR} \tag{2.10}$$

3.4.4.2 Lateral or Spanwise Induced Velocity

Spanwise induced flows are generally neglected and have only recently come into consideration in the flapping wing aerodynamics field. Two articles have been published by Hong and Altman who experimentally explored the lift contributions of spanwise flow in flapping wings [72, 73]. This research isolated the vortices due to spanwise flow over the wing and proved that there was a measurable lift produced. There is still speculation as to how these vortices produce lift, but it was postulated that they may act like a delta wing vortex or tip vortices to increase lift. Spanwise flow research is still in its infancy, and the ability to model its effects are yet to be developed. Spanwise flow will not be included in the aerodynamic flapping wing model of this thesis, but its effects are interesting to consider.

3.4.5 Dynamic Stall

Dynamic stall occurs in oscillating wings and is seen as a hysteresis in the lift, drag and pitching moment curves of wings or rotors undergoing pitching and plunging motions or vibrations. Helicopter rotors, wind turbines, and any flapping or pitching wing can experience dynamic stall, which results from the repetitive motion between attached, separated and stalled flow over the airfoil. The dynamic stall process is explained pictorially by Leishman in Figure 3.20, [71]. Dynamic stall causes a delay in separation to higher angles of attack, which momentarily increases the airfoil lift. When stall is breached, a vortex detaches from the leading edge and momentarily increases lift as it sits above the leading edge. As the vortex moves toward the trailing edge, it induces a large pitch-down moment and an increase in loading and stress on a wing or rotor. Once the vortex is shed, a more typical lifting stall occurs, followed by reattachment as the angle of attack reduces to an operational level. The instability of loading during dynamic stall creates a dangerous boundary for the flight envelope that should not be crossed. Computational fluid dynamics or wind tunnel experiments are used to predict the onset and behavior of an airfoil in dynamic stall so that it can be avoided in flight. Generally, membrane wings and feathers reduce the presence of dynamic stall on an oscillating wing.

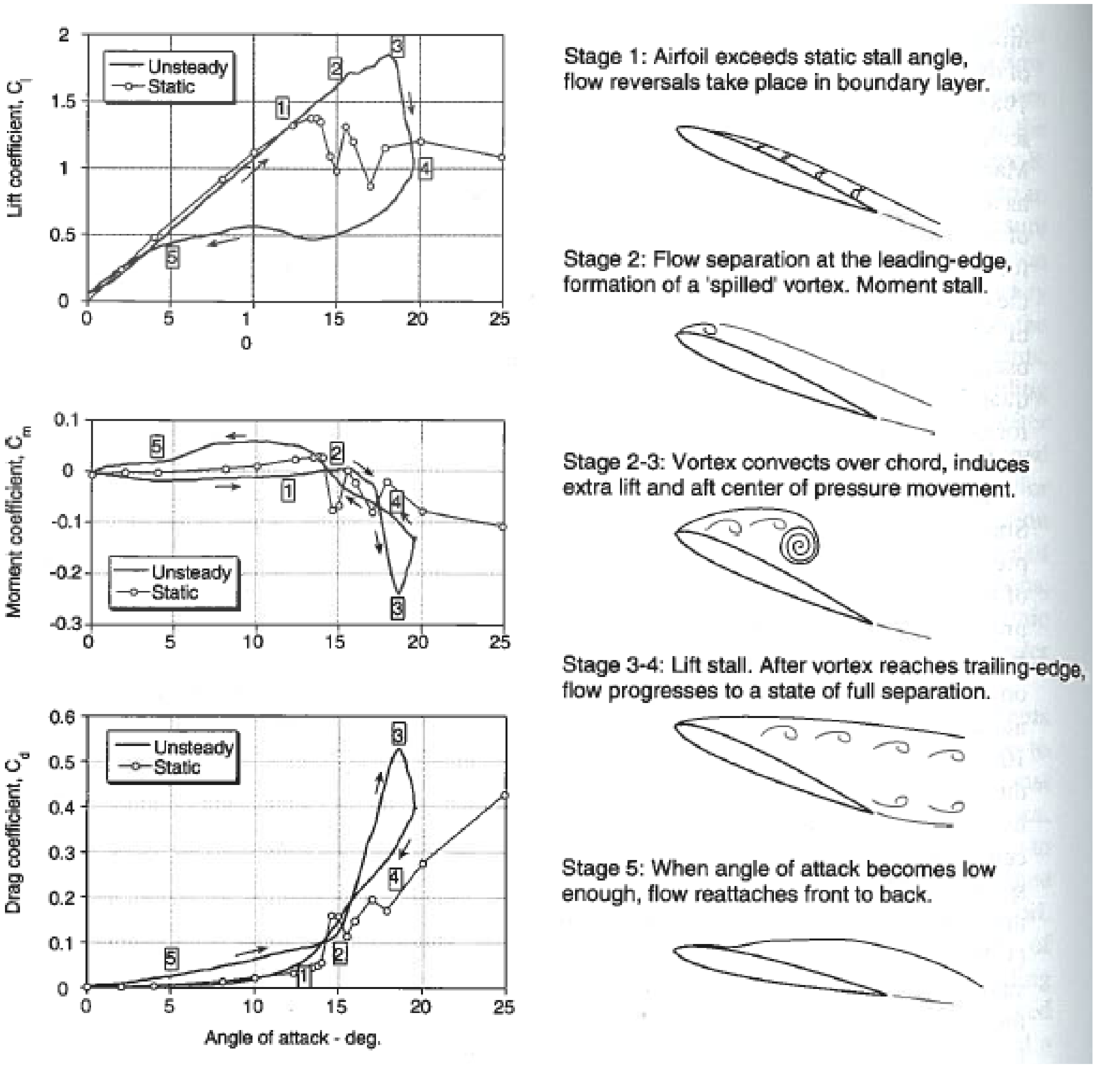

Figure 3.20: The dynamic stall process and its effect on forces and moments, [71].

3.5 Conclusions

This chapter provided a review of fixed wing aerodynamics and analysis tools and an introduction to membrane aerodynamics and unsteady aerodynamic phenomena as they apply to flapping flight. Several simple analytical methods were re-derived to solve complex problems, including the linear membrane lift equation, blade element analysis and momentum theory to quantify finite wing problem. These methods are used to formulate an aerodynamic model of flapping flight in Ch. 5.

Chapter 4. Wing Tracking Experiments

The primary task of this thesis is to produce an aerodynamic model of flapping flight for application in autonomous control and stability. This task is completed by analyzing the flapping wing kinematics and flexible wing membrane shapes of two remote control ornithopters. The kinematic results are then applied to a blade element model which utilizes the linear membrane aerodynamic equation and unsteady aerodynamics results from Ch. 3. This chapter will present the motion tracking experiments required to characterize the wing kinematics and the flexible membrane shapes as well as force measurement results.

4.1 Experiment Objective

There were two primary objectives to be completed through the wing tracking experiments, first to isolate the wing shape and kinematics with time in three dimensional space, and secondly to measure the vertical and horizontal forces produced by the ornithopter during the tracking period for a variety of flapping frequencies. The following sections present the experimental setup and equipment, procedure and post-processing. A detailed analysis of wing kinematics will follow, including a discussion of tip paths and leading edge bending as well as membrane behavior. The post-processed wing tracking data is used as input to a MATLAB® aerodynamic modeling program to predict the vertical and horizontal forces produced as a function of forward flight speed and stroke angle in Ch. 5.

4.2 Experiment Setup and Procedure

The following sections examine the experimental setup including equipment and placement of the motion tracking markers. The test matrix and operating procedures are established for recording the kinematic and aerodynamic load data.

4.2.1 Vicon Motion Tracking System

Key to the experimental process was the use of a Vicon MX motion tracking system, available in the Autonomous Vehicle Laboratory at the University of Maryland. The Vicon MX motion tracking system was an ideal solution for characterizing the dynamic wing shapes during flight because it is a passive sensor with minimal interference on the wing motion and can record data with resolution of 1-2 millimeters at rates of 350 Hertz. Six cameras are included in this Vicon setup with the capability of tracking a 15 by 15 meter capture volume. Vicon targets are tracked using small retro-reflective markers placed on the moving object, in this case the ornithopter wing. The reflective markers are highlighted when the cameras illuminate the wing at a specific wavelength and image sensitivity level to remove the background image so only the markers are visible. Each camera looks onto the wing from a different angle to assure each marker's motion is captured by enough cameras to locate the marker's position in 3D space over time. Data from the cameras is sent to the Vicon Tracker software which reproduces the motion with a 10 ms delay. This data can be exported directly or used as post-processor input to develop a six degree of freedom motion model that can interpolate a markers location if it goes missing for a frame and also reformat the data for further analysis. Specific experimental details follow.

4.2.2 Wing Marker Placement

To prepare for this experiment the left wing of each ornithopter was outfitted with approximately one hundred 3 mm hemispherical reflective markers in a grid pattern over the wings, as shown in Figure 4.1 and Figure 4.2. Additionally, four markers were placed on the tail and two along the spine to locate the origin of the body coordinate system and track the tail rotation and vibrations. Rather than place the markers on a purely rectangular grid, the placement was determined largely by the location of the carbon fiber fingers that support the trailing edge. To avoid influencing the shape of the flap region, markers were placed directly next to these fingers. The locations of the leading edge marker columns were determined by the intersection of the fingers with the diagonal spar to minimize the quantity of markers required. This grid forms a series of twelve blade elements, four aft of the diagonal spar along the trailing edge and eight in the triangular lifting region; the blade pattern is indicated on Figure 4.2.

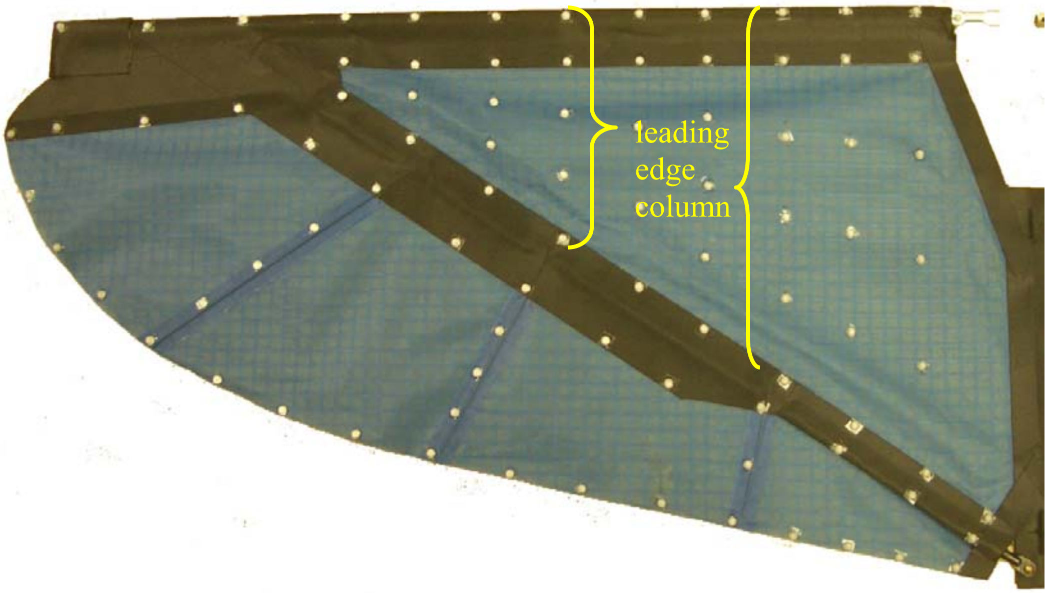

Figure 4.1: Wing marker placement on the blue wing (42" span), to be tracked visually.

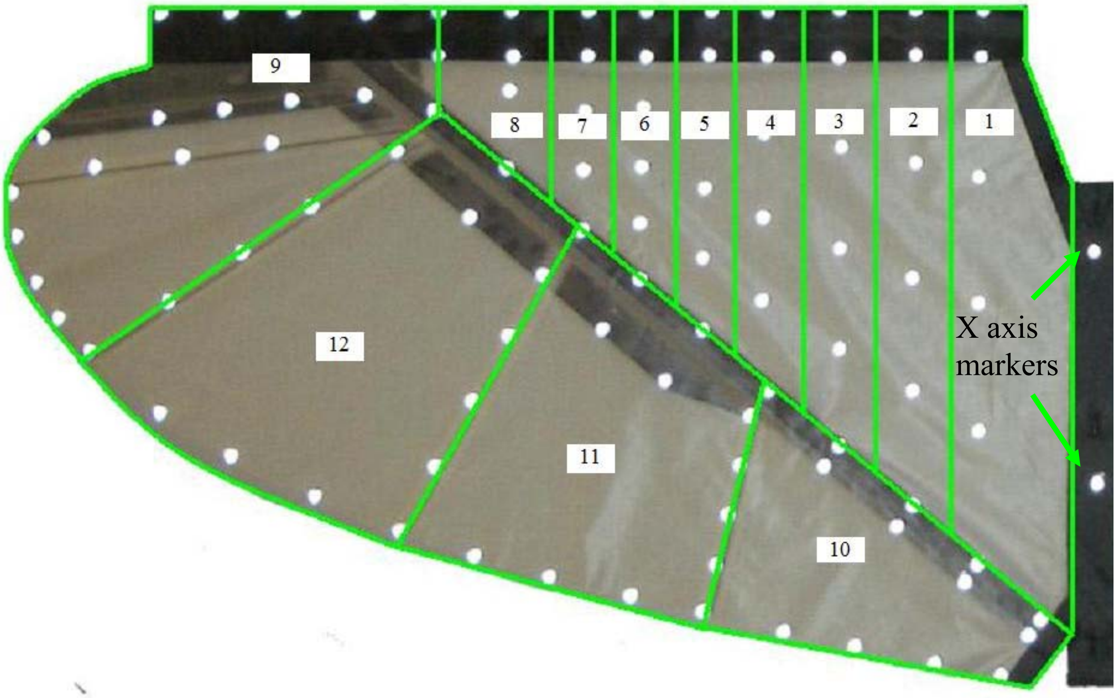

Figure 4.2: Locations of reflective marker on white wing with blade elements marked.

The markers weighed 0.01 gram each to give a total added weight of one gram to the wing. Previous research regarding ornithopter wing design determined that an added mass of five grams or more is required to negatively affect the wing dynamics; therefore the added mass of the reflective markers was considered negligible.

4.2.3 Test Setup

The experiment was setup in the middle of a large laboratory space so that the cameras could be best placed to register the reflective markers. When each camera was set in place the system was calibrated and the measurement coordinate system was established using a T-bar with reflective markers at the tips as shown in Figure 4.3. The final ornithopter coordinate system origin is located at the intersection of the leading edge and the symmetry axis of the body, the markers are used to locate this point and adjust the marker locations to the appropriate reference frame.

Figure 4.3: Setting the tracking coordinate system.

The ornithopters were rigidly secured by a custom test stand consisting of an aluminum base plate attached to a reinforced PVC pipe by means of large aluminum slugs shown in Figure 4.4. A six degree of freedom strain gauge transducer from Advanced Mechanical Technology Inc was mounted between the test stand and the vice that held the ornithopter to measure the vertical and horizontal forces produced during the flapping tests. This mounting setup is shown in Figure 4.5.

Figure 4.4: Vicon system testing setup.

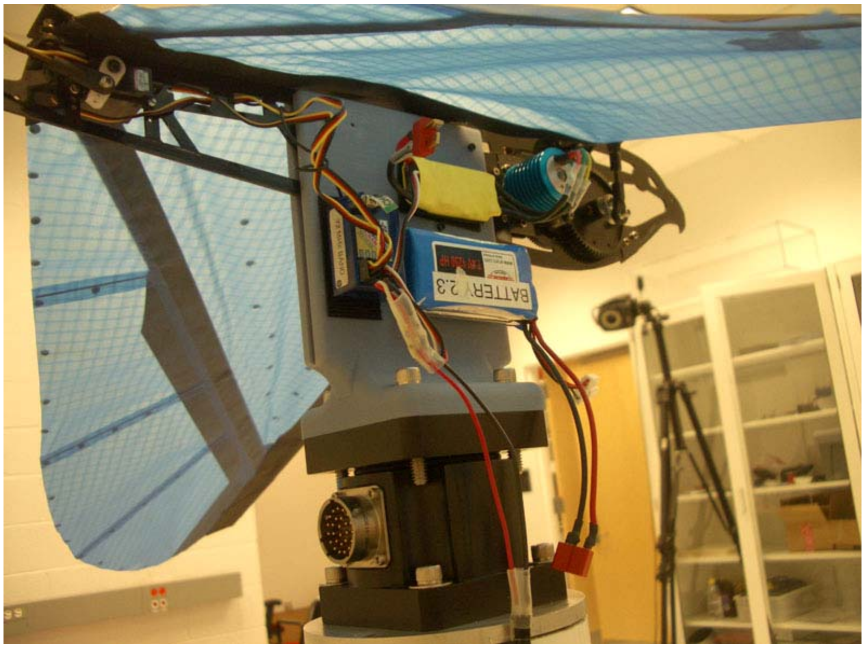

Figure 4.5: Test mount setup with 6-DOF force transducer

This constrained testing method limits the ornithopter to a hovering condition for experiment simplicity and allows the force measurements to be taken. Free flight or tethered experiments would provide more accurate wing motions, but would not allow force measurements to be made. A wind tunnel test is planned to measure forces and moments on the ornithopter in a low speed flow, with the option of tracking the wing motions. It is believed that the wing motions will be similar between hover and low speed forward flight, therefore the kinematics will be used for both hover and forward flight conditions in the aerodynamic model. However, additional motion tracking experiments should be completed with a freestream flow to confirm the similarity between hover and forward flight wing kinematics.

In addition to the force measurements, the wing stroke angle, which is required to synchronize the measured forces to the motion tracking data, was measured by magnetic potentiometer. The potentiometer, shown in Figure 4.6, was mounted to the ornithopter body just behind the wing root where it could track the rotation angle of a small permanent magnet placed on the rotating wing root. The wing angle signal was noisy due to electro-magnetic interference from the electric motor, but the underlying motion was still detectable.

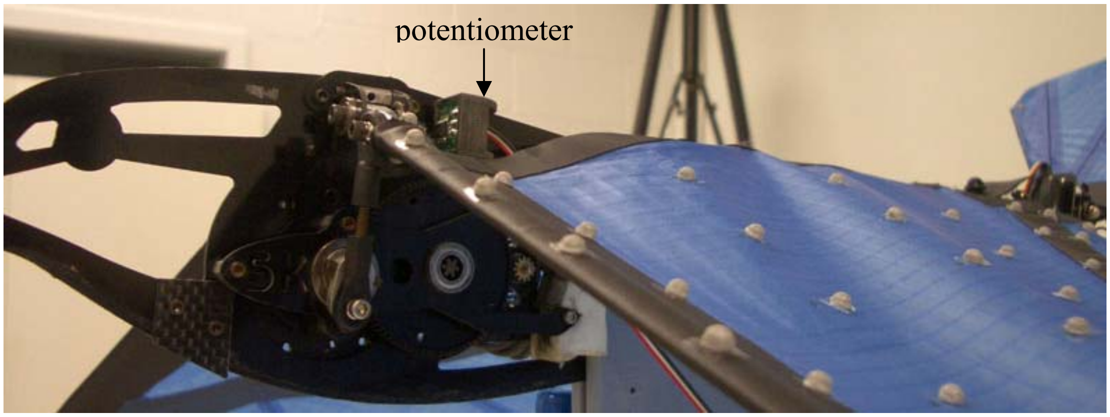

Figure 4.6: Magnetic potentiometer placed behind wing root to track wing angle.

The force measurement data channels in the experiment were conditioned by strain gauge amplifiers before being connected to the data acquisition module and recorded on a separate computer using LabVIEW and a National Instruments 6036E data acquisition card as shown in Figure 4.7.

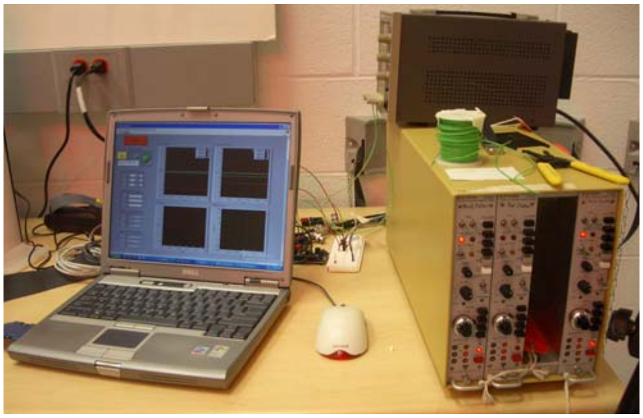

Figure 4.7: DAQ module and force observation station

Since the experiments were relatively short, data channels were sampled at 1 kHz. Each signal had a channel as specified in Table 4.1. Channel three was a throttle measurement; however it could not be obtained successfully from sampling the pulse-width modulated signal from the RF transmitter. Instead, throttle was estimated as a percentage of the maximum value using the throttle position on the remote transmitter. These voltage supplied by the throttle settings are not repeatable due to variable battery voltage levels, instead the flapping frequencies produced are measured and matched for different test cases. The resulting data, including the time history, force measurements, and stroke angle were then recorded to text files.

Table 4.1: Force and stroke angle measurement channels.

MEASUREMENT	CHANNEL
Time	1
Horizontal Force	2
Throttle	3 – N/A
Vertical Force	4
Stroke Angle	5

4.2.4 Test Matrix and Procedure

A test matrix was created before testing and adjusted based on time availability and lessons learned as the testing progressed. The final test matrix is shown in Table 4.2; it is based upon testing at a series of throttle levels, and therefore flapping rates. Both ornithopters reach throttle saturation and peak flapping rate at approximately 70% throttle and no tests went higher than this. Flapping rates varied from 3 to 7 Hertz. Typical flapping rates during flight are 4.5 to 5 Hz.

Table 4.2: Completed test matrix for each ornithopter

Case	**1**	**2**	**3**	**4**	**5**	**6**	**7**	**8**	**9**
Blue	30% Level	40% Level	50% Level	60% Level	60% Up	60% Down	60% Right	60% Left	Step 25-70% Level
White	15% Level	30% Level	45% Level	60% Level	55% Up	55% Down	55% Right	55% Left	Step 20-65% Level

First, a series of tests were completed with the tail trimmed for zero elevator and roll at incremental flapping rates, followed by moving the tail to its full left, right, up and down positions at the optimal throttle level of 55-60%. This was done to detect if the tail had any affect on the wing shape and loading and provide information on tail vibrations frequencies for tail redesign. Additionally, a throttle sweep with a trimmed tail was completed to identify directly how the aerodynamic forces changed with variable flapping rate. All the tests for the blue ornithopter were completed with zero fuselage angle of attack while the white ornithopter was tested at zero and ten degrees because time allowed extra testing. Future testing should include angle of attack variation and low speed oncoming flow, if possible, to observe changes in wing shape and loading for more realistic flight conditions.

4.3 Post-processing

Post-processing of the reflective marker data was completed using Vicon software to label the marker locations and create a model of their kinematic motion so any brief loss of a marker during tracking could be interpolated by the software. With full matrices of marker data points over the tracking time, the data was formatted into a text file for use in the MATLAB aerodynamic modeling program. In addition, the aerodynamic force and stroke angle measurements which were recorded separately from the Vicon data must be synchronized to the marker data in order to compare results from the aerodynamic modeling. These post-processing steps are discussed in the following sections.

4.3.1 Labeling and Formatting

Post-processing of the Vicon data first required the identification and labeling of every marker in a single frame of the wing motion. Labeling was completed using a combination letter-number scheme similar to quantifying matrix rows and columns as specified below. The blue ornithopter's reflective markers are labeled in Figure 4.8 using this scheme.

- Leading Edge (LE#): LE1 to LE*n* from root to tip for both ornithopters
- Luff Region (M##): M11…M*nm* in a matrix-like format for luff region
- Middle Leading Edge (ME#): ME1 at root to ME*n* at end of luff region
- Middle Trailing Edge (MT#): MT1 at root to MT*n* at end of luff region
- Fingers (F##): F11 closest to root, F2*n* to F*nn* moving toward wing tip
- Trailing Edge (TE#): TE1 to TE*n*, with final value called TIP at wing tip
- X Axis set by X1 and X2
- Tail: TUL (upper left), TLL (lower left), TUR (upper right), TLR (etc)

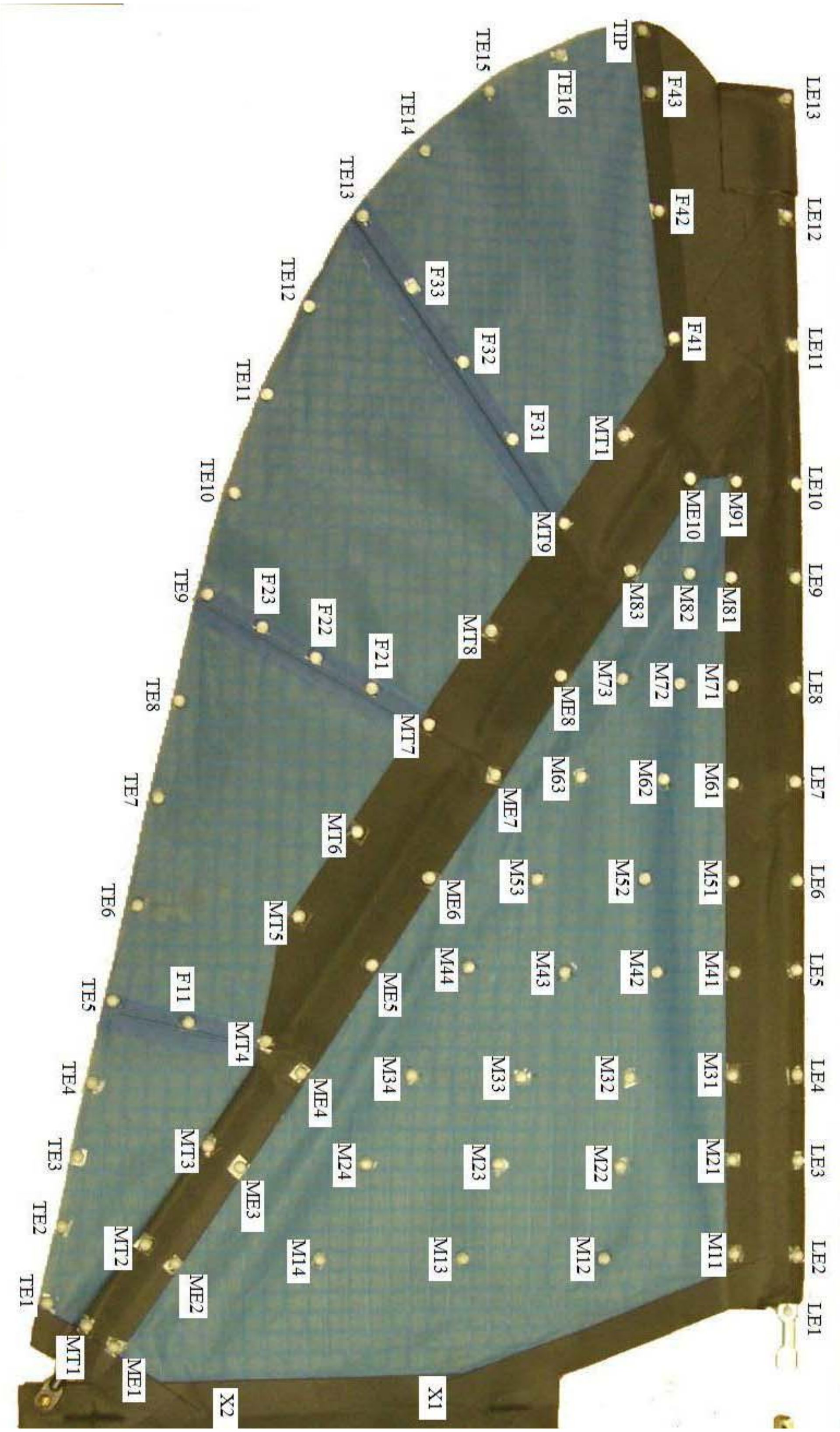

Figure 4.8: Labeling of marker points on blue wing.

Once labeled in the Vicon software, as shown in Figure 4.9, the Vicon post-processing module creates a model for the behavior of the wing so it can successfully follow a specific marker motion. If a marker is not visible for a few frames, the system interpolates where it would be based on previous and future motions. This process was completed for each test case to generate a file containing the (x,y,z) coordinates of each labeled marker with the time also specified in matrix format.

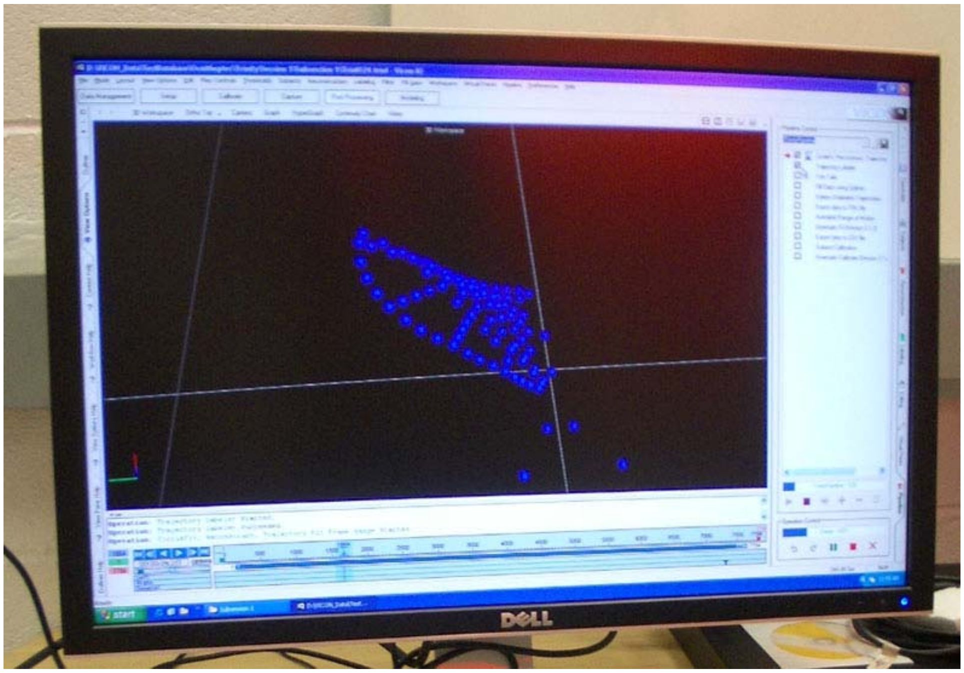

Figure 4.9: Post-processing of tracking data

Two MATLAB® programs were created to read the Vicon data sets for each ornithopter and separate individual marker information into variables using the marker's Vicon label. The programs first locate the origin of the coordinate system at the intersection body symmetry axis (X1, X2) and the wing leading edge. Marker points are then calibrated to this origin to ensure the correct coordinate system is used by the aerodynamic code. The entire set of marker variables and the time variable are then saved in '.mat' files for future use.

4.3.2 Data Synchronization

Another post processing task was to synchronize the marker tracking data to the force measurement data set because the two data sets started recording at slightly different times. This correlation was completed by filtering and smoothing the noisy stroke angle measurement which is included in the load measurement files and comparing it to the stroke angle calculated from the position of the first three reflective markers on the leading edge (LE1, LE2, LE3). The stroke angles are correlated by determining the time offset of the measured stroke angle to the calculated stroke angle. This time offset is requested as input by the aerodynamic modeling program which shifts the measured data by the appropriate amount of time. While this technique can be completed without synchronization programs, there are cross-correlation codes (xcorr.m) available which are used to determine lag between data, if a different approach synchronization method is preferred.

4.4 Kinematic Results

The reflective marker motion tracking data is an outstanding tool for both quantitative and qualitative analysis of the wing kinematics. The following sections will examine the kinematic behavior, including the wing tip path, membrane shape and leading edge bending as the stroke angle and flapping frequency vary. Chapter 5 will bring the kinematic analysis to the aerodynamic realm by forming blade elements characterized by the marker generated membrane airfoil sections. High fidelity measurements of each section’s membrane slack, position, velocity and acceleration will then be used to calculate the aerodynamic forces.

4.4.1 Wing Tip Paths

As explained in Ch. 2, variations in the wing tip path direction and stroke plane angle can provide insight into how a flapping wing produces both lift and thrust. Unlike birds, the remote control ornithopters are limited to vertical flapping by their single rotational degree of freedom; any variation from this vertical motion is due to passive bending of the wing. Figure 4.10 and Figure 4.11 show the side view and top view of the wing tip path for the blue and white ornithopters respectively. The side view only shows the 5.0 Hz and for the blue ornithopter and the 4.65 Hz result for the white ornithopter because the vertical tip path taken during all frequencies was too similar to differentiate. The top view shows the lead-lag motion of the tip for three flapping frequencies because there path varies with frequency. Arrows also indicate the direction of motion in the both views.

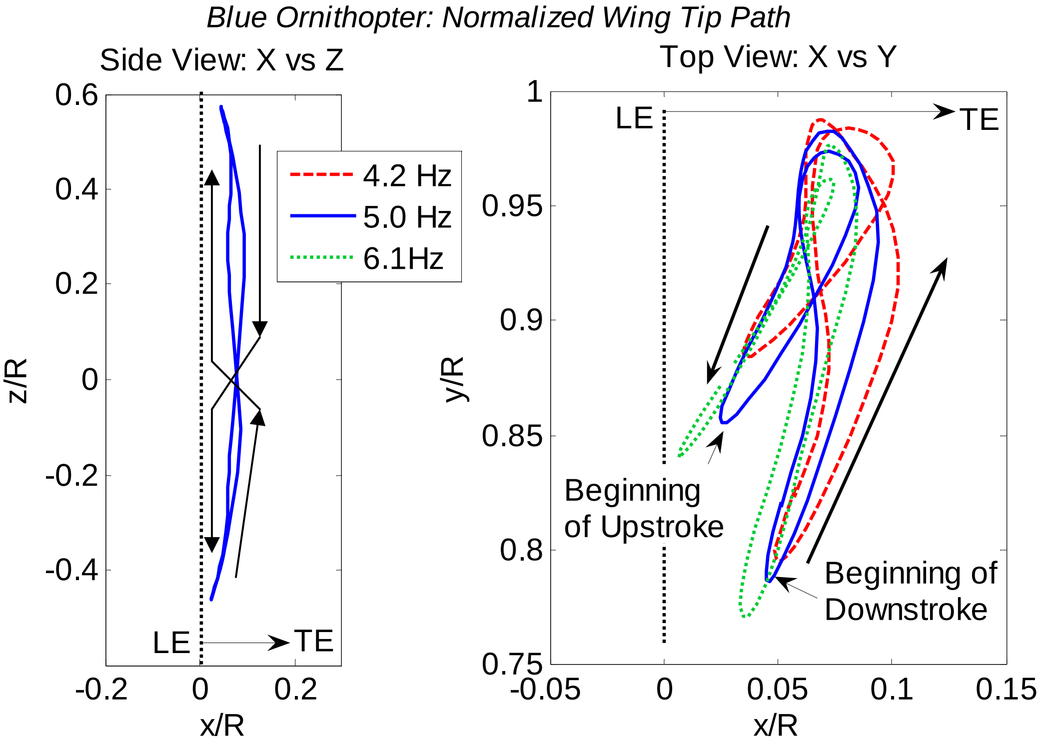

Figure 4.10: Normalized tip paths x vs z and x vs y for the blue ornithopter, R = 0.533m.

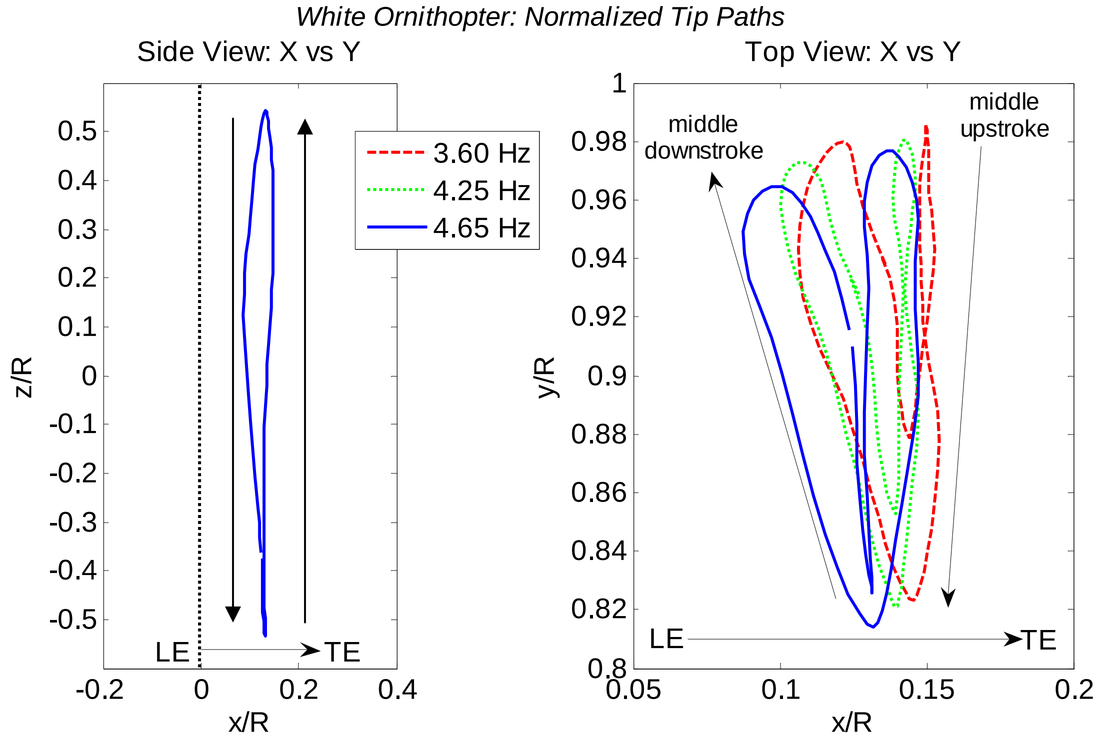

Figure 4.11: Normalized tip paths x vs z and x vs y for the white ornithopter, R = 0.599m.

Both the side and the top view of the tip path show up to 5cm (10% span) of rearward variation in the x axis due to passive leading edge bending. However, the stroke angle is still essentially vertical as expected so the primary generation of thrust must come from the pitch variation across the wing span and the larger beating motion of the trailing edge which pushes the bird forward like a swimming fish. The top view also shows the normalized span value, y/R, reducing as the wing tip reaches the peak of downstroke and upstroke. While the motion of the wing tips out of the vertical plane is small, the variation in tip paths between the two ornithopters is quite significant. The blue ornithopter has a figure eight vertical tip path, while the white ornithopter's vertical tip path is closer to elliptical. This figure-eight versus elliptical pattern is also seen in the lead-lag motion where the blue ornithopter's wing tip crosses its own path at the middle of the stroke, while the white ornithopter has no tip path convergence at a 4.65 Hz. The reason for these tip path differences is unknown.

4.4.2 Leading Edge Spar Bending

Another characteristic of the flexible flapping wing is the bending that occurs in the leading edge spar. Figure 4.12 and Figure 4.13 demonstrate the leading edge bending in the y-z plane (front view) at the typical flapping frequencies of 5.0 Hz and 4.67 Hz for the blue and white ornithopter respectively.

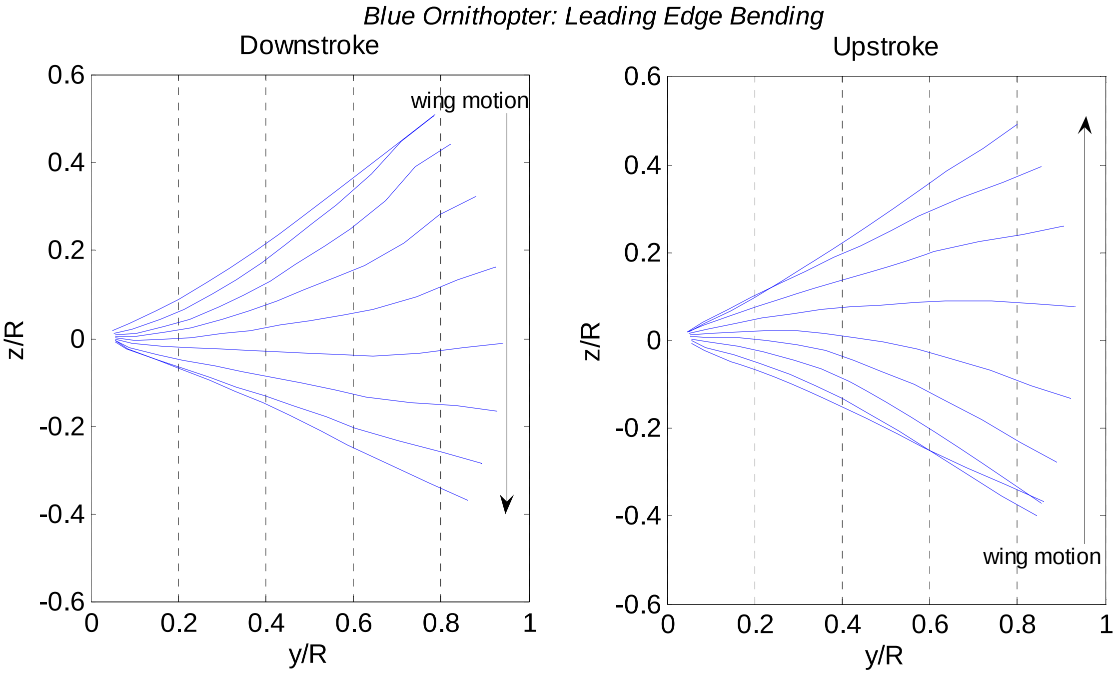

Figure 4.12: Leading edge bending of the blue ornithopter at 5.0 Hz flapping rate.

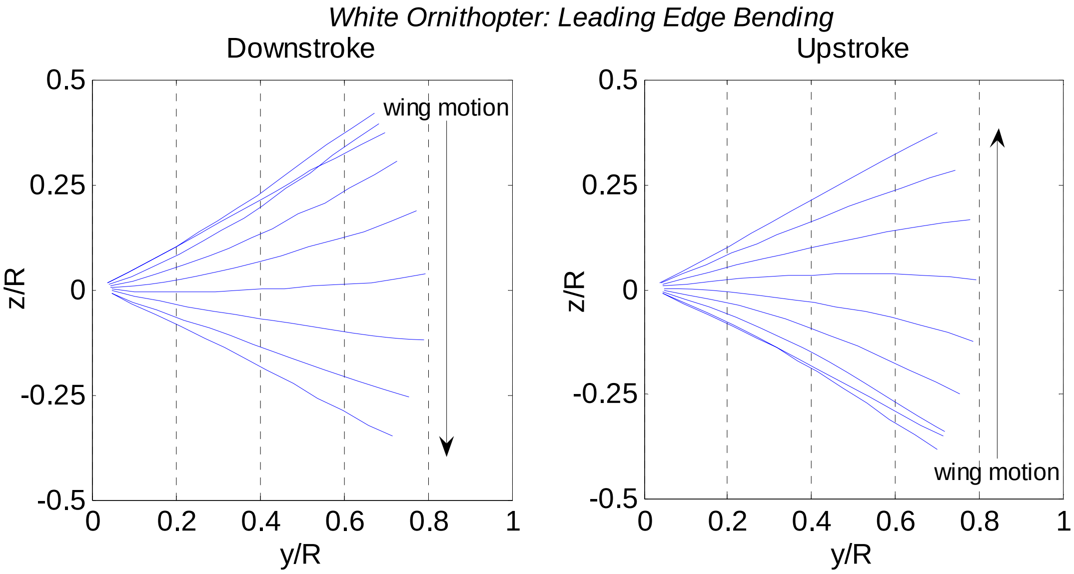

Figure 4.13: Leading edge bending of the white ornithopter at 4.67 Hz flapping rate.

The bending is largest at the beginning of upstroke and downstroke as the wing reaches peak acceleration through the stroke transition. This is a response to high inertial loading which is especially strong near the wing tip where it increases the local stroke angle. A lag then forms between the wing root and wing tip stroke angle, which is why the aerodynamic model must take into account the local stroke angle rather than the root stroke angle. Chapter 5 will show how the stroke angle lag affects the aerodynamic forces due to differences in the sign of the local velocity at the wing root and tip near the upstroke-downstroke transitions.

4.4.3 Membrane Shape

The final element of the kinematics to consider is the shape of the wing membrane in the luff region during the flapping cycle. (The trailing edge flap region is assumed to be a flat plate so the sail theory result does not apply). The triangular luff region between the two spars has a large slack ratio which varies as the spars move. The larger slack ratio combined with the pitching motion may induce inflections in the membrane shape and cause higher order behavior. The membrane shape for each blade element in the luff region must be verified to have a predominately first order, concave or convex shape, in order to apply the empirical relation for the membrane lift coefficient, $c_l = 2\pi\alpha + 0.636\sqrt{l/c}$. To verify that the membrane behavior is first order, blade element four, which is located in the center of the luff region at about 1/3 of the semi-span as shown in Figure 4.14, was examined by fitting a cubic function to the reflective marker points at multiple stroke angles for downstroke and upstroke.

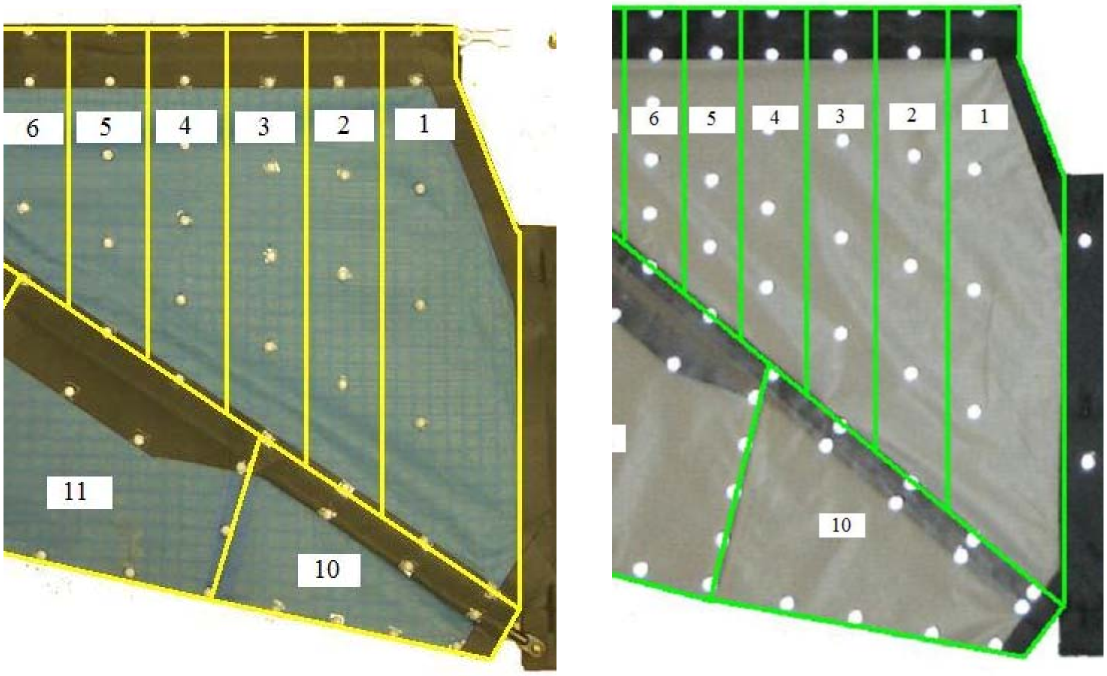

Figure 4.14: Locationof blade element four for both ornithopterwings.

The resulting membrane shape in the x-z plane or side view is shown as a sequence of stroke angles in Figure 4.15 and Figure 4.16 for the downstroke and upstroke of the blue ornithopter at 5.37 Hz flapping frequency. Likewise, Figure 4.17 and Figure 4.18 show blade element four's membrane shape for the white ornithopter during downstroke and upstroke at the flight frequency of 4.67 Hz. These figures represent half of the wing stroke, with the motion indicated by the arrows to the right, and the variation in line color from blue at the beginning of motion to red at the end of the motion. The blade length and vertical travel are normalized using the maximum stretched blade length *L*, this allows the amount of slack in the membrane to be seen visually. The stroke angle and color legend for for each line is specified to the right of the figure for easy reference.

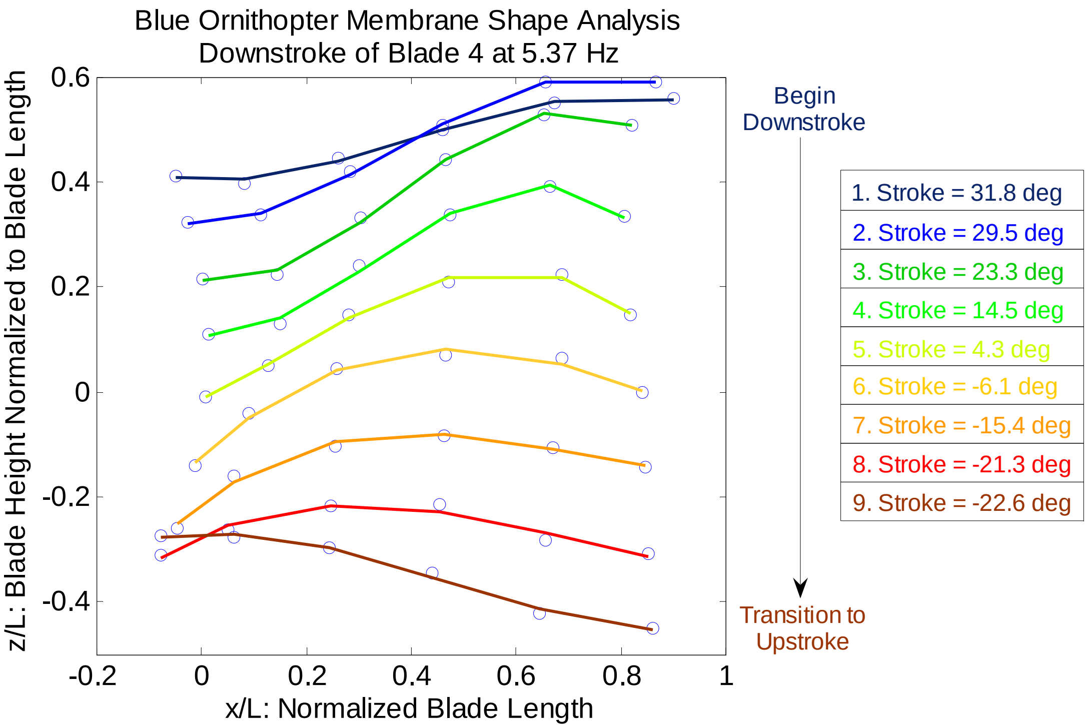

Figure 4.15: Blue ornithopter: Downstroke behavior of blade element four's membrane airfoil.

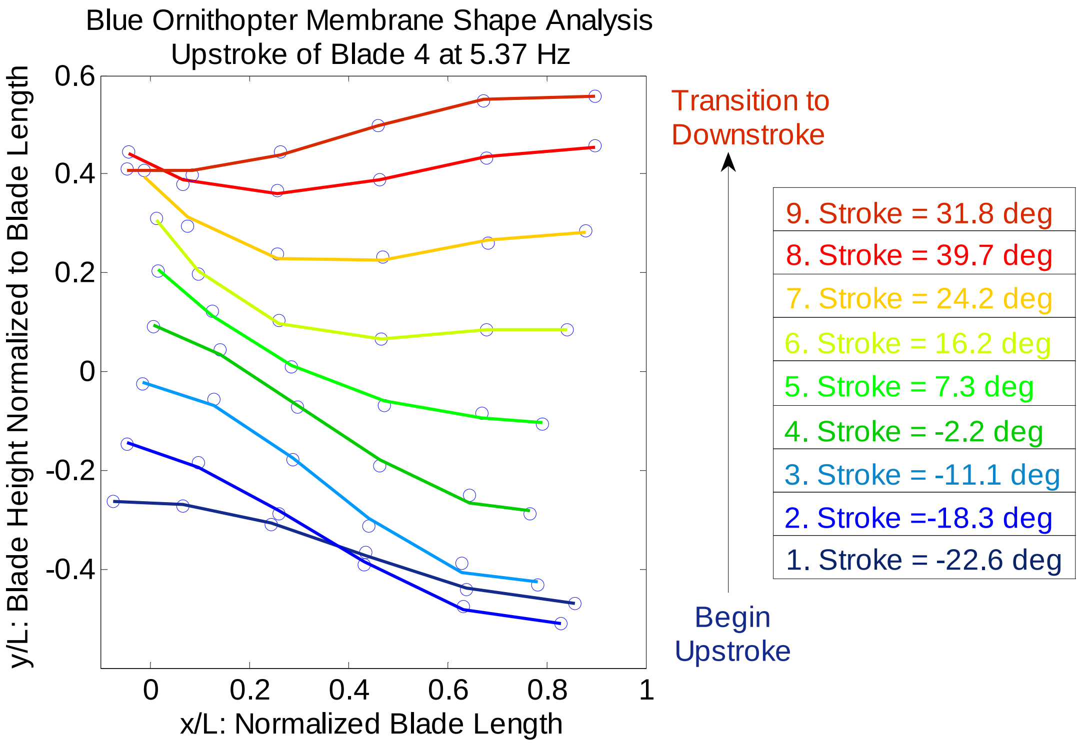

Figure 4.16: Blue ornithopter: Upstroke behavior of blade element four's membrane airfoil.

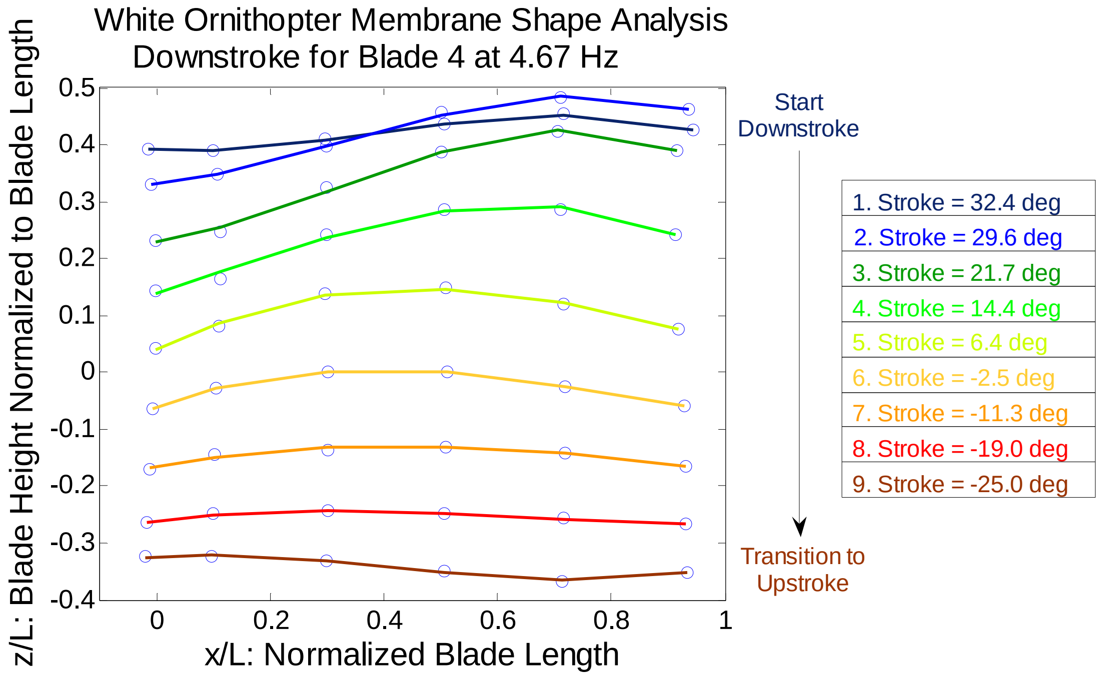

Figure 4.17: White ornithopter: Downstroke behavior of blade element four's membrane airfoil.

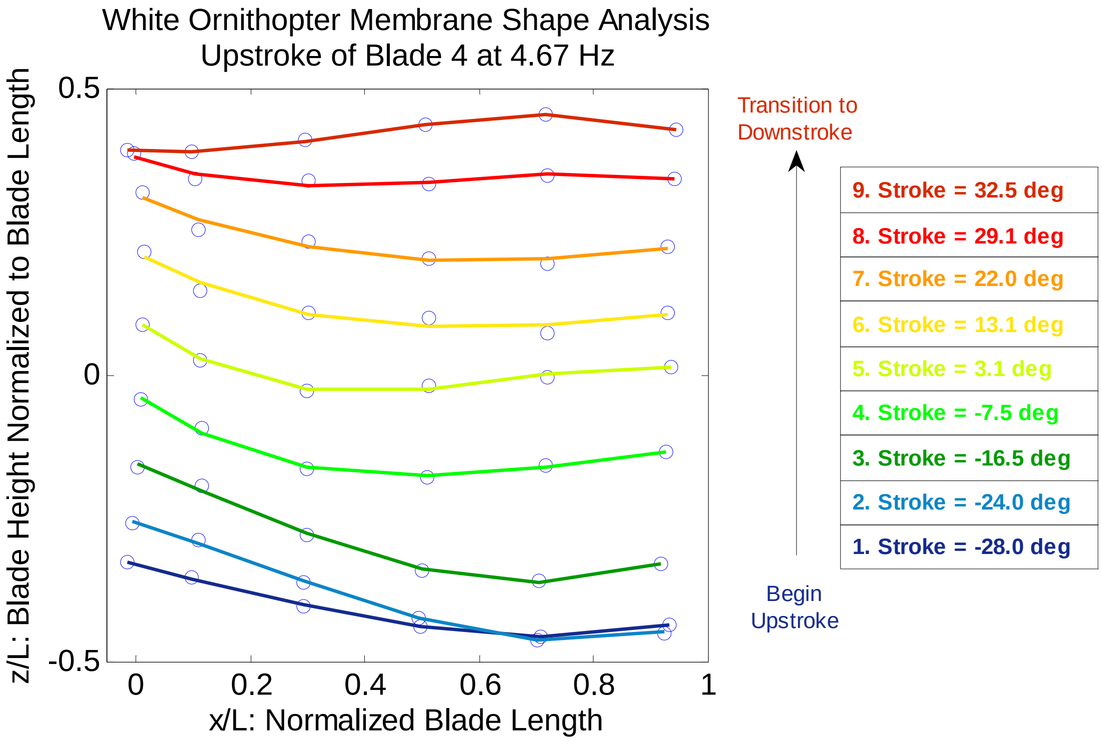

Figure 4.18: White ornithopter: Upstroke behavior of blade element four's membrane airfoil.

A closer looks shows that the white ornithopter has a more consistent concave or convex membrane shape than the blue ornithopter with smaller inflections near the leading and trailing edge the stroke during downstroke and upstroke transitions. This is because the blue ornithopter experiences a large degree of pitching motion during the entire stroke while the white ornithopters's blade element chord only varies from horizontal when the transition region between upstroke and downstroke is approached. If the two dimensional membrane airfoil is at an extreme pitch value or a region of transition it is more likely to experience inflections in the membrane shape. These inflections would be close to the leading or trailing edge the blade element approaches or exits transition. The inflection point moves through the center of the membrane as transition occurs and the membrane reverses camber; this is indicated by the deep blue and red camber lines at the beginning and end of downstroke in these figures.

As a whole, Figure 4.15 through Figure 4.18 demonstrate that the membrane shape is of the first order during the majority of the wing stroke, especially for the white ornithopter. The blue ornithopter does experience some deviation from the first order shape with slight inflections near the leading and trailing edge; however these are minor enough that the membrane lift coefficient equation should still be valid. While the transition region clearly violates the first order mode shape rule, it occurs in such a short period of time that assuming this region is first order in the lift approximation should be negligible. Therefore the assumption of first order membrane behavior is assumed to be valid and the linear sail equation for lift coefficient can be utilized in the aerodynamic model.

4.5 Force Measurement Results

In addition to the kinematic data, vertical and horizontal force data from the strain gauge amplifier can be examined. Some of the most important aerodynamic force results came from the throttle sweeps because they clearly show continuous force measurement trends with variation in flapping frequency. These throttle sweeps are shown in Figure 4.19 and Figure 4.20 for the blue and white ornithopter respectively. For flapping frequencies up to 5 Hz, both ornithopters experience a linear increase in vertical and horizontal force with increasing flapping rate. Also notice that the vertical force is symmetrical about zero which means there is no net vertical force produced when the flapping axis is horizontal. This result is expected because the wing behavior is almost symmetrical; therefore the wing behaves like a symmetrical airfoil which requires positive angle of attack to produce a net vertical force.

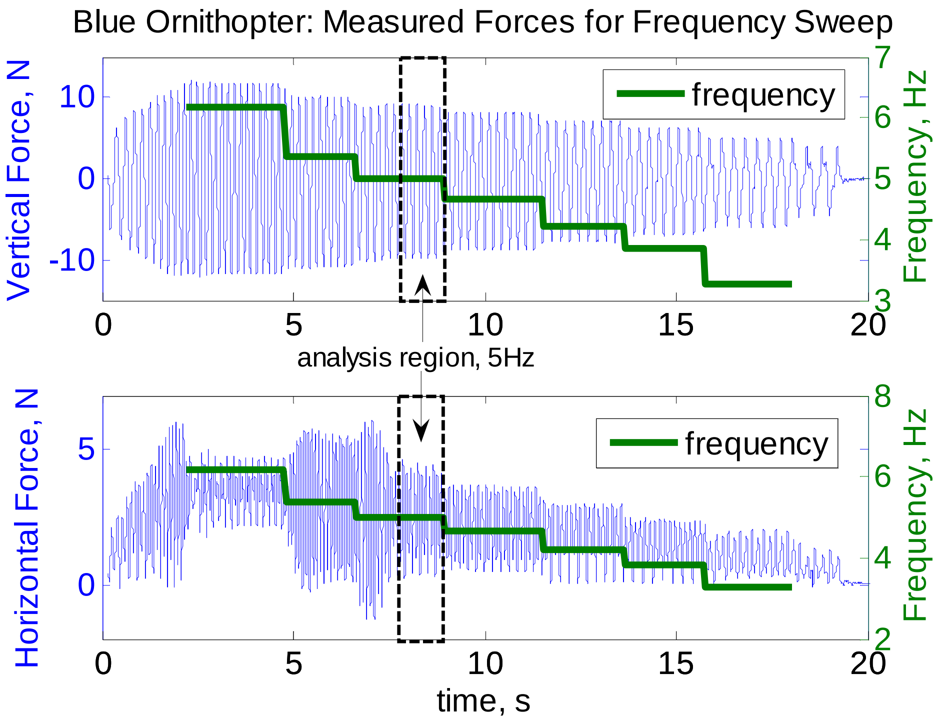

Figure 4.19: Blue ornithopter forces measurements during a frequency sweep from 6Hz to 2Hz.

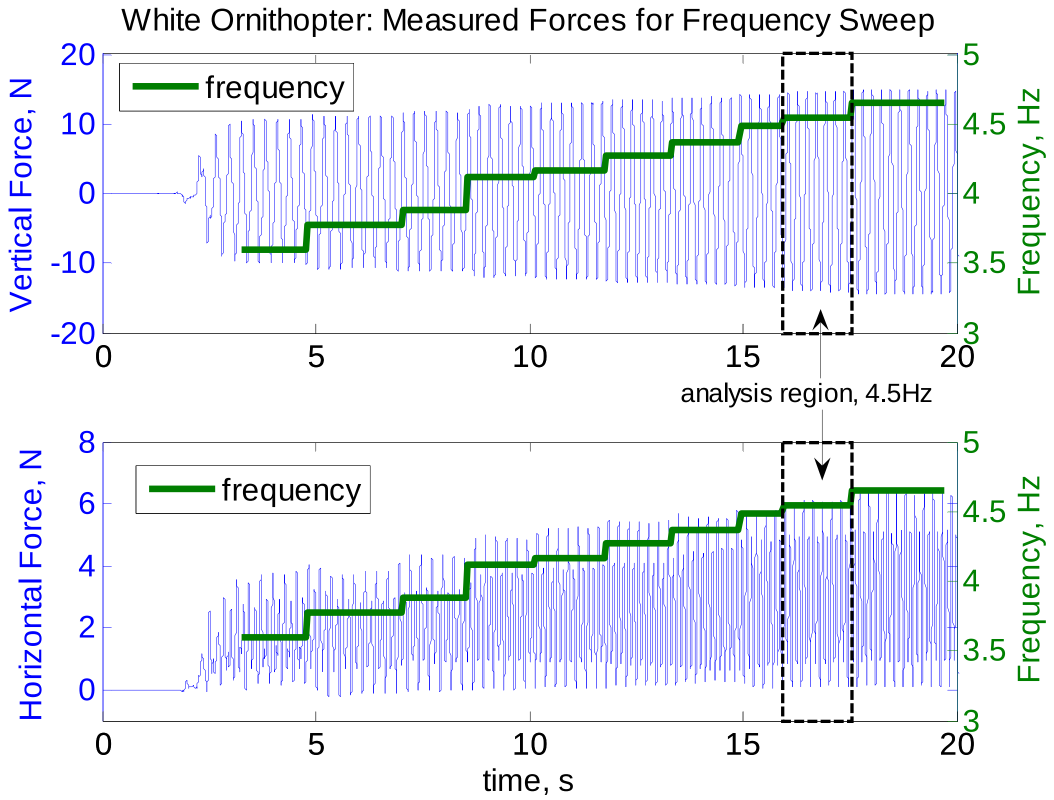

Figure 4.20: White ornithopter force measurements for a frequency sweep from 3.5 to 4.7 Hz.

The blue ornithopter also demonstrates a period of horizontal force resonance or vibration from 5.4 to 6 Hz in comparison with results at 5 Hz and below. The resonance is seen as both a spike in force magnitude and as a phase shift forward by 60° to the downstroke-upstroke transition. It is not known where or why this resonance occurs, it could be in the wing structure, in the ornithopter fuselage or even an experimental anomaly. No resonance is experienced by the white ornithopter. The phase and magnitude trends of the vertical and horizontal forces versus flapping frequency are presented for further analysis in Figure 4.21 and Figure 4.22 for the blue and white ornithopters respectively.

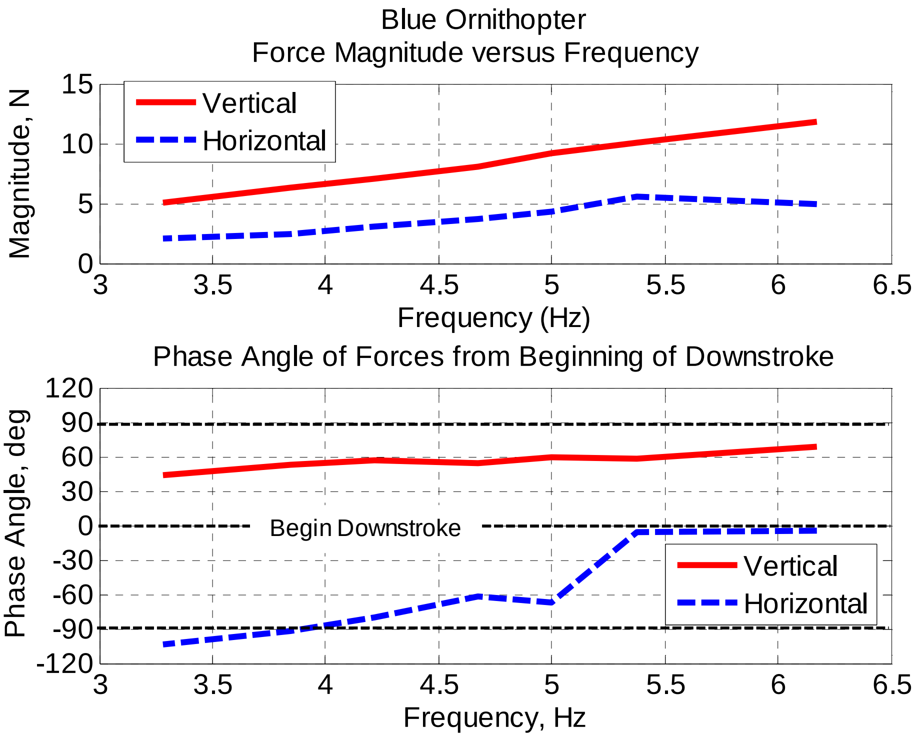

Figure 4.21: Magnitude and phase angle with respect to beginning of downstroke of measured vertical and horizontal force as a function of frequency for the blue ornithopter.

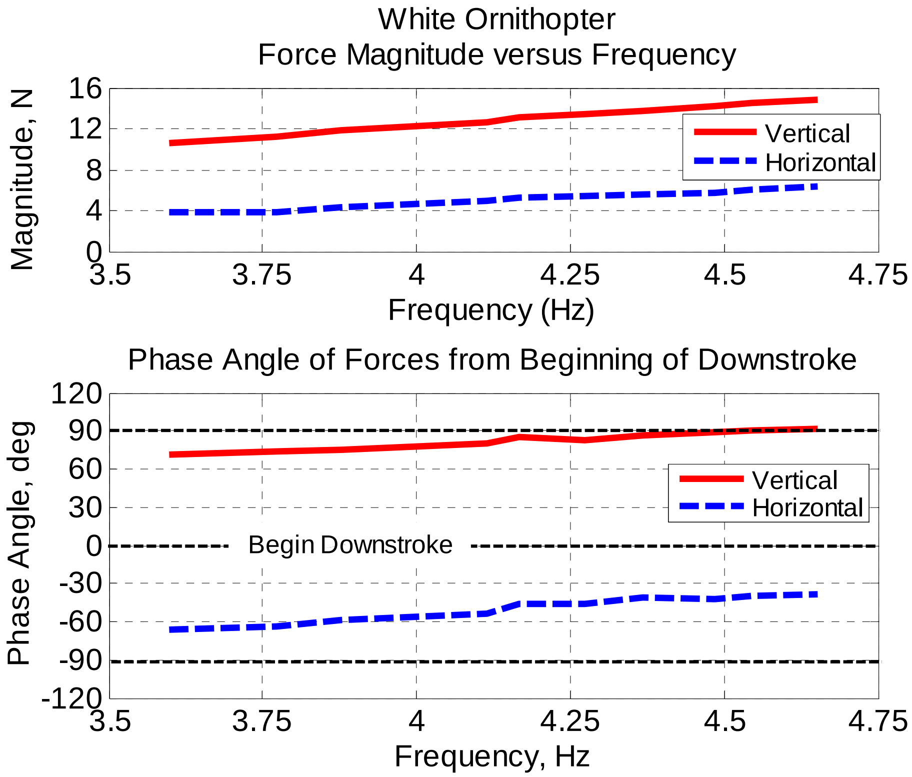

Figure 4.22: Magnitude and phase angle with respect to beginning of downstroke of measured vertical and horizontal force as a function of frequency for the white ornithopter.

The horizontal force operates at twice the flapping frequency and is always positive. Horizontal force should achieve a maximum value during the middle of downstroke and upstroke which equates to a phase difference of +/- 90˚ from the beginning of downstroke. Figure 4.21 shows the blue ornithopter's horizontal force phase at a reasonable $-100°$ to -60˚ before the beginning of downstroke as frequency increases to 5Hz. At 5.4 Hz the horizontal force phase quickly jumps to zero which may be caused by the beginning of resonant behavior. The white ornithopter does not experience a strucutural resonance, but the maximum horizontal force still occurs towards the end of upstroke and downstroke with a phase lag of -65˚ to -45˚ as shown in Figure 4.22. It is expected that the maximum positive vertical force, which oscillates at the same frequency as the wing angle, should also occur near the middle of downstroke at a 90˚ positive phase shift from the beginning of downstroke. The white ornithopter achieves this 90˚ phase mark in the vertical force as it reaches maximum flapping frequency of 4.545 Hz, while the blue ornithopter has an average vertical force phase of about 60˚. Using these phase and magnitude charts the optimal frequency for analysis was chosen as 5Hz for the blue ornithopter and 4.545 Hz for the white ornithopter. These selections avoid the body resonance and are often achieved during flight testing.

The optimal frequencies are examined detail for one flapping period. The resonance and linear behavior in the blue ornithopter's performance is compared by examining the 6.17 Hz and 5 Hz force results in Figure 4.23 and Figure 4.24 respectively. While the vertical force curves are very similar, the shift in horizontal force phase to 0° at the upstroke and downstroke transitions is clear for the 6.17 Hz case.

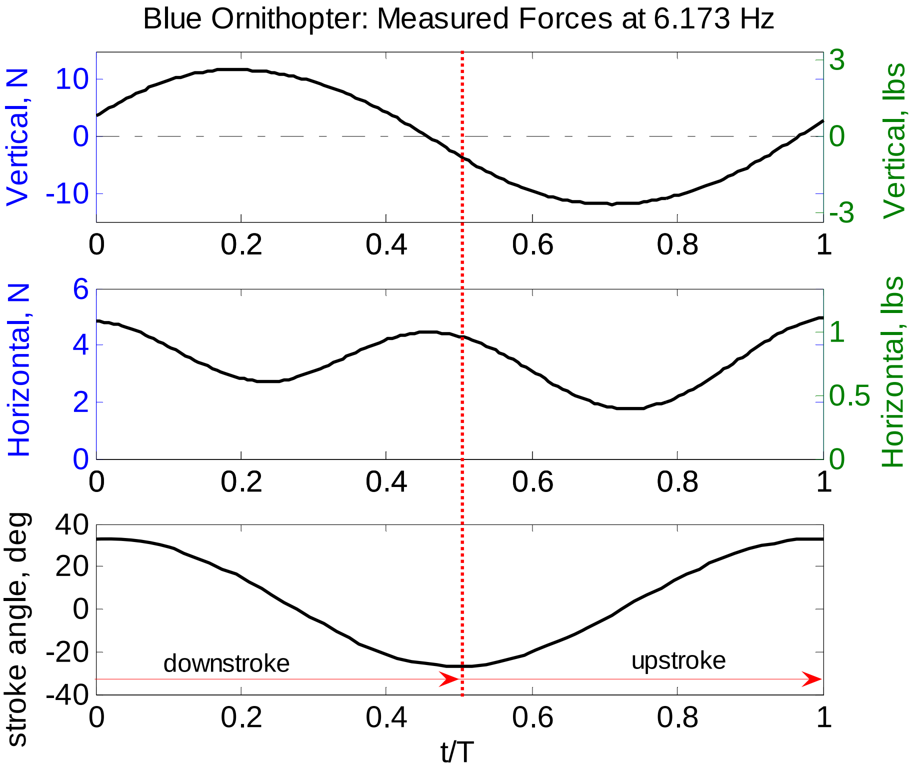

Figure 4.23: Blue ornithopter measured forces at 6.17Hz. The horizontal force is out of phase with the middle of the downstroke due to resonant structural behavior.

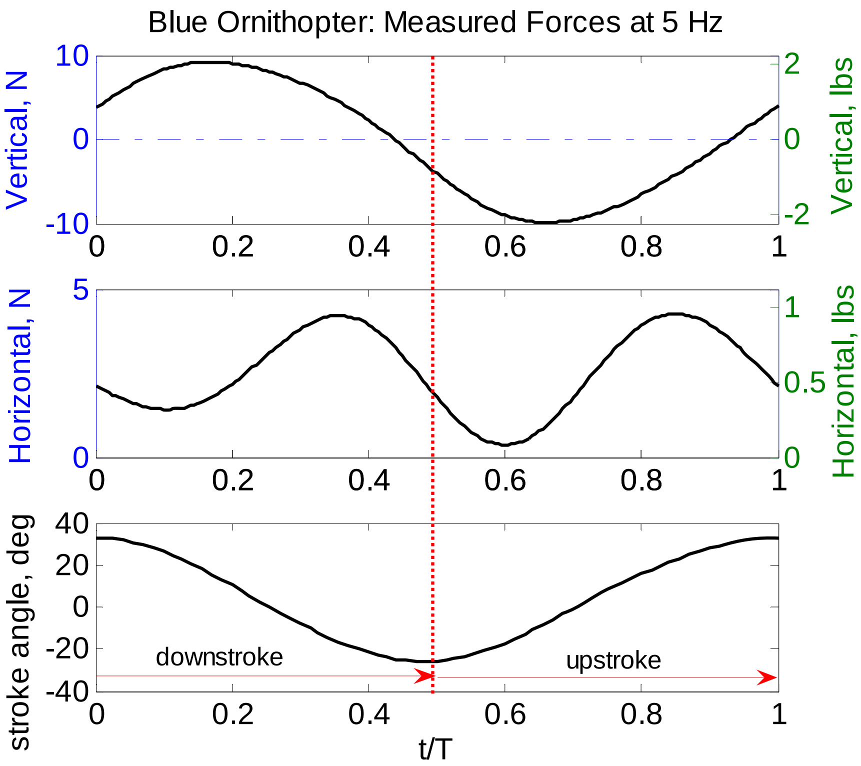

Figure 4.24: Blue ornithopter measured forces at 5 Hz, where the structural resonance dissipates and the horizontal force is maximum near the middle of downstroke as expected.

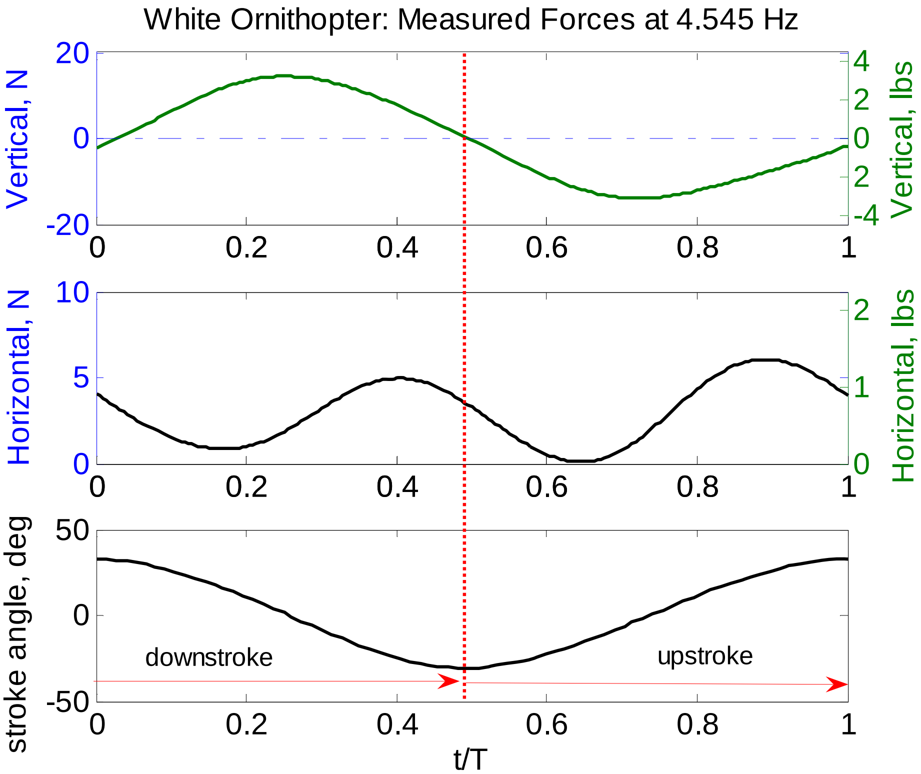

Figure 4.25: White ornithopter measured forces at 4.545 Hz, where the vertical force is exactly at the middle of downstroke. The horizontal force is phased -30˚ from the start of downstroke, as frequency decreases both forces shift back in phase to 70˚ and -65˚ respectively.

The white ornithopter's vertical and horizontal force production at 4.545 Hz are shown above in Figure 4.25. Maximum vertical force is at the middle of downstroke for this vehicle, rather than the 30˚ lead that existed for the blue ornithopter. For both ornithopters the horizontal force is maximum near the end of downstroke and upstroke, this may be due to the apparent mass force which results from the increasing acceleration near stroke transition. The peak to peak lift magnitudes are two to three times larger than the vehicle weight, but the net lift remains near zero. It is believed that net lift is produced when the flapping axis has a positive pitch angle, which is required in actual flight testing. Also note that the duration of downstroke and upstroke, known as the downstroke and upstroke ratios, are equal at half of the frequency period. During flight inertial effects are working against the upstroke of the wing and these ratios may change and adjust the net lift to a positive value.

Another way to examine the force production is to plot the forces versus the mean stroke angle as shown in Figure 4.26 and Figure 4.27 for the blue and white ornithopter respectively. This approach directly correlates the forces to the stroke angle for phase estimates and can provide information on the asymmetries in force production through the wing stroke. The blue ornithopter force measurements are centered at 5° positive stroke angle instead of zero, possibly because the maximum stroke angle is about 5° larger than the minimum stroke angle. The horizontal force minumum magnitudes are also asymmetric during downstroke and upstroke.

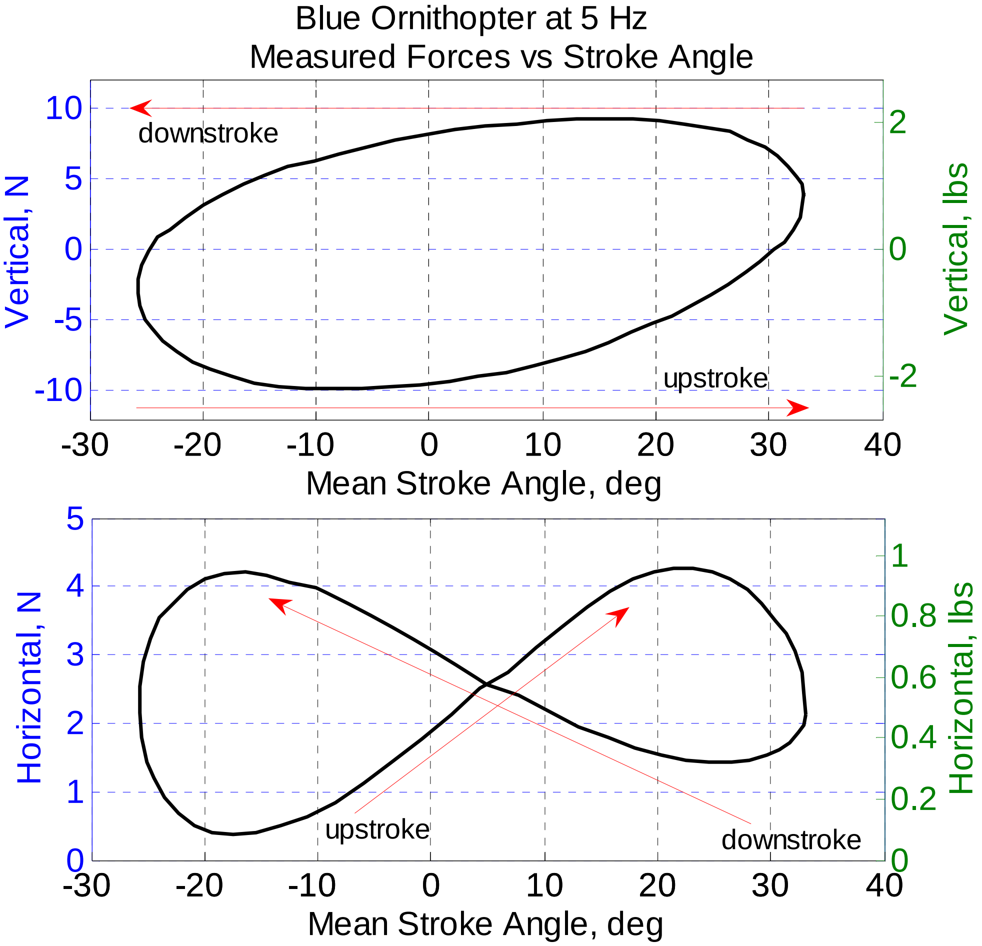

Figure 4.26: Blue ornithopter forces vs stroke angle at 5Hz.

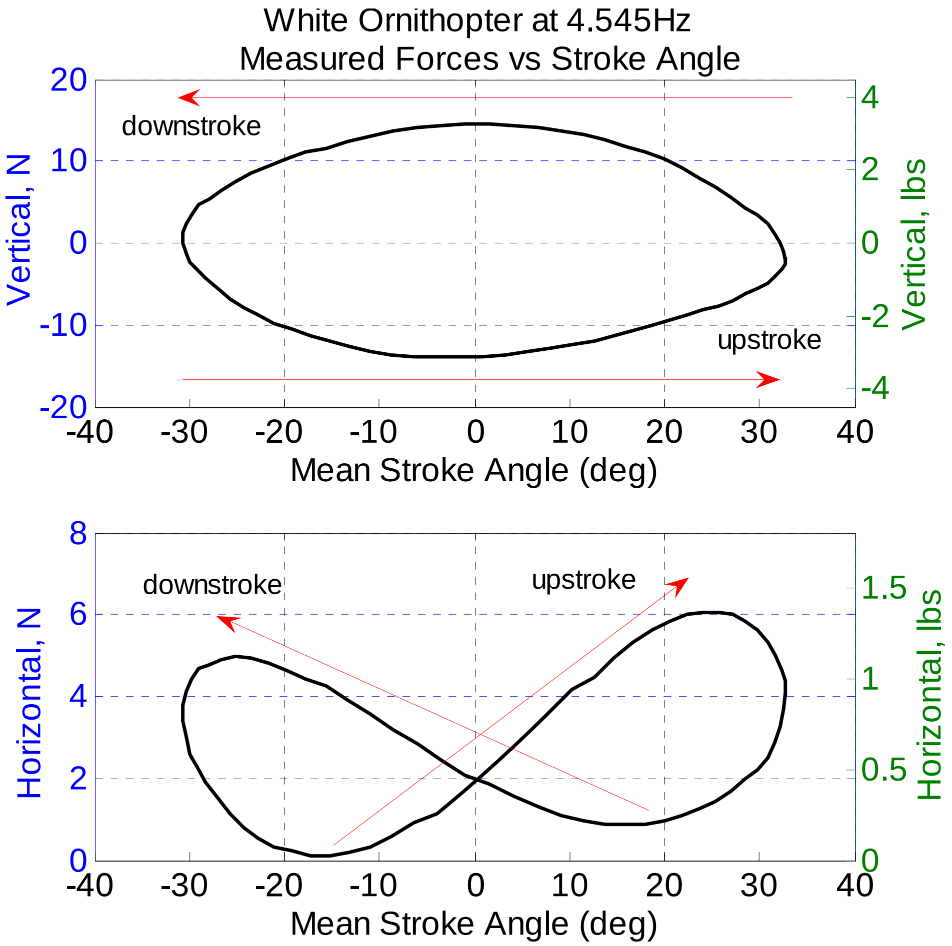

Figure 4.27: White ornithopter forces vs stroke angle at 4.545Hz.

This discussion of the variation of the measured forces and kinematics with flapping frequency and stroke angle was necessary to compare the actual wing behavior with the expected performance. Three important findings from this analysis include: the presence of phase lag in the wing motion due to leading spar bending, the variation in the forces phase with wing angle, and the verification that the membrane behavior is first order except near transition. These results are used in Ch. 5 to devlop an accurate aerodynamic representation of the wing.

Chapter 5. Aerodynamic Modeling Theory

An aerodynamic model is desired to predict the behavior of the aerodynamic forces and moments of the ornithopters at various flight conditions for use in stability and control algorithms. The analytical aerodynamic model developed in this chapter combines traditional fixed wing force and moment concepts with linear membrane aerodynamics and unsteady aerodynamics adjustments. These techniques are then applied to the wing using the kinematic data from the motion tracking experiments to form a blade element analysis of the wing. The output of the aerodynamic analysis predicts the vertican and horizontal force produced throughout the wing stroke at a specific steady flapping flight condition specified by the program user. These results can then be compared to measured aerodynamic loading data from the same motion tracking experiments for specific flapping frequencies. If the results of this analytical and empirical model match the measured data then assumptions can be made to simplify or reduce the need for complex computational fluid dynamic studies.

5.1 Assumptions

The following assumptions were made for this aerodynamic model.

1. The wing kinematics can be defined by quasi-steady motions, including flapping or plunging, pitching, and forward motion.
2. A quasi-steady circulation model can capture the aerodynamic behavior when adjusted to account for unsteady motion and membrane aerodynamics
3. The effects of unsteady flow mechanisms, such as leading edge suction, wake capture, dynamic stall, or spanwise-flow, are small enough to be neglected.

4. The induced velocity magnitudes can be adequately captured using momentum theory with an actuator disk that is the swept area of the wing.
5. An elliptical lift deficiency factor, *e*, of 0.8
6. The membrane behavior in the luff region is first order and has a pitching axis located at the ¼-chord point. The length of blade elements in this region is time-varying, but the blade width is constant.
7. The flap region blade elements behave as flat plates with fixed length and width. They have pitching roation about their leading edge.
8. Attached flow is assumed regardless of the relative angle of attack.
9. The stroke plane is vertical
10. The inflow angle for blade elements ten to twelve is adjusted by the pitch angle of the blade elements that are in the luff region.
11. The parasite drag of the fuselage can be neglected
12. The luff region camber is positive during downstroke and negative during upstroke, fluctations during stroke transition are neglected.

5.2 Algorithm

A series of MATLAB® codes were generated to complete the aerodynamic analysis. This section formulates the algorithm established to process the kinematic data, apply the aerodynamic equations and produce and compare the model's results with measured aerodynamic force data. A flow chart with tasks and their corresponding MATLAB® files has been generated on the following page including processing of the measured kinematics and aerodynamic forces so they can be used by the primary modeling program. Each process is addressed in a following section.

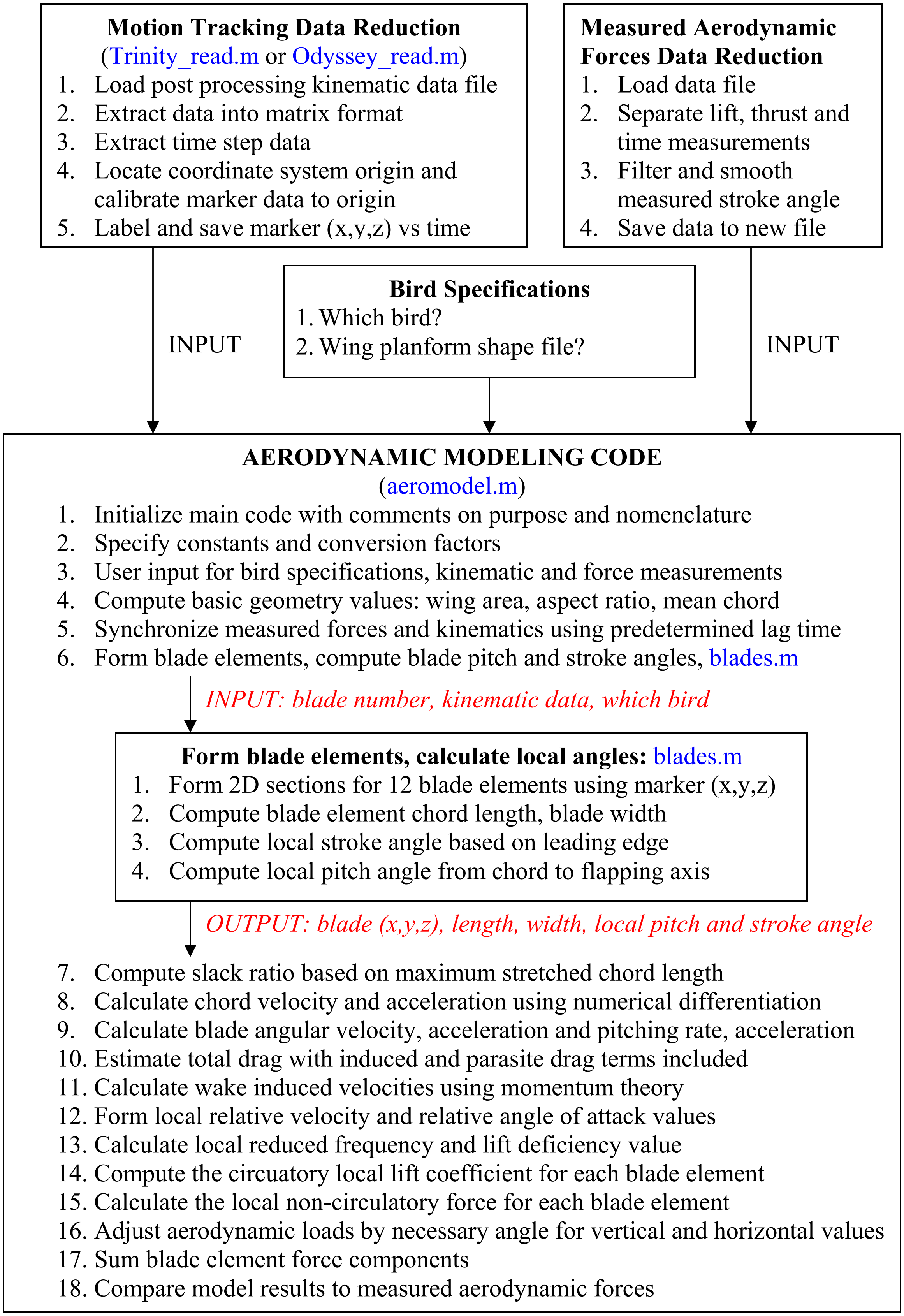

Motion Tracking Data Reduction
(Trinity_read.m or Odyssey_read.m)

1. Load post processing kinematic data file
2. Extract data into matrix format
3. Extract time step data
4. Locate coordinate system origin and calibrate marker data to origin
5. Label and save marker (x,y,z) vs time

Measured Aerodynamic Forces Data Reduction

1. Load data file
2. Separate lift, thrust and time measurements
3. Filter and smooth measured stroke angle
4. Save data to new file

Bird Specifications

1. Which bird?
2. Wing planform shape file?

AERODYNAMIC MODELING CODE
(aeromodel.m)

1. Initialize main code with comments on purpose and nomenclature
2. Specify constants and conversion factors
3. User input for bird specifications, kinematic and force measurements
4. Compute basic geometry values: wing area, aspect ratio, mean chord
5. Synchronize measured forces and kinematics using predetermined lag time
6. Form blade elements, compute blade pitch and stroke angles, blades.m

INPUT: blade number, kinematic data, which bird

Form blade elements, calculate local angles: blades.m

1. Form 2D sections for 12 blade elements using marker (x,y,z)
2. Compute blade element chord length, blade width
3. Compute local stroke angle based on leading edge
4. Compute local pitch angle from chord to flapping axis

OUTPUT: blade (x,y,z), length, width, local pitch and stroke angle

7. Compute slack ratio based on maximum stretched chord length
8. Calculate chord velocity and acceleration using numerical differentiation
9. Calculate blade angular velocity, acceleration and pitching rate, acceleration
10. Estimate total drag with induced and parasite drag terms included
11. Calculate wake induced velocities using momentum theory
12. Form local relative velocity and relative angle of attack values
13. Calculate local reduced frequency and lift deficiency value
14. Compute the circuatory local lift coefficient for each blade element
15. Calculate the local non-circulatory force for each blade element
16. Adjust aerodynamic loads by necessary angle for vertical and horizontal values
17. Sum blade element force components
18. Compare model results to measured aerodynamic forces

5.3 Nomenclature, Inputs, Constants, and Conversions

The first component of the MATLAB® modeling code is to inform the user of the codes' purpose through comments; this includes an introduction to the nomenclature which is used and the sub-programs that are called. A summary of the nomenclature was provided at the beginning of this document.

The important conversion factors used in the model are established first so adjustments can be made to the input data to correlate measurement units; metric units are assumed for all computations but conversion to English units can be completed easily at the end of the analysis if desired. The density and viscocity of the air are also set at sea level conditions in this portion of the MATLAB® code. After this the user interactively specifies which ornithopter is being analyzed and provides the desired ornithopter's wing geometry file. Wing geometry values are then computed using methods specified in Section 5.4.1. Next the motion tracking kinematics and measured aerodynamic force files to be used are specified by the user along with the time-lag for the measured forces as determined in Section 4.3.2. After synchronizing the data, the measured forces are interpolated to match the time points of the motion tracking data. This is done to estimate the uniform induced velocities in the aerodynamic model using momentum theory and to provide easier comparison of results. With synchronization completed, the marker motion tracking variables can be formed into blade elements to continue the aerodynamic analysis.

5.4 Wing Geometry and Blade Element Definition

A discussion of the wing geometry and how blade element theory is applied to this geometry is discussed in this section. Descriptions and diagrams will show the orientation of the blade elements and explain why this orientation was chosen, as well as how the blade elements are implemented in the aerodynamic model.

5.4.1 Wing Geometry

The wing planform of each ornithopter is unique, though similar in shape. Detailed drawings of the wings' planform were completed on a measurement grid and formatted into a data file for each ornithopter; this file is input at the beginning of the aerodynamic analyss. The x and y points that mark the wing's planform are then used to compute the span, *B*, and semi-span length, *R* as shown in Eq. (5.1). Any spanwise point along the wing is designated by its local span position *r*, which can be nondimensionalized for easier interpretation. The wing area, *S*, aspect ratio, *AR*, and mean chord, $\bar{c}$, are found using Eq. (5.1) through Eq. (5.4) respectively.

$$\begin{aligned} B &= 2 \cdot \max(\mathrm{y}) \\ R &= B/2 \end{aligned} \tag{5.1}$$

$$S = 2\int_0^b x\,dy = trapz(x, y) \tag{5.2}$$

$$AR = \frac{B^2}{S} \tag{5.3}$$

$$\bar{c} = \frac{B}{AR} \tag{5.4}$$

Additionally, the spanwise location of the mean chord is given by $\bar{r}$. Table 5.1 provides these geometric values for both ornithopters. The aspect ratio for both ornithopters is between four and five, which is large enough to minimize induced velocity effects near the wing root. Mean chord values are approximately 75% of the maximum chord at the wing root. The mean chord is located at approximately two-thirds of the semi-span between blade elements eight and nine, or near where the diagonal spar connects with the leading edge spar.

Table 5.1: Wing geometric values.

BIRD	B (m)	R (m)	S (m^2)	AR	$\bar{c}$	$\bar{c}/c_{\max}$	$\bar{r}$	$\bar{r}/R$
Blue	1.073	0.5366	0.1158	4.972	0.2158	0.759	0.3378	0.6296
White	1.198	0.5994	0.1653	4.347	0.2758	0.7646	0.3981	0.6642

5.4.2 Blade Element Selection

The blade element method was introduced in Section 3.3 as a technique to analyze the aerodynamics of a wing with variable geometry that experiences both forward and rotary motion. The first choice for blade orientation was a network of blades that covered the entire distance from the leading to trailing edge across the chord. It was thought that the rotation around the spar could be analyzed using thin airfoil theory and treating the trailing edge section as a flap. However the application was not valid because the trailing edge region is a very significant portion of the chord length and the flap analysis is not accurate for flaps greater twenty five percent of the chord. The flap deflections of up to 90° are also much larger than the small flap angle assumption of thin airfoil theory, which holds up to about 20°. Therefore blade element shapes that covered the entire chord length were eliminated and a fore and aft blade element approach was attempted, with much more accurate results.

The blade element configuration selected for this analysis separates the wing into two regions, one to the fore of the diagonal spar and one to the aft. Using the reflective marker tracking variables, these two regions were further subdivided into a series of twelve blade elements with a similar orientation utilized for each ornithopter as shown in Figure 5.1 and Figure 5.2. While the blades can be configured in a variety of ways, the method selected separated the leading edge triangular "luff" region of the wing from the trailing edge "flap" region. This orientation was chosen because there is significant rotation in the wing about the diagonal spar which causes a large pitching motion and an indirect oncoming flow for blades ten to twelve. In order to account for these effects blade elements ten to twelve are set perpendicular to the diagonal spar with the blade width determined by the location of the carbon fiber fingers. Due to their orientation, the oncoming flow for the blades ten through twelve is assumed to come directly off the trailing edge of blades one through eight.

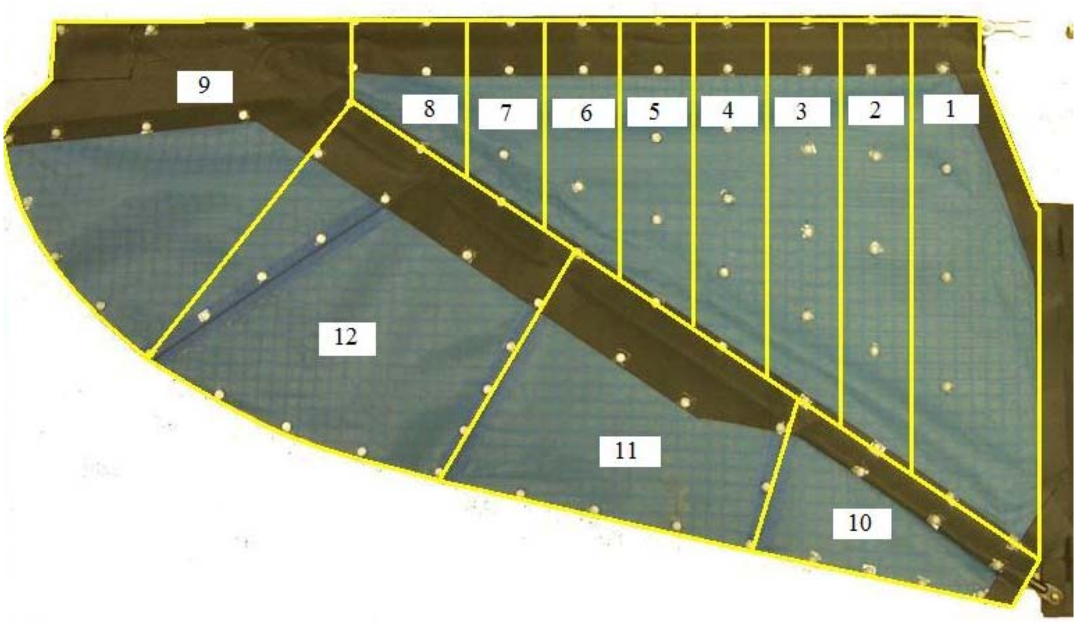

Figure 5.1: Blade element identification for blue ornithopter.

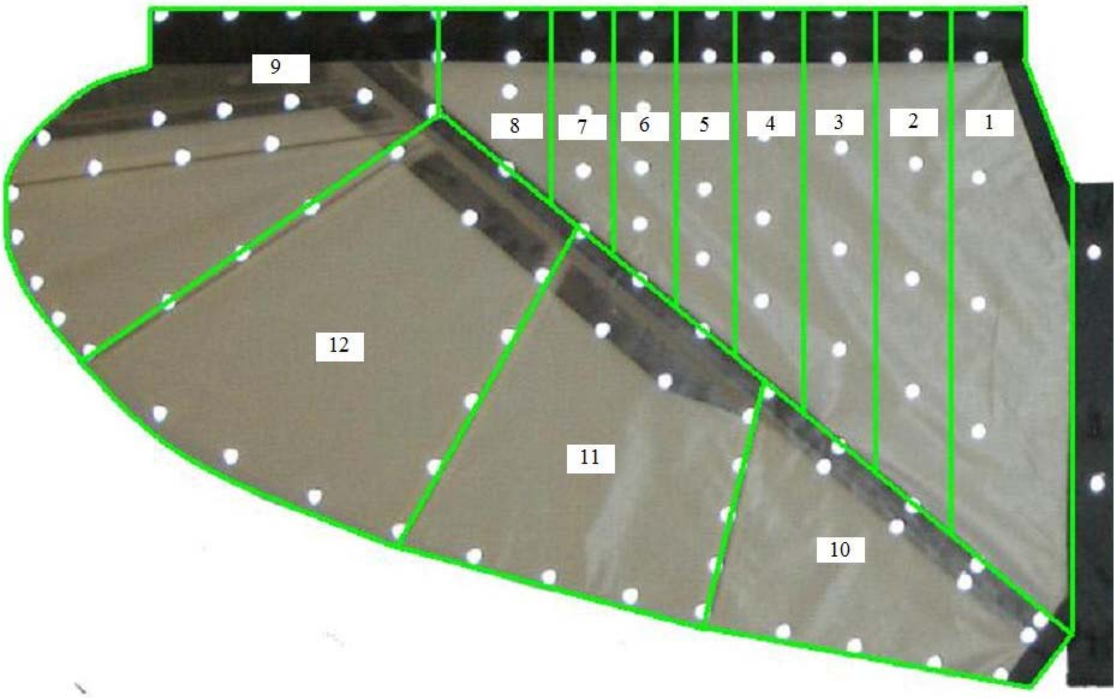

Figure 5.2: Blade element identification for white ornithopter.

The front or leading edge blades labeled one through eight are parallel to the x-axis and are nearly rectangular in shape. These blades experience lower pitching values and are more likely to maintain an angle of attack where the flow remains attached. The wing tip forms blade element number nine which sits on both the leading and trailing edge beyond the end of the diagonal spar. Blade element nine was shaped as shown because wing tip bending rotates the tip region about a line that connects the intersection of the two spars to the trailing edge of the third finger. This tip rotation can be seen in Figure 1.5. The interior boarder of the tip blade element was chosen to fall near this line of rotation.

5.4.3 Blade Element Geometry

Within the aerodynamic code the blade elements are formed by iterative calls to the MATLAB program 'blades.m' which requires the blade number, bird specification and marker data as inputs. The program outputs the reorganized (x,y,z) points that define the blade element camber as well as the blade element length, width, pitch and local stroke angle with time. To determine the blade element chord length, *dc*, and the blade width, *dr*, a series of algorithms is provided for each blade element in Table 5.2 and Table 5.3 for the blue and white ornithopter respectively. To better understand these equations, refer to the marker labeling diagram of Figure 4.8. Also note that *dc* is considered time varying for the luff region blade elements, but *dc* is a constant for the trailing edge flap region which behaves like a flat plate. The blade width, *dr*, is also assumed to be a constant. In addition to these values, a taught blade element chord length, c_{max}, is defined based upon pre-measured values; this is utilized in the membrane aerodynamics computations.

Table 5.2: Algorithms for determining blade element length and width of the blue ornithopter.

Blade #	Blue Ornithopter	
$n = 1$	$dc_1 = LE_2 - ME_2$	$dr_1 = \frac{LE_3 - LE_2}{2} + \frac{LE_2 - X1}{2}$
$n = 2,3 \ldots 7$	$dc_n = LE_{n+1} - ME_{n+1}$	$dr_n = LE_{n+2} - LE_{n+1} + \frac{LE_{n+1} - LE_n}{2}$
$n = 8$	$dc_8 = LE_9 - ME_9$	$dr_8 = LE_{10} - LE_9 + \frac{LE_9 - LE_8}{2}$
$n = 9$	$dc_9 = LE_{12} - TE_{13}$	$dr_9 = LE_{13} - LE_{11}$
$n = 10$	$dc_{10} = \left(ME_2 + \frac{ME_3 - ME_2}{2} \right) - TE_3$	$dr_{10} = \frac{1}{2}\left[(ME_4 - ME_1) + (TE_5 - TE_1) \right]$
$n = 11$	$dc_{11} = \left(ME_5 + \frac{ME_6 - ME_5}{2} \right) - TE_7$	$dr_{11} = \frac{1}{2}\left[(ME_7 - ME_4) + (TE_9 - TE_5) \right]$
$n = 12$	$dc_{12} = \left(ME_8 + \frac{ME_9 - ME_8}{2} \right) - TE_{11}$	$dr_{12} = \frac{1}{2}\left[(ME_{10} - ME_7) + (TE_{13} - TE_9) \right]$

Table 5.3: Algorithms for determining blade element length and width of the white ornithopter.

Blade #	White Ornithopter	
$n=1$	$dc_1 = LE_2 - ME_2$	$dr_1 = \frac{LE_3 - LE_2}{2} + \frac{LE_2 - X1}{2}$
$n=2,3\ldots7$	$dc_n = LE_{n+1} - ME_{n+1}$	$dr_n = LE_{n+2} - LE_{n+1} + \frac{LE_{n+1} - LE_n}{2}$
$n=8$	$dc_8 = LE_9 - ME_9$	$dr_8 = LE_{10} - LE_9 + \frac{LE_9 - LE_8}{2}$
$n=9$	$dc_9 = LE_{14} - F_{33}$	$dr_9 = LE_{14} - LE_{10}$
$n=10$	$dc_{10} = ME_3 - TE_3$	$dr_{10} = \frac{1}{2}\left[\left(ME_5 - ME_1\right) + \left(TE_5 - TE_1\right)\right]$
$n=11$	$dc_{11} = \left(ME_6 + \frac{ME_7 - ME_6}{2}\right) - TE_7$	$dr_{11} = \frac{1}{2}\left[\left(ME_8 - ME_5\right) + \left(TE_9 - TE_5\right)\right]$
$n=12$	$dc_{12} = ME_9 - TE_{11}$	$dr_{12} = \frac{1}{2}\left[\left(ME_{10} - ME_8\right) + \left(TE_{13} - TE_9\right)\right]$

Blades one through eight utilize the columns of markers down their center to form the local cambered airfoil shape. These blades use their leading edge and middle edge points to compute blade length, and a mean value for blade width is achieved using the neighboring leading edge markers. The flap region of blades nine to twelve are treated as flat plates so only the leading and trailing edge points are recorded to mark the chord length and orientation. For blades ten through twelve, the chord is established by linear interpolation to the center most point on the blade leading and trailing edge; this interpolated chord is also used to establish the blade length. The blade width is calculated as the average of the blade's leading edge and trailing edge distances, since the blades are nearly trapezoidal this is a good approximation. Blade nine is highly irregular in shape. However, since the blade length and width are primarily utilized to calculate the surface area, the blade shape can be reconfigured to provide a better estimation. The lengths and widths for blade nine are drawn for clarification in Figure 5.3 for both ornithopters. The camber-line (or chord-line) data points are recorded for all blades when the 'blades.m' program returns a set of matrix coordinates representing the blade element to the main program, 'aeromodel.m'.

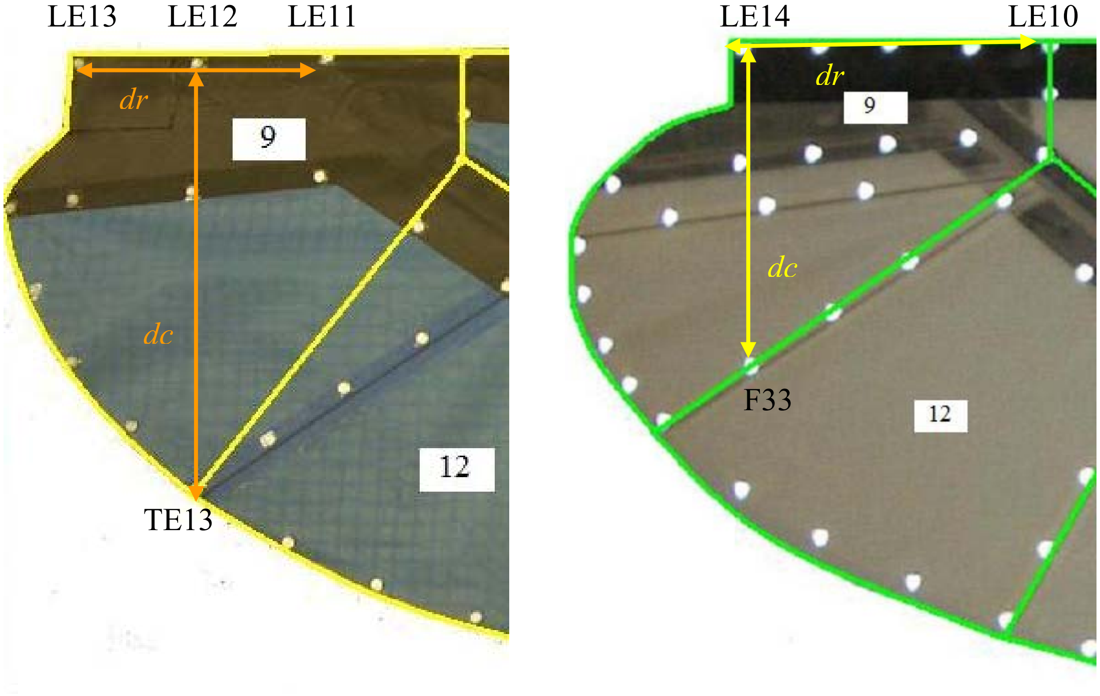

Figure 5.3: Blade nine length and width approximation.

5.5 Blade Element Orientation and Kinematics

A detailed kinematic description of a flapping wing is the key to creating an accurate description of the quasi-steady aerodynamics. This section will analyze the blade element orientation, including pitch, stroke angle and camber direction. Blade motion, including pitching and plunging rates and accelerations are examined and implemented in the aerodynamic modeling code. The membrane slack percentage will also be calculated where appropriate.

5.5.1 Quasi-Steady Kinematics

The quasi-steady motions experienced by the flapping and pitching ornithopter wing are defined with front and side views in Figure 5.4 and Figure 5.5 respectively. The front view indicates the wing stroke angle, β, which is positive above the Y axis, and the angular velocity and acceleration due to the flapping motion, $\dot{\beta}$ and $\ddot{\beta}$. Also identified is the spanwise location *r* which varies from zero to the half-span; this length can be nondimensionalized by the half-span length *R* for easier interpretation of the span location being considered.

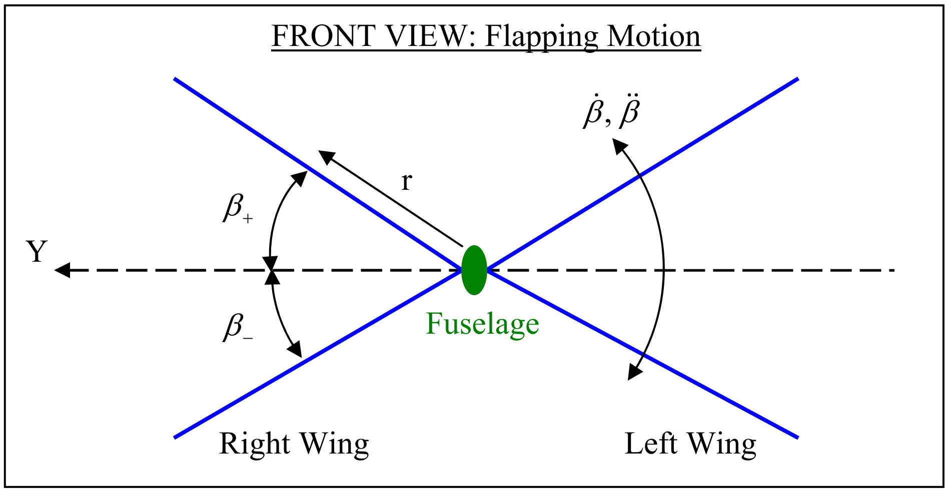

Figure 5.4: Front view diagram of flapping motion.

Figure 5.5 shows the side view (X-Z plane) of the chord of a representative blade element at span location *r* undergoing typical downstroke motion. The flapping axis is indicated along the X-axis at the wing root and all pitch angles are taken with respect to this symmetry axis of the vehicle. The velocity of the vehicle with respect to the surrounding air is given by the vector *U*. The flapping axis is oriented by the angle δ to *U* and the flight path angle between *U* and the ground horizontal line is given by γ. This blade element segment is pitched down (negative) θ degrees with the pitching axis located a distance a from the mid chord, where a can vary from -1 at the leading edge to 1 at the trailing edge. The quantity b is the half-chord length as indicated in Figure 5.5; b is positive for the trailing edge half of the chord and negative for the leading edge half of the chord. Also shown are the pitching rate and pitching acceleration, $\dot{\theta}$ and $\ddot{\theta}$, and the plunging velocity and acceleration of the blade element, $r\dot{\beta}$ and $r\ddot{\beta}$.

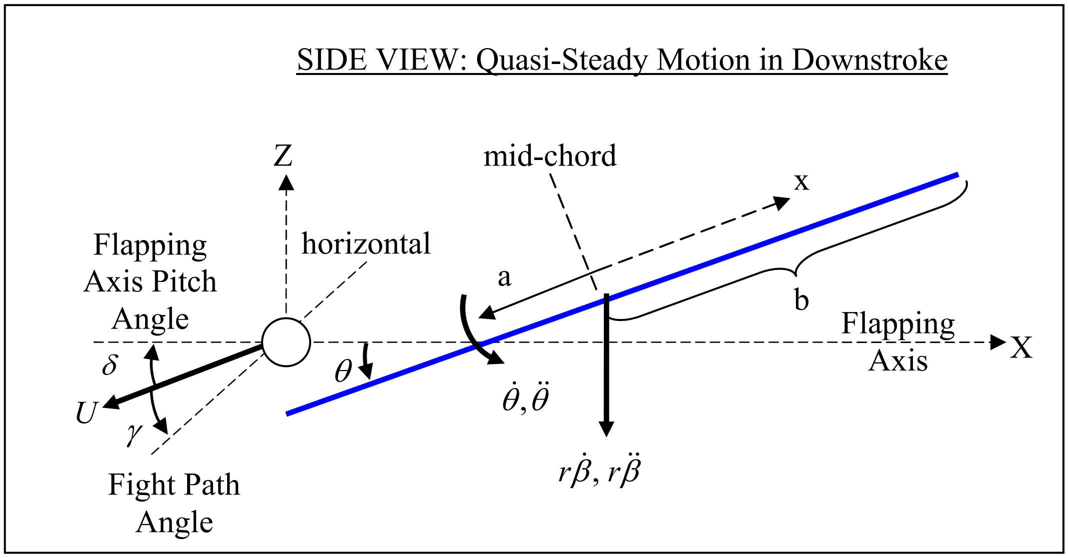

Figure 5.5: Side view diagram of wing under quasi-steady motion.

These quasi-steady motions can be explored further to understand the velocity distributions acting on the flapping wing due only to the wing's motion (no induced velocities). Figure 5.6 portrays the velocity distributions acting on the wing during downstroke; which are of opposite sign to the wing motions shown in Figure 5.5. This diagram also assumes the flight path angle γ and flapping axis angle δ are zero for easier interpretation. The flight speed U and the plunging velocity, $-r\dot{\beta}$ are both uniform velocity distributions, but the pitching rate velocity varies in a triangular distribution fore and aft of the pitching axis a and is given by $\dot{\theta}(x-ab)$. Only the flight speed U is assumed constant in the aerodynamic model; the flapping velocity,

$-r\dot{\beta}$, will be positive during downstroke and negative during upstroke. The pitching velocity sign is less quantifyable, especially near transition where the pitch angle fluctuates dramatically.

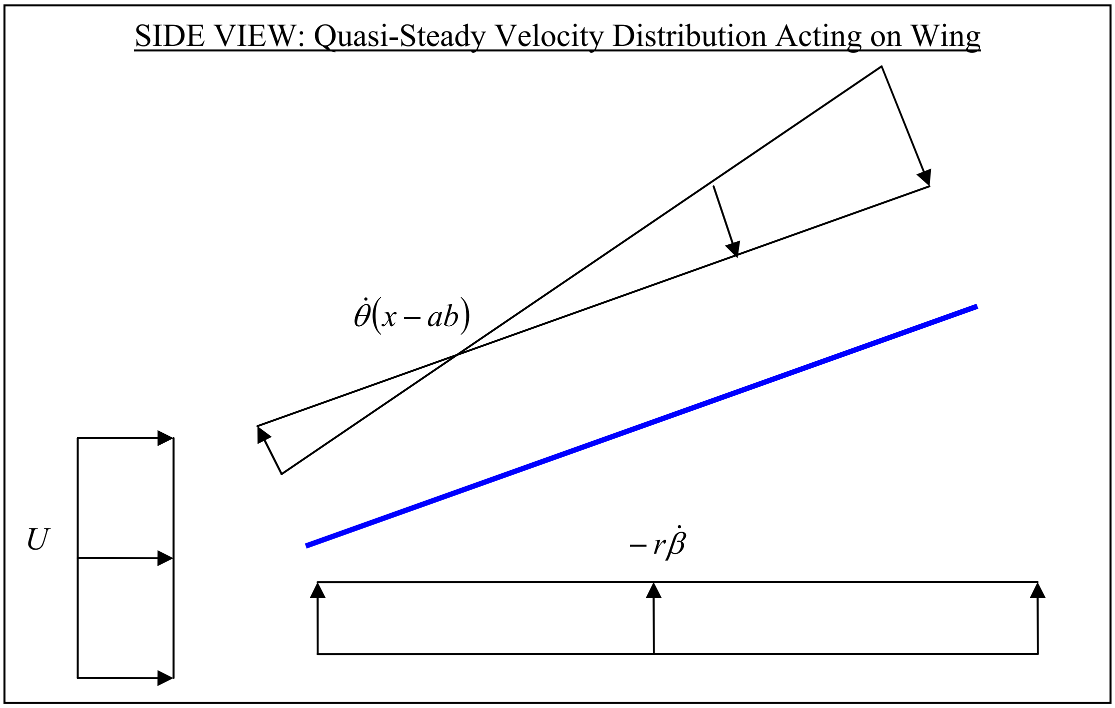

Figure 5.6: Quasi-steady velocity distribution acting on the flapping wing.

5.5.2 Kinematic Calculations

The orientation of each blade element is determined by the 'blades.m' program and returned to 'aeromodel.m' as a time history. Pitch, θ, is calculated using the relative position of the leading and trailing edge points on the blade chord. Figure 5.7 shows the two-dimensional membrane element during downstroke and upstroke with the pitch sign marked. Figure 5.7 also gives the equations to calculate pitch using the distance between the leading and trailing edge points, *dz* and *dx*. Also note the camber shape of the membrane is specified; it will generally be positive for positive angle of attack (generally downstroke) and negative for negative angle of attack (generally upstroke).

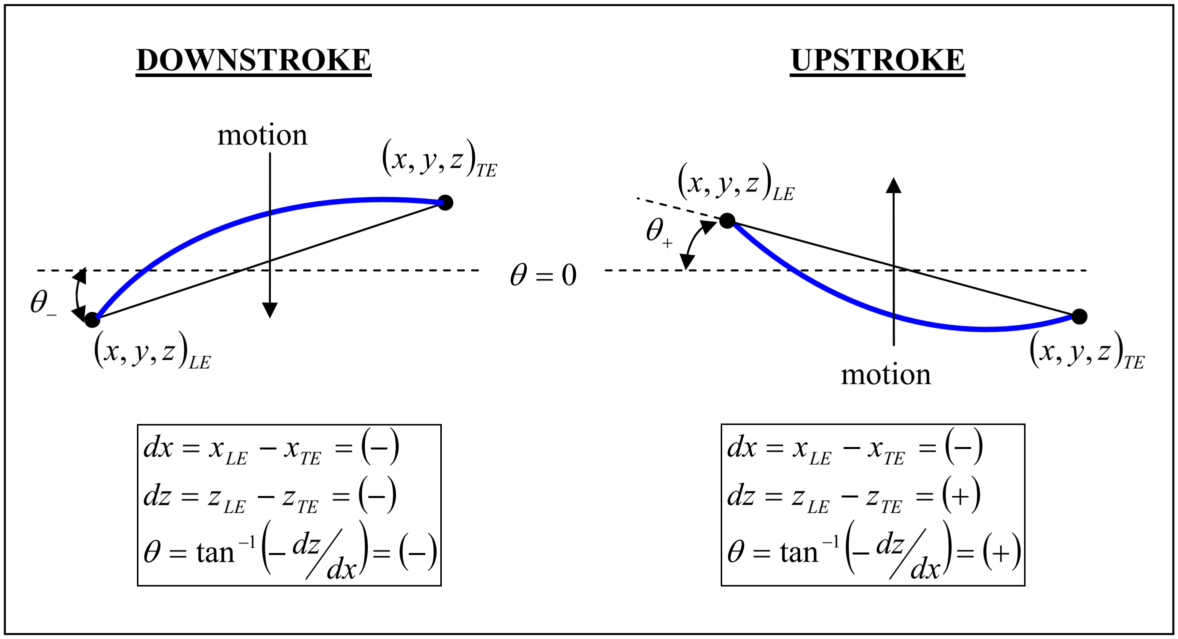

Figure 5.7: Drawing of membrane shape (blue) and pitch during downstroke and upstroke.

In addition to the pitch angle, it is necessary to calculate the local stroke angle versus time because spar bending increases the stroke angle near the wing tip and causes a phase-lag between the wing root and wing tip in the flapping motion as identified in Section 4.4.2. The local stroke angle of a blade element is determined using the leading edge reflective markers (or middle leading edge markers for blades 10 to 12). MATLAB® program ‘local_stroke.m’ takes two leading edge marker locations as input and calculates the angle that a line connecting the points makes to y-axis; this is a measure of the local stroke angle. For the narrow blade elements one through eight, the first leading edge markers inboard and outboard of a blade element are used as input to ‘local_stroke.m’ to best estimate the stroke angle over the entire width of the blade. For blade elements nine through twelve the blade’s leading edge markers furthest inboard and outboard are used to calculate the local stroke angle.

Once the bladed element size, stroke angle, and pitch angle are calculated, 'blades.m' returns the blade information to the primary MATLAB® program 'aeromodel.m' which then calculates the amount of slack in each blade element over time. The slack length, *l*, is determined by taking the difference between the blade chord length, *dc*, and the maximum blade length, c_{max}, set as a constant in the program. Zero slack is assumed for blades nine through twelve. The slack ratio, ε, which partially determines the membrane lift coefficient, is calculated by dividing the slack length with the blade element chord length, *dl*, as shown in Eq. (5.5).

$$slack\ ratio = \varepsilon = \frac{c_{\max} - dc}{dc} = \frac{l}{dc} \tag{5.5}$$

To determine the quasi-steady velocities and accelerations associated with the flapping, pitching and plunging of the wing, the MATLAB® program 'take_deriv.m' was developed to take the derivative of a time varying function. The program uses a third-order Adams-Bashforth method (AB3) on the central points with an Euler-Explicit and second-order Adams-Bashforth method (AB2) near the time boundaries. Each of these methods is described in equation format by Table 5.4 where *u* is the time varying function and *t* is the time for the n^{th} timestep.

Table 5.4: Methods for taking time derivatives.

METHOD	USE	EQUATION
Euler Explicit	u_1 u_N	$u'_n = \frac{u_{n+1} - u_n}{t_{n+1} - t_n}$
AB2	u_2	$u'_n = \frac{1}{3}\left(u'_{n-1} + 2\frac{u_{n+1} - u_n}{t_{n+1} - t_n} \right)$
AB3	$u_3 \ldots u_{N-1}$	$u'_n = \frac{1}{23}\left(-5u'_{n-2} + 16u'_{n-1} + 12\frac{u_{n+1} - u_n}{t_{n+1} - t_n} \right)$

The Euler-Explicit method is first order accurate while the Adams-Bashforth methods are second and third order accurate as their name indicates. In addition to the time and function whose derivative is being determined, “take_deriv.m” also low-pass filters the derivative results to eliminate high frequency spikes in the derivatives near kinematic discontinuities. The user must specify the frequency cutoff and the time step of used in the u function data and the derivative program will output the filtered derivative vector. In total the local flapping angular velocity and acceleration ($\dot{\beta}, \ddot{\beta}$), and the pitch rate and acceleration ($\dot{\theta}, \ddot{\theta}$) are computed using this technique with an 8Hz low-frequency cutoff. With these quasi-steady motions determined, the aerodynamic equations can be formulated.

5.6 Application of Aerodynamic Equations

This section will identify the aerodynamic equations used to calculate the total vertical and horizontal forces produced by the flapping membrane wing. This will include a discussion of drag estimation, induced velocities, and the circulatory and non-circulatory forces developed by the flapping wing with representative diagrams and plots where relevant.

5.6.1 Reference Quantities

Many of the aerodynamic computations require knowledge of reference quantities, including velocities, lengths and parameters such as the Reynold’s number and reduced frequency. The mean chord, $\bar{c}$, which acts at the span location, $\bar{r}$, is used as mean reference length for the entire wing. Similarly, a mean reference velocity, $\bar{V}(\bar{r})$, combines the quasi-steady velocities at $\bar{r}$ using Eq. (5.6).

$$\bar{V}(\bar{r})=\begin{Bmatrix}\left[U\sin(\gamma+\delta)+\left[-\bar{r}\dot{\beta}(\bar{r})+\dot{\theta}(\bar{r})(x-ab)\cos\theta(\bar{r})\right]\cdot\cos\beta\right]^2+\\ \left[U\cos(\gamma+\delta)+\dot{\theta}(\bar{r})(x-ab)\sin\theta(\bar{r})\right]^2\end{Bmatrix}^{1/2} \tag{5.6}$$

This velocity equation includes the angle adjustments for the flight path angle γ and the pitch angle of the flapping axis δ, though these values were zero for the motion tracking experiments. Likewise, a local velocity magnitude, $V(r)$, due to the wing motion can be computed for any position *r* along the span using Eq. (5.7).

$$V(r)=\begin{Bmatrix}\left[U\sin(\gamma+\delta)+\left[-r\dot{\beta}(r)+\dot{\theta}(r)(x-ab)\cos\theta(r)\right]\cdot\cos\beta\right]^2+\\ \left[U\cos(\gamma+\delta)+\dot{\theta}(r)(x-ab)\sin\theta(r)\right]^2\end{Bmatrix}^{1/2} \tag{5.7}$$

The mean chord and mean velocity are used to compute the mean Reynolds number, $\overline{\mathrm{Re}}$, for the flapping wing in Eq. (5.8). This mean Reynolds number still varies with time because of the pitching and flapping motion components of the velocity term, its minimum and maximum bounds are considered here. The local Reynolds number for a spanwise location *r* is given by Eq. (5.9).

$$\overline{\mathrm{Re}}=\frac{\rho\bar{c}\bar{V}}{\mu} \tag{5.8}$$

$$\mathrm{Re}=\frac{\rho cV}{\mu} \tag{5.9}$$

Figure 5.8 and Figure 5.9 present a comparison of the magnitude range (minimum and maximum) of the mean chord Reynolds number and local Reynolds number at the wing root and wing tip as the flight velocity and flapping frequency are varied for the blue and white ornithopter, repectively.

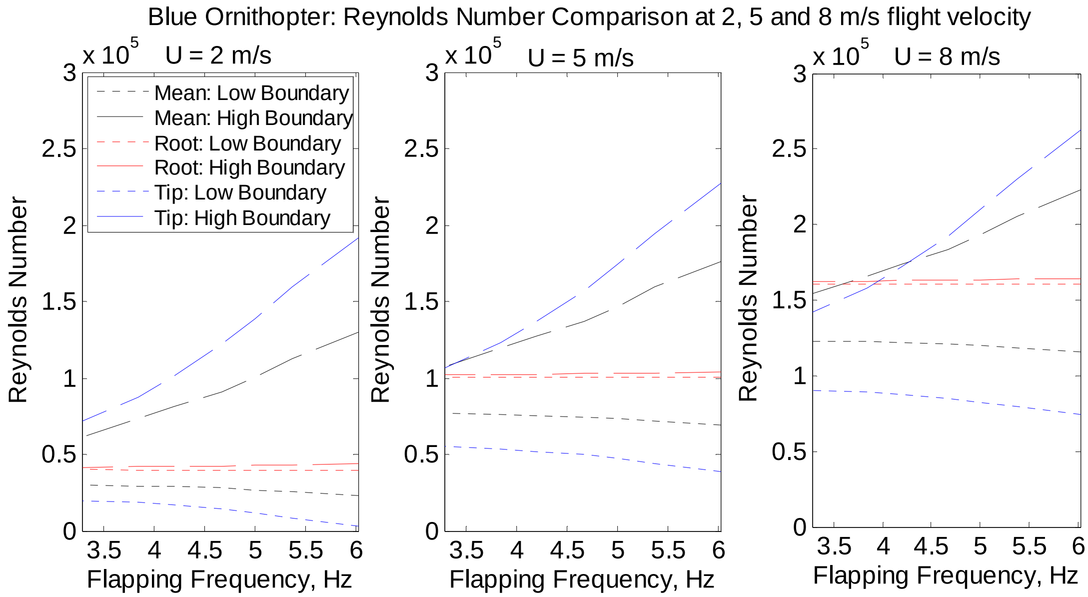

Figure 5.8: Reynolds number of the blue ornithopter at the mean chord, wing root, and wing tip for 2, 5 and 8 m/s cases. RE variation is between 20,000 and 260,000, with a mean at 100,000.

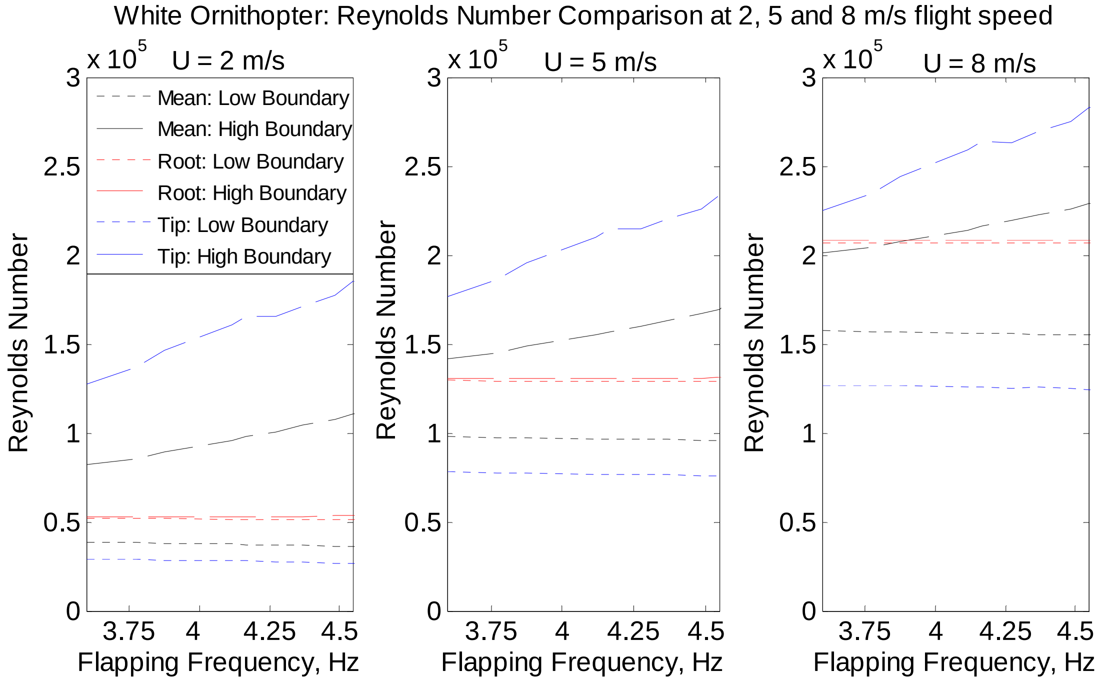

Figure 5.9: Reynolds number of the white ornithopter at the mean chord, wing root, and wing tip for 2, 5 and 8 m/s cases. RE variation is between 20,000 and 285,000, with a mean of 130,000.

The total Reynolds number range for the blue ornithopter is 20,000 to 260,000 for the entire flight speed (2 to 8 m/s) and flapping frequency envelope (3.5 to 6 Hz).

A slightly higher Reynolds number range from 20,000 to 285,000 is seen by the white ornithopter for the same flight speed window and flapping frequcies from 3 to 5 Hz. As a whole the wing root Reynolds number seems to be the closest to the average value and it essentially constant with flapping frequency. This provides evidence that computing the Reynolds number based on the root chord value and the flight velocity U is an accurate approximation of the actual Reynolds number value for the entire wing. The lower bounds of the mean and tip Reynolds numbers are relatively constant with flapping velocity and their magnitude is actually less than the root value because some components of the flapping velocity counteract the flight speed U. However, the upper bounds for the mean and tip Reynolds number experience a large linear increase with flapping frequency, which indicates the impact of the flapping velocity on these values. For a typical flight speed of 5 m/s, the average Reynolds number is approximately 100,000 for the blue ornithopter and 130,000 for the white ornithopter.

Next the reduced frequency, k, is considered. Recall that the reduced frequency is a ratio of the flapping frequency to the reference velocity. Qualitatively, the reduced frequency is a measure of the unsteadiness in the flow, with values of k less than 0.05 indicating quasi-steady flow, values between 0.05 and 0.2 indicating unsteady flow, and values greater than 0.2 indicating highly unsteady flow.

$$k = \frac{\omega c_{ref}}{2U_{ref}} \tag{5.10}$$

The reference velocity for the reduced frequency is usually taken as the flight speed U for non hovering cases, but for hovering cases it is the the plunging velocity of the flapping wing. Since both flapping modes are applicable in this analysis, the combined quasi-steady motion is used as the reference velocity at either the local or mean chord location. The mean and local root and tip reduced frequency values are plotted versus flapping frequency range and flight speed in Figure 5.10 and Figure 5.11 for the blue and white ornithopter, respectively. As would be expected, the reduced frequency decreases considerably with increasing flight speed, but nearly all of the reduced frequency values are within the highly unsteady region with *k* greater than 0.2. In general the white ornithopter has slightly higher reduced frequency values under the same conditions as the blue ornithopter, this is because the flapping velocity is lower and the chord lengths are higher. For reduced frequencies in this range the lift deficiency is very high, with a typical reduction of 30% to 40% of the classical circulation lift value. However, the accuracy and implementablity of these results can be questioned because of the large magnitude of the wing oscillations, which do not fit the lift deficiency theory's assumptions of small quasi-steady motions. Flow visualization experiments are required to accurately quantify unsteady behavior.

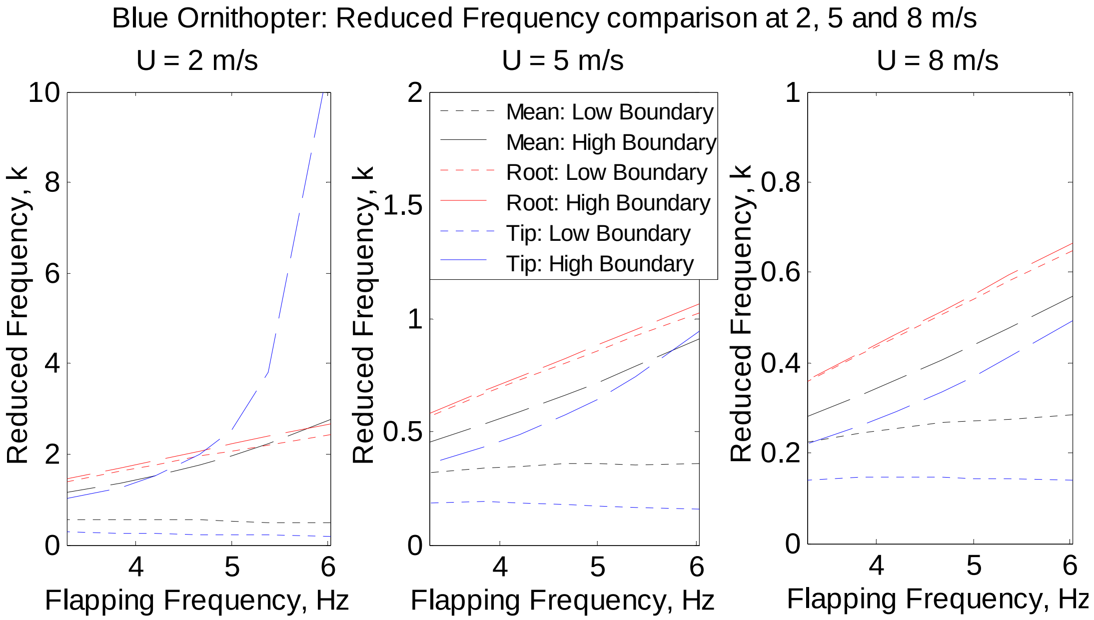

Figure 5.10: Blue ornithopter reduced frequency at span locations for U = 2, 5 and 8 m/s

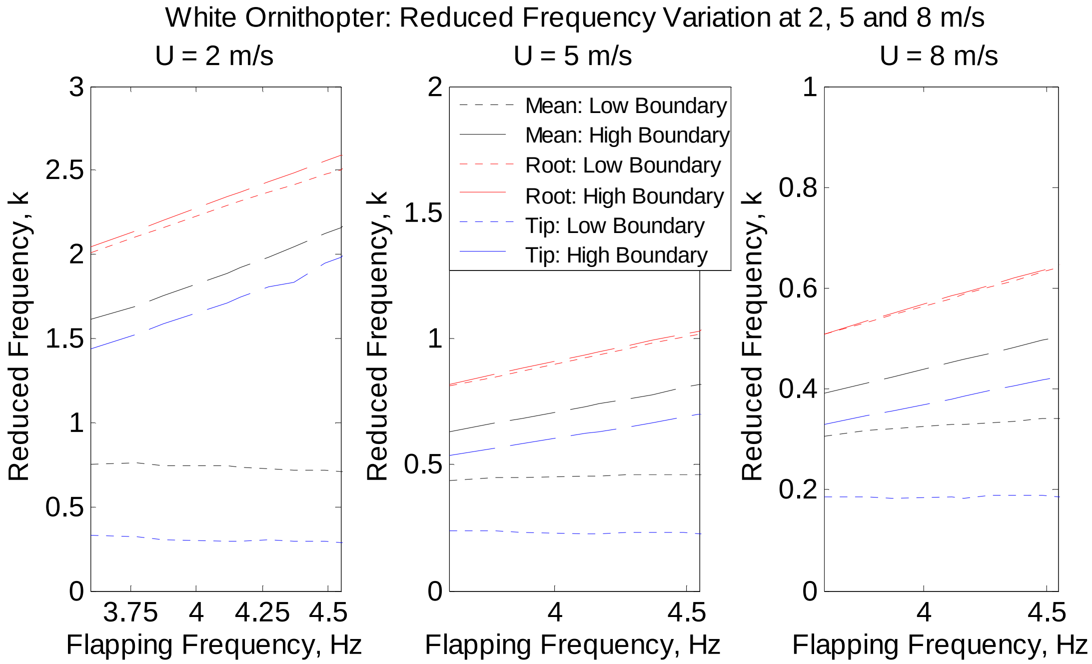

Figure 5.11: White ornithopter reduced frequency at span locations for U = 2, 5 and 8 m/s

Finally, the Strouhal number is considered. Recall that Strouhal number is a measure of the flapping amplitude to the flight velocity and it can be interpreted as the thrust efficiency metric. Strouhal number also provides insight into the length and direction of the von Karman vortices. If the ornithopter is producing thrust then the vortices are reversed in direction. Optimal thrust is achieved when the Strouhal number is in the optimal range of 0.2 to 0.4.

$$St = \frac{fA}{U} \tag{5.11}$$

In this case it is important to use the flight speed U as the reference velocity to maintain the meaning of the parameter. The tip amplitude A can vary slightly because of leading edge bending near the wing tip, but the flapping frequency variation is the most important. Strouhal number versus flight speed and flapping frequency is plotted in Figure 5.12 and Figure 5.13 for the blue and white ornithopters respectively.

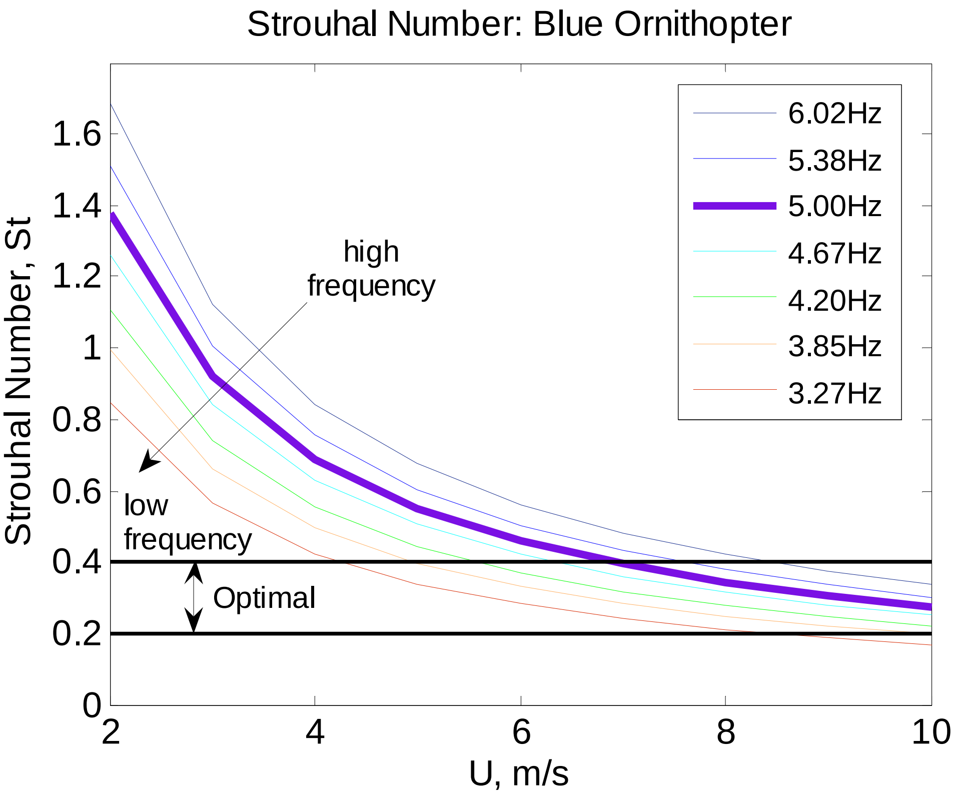

Figure 5.12: Strouhal number for the blue ornithopter vs. flapping frequency and flight speed.

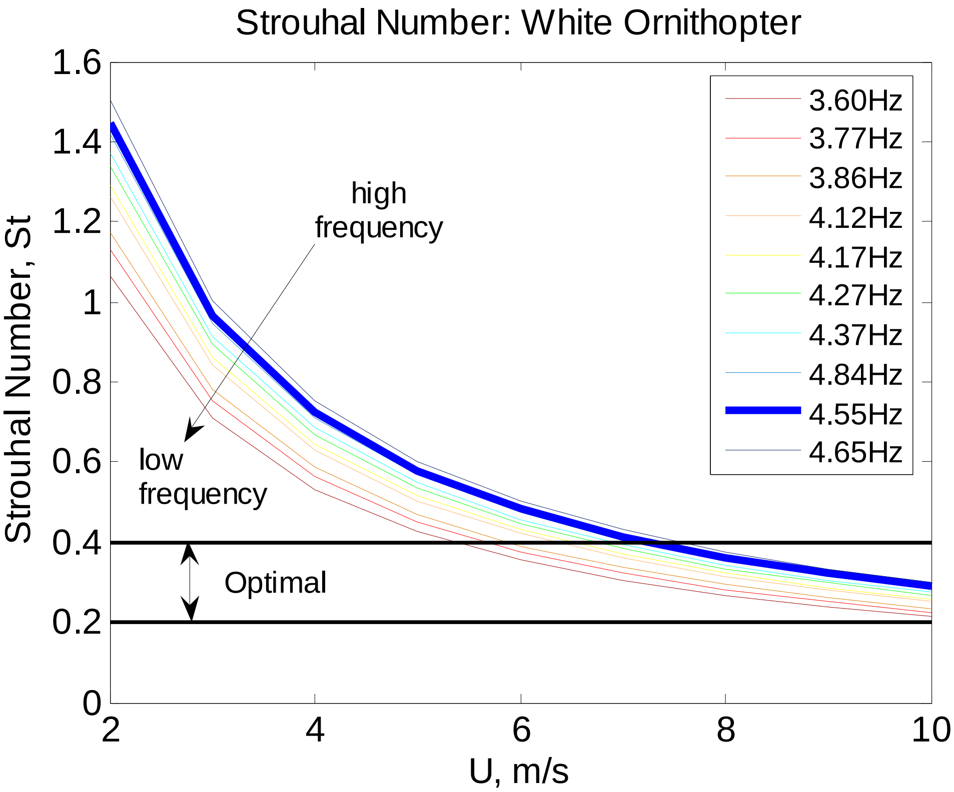

Figure 5.13: Strouhal number for the white ornithopter vs. flapping frequency and flight speed.

These plots show that the blue ornithopters' optimal Strouhal number range is met for the for low flapping frequencies of 3 to 4 Hz at flight speeds of 4 to 6 m/s, but the optimal flapping rate of 5 Hz does not reach the optimal Strouhal number range until 7 m/s. The white ornithopters performance is similar, with flapping frequencies between 3 and 4 Hz reaching the optimal Strouhal number range at 5 to 6 m/s and the typical flapping frequency of 4.5 Hz coming into the optimal Strouhal range at 7 m/s. Note that for all possible flapping frequencies, the Strouhal number never drops below the minimum optimal bound of 0.2. These plots indicate that optimal thrust is achieved at low speeds only for low flapping frequencies, but as the flight velocity increases over 7 m/s (25 km/hr), any flapping rate will provide good thrust efficiency.

These parameters provide important information about the characteristics of the flow surrounding the flapping wing. The Reynolds number range indicates the flow is in a low Reynolds number transition region, which is dominated by turbulent flow with the possibility of laminar separation bubbles or stall. Reduced frequency values are in the highly unsteady region for these vehicles, which indicates there may be unsteady methods used by the wing to generate lift and thrust. However, the accuracy and relevance of the reduced frequency is questionable because the wing kinematics do not meet the small quasi-steady motion assumptions of this theory. Finally, Strouhal number indicates that optimal thrust is produced primarily for flight speeds greater than 5 m/s, with improving performance as the speed increases further. The optimal thrust flight speed is compared to the minimum required power flight speed in the following section to generate an optimal flight envelope.

5.6.2 Drag Estimates and Power Requirements

In order to estimate induced velocities in the next section, an approximation of the total drag on the flapping wing vehicle must be established. The total drag on a vehicle is a sum of the induced drag and parasite drag, where the parasite drag includes both the profile and form drag components. A comparison of the drag trends with reference velocity was completed for two cases, one with the reference velocity equal to the flight speed, *U*, and a second with the reference velocity equal to the mean velocity, $\overline{V}$. It is expected that using *U* as the reference velocity will provide better predictions at high velocities, while using $\overline{V}$ will be more accurate at lower flight velocities when the flapping velocity is dominant.

Induced drag for steady flight conditions is usually approximated using Eq. (5.12) where the lift *L* can be approximated by the weight of the vehicle adjusted by the flight path angle. The elliptical lift deficiency factor, *e*, is also included and is assumed to be 0.8 for the flapping wing vehicles in this research.

$$D_i = \frac{2L^2}{e\pi B^2 \rho U_{ref}^2} = \frac{2(W\cos\gamma)^2}{e\pi B^2 \rho U_{ref}^2} \tag{5.12}$$

The parasite drag is determined using a technique provided by Tucker [54]. This method begins by computing the friction drag coefficient, C_f, of a flat plate in turbulent flow using Prandtl’s equation, as shown in Eq. (5.13). The reference Reynolds number used in Eq. (5.13) is calculated using the flight speed *U* for case one, and using the mean velocity for case two.

$$C_f = 0.455\left(\log_{10}\mathrm{Re}_{ref}\right)^{-2.58} \tag{5.13}$$

Next, the ratio, *K*, of the flapping wing vehicle's parasite drag coefficient, C_{Dp}, to the friction coefficient for a flat plate, C_f, at the specified Reynolds number is computed as shown in Eq. (5.14). *K* has been determined empirically for many bird species where it varies from 2 to 4.4; the largest value of 4.4 is assumed for the ornithopters in this study.

$$K = C_{Dp} / C_f \tag{5.14}$$

The parasite drag is computed using Eq. (5.15), where the the drag coefficient ratio *K* and the flat plate drag coefficient are applied to a wetted surface area S_w , which is defined as twice the wing area *S*, (the fuselage drag is neglected). The total drag due to induced and parasite components during steady flight conditions is then given by Eq. (5.16).

$$D_p = \frac{\rho U_{ref}^2 S_w C_{Dp}}{2} = \frac{\rho U_{ref}^2 S_w K C_f}{2} \tag{5.15}$$

$$D_{tot} = D_i + D_p = \frac{2(W\cos\gamma)^2}{e\pi R^2 \rho U_{ref}^2} + \frac{\rho U_{ref}^2 S_w K C_f}{2} \tag{5.16}$$

Figure 5.14 and Figure 5.15 show the trend in drag values with flapping frequency and flight speed for both reference velocity cases for the blue and white ornithopter. In general, the red lines indicate induced drag, the blue lines indicate parasite drag, and the black lines show the total drag values. The single dashed-dot lines are for case one where the flight speed *U* is used as the reference velocity, while the clumps of dotted, dashed and solid lines present case two results for the mean velocity at various flapping frequencies from 3 to 6 Hz. The induced drag trend is characterized by U_{ref}^{-2}, therefore the induced drag is maximum at hover and decreases with increasing flapping frequency and flight speed. Conversely, parasite drag is characterized by $\overline{V}^2$, so it increases as flapping frequency and flight speed increase. The mean velocity drag for the optimal flapping rates of 5 Hz and 4.5 Hz are bolded for the blue and white ornithopters respectively. If the total drag due to the mean velocity at the optimal frequency is compared to the total drag due to only the flight speed, a minimum drag flight speed range is formed between 3 m/s and 6 m/s. This flight speed range is not atypical from actual cruising flight conditions, and is half the optimal speed range from maximum thrust indicated by the Strouhal number analysis.

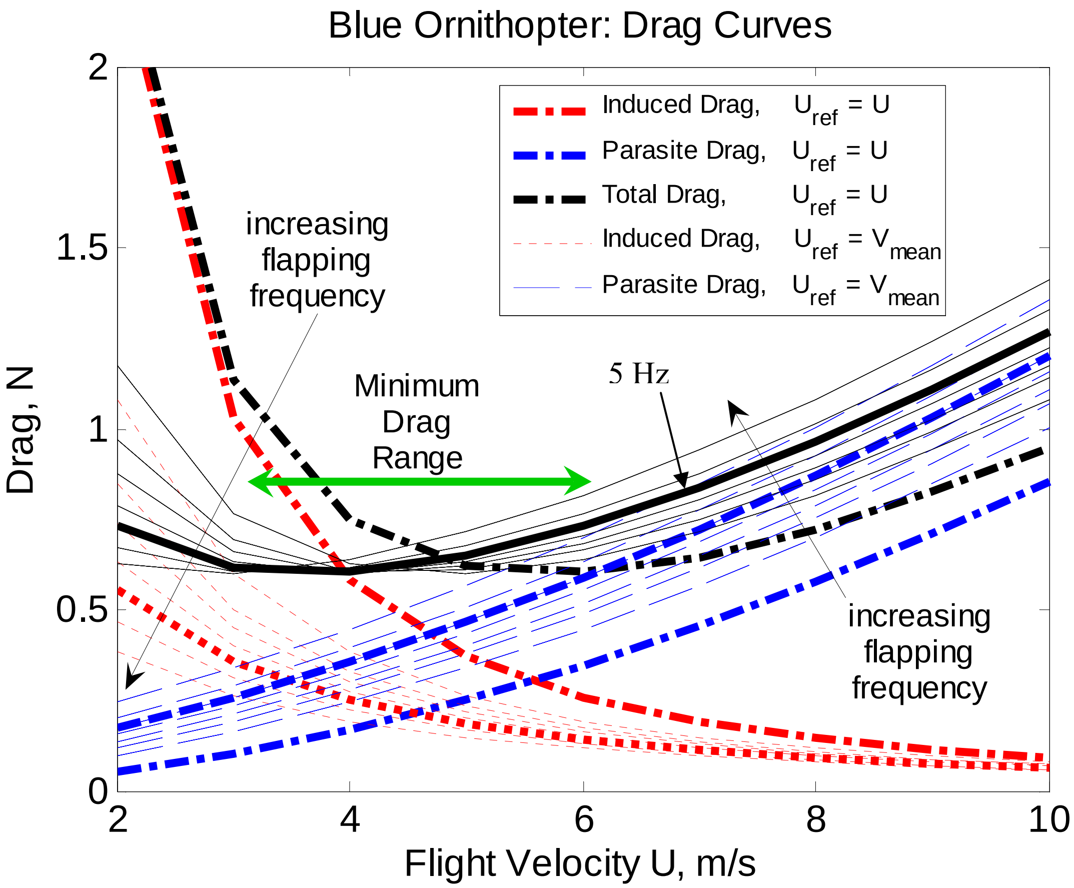

Figure 5.14: Drag curves for the blue ornithopter, total drag is indicated in black.

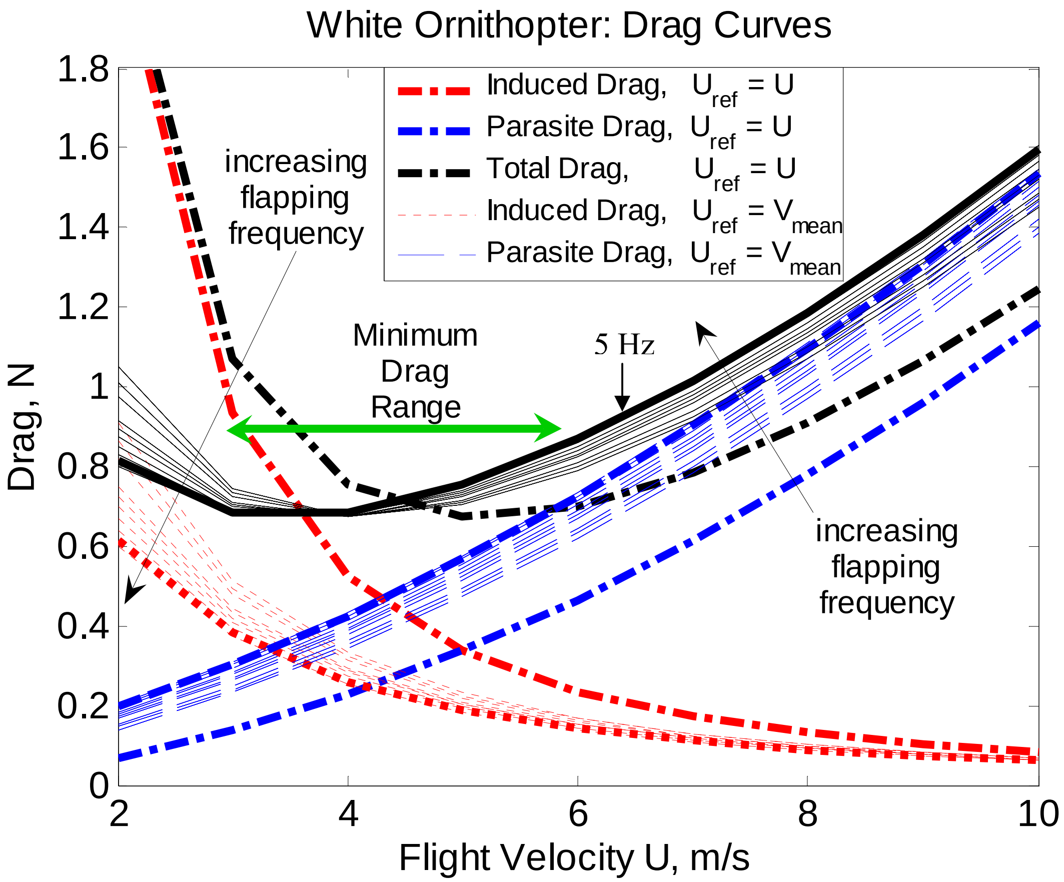

Figure 5.15: Drag curves for the white ornithopter, total drag is indicated in black.

Note that the minimum total drag values are the same for both cases at approximately 15% of the ornithopter weight. This would equate to a best case lift to drag ratio of 6.6. Likewise, the maximum drag values at large flight velocities are on the order of 30% of the vehicle weight, which corresponds to a worst case lift to drag ratio of 3.3. These are ideal lift to drag ratio values, actual values will vary based on flight conditions and the behavior of the fluid.

The total power required to overcome drag during flapping flight, neglecting electrical and mechanical power requirements from the vehicle, is determined by taking the product of the drag and the mean velocity as shown in Eq. (5.17). Note that the induced power term varies as U_{ref}^{-1} and the parasite power term varies as U_{ref}^{3}.

$$P_{req} = U_{ref} D_{tot} = \frac{2(W\cos\gamma)^2}{e\pi R^2 \rho U_{ref}} + \frac{\rho U_{ref}^3 S_w K C_f}{2} \tag{5.17}$$

Equation 5.1: Total power required to overcome drag in steady flight conditions.

A power curve analysis was completed for each ornithopter to compare the contribution of the induced and parasite drag terms to the total power required for both reference velocity cases. This analysis is produced in Figure 5.16 and Figure 5.17 for the blue and white ornithopter respectively. As with the drag curves, the induced, parasite and total power are represented by red, blue black lines respectively. For the power calculated using the mean velocities there is a decreasing importance of the induced power at low flight speeds becase of its $\overline{V}^{-1}$ dependence. However, for the power calculated using the flight velocity U, the induced power increases significantly as the hover condition is approached.

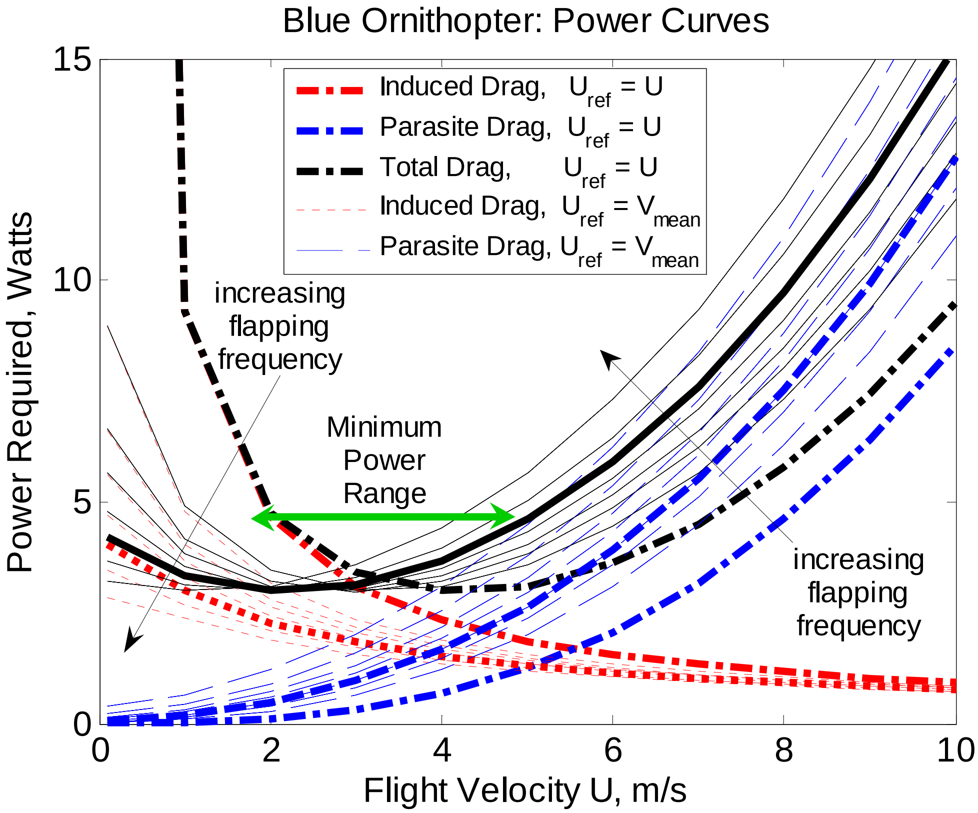

Figure 5.16: Power curves for the blue ornithopter, total power is indicated in black.

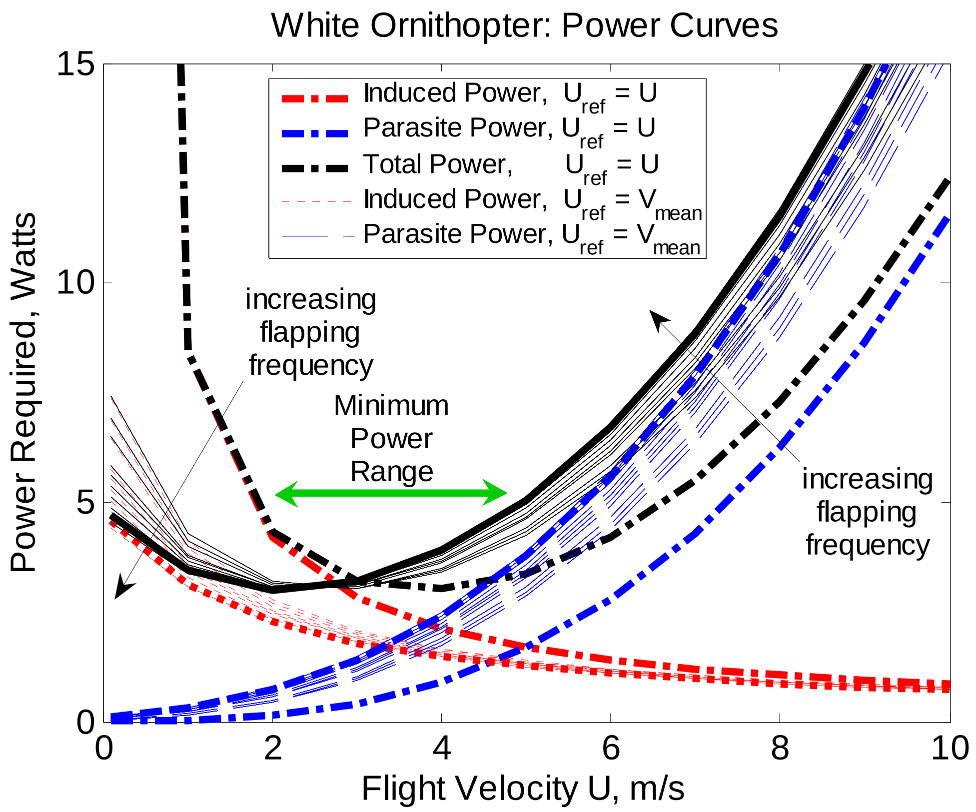

Figure 5.17: Power curves for the white ornithopter, total power is indicated in black.

The general trends are the same for both vehicles, with a minimum power of about 3 Watts between 2 m/s and 5 m/s (7 to 18 km/hr) flight speed at the optimal flapping frequencies of 4.5 and 5 Hz for the blue and white ornithopters respectively. Considering these power plots with the Strouhal number and reduced frequency results, the 5m/s flight speed is the best compromise to maintain good thrust performance, moderate unsteadiness in the flow and acceptable power requirements. Therefore, the remaining anlysis is completed at a 5m/s flight condition, which is a very common steady flight speed for the ornithopters. The drag and power estimates are based on empirical values and assumptions of steady flight conditions – actual flight conditions will vary.

5.6.3 Induced Velocity

Recall from Section 2.6.2.1 and Section 3.4.4.1 that the induced velocities created by the wake of a flapping or rotary wing vehicle can be approximated using an actuator disk and momentum theory. Momentum theory analysis produces uniform horizontal and vertical induced velocity values, u and v, for the vehicle. Although these induced velocities do not vary with spanwise location, the method is commonly used because of its simplicity and because the results are the same as those for an untwisted, elliptical, finite wing from thin airfoil theory. Other approaches, such as lifting line theory, calculate the local induced velocities using the known geometric pitch values at a spanwise location r. However, because of the large and irregular pitching angles of the wing, the lifting line theory produces unrealistic results for the induced angle of attack, on the order of 1000 degrees. Outside of lifting line theory, only computational fluid dynamics or experimental PIV methods can accurately analyze the wake produced by the flapping wings and compute the induced velocities.

Due to these complications, only the momentum theory approach was used to compute the horizontal and vertical induced velocities, u and v. In order to apply momentum theory only the flight speed U, actuator disk area A_e, and the vehicle vertical and horizontal forces must be known. Two methods were used to compute these forces. Method one applies a steady level flight assumption to generate the force values, while method two uses the measured vertical and horizontal forces from the motion tracking experiments. The momentum theory result from the avian analysis in Section 2.6.2.1 is applied to the ornithopters with an adjustment to account for the fact that the wing stroke does not cover the entire actuator disk circle. An equivalent disk area, A_e, is defined in Eq. (5.18), where Φ is the stroke amplitude (approximately 55°). The flight path angle is included because the actuator disk is tilted by the flight path angle to the horizontal line.

$$A_e = \Phi R^2 \cos\gamma \tag{5.18}$$

With this adjustment, Eq. (5.19) and Eq. (5.20) are the horizontal and vertical induced velocities, respectively, for the two methods of application during forward flight. The elliptical deficiency factor, *e*, is included to improve the accuracy. Also note that these equations assume only the flight speed U, and not a net velocity due to the flapping motion; this is because momentum theory cannot account for the kinetics of the wings. This application of the flight speed *U* also extends to the value of the drag, *D*, used in these equations; no flapping velocity is acknowledged.

$$\begin{aligned} METHOD\,1: \quad u &= \frac{(W\sin\gamma + D)}{2A_e\rho Ue} \\ METHOD\,2: \quad u &= \frac{T_{meas}}{2A_e\rho Ue} \end{aligned} \tag{5.19}$$

$$\begin{aligned} METHOD\,1: \quad v &= \frac{W\cos\gamma}{A_e\rho Ue} \\ METHOD\,2: \quad v &= \frac{L}{A_e\rho Ue} \end{aligned} \tag{5.20}$$

If the ornithopter is experience a hovering flight condition, then these equations are not valid. For a true hover case the thrust produced is zero and therefore *u* is zero, however for the motion tracking experiments the ornithopter was held rigidly while the thrust force was still produced. Equation (5.21) and Eq. (5.22) are used to compute the induced velocities for this constrained hovering condition.

$$\begin{aligned} &METHOD\,1: \quad u = 0 \\ &METHOD\,2: \quad u = \sqrt{\frac{T_{meas}}{2A_e\rho}} \end{aligned} \tag{5.21}$$

$$\begin{aligned} &METHOD\,1: \quad v = \sqrt{\frac{W}{A_e\rho}} \\ &METHOD\,2: \quad v = \sqrt{\frac{L_{meas}}{A_e\rho}} \end{aligned} \tag{5.22}$$

Results for method one and method two are shown in Figure 5.18 and Figure 5.19 for the blue ornithopter and in Figure 5.20 and Figure 5.21 for the white ornithopter, for forward flight and hover conditions respectively. For all of these plots, the horizontal induced velocity, *u*, is indicated by a dashed blue line, while the vertical induced velocity, *v*, is indicated by a red dotted line. Note that the vertical induced velocity for all methods is of opposite sign to the actual downwash value; this is accounted for in the aerodynamic model. Method one results are shown for flight velocities from 1 to 10 m/s, the flight velocity is the only changing variable for this method. The induced velocity results for method two are only for the hovering condition and are plotted for one flapping cycle at the optimal flapping rate between 4.5 and 5 Hz. Method two is the only way to compute the horizontal induced velocity in hover, and it will provide more accurate and finite results at the hover condition in comparison with method one. However, method two is not directly applicable outside of the constrained hover scenario because the measured forces will change with increasing flight speed, *U*.

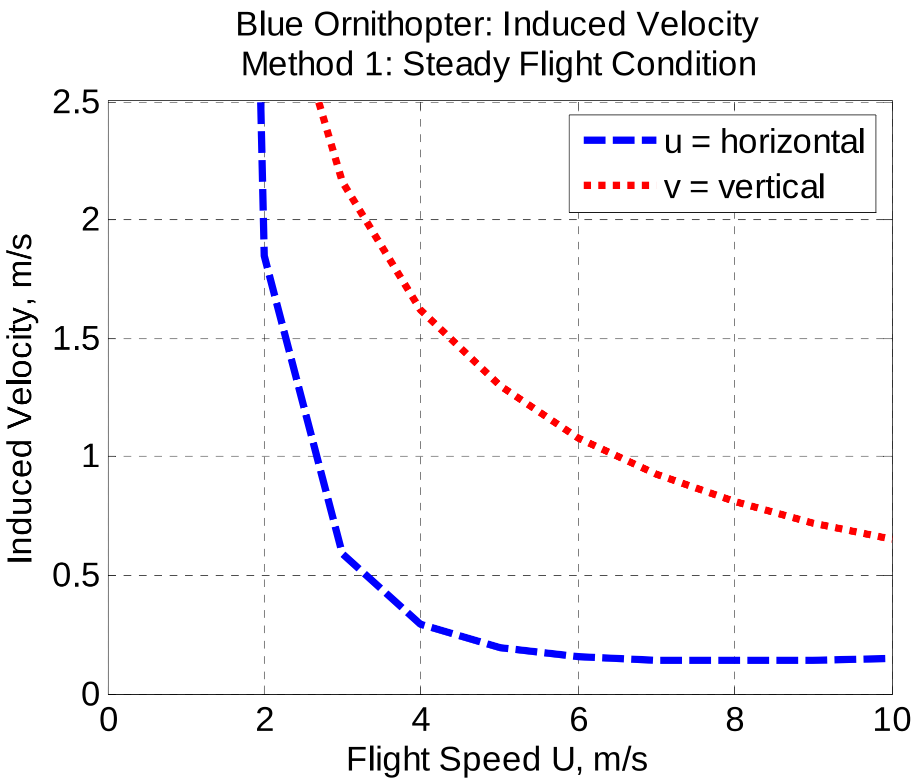

Figure 5.18: Blue ornithopter induced velocities using method one in forward flight.

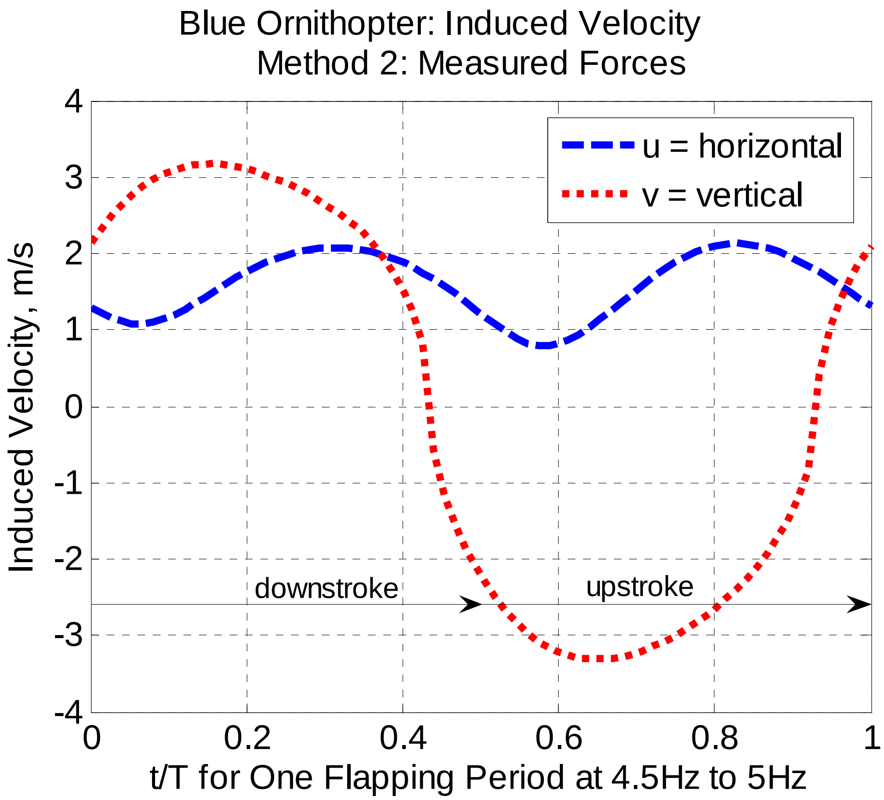

Figure 5.19: Blue ornithopter induced velocities using method two in hover.

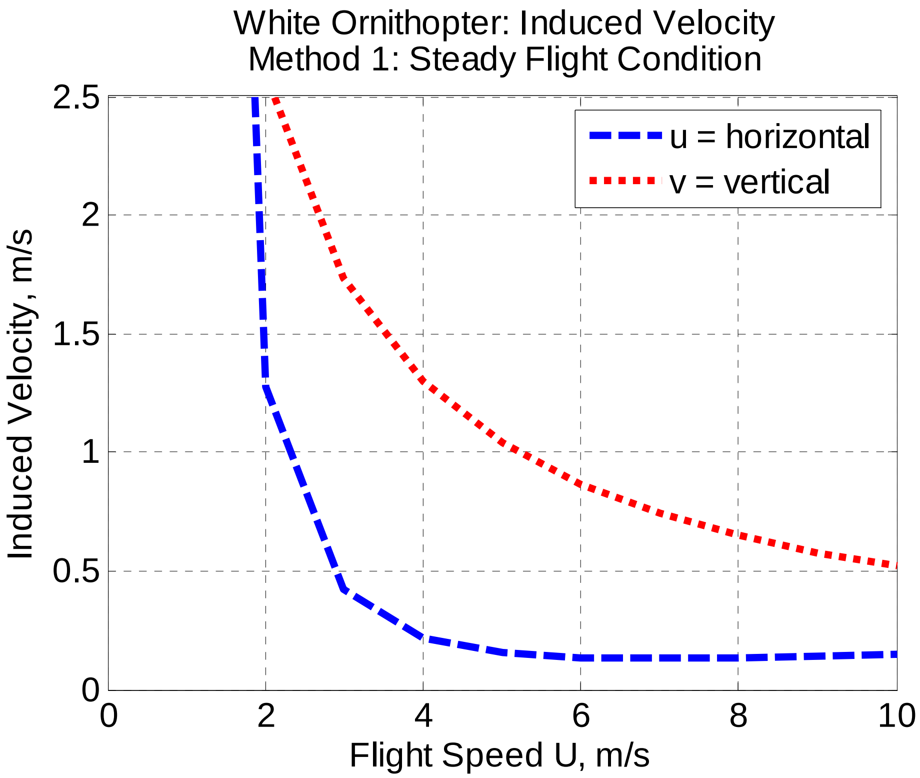

Figure 5.20: White ornithopter induced velocities using method one in forward flight.

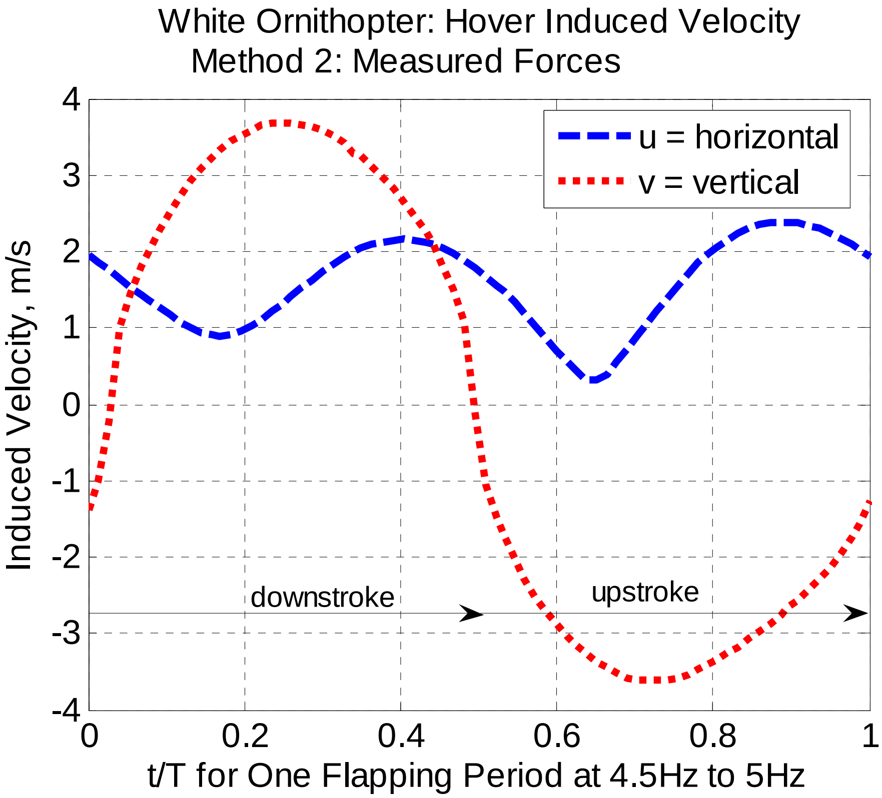

Figure 5.21: White ornithopter induced velocities using method two in hover.

The shape of method one's results vary as U^{-1}, while velocity is not accounted for in the hover condition of method two. Method one shows a steep increase towards infinity of the induced velocities as flight speeds less than 2 m/s. At 2m/s the horizontal induced velocity has a magnitude of 1.8 and 1.3 m/s and the vertical induced velocity has a magnitude of 4 and 2.6 m/s for the blue and white ornithopter respectively. As flight speed increases past 2 m/s the horizontal induced velocity reduces and levels off at 6 m/s with a magnitude of 0.2 and 0.3 m/s for the blue and white ornithopter respectively. The vertical induced velocity levels off more gradually to speeds around 0.5 m/s for flight speeds greater than 10 m/s.

Method one results produce a constant induced velocity value for a given flight speed *U*. In actuality the sign of the vertical or downwash induced velocity fluctuates with the sign of the vertical circulatory force at the wing tip, or equivalently the sign of the angular velocity at the wing tip. During downstroke the circulatory force is positive, so *v* is expected to be negative; but during the upstroke the circulatory force is negative so *v* is expected to be positive. While this fluctuation between positive and negative downwash can be thought of as a square wave, it is more likely the downwash behaves sinusoidally with an amplitude that equals the constant vertical induced velocity value from method one. Method two, which uses the measured force values, captures this induced velocity sign.

Method two's results for the hover case are sinusoidal in shape as postulated above. The horizontal induced velocity has a 10 Hz or twice per flapping cycle frequency, while the vertical induced velocity has a 5 Hz or once per flapping cycle frequency. These oscillations correspond to the oscillations of the measured thrust and lift terms respectively. As with the measured thrust values, the horizontal induced frequency is always positive; it oscillates between zero and 2.2 m/s for both vehicles. The vertical induced velocity is symmetric about zero with maximum amplitudes of 3.2 m/s and 3.7 m/s for the blue and white ornithopters, respectively.

These induced velocity values are large, with magnitudes greater than the actual flight speed at flight speeds under 2 m/s, and magnitdes of 10% to 20% of the flight speed for moderate speeds of 5 m/s to 6 m/s. The small induced velocity assumption that many aerodynamic theories assume is only valid for flight speeds greater than 10 m/s, where the induced velocity is reduced to 5% of the flight speed. These results are important to consider when establishing the aerodynamic model, which is discussed in the following sections.

5.6.4 Quasi-Steady Circulatory Force

The aerodynamic model will assume a quasi-steady circulatory lift force is acting on the membrane wing, with adjustments to the force from sail theory and the lift deficiency function *C(k)*. Quasi-steady analysis was introduced in Section 3.4.1 and the quasi-steady motions were reviewed earlier in Section 5.5.1. Adjustments for sail theory and the unsteady lift deficiency are applied to the classical thin airfoil theory result for lift coefficient. The thin airfoil result usually given by $C_l = 2\pi\alpha_{eff}$, however this is a linearized simplification for small angles of attack. The nonlinear thin airfoil theory result for the lift coefficient is given by Eq. (5.23).

$$C_l = 2\pi \sin\left(\alpha_{eff}\right) \tag{5.23}$$

Given this equation, the first task at hand is to calculate the effective angle of attack of the inflow velocity on the flapping wing. Figure 5.22 shows the respective velocities acting on a flapping and pitching airfoil during the downstroke, including the induced velocities. The airfoil pitch, θ, the pitch of the flapping axis with respect to the flight velocity vector, δ, the flight path angle, γ, and the zero lift angle of attack, α_{L0}, are also shown. Given these quantities, the inflow velocity, V_{rel}, the inflow angle, ϕ, and the relative angle of attack, α_{rel}, can be determined. The induced velocities are computed using method one introduced in Section 5.6.2. However, the vertical induced velocity is made sinusoidal by multiplying by the fixed *v* value by the normalized angular velocity curve. This will allow a smooth transition between the positive and negative sign of the vertical induced velocity as the lift force changes directions. The horizontal induced velocity, *u*, remains a constant.

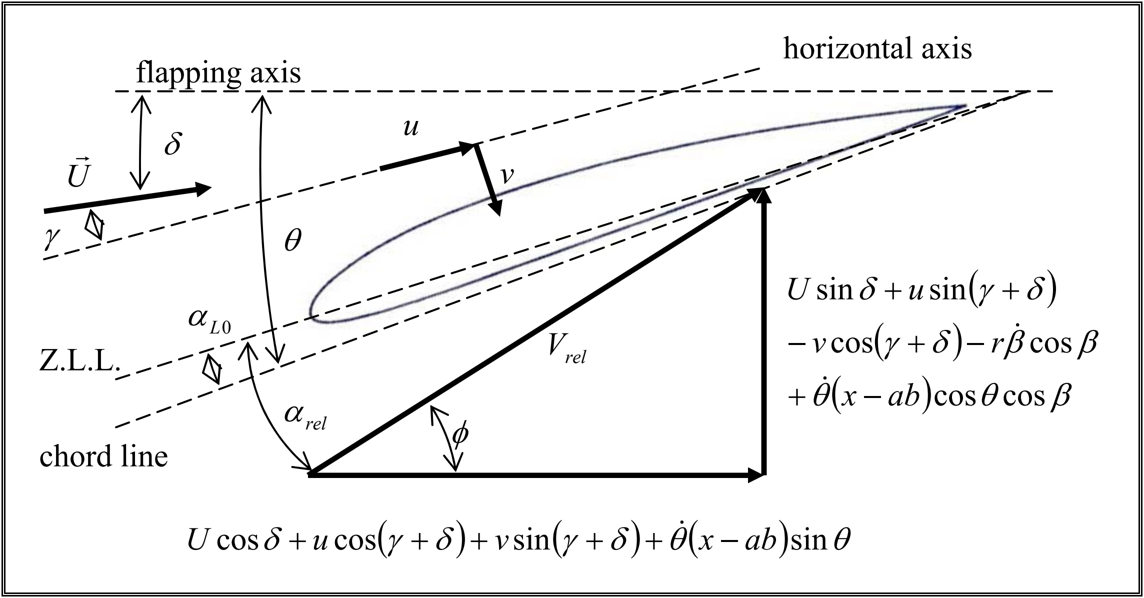

Figure 5.22: Determining relative angle of attack.

First the inflow velocity, V_{rel}, and inflow angle, ϕ, are determined for the angle of attack incident at the ¾ chord location using Eq. (5.24) and Eq. (5.25). Then the relative angle of attack is determined by Eq. (5.26). Each of these equations is applied to a specific spanwise blade element or airfoil segment with known kinetics and orientation to determine the local circulation lift coefficient.

$$V_{rel} = \left\{ \begin{array}{l} \left[U\cos\delta + u\cos(\gamma+\delta) + v\sin(\gamma+\delta) + \dot{\theta}(x-ab)\sin\theta\right]^2 + \\ \quad \left[U\sin\delta + u\sin(\gamma+\delta) - v\cos(\gamma+\delta) - r\dot{\beta}\cos\beta + \dot{\theta}(x-ab)\cos\theta\cos\beta\right]^2 \end{array} \right\}^{1/2} \tag{5.24}$$

$$\phi = \tan^{-1}\left(\frac{U\sin\delta + u\sin(\gamma+\delta) - v\cos(\gamma+\delta) - r\dot{\beta}\cos\beta + \dot{\theta}(x-ab)\cos\theta\cos\beta}{U\cos\delta + u\cos(\gamma+\delta) + v\sin(\gamma+\delta) + \dot{\theta}(x-ab)\sin\theta}\right) \tag{5.25}$$

$$\alpha_{rel} = \phi + \theta - \alpha_{L0} \tag{5.26}$$

The relative angle of attack can now be used to compute the two dimensional circulatory lift coefficient for that specified spanwise location, *r*. As shown in Section 3.4.2, the lift coefficient can be adjusted by the lift deficiency magnitude, *C(k)*, to account for the unsteady effects on the vehicle. Additionally, the empirical relation for added circulation force for a sail with first order behavior and membrane slack length, *l*, must be added (Section 3.2.1.5). Combining these results in Eq. (5.27) gives the final circulation lift coefficient, where *dc* is the local chord length.

$$C_{l\_c} = 2\pi C(k)\sin\alpha_{rel} + 0.636\sqrt{l/dc} \tag{5.27}$$

The left hand term of Eq. (5.27) is the quasi-steady, lift deficiency adjusted lift coefficient, and the right hand term is the additional lift due to membrane behavior based on the membrane slack ratio. This lift coefficient can be converted to a lift force using Eq. (5.28), for a wing segment or blade element with chord length *dc* and blade width *dr*.

$$dL_c = qSC_{l\_c} = \frac{1}{2}\rho V_{rel}^2 C_{l\_c} \cdot dc \cdot dr \tag{5.28}$$

This local circulatory lift force acts normal to the inflow velocity, and therefore it produces both vertical and horizontal forces. The transformations necessary to compute the vertical and horizontal components of the circulatory lift are discussed in Section 5.6.6.

5.6.5 Quasi-Steady Non-Circulatory Force

The non-circulatory or apparent mass force generated by a moving wing was discussed in Section 3.4.3. Qualitatively, the non-circulatory force is the result of the acceleration of a body of air normal to the wing surface as the wing undergoes quasi-steady motion. For a flapping and pitching wing with a non-zero flight speed, the non-circulatory normal force generated by the wing is given by Eq. (5.29).

$$dN_{nc} = -\frac{\rho\pi\left(dc^2\right)}{4}\left(\dot{\theta}U + r\ddot{\beta}\cos\theta - ba\ddot{\theta}\right)\cdot dr \tag{5.29}$$

This is the normal force value for a wing segment of length *dr*, where *r* is the mean spanwise position of the segment and *dc* is the chord length. The non-circulatory force acts normal to the wing, and therefore must be broken down into vertical and horizontal components as well.

5.6.6 Vertical and Horizontal Force Components

The vertical and horizontal force components are computed using the angles defined in Figure 5.22. Since the local blade element orientation varies along the span, the vertical and horizontal components of each force should be computed before the blade element forces are summed over the entire wing. The resulting vertical and horizontal components of the calculated forces are provided in Table 5.5.

Table 5.5: Vertical and horizontal force components.

Force	**Vertical Component**	**Horizontal Component**
Circulatory	$dF_{vert\_c} = dL_c \cos\phi \cos(\delta+\gamma)$	$dF_{horiz\_c} = dL_c \sin\phi \cos(\delta+\gamma)$
Non-Circ.	$dF_{vert\_nc} = dN_{nc} \cos(-\theta)\cos(\delta+\gamma)\cos\beta$	$dF_{horiz\_nc} = dN_{nc} \sin(-\theta)\cos(\delta+\gamma)$

These force components are computed using the local values for the blade element pitch, inflow angle and stroke angle. The non-circulatory vertical force has a stroke angle term because there is a spanwise component due to the normal force orientation. For the motion tracking experiments the flight path angle and flapping axis angle were zero, so $\cos(\delta+\gamma)$ becomes one and the equations will simplify.

5.6.7 Blade Element Force Summation

The last step in the aerodynamic model is to sum the vertical and horizontal force components over the blade elements as shown in Eq. (5.30) and Eq. (5.31).

$$F_{vert} = \left[\sum_{n=1}^{12} dF_{vert\_c} + dF_{vert\_nc}\right] + \overline{D}\sin\overline{\phi}\cos(\delta+\gamma) \tag{5.30}$$

$$F_{horiz} = \left[\sum_{n=1}^{12} dF_{horiz\_c} + dF_{horiz\_nc}\right] + \overline{D}\cos\overline{\phi}\cos(\delta+\gamma) \tag{5.31}$$

Also note the presence of the mean drag force, $\overline{D}$, adjusted by the inflow angle at the mean chord location. The mean drag force is computed using Eq. (5.16) with the mean inflow velocity and the mean Reynolds number. This drag should be very similar to the mean drag values presented using case two in Section 5.6.2. Now the model can be applied and the results compared to measured force values.

Chapter 6. Aerodynamic Modeling Results

The results of the aerodynamic model applied to the wing kinematics are presented graphically in this chapter. Modeling results are compared with the measured forces and with preliminary results from a computational fluid dynamics model [74]. Differences between the model and measured forces are summarized by a magnitude and phase analysis for the frequency sweep cases.

The aerodynamic modeling results are compared with the measured forces for an assumed flight velocity of 5m/s in the aerodynamic model. This speed was selected because the angle of attack values are generally below thirty degrees and the effect of induced velocities are minimized. This is also a velocity that showed great promise for minimizing drag and power requirements while maintaining high thrust efficiency. A hovering condition could not be met because the inflow angles and angles of attack would approach 90˚. At hover, the stall effects and unsteadiness of the flow are not adequately captured by this aerodynamic model. While the flight conditions are different for the modeled and the experimental cases, comparing the magnitude and phase of the results will still indicate model accuracy.

6.1 Comparison of Modeled and Measured Forces

This section presents detailed results for the optimal flapping frequencies between 4.5 and 5 Hz for both ornithopters; including a magnitude and phase comparison of the results in comparison to experimental values.

6.1.1 Blue Ornithopter Results

The blue ornithopter is examined first, starting with Figure 6.1, which shows a comparison of the vertical and horizontal forces from the experiment and the model versus the non-dimensional flapping period time. This plot also indicates the local flapping stroke angle and decomposes the model into its circulatory and non-circulatory force components. The same modeling results are presented in Figure 6.2 against the stroke angle to show the cyclical path of the force variation. In this plot the direction of wing motion is indicated by the arrows.

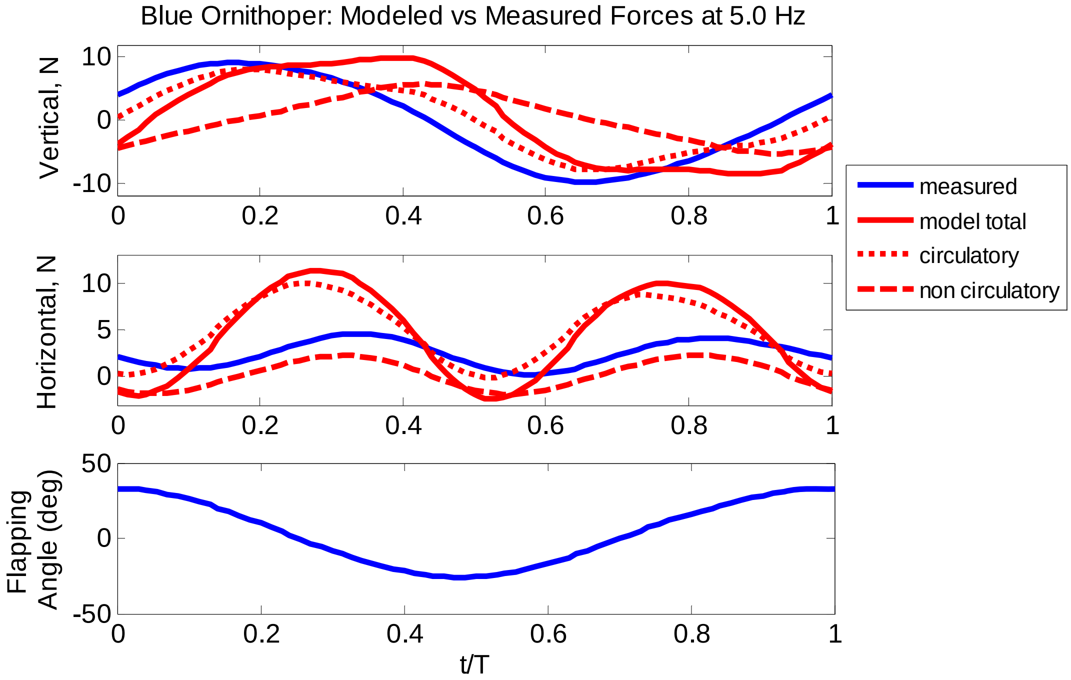

Figure 6.1: Blue ornithopter model results for one flapping period at 5 Hz.

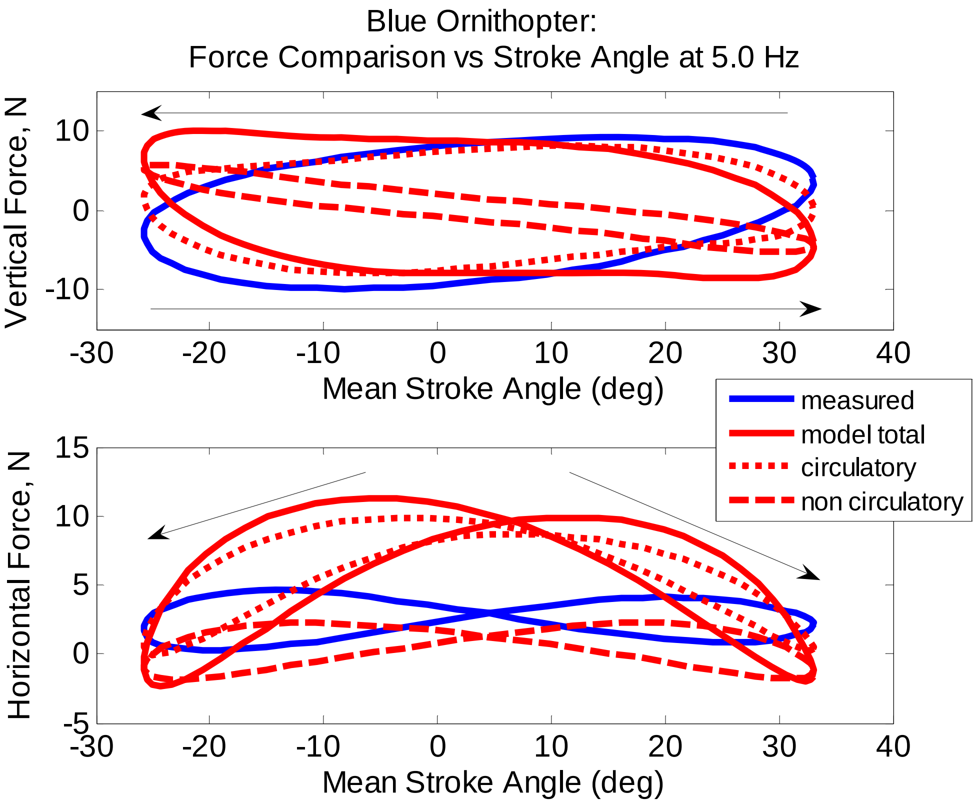

Figure 6.2: Blue ornithopter results vs stroke angle, arrows indicate the direction of motion.

Examing the model results closely shows better correlation for the vertical force than for the horizontal force and the circulation force clearly dominates the non-circulatory force. The modeled vertical force magnitude is approximately 10% larger than the experimental value, while the modeled thrust has a large over-estimation of 1.5 times the magnitude of the measured value. However, the model captures the phase of the horizontal force better than the vertical force, with phase lags of -20˚ and 20˚ to 75˚, respectively. The vertical force has a phase lag range because the modeled force plateaus at a contant maximum magnitude between 40% of the downstroke and 80% of the downstroke. As expected, the circulatory force peaks near the middle of the downstroke and upstroke, while the non-circulatory vertical and horizontal forces peak at 80% and and 60% of the downstroke period, respectively. Although the non-circulatory force seems small, Figure 6.2 shows the horizontal force component precicely matches the measured force’s phase and the relative magnitude between maximum and minimum force values. This overestimation of the total horizontal force leads to speculation that the circulatory force component may be inaccurately modeled, and the contribution of each part of the wing should be analyzed.

To take a closer look at how the modeled forces are conceived the force components due to the luff region (blades 1 to 8), the trailing edge flap region (blades 10 to 12) and the wing tip blade element are presented in Figure 6.3 and Figure 6.4 for the circulatory and non-circulatory forces respectively. As expected, the luff region creates the most vertical circulatory force, followed by the flap region. The tip produced very little vertical circulatory force because it had low angle of attack values and the large inflow angle orients the forces horizontally. For the horizontal circulatory force, the luff and tip force magnitudes are one-half of the magnitude of the actual horizontal force, though they experience a phase lead of 60˚. The flap region horizontal circulatory force is very dominant, and produces the primary error with a 30% to 40% over-prediction of the measured value. However, the phase lead of the flap component is more accurate, with a typical lead of only 10˚ to 15˚.

Both the vertical and horizontal non-circulatory forces are dominated by the flap region in Figure 6.4. The vertical non-circulatory force has a maximum magnitude of half the measured value and it acts at the middle of the downstroke. This phase is somewhat earlier than the 180˚ phase from the beginning of downstroke that the wing acceleration experiences. The luff and tip produce little to no horizontal force, and the flap contribution has the same net magnitude and phase as the measured value, it is just shifted down to be symmetric about zero.

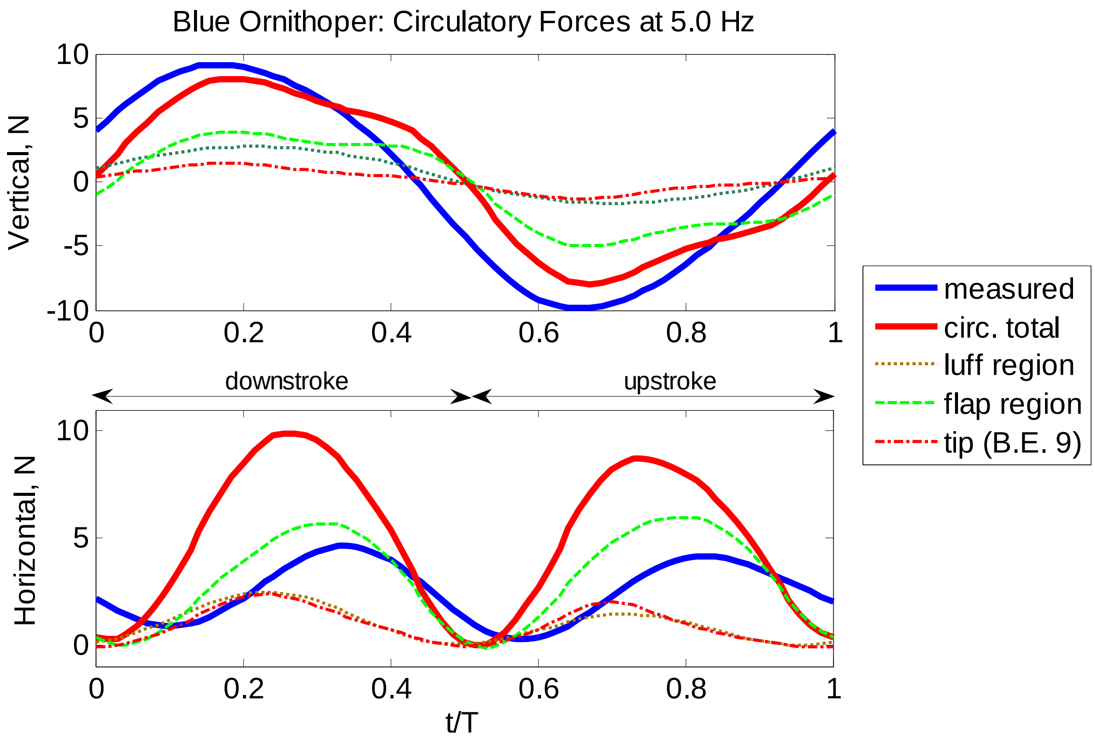

Figure 6.3: Blue ornithopter, circulatory force break-down by wing component.

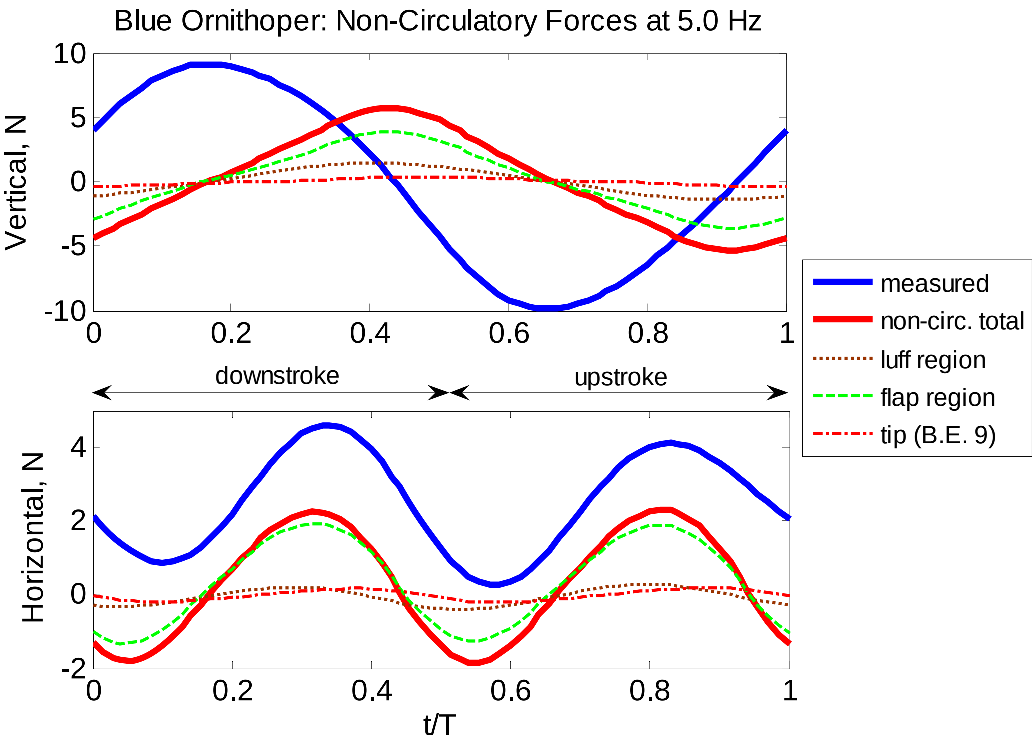

Figure 6.4: Blue ornithopter, non-circulatory force break-down by wing component.

6.1.2 White Ornithopter Results

With these results from the blue ornithopter, the model behavior for the white ornithopter must be examined to see if it follows the same trend. The white ornithopter’s modeled vertical and horizontal forces are compared to measured values for one flapping cycle at 4.5 Hz in Figure 6.5. This plot includes the measured force, the total modeled force, and the circulatory and non-circulatory components of the modeled forces. The same results are plotted versus stroke angle in Figure 6.6 to compare the phase and shape of the forces generated during downstroke and upstroke.

Like the blue ornithopter, these figures show excellent correlation between the magnitude of the vertical force for the measured and modeled results, with less than 5% error. Trends for the magnitude and phase of the total vertical force are similar to the blue ornithopter, having a maximum value plateau over the entire bottom half of the downstroke, while the measured value peaks at 40% of the downstroke. This equates to a large phase lag window of from zero to ninety degrees. The vertical circulatory force result is particularly good, with exactly the same phase as the measured force and an amplitude deficiency of only 10% during the last half of each stroke cycle. Figure 6.6 shows the accuracy of the vertical circulation force particularly well, with the measured and circulatory curves nearly on top of one another for the entire stroke cycle. The vertical non-circulatory force component also predicts the vertical measured force within 5%, with a phase precisely at the downstroke-upstroke transition which matches theoretical predictions. This non-circulatory component is what pulls the phase of the total vertical force toward the downstroke-upstroke transition.

Turning to the horizontal forces, the disparity of the results is even greater than with the blue ornithopter. The total modeled horizontal force is nearly three times the measured value and has a phase lag of -30˚. Breaking the modeled force into components shows that the horizontal circulatory force is the root of both the over-amplification and the phase lag. The horizontal circulatory force component is maximized near the middle of downstroke, while the measured force and horizontal non-circulatory force match in maximum amplitude and have equivalent phases at 80% of the downstroke period. However, when presented alone, the horizontal non-circulatory force has a significant negative component near the beginning of upstroke and downstroke that is not seen in the measured forces. The large positive magnitude of the circulatory force at the beginning of the downstroke helps to alleviate but does not eliminate this presence of a negative force component that equates to drag.

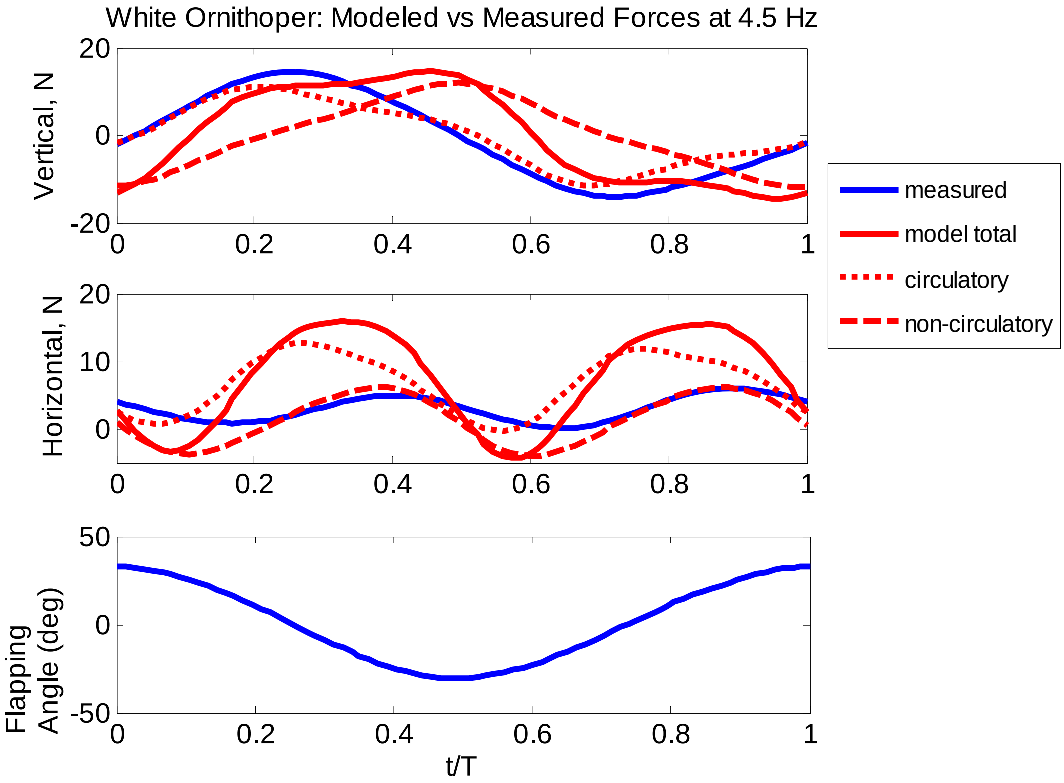

Figure 6.5: White ornithopter model results for one flapping period at 4.5 Hz.

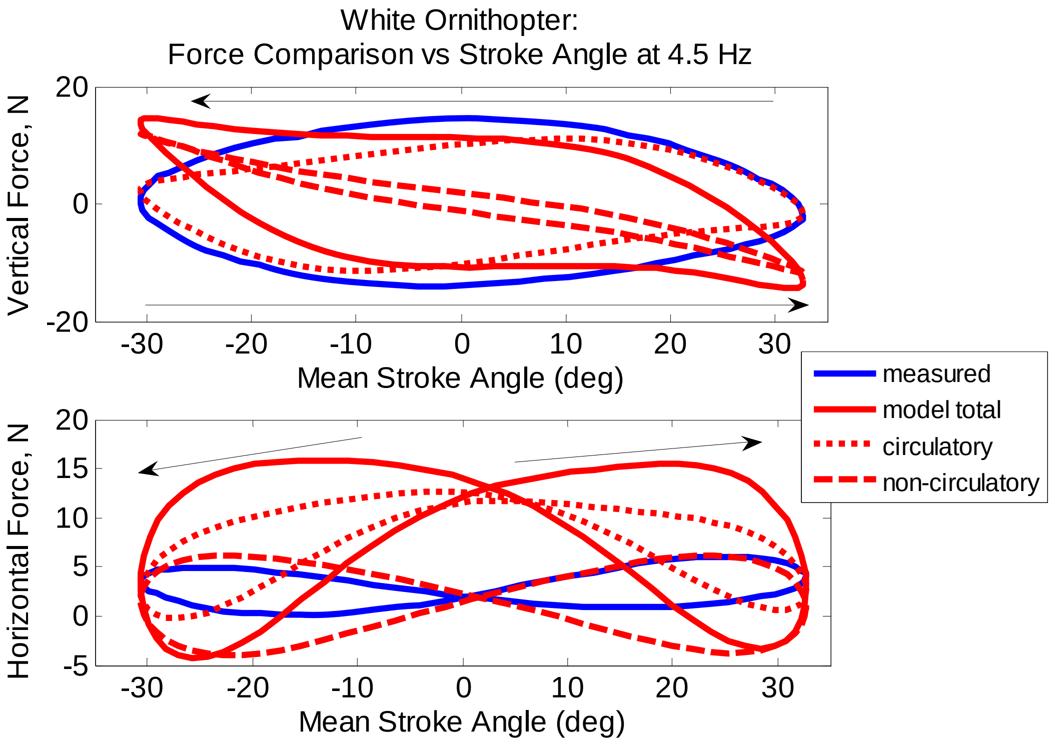

Figure 6.6: White ornithopter results vs stroke angle, arrows indicate the direction of motion.

The circulatory and non-circulatory forces are broken down into the components generated by the luff, flap and tip regions of the wing in Figure 6.7 and the Figure 6.8, respectively. Unlike the blue ornithopter, the luff and tip regions, which cover the entire leading edge surface, dominate the circulatory forces. The phases of these regions match the middle of the downstroke fairly well and consequently they match the vertical measured force phase, but lead the horizontal measured force phase by 60˚. However, the flap region component of the circulatory force is in phase with the measured horizontal force, but its magnitude only 50% to 80% of the measured value, which is not large enough to counteract the phase of the luff and tip horizontal circulatory forces. The total contribution of the circulatory force approximates the vertical force magnitude and phase well, but significantly over-estimates the horizontal force magnitude and while having a large phase lag.

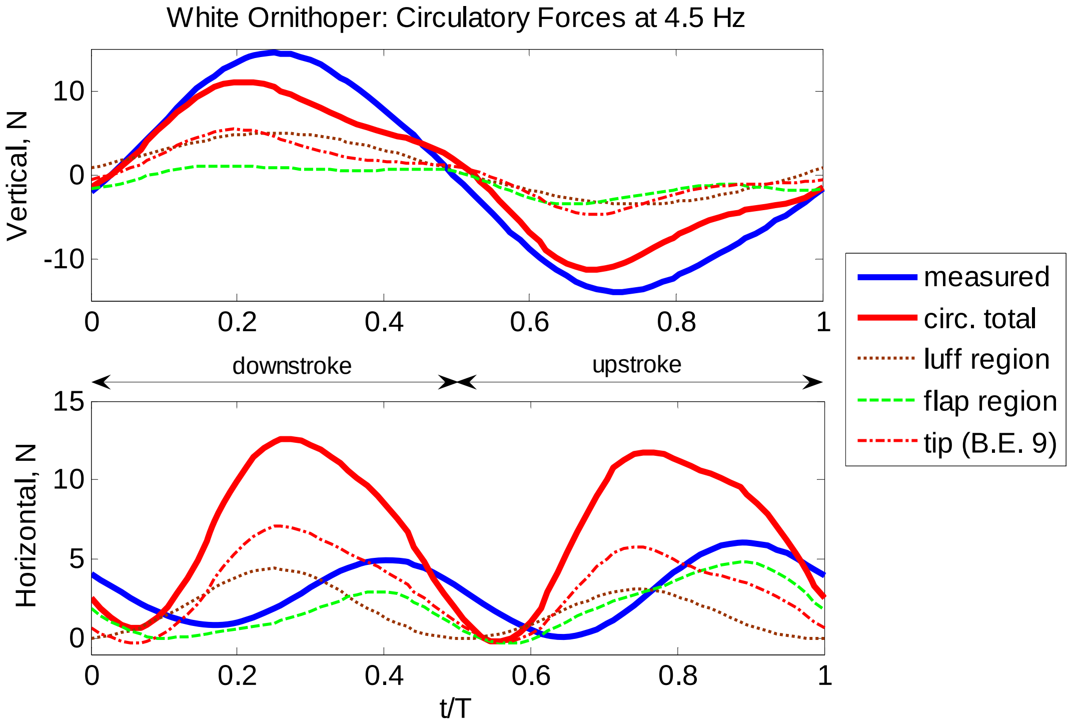

Figure 6.7: White ornithopter, circulatory force components from each wing region.

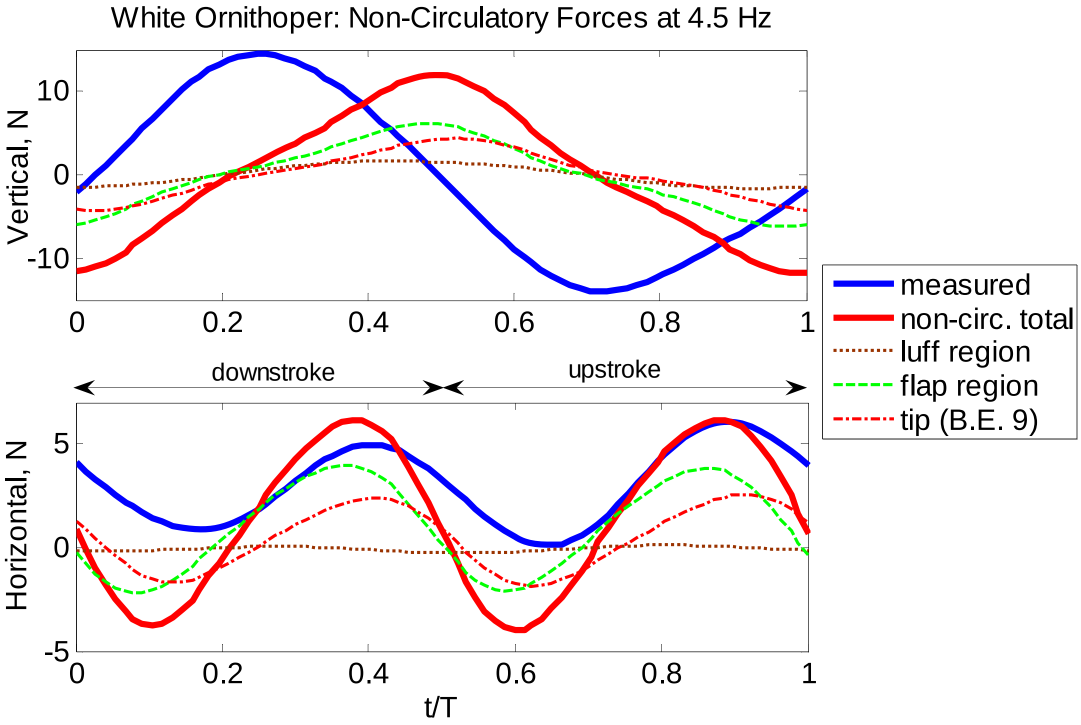

Figure 6.8: White ornithopter, non-circulatory force components for each wing region.

The non-circulatory forces on the white ornithopter are much more accurate in both phase and magnitude for the horizontal force than the circulatory force. The primary contribution to the non-circulatory force comes from the flap region and wing tip, with the wing tip having 70% of the flap regions magnitude and a phase lag of 15° from the flap region. As with the blue ornithopter, there is no appreciable contribution of the luff region to the non-circulatory forces. Vertical force predictions by the non-circulatory force reach 80% of the measured force magnitude, but the non-circulatory phase is oriented exactly at the downstroke-upstroke transition, which creates a large phase lag up to 135° from measured values.

6.1.3 Conclusions

Several important conclusions can be made from the comparison of the modeled and measured forces. First, the total circulatory lift very closely approximates the measured lift value and phase. This shows that the quasi-steady lift model, which was extended to apply unsteady effects and the additional sail theory lift, can accurately predict the lift produced by the ornithopters used for research. In turn, the quasi-steady model can be applied in a stability and control algorithm to implement autonomous flight controls. Secondly, the non-circulatory force provides the best prediction of the horizontal or thrust force, with the majority of the force being produced by the wing area aft and outboard of the diagonal spar. This confirms suspicions that the rotational flexibility of the trailing edge flap region is required to generate thrust during flight. If this region of the wing is compromised, the ornithopter will not be able to fly. Also note that the forces produced by the trailing edge region of the white ornithopter were much larger than that of the blue ornithopter. Comparing the two wings, the flap and tip regions of the white ornithopter are much larger in area and the diagonal spar intersection with the leading edge occurs earlier. This geometry difference may be why these regions have greater importance in the both the circulatory and non-circulatory force magnitudes for the white ornithopter. Finally, the contribution of the circulatory force to the horizontal force, and the contribution of the non-circulatory force to the vertical force, only act to diverge the total modeled forces from the measured quantites. While these forces cannot be neglected, they should be examined further to ensure their accuracy. Considering the simplicity of the model it does a good job of matching the trends of the measured forces, expecially the circulatory vertical force magnitude and phase.

6.2 Comparison with Computational Fluid Dynamics

A computational fluid dynamics (CFD) analysis of blue ornithopter was completed by two research scientists using the same kinematic data as the analytical aerodynamic model [74]. A summary of this research and a comparison of CFD results with the analytical model are now presented. Conclusions are drawn regarding which method provides the most accuracy and insight while minimizing computational expenditure.

The CFD model was completed by Sitaraman and Roget at the National Institute of Aerospace [74]. Their approach involved developing a deforming grid mesh that tracks the wing motion and applying a RANS packages, UMTURNS, to the ornithopter at the hovering condition for a flapping rate of 3.2 Hz. This frequency is quite a bit lower than the actual frequency used in flight, but the shape of vertical (lift) and horizontal (thrust) curves are very similar to the 5 Hz case before resonance is reached for the blue ornithopter. Since the CFD approach is capable of modeling the flow behavior at hover, it should provide more accurate results than the analytical model, which must assume a forward flight velocity. Also, the CFD code will capture the unsteadiness of the flow and any stall behavior that is present. The CFD model structure was also adjusted to account for the intertial effects of the wings, though they were quite small.

Qualitative results from the CFD analysis showed that the flow around the wing separates at the transitions between upstroke and downstroke, shedding a vortex which is pushed slowly backward by the horizontal induced velocity. The wing passes through this wake region as it moves through its stroke towards the next transition point; this causes an increase in the lift force similar to the wake capture for insects. The separation that causes the shed vortices is not symmetric for the wing, it is larger on the lower side than the upper side, which could effect the net lift value.

Quantitative comparisons of the CFD results with the measured forces are presented in Figure 6.9 and Figure 6.10 for the 3.2 Hz case. The CFD results match the measured vertical (lift) force values within 10%, with the majority of overprediction occurring at the middle of downstroke where the computed lift lags the measured value by 30˚. Horizontal (thrust) forces results deviate by up to 50% to the positive and negative side of the measured horizontal force values, but the thurst phase is captured well.

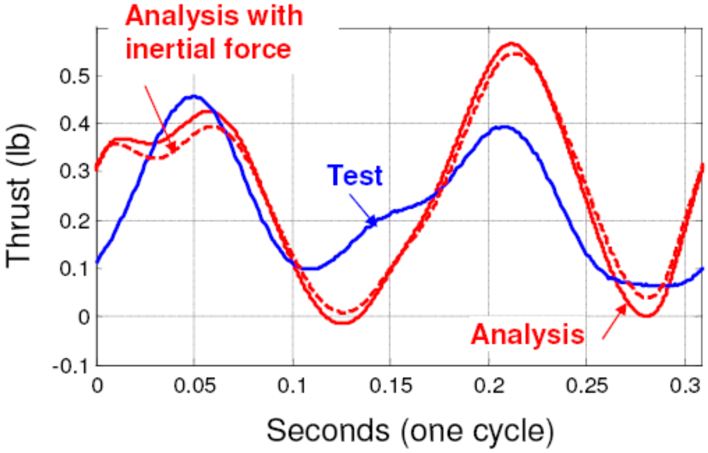

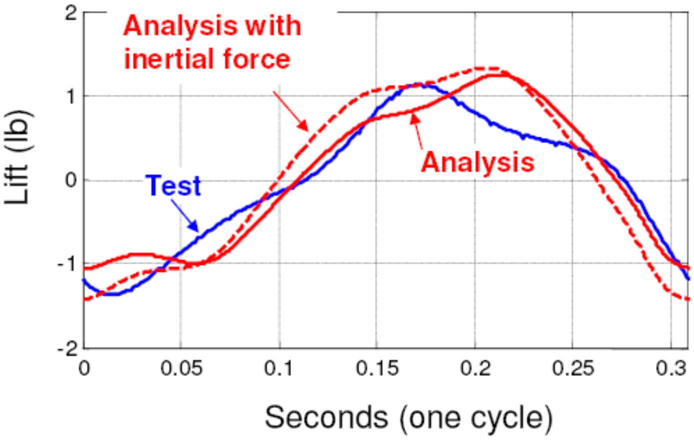

Figure 6.9: CFD results compared to measurements for the blue ornithopter at 3.2 Hz.

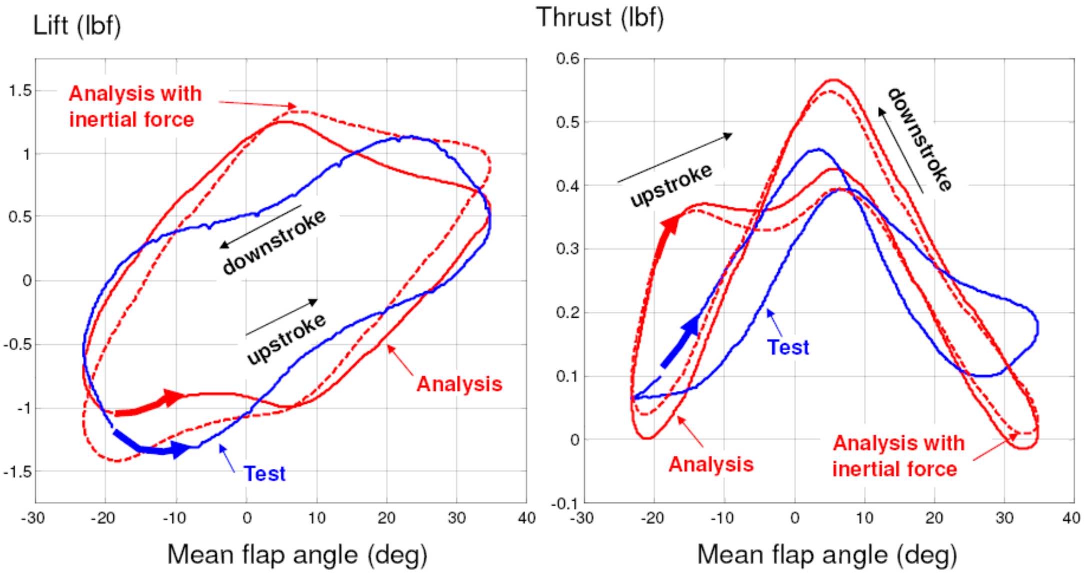

Figure 6.10: CFD results versus mean stroke angle for blue ornithopter at 3.2 Hz.

Comparing the accuracy of the CFD results to the analytical model accuracy shows that they have similar trends. Both approaches capture the magnitude of the vertical force very well, but overpredict the thrust values. The phase accuracy is also similar for the blue ornithopter results, with the vertical force lagging the measured force slightly and good correlation between the modeled horizontal force phase and measured values. Where the analytical model produces poorer results, it can be partially attributed to the flight condition. The flapping velocity will differ enough between 5 and 3.2 Hz to reduce the effect of the non-circulatory force on the analytical model results, which reduces the error in the vertical force phase and the horizontal force magnitude.

As a whole, both approaches work fairly well and both could use further revision based on additional experiements or more nonlinear and unsteady modeling approaches. However, considering the simplicity of the quasi-steady analytical model, it does an adequate job of predicting the behavior of a very complex flight system. Realistically, the CFD results should be used to amend the analytical model so that it can account for stall effects and so that a more accurate model of induced velocities can be developed. Using the CFD results to iterate on the analytical model is less expensive than doing additional experiments. The advantage of the analytical model is its low computational cost and simplicity, which will allow it to be imterpreted into a flight model for stability and control purposes.

Chapter 7. Conclusions

This final chapter will present a summary of the research, results and conclusions, as well as their impact on the design considerations for future ornithopters. Lastly, future work prospects are considered.

7.1 Summary of Research

This thesis presented a method to develop a flapping membrane wing analytical aerodynamic model using experiments that measure the wing kinematics. The motivation for this research was to develop a simple aerodynamic model that can be applied to stability and control of the flight dynamics to stabilize the flapping wing vehicle and allow an autopilot to be implemented. Background regarding the implementation and aerodynamic modeling of man-made ornithopters was presented, along with an overview of avian flight which provides a starting point for all flapping wing research. Fixed and flapping wing aerodynamics theories were presented to support the development of the quasi-steady aerodynamic model utilized for this research. The final aerodynamic model accounted for quasi-steady motions with unsteady effects and membrane wing performance as well as the non-circulatory apparent mass force generated by the accelerating wing. Blade element theory was used to apply the aerodynamic theory to the membrane wing so that local kinematics could be accounted for.

Motion tracking experiments were applied to two ornithopters in order to capture the wing kinematics. Kinematic results showed the flapping wings utilize a vertical stroke plane but experienced significant leading edge bending and chordwise pitching along the wing span. The membrane wing behavior was shown to be first order in regions where slack was present, which validated the use of the membrane aerodynamic equation for lift coefficient. Finally the vertical and horizontal forces measured during the motion tracking experiments were analyzed for magnitude and phase trends in relation to the wing stroke angle.

An analysis of the wing parameters was conducted. Reynolds number was found to vary between 20,000 and 285,000, with an average of 100,000 for the optimal flapping rate of 5Hz and the optimal flight speed of 5 m/s. The optimal flight speed was determined by analyzing the drag and power curves, the optimal flight speed range was found to be between 3 and 5 m/s. This optimal velocity range was limited to 5 m/s by the Strouhal number calculations, which required flight speeds of 5 m/s or higher to produce optimal thrust. Reduced frequency was also examined, with results varying from 0.2 to 2 depending on flight conditions. This implies the wing is in highly unsteady flow and the lift deficiency function will reduce the circulatory lift by 50%. An analysis was also completed to determine the induced velocities on the flapping wing using momentum theory; these results were utilized later in the aerodynamic model.

Finally, the aerodynamic model was applied to the flapping wing for a flight speed of 5 m/s at the optimal flapping frequency range of 4.5 to 5 Hz. Results showed a good approximation of the vertical force magnitude, with a phase lag of 30° between the maximum measured force and the maximum modeled force. The circulation forces in particular showed excellent correlation with the vertical force magnitude and phase. Horizontal forces were grosslly overestimated by the model due to the impact of the circulatory forces developed by the trailing edge flap region, if only non-circulatory forces were considered the horizontal force was fairly accurate in both peak to peak magnitude and phase. These general trends seem to indicate that the circulatory force dominates the actual vertical or lift force generated by the wing, while the non-circulatory force generated by the trailing edge flap region produces the majority of the thrust. Further scrutiny of the modeling method would be required to improve these results, including a more accurate description of the induced velocities and inclusion of additional unsteady effects such as stall behavior and wake capture. These effects can be examined using the computational fluid dynamics results developed in tandem with the analytical model. Despite its simplicity, the analytical model still showed sufficient modeling capacity that was only slightly worse than the predictions of the CFD analysis.

7.2 Impact on Design

This analysis provides some confirmation regarding how the flapping membrane wing produces the lift and thrust necessary to fly. The luff region and the wing tip produce the majority of the lift on the wing; while the trailing edge flap region produces thrust using both circulatory and non-circulatory methods. These results indicate that the wing structure is very important, especially the intersection of the two spars at the leading edge. To maintain flight using a membrane wing it is necessary to allow for flexibility so the wing can twist and bend to produce both circulatory and non-circulatory thrust forces. Without the rotation of the trailing edge flap and the twisting along the span the ornithopters are unlikely to fly.

Improvements to the wing design are desired to increase the lift and thrust efficiency of the ornithopter. Carbon fiber fingers could be inserted into the luff region of the wing from the leading edge spar to the diagonal spar to establish a desired camber shape while still allowing enough flexibility in the membrane to maintain a high stall angle of attack. The wing tip could also be tailored to allow for additional bending by placing a passive morphing device such as a torsional spring at the intersection of the two spars. The bending retraction of the wing tip will significantly increase the net lift without producing a large thrust penalty. This design change will require reinforcing the trailing edge flap region to maintain the current non-circulatory thrust profile. A long term goal may include applying a more complex morphing method, such as multiple degrees of freedom at the shoulder or elbow to mimic actual bird anatomy. These joints would fundamentally change the way the current wing produces lift and thrust and would allow for more complex flight behavior, such as perching.

Additional design concepts can be taken directly from avian and bat flight. Leading edge roughness could be adapted from owl flight to trigger turbulent flow and delay the effects of stall, while also decreasing the noise profile of the flapping wings. A membrane based leading edge flap similar to that seen on bat wings could also be added to act as a high lift device. Perhaps the simplest design feature to explore is the use of slots or winglets at the ornithopter wing tips to reduce induced drag. Further research studies should be completed on the techniques used by bats and birds to influence their aerodynamic performance, efficiency and maneuverability to determine their implementation in ornithopters. Trade studies in the design and optimization of membrane wings should also be completed.

7.3 Future Work

Both experimental and computational tasks could be completed to improve the aerodynamic modeling results and provide more insight into ornithopter flight. These tasks are summarized below.

1. Complete additional motion tracking experiments with test cases that vary the flapping axis angle. Experimenting with different wing shapes and structures would also be useful to determine the contribution of specific wing design elements to the measured force values.
2. Complete a motion tracking experiment in free flight conditions to confirm that the wing kinematics are similar for the constrained hover condition.
3. Complete a wind tunnel test using the motion tracking setup and PIV measurements to extract the vortex wake behavior. Experiment with both fixed and free flight conditions. The wake behavior can then be used to determine the circulation and induced velocity values.
4. Extract the stall conditions and induced velocities from the CFD results and apply them to the analytical model.
5. Isolate the aerodynamic versus inertial forces by measuring the forces produced by the ornithopter while flapping in a vacuum.
6. Measure the individual contribution of the luff and flap regions of the wing by making partial wing sections.
7. Test individual components of the lift coefficient equation for accuracy.

Appendices: MATLAB codes

```
% aeromodel.m
% Aerodynamic Modeling of Ornithopters with Segmented Wings (TE Flaps)

% Author: Robyn Harmon, UMD Morpheus Laboratory

clear   % Clear workspace
clc     % Clear command window

%------------------------------- NOMENCLATURE -----------------------------

%       B = full wing span (m)
%       b = half-chord length (m)
%       dc = blade element chord length (m)
%       dr = blade element width (m)
%       c = local chord length (m)
%       r = local span position
%       c_mean = mean chord length (m)
%       r_mean = span position at mean chord length (m)
%       S = total wing surface area (m^2)
%       AR = wing aspect ratio
%       n_blades = number of blade elements

%       alpha = relative angle of attack (rad)
%       beta = flapping angle (rad) (time history input)
%       theta = blade pitch angle from body axis (rad)
%       gamma = flight path angle (rad)
%       delta = pitch of flapping axis with respect to flight velocity

%       U = flight velocity (m/s)
%       V = total velocity due to quasi-steady motion (m/s)
%       Vrel = relative velcoity (m/s)
%       u = longitudinal induced velocity (m/s)
%       v = vertical induced velocity (m/s)
%       hdot = vertical plunging velocity of wing (m/s)
%       beta_dot = time varying angular velocity of wing (rad/sec)
%       beta_ddot = time varying angular acceleration of wing (rad/sec)
%       w = mean angular velocity of wing (2*pi*f) (rad/sec)

%       Cl or CL = lift coefficient (local)
%       Cd or CD = drag coefficient (local)
%       Cn or CN = normal force coefficient (local)
%       K = parasite drag coefficient ratio
%       CDp = parasite drag coefficient of ornithopter
%       Cf = flat plate drag coefficient

%       Ck = Theodorsen's lift deficiency function
%       F = Theodorsen's function component
%       G = Theodorsen's function component

%       k = reduced frequency
%       f = flapping frequency (Hz)
```

```
%       rho = air density (kg/m3)
%       mu = viscosity of air
%       Re = Reynold's number
%       Sr = Strouhal number

%------------------------ CONVERSIONS & CONSTANTS -----------------------

dtr = pi/180;      % degrees to radians
rtd = 180/pi;      % radians to degrees
intom = 0.0254;     % inches to meters
mtoin = 1/intom;   % meters to inches
NtoP = 0.2248;      % newtons to pounds force
PtoN = 4.4482;      % pounds to newtons force
rho = 1.293;        % air density STP (kg/m3)
mu = 1.8e-5;        % viscosity
display('Conversion factors and constants calculated');

%-------------------------------- GEOMETRY ------------------------------

% Specify which ornithopter is being analyzed: Trinity or Odyssey
bird = input('What bird is being used, Trinity (T) or Odyssey (O)? ','s');

% Specify vehicle weight
mass = input('What is the mass of the vehicle (kg)? ');
weight = mass*9.81;

% Specify which file has the wing planform (x,y) data
wing_data = input('What file has the wing planform data ','s');
wing = load(wing_data);

% Locate x,y data in file, convert from inches to meters
x = abs(wing(:,1));    % wing boundary points in x (chord) direction (m)
y = abs(wing(:,2));    % wing boundary points in y (span) direction (m)

% Calculate wing geometry: span, area, aspect ratio, etc.
R = max(y);             % half-span (m)
B = R*2;                % full-span (m)
C = max(abs(x));        % chord at wing root
S = trapz(abs(x),y);    % wing surface area for half wing
AR = B^2/(2*S);         % aspect ratio
Sw = 4*S;               % approx wetted wing area
c_mean = B/AR;          % mean chord

% Specify number of blade elements to be used in the analysis
n_blades = 12;

% Specify maximum blade element lengths for each bird, local r/R, c values
if bird == 'T'
   % L = maximum blade length, m
   Cmax = [230 209 188 162 142 118 92 66 51 100 152 158]/1000;
   r = [26 42 55 73 87 103 119 137 196 33 88 138]/229*R;
   c = [123 120 116 113 110 105 102 98 72 121 110 98]/125*C;
elseif bird == 'O'
   Cmax = [120 107 94 82 69 58 48 34 64 35 65 85]/235*R;
```

```
    r = [25 29 56 71 83 97 110 126 202 39 97 142]/235*R;
    c = [143 141 138 135 133 129 125 122 90 141 129 117]/143*C;
end

% Nondimensional span
r_R = r/R;

% Calculate location of mean chord, r_mean is between blades 8 and 9
r_mean = r(8) + (c_mean-c(8))*(r(9)-r(8))/(c(9)-c(8));

display('Wing geometry determined');

%----------------------- VICON & MEASURED FORCE DATA ----------------------

% Specify and load reflective marker data set, this data set should be
% preprocessed to correlate with the measured force data in time.
markers = input('What reflective marker data should be used? ','s');
load(markers);    % marker locations on wing, (m)
display('Vicon experimental data has been loaded')

% Calculate number of time steps (rows) of data, calibrate time sequence
rows = length(time);    % how many time steps there are
time = time - time(1);  % calibrate time so initial time is zero

% Load measured force data from the same motion tracking experiment, this
% data should be cross-correleated with the marker data set.
forces = input('What measured force data set should be used? ','s');
meas_force = load(forces); % will have format: [time thrust 0 lift stroke]

% What is the time delay required for data synchronization?
sync = input('What time delay synchronizes the measured forces? ');

% Extract measured forces, time sequence and measured stroke angle
time_meas = meas_force(:,1) + sync;    % Syncronized time
axial_meas = meas_force(:,2)*PtoN;      % axial force, (N)
normal_meas = -meas_force(:,4)*PtoN;    % normal force, (N)
stroke_meas = lsmoo(meas_force(:,5),50);    % measured stroke angle
% Remember that the normal force must be corrected for sign as shown

% Linear interpolation of axial and normal forces at marker time points
axial_interp = interp1(time_meas,axial_meas,time);
normal_interp = interp1(time_meas,normal_meas,time);

% Input frequency and data partitioning information
freqdata = input('What is the name of the frequency info file? ','s');
load(freqdata)

% assign frequencies to time span
frequency = zeros(rows,1);
int = 1;
for j = 1:rows
    if int <= length(freq)
        if time(j) >= stop_freq(int)+0.05
```

```
            freq_change(int) = j;
            int = int + 1 ;
        end
        if int <= length(freq)
            frequency(j) = freq(int);
        end
    end
end

if bird == 'T'
    start = 771;
else
    start = find(time==start_freq(1));
end
stop = freq_change(end);
display('Experimental results uploaded and synchronized');
display('    ');

%------------------------ SPECIFY FLIGHT CONDITIONS------------------------

% Input flight speed of ornithopter in m/s
U = input('What is the flight speed (m/s)? ');

% Input flight path angle of ornithopter (deg)
gamma_deg = input('What is the flight path angle (deg)? ');
gamma = gamma_deg*dtr;

% Input pitch angle of flapping axis with respect to flight velocity U
delta_deg = input('What is the pitch angle of flapping axis (deg)? ');
delta = delta_deg*dtr;

display('    ');
display('Flight conditions specified');

%------------- FORM BLADE ELEMENTS, CALCULATE LOCAL ORIENTATION -----------

% Initialize pitch, yaw and stroke angle matrices
theta = zeros(rows,n_blades);
theta_adj = zeros(rows,n_blades); % final adjusted pitch for rear blades
yaw = zeros(rows,n_blades);
beta = zeros(rows,n_blades);
hdot = zeros(rows,n_blades);
beta_dot = zeros(rows,n_blades);
beta_ddot = zeros(rows,n_blades);
theta_dot = zeros(rows,n_blades);
theta_ddot = zeros(rows,n_blades);


% Set yaw for blades 10 through 12 to 35 degrees
yaw(:,10:12) = 35*dtr;

% Form leading edge (x,y,z) matrices
LEx = [LE1(:,1) LE2(:,1) LE3(:,1) LE4(:,1) LE5(:,1) LE6(:,1) LE7(:,1)...
    LE8(:,1) LE9(:,1) LE10(:,1) LE11(:,1) LE12(:,1) LE13(:,1)];
```

```
LEy = [LE1(:,2) LE2(:,2) LE3(:,2) LE4(:,2) LE5(:,2) LE6(:,2) LE7(:,2)...
   LE8(:,2) LE9(:,2) LE10(:,2) LE11(:,2) LE12(:,2) LE13(:,2)];
LEz = [LE1(:,3) LE2(:,3) LE3(:,3) LE4(:,3) LE5(:,3) LE6(:,3) LE7(:,3)...
   LE8(:,3) LE9(:,3) LE10(:,3) LE11(:,3) LE12(:,3) LE13(:,3)];
if bird == 'O'
   LEx(:,14) = LE14(:,1);
   LEy(:,14) = LE14(:,2);
   LEz(:,14) = LE14(:,3);
end

% Calculate mean stroke angle along span
dy = LEy(:,2:end)-LEy(:,1:end-1);
dz = LEz(:,2:end)-LEz(:,1:end-1);
LEangle = atan(dz./dy);
stroke_mean = mean(LEangle,2)*rtd;
stroke_amp = (max(stroke_mean) + abs(min(stroke_mean)))*dtr;

% Form blade elements and calculate local pitch, yaw and stroke angle
for j = 1:n_blades    % 12 blades
   % Call blades.m for each blade element
   % Input: Which ornithopter, blade number, marker data, max freq & dt
   % Output: 2D airfoil points, length and width, pitch and stroke angle


   f_high = 8; % maximum frequency for low pass filter
   dt = time(2)-time(1);   % time step size
   [Bx,By,Bz,dr(j),dc(:,j),theta(:,j),beta(:,j)] = ...
      blades(bird,j,markers,f_high,dt);

   % Calculate maximum stroke size for each blade element
   stroke_size(1,j) = max(beta(:,j))-min(beta(:,j));

   % Determine slack percentage in blade
   % Remove any dc's longer than Cmax due to any inaccurate marker points
   dc_rough(:,j) = min(dc(:,j),Cmax(j));
   [dc(:,j),Hgain,fgain,hgain,tgain] = hsmoo(dc_rough(:,j),f_high,dt);
   if j < 9
      slack(:,j) = abs(Cmax(j)-dc(:,j)); % slack length
   else
      slack(:,j) = zeros(rows,1);
      dc(:,j) = Cmax(j)*ones(rows,1);
   end
   epsilon(:,j) = slack(:,j)./dc(:,j); % slack length as % chord
   b = dc/2;   % Half chord length

   % Store blade data points, set local yaw angle and adjust pitch for
   % non leading edge blades by the mean pitch of the blades in front
   % ...
   % Blades 1-9 are on the leading edge and have zero yaw and no pitch
   % adjustments are necessary so set pitch(:,j) = pitch_tot(:,j);
   if j==1 B1X = Bx; B1Y = By; B1Z = Bz; theta_adj(:,j) = theta(:,j);
   elseif j==2 B2X = Bx; B2Y = By; B2Z = Bz; theta_adj(:,j) = theta(:,j);
   elseif j==3 B3X = Bx; B3Y = By; B3Z = Bz; theta_adj(:,j) = theta(:,j);
   elseif j==4 B4X = Bx; B4Y = By; B4Z = Bz; theta_adj(:,j) = theta(:,j);
   elseif j==5 B5X = Bx; B5Y = By; B5Z = Bz; theta_adj(:,j) = theta(:,j);
   elseif j==6 B6X = Bx; B6Y = By; B6Z = Bz; theta_adj(:,j) = theta(:,j);
```

```
    elseif j==7 B7X = Bx; B7Y = By; B7Z = Bz; theta_adj(:,j) = theta(:,j);
    elseif j==8 B8X = Bx; B8Y = By; B8Z = Bz; theta_adj(:,j) = theta(:,j);
    elseif j==9 B9X = Bx; B9Y = By; B9Z = Bz; theta_adj(:,j) = theta(:,j);
    % ...
    % Blades 10-12 are on the leading edge and have 55 degree yaw and pitch
    % is reduced by the mean pitch of the blades in front of them
    elseif j==10 B10X = Bx; B10Y = By; B10Z = Bz;
        theta_adj(:,j) = theta(:,j) - mean(theta(:,1:3),2);
    elseif j==11 B11X = Bx; B11Y = By; B11Z = Bz;
        theta_adj(:,j) = theta(:,j) - mean(theta(:,3:6),2);
    elseif j==12 B12X = Bx; B12Y = By; B12Z = Bz;
        theta_adj(:,j) = theta(:,j) - mean(theta(:,6:8),2);
    end

%------------------- CALCULATE VELOCITY & ACCELERATION---------------------

% Calculate local velocities and accelerations, blade slack percentage

% Derivatives will be calculated using take_deriv.m which numerically
% utilizes Adams-Bashforth 3 method for central points, and Euler-explicit
% or Adams-Bashforth 2 near boundaries. The motion of the front and rear
% chord points for each blade will be used for the derivatives because they
% are limited in vibrations by the leading edge and diagonal spars

    % Determine blade velocity average between LE and TE of blade

    hdot(start:stop,j) = take_deriv(time(start:stop),[Bz(start:stop,1)...
        Bz(start:stop,end)],f_high,dt);

    % Calculate pitching rate of blades
    theta_dot(start:stop,j) = take_deriv(time(start:stop),...
        theta(start:stop,j),f_high,dt);

    % Calculate pitching acceleration of blades
    theta_ddot(start:stop,j) = take_deriv(time(start:stop),...
        theta_dot(start:stop,j),f_high,dt);

    % Calculate the angular velocity of the wing (rad/sec)
    beta_dot(start:stop,j) = take_deriv(time(start:stop),...
        beta(start:stop,j),f_high,dt);

    % Calculate the angular acceleration of the wing
    beta_ddot(start:stop,j) = take_deriv(time(start:stop),...
        beta_dot(start:stop,j),f_high,dt);

    fprintf('Blade element %f complete.\n',j)
end

display('Blade elements formed and local orientation calculated');
disp('Blade velocities and accelerations have been calculated')
```

```
%---------------------------- AERO PARAMETERS -----------------------------

% Calculate and set aerodynamic parameters
K = 4.4;                    % Profile drag factor
e = 0.8;                    % Elliptical lift factor
% Define set of test flight velocities, m/s
Utest = [0.1 1 2 3 4 5 6 7 8 9 10]';


%
%
%
%           ANALYSIS OF LOCAL AND MEAN QUANTITIES, DRAG & POWER
%
%
%------------------------- QUASI-STEADY VELOCITY --------------------------

% Calculate mean pitch and pitch rate values between blades 8 and 9
theta_mean = theta(:,8)+(c_mean-c(8))*(theta(:,9)-theta(:,8))/(c(9)-c(8));
theta_dot_mean = theta(:,8)+(c_mean-c(8))*(theta_dot(:,9)-...
   theta_dot(:,8))/(c(9)-c(8));

% Calculate angular position and velocity at r_mean
beta_mean = beta(:,8)+(c_mean-c(8))*(beta(:,9)-beta(:,8))/(c(9)-c(8));
beta_dot_mean = beta_dot(:,8)+(c_mean-c(8))*(beta_dot(:,9)-...
   beta_dot(:,8))/(c(9)-c(8));

% Velocities at Utest values
for j = 1:length(Utest)
   % Mean velocity at r_mean, c_mean location
   V_mean(:,j) = ((-Utest(j)*sin(gamma)+(c_mean/2*theta_dot_mean-r_mean...
      *beta_dot_mean).*cos(theta_mean)*sin(gamma+delta).*...
      cos(beta_mean)).^2 + (-Utest(j)*cos(gamma) + (c_mean/2*...
      theta_dot_mean - r_mean*beta_dot_mean).*sin(theta_mean)*...
      cos(gamma+delta)).^2).^(1/2);

   % Velocity due to wing motion at wing root
   V_root(:,j) = ((-Utest(j)*sin(gamma)+(3*c_mean/4*theta_dot(:,1)-...
      r(1)*beta_dot(:,1)).*cos(theta(:,1))*sin(gamma+delta).*...
      cos(beta(:,1))).^2 + (-Utest(j)*cos(gamma)+ (3*c_mean/4*...
      theta_dot(:,1) - r(1)*beta_dot(:,1)).*sin(theta(:,1))*...
      cos(gamma+delta)).^2).^(1/2);

   % Velocity due to wing motion at wing tip
   V_tip(:,j) =((-Utest(j)*sin(gamma) + (c_mean/2*theta_dot(:,9) - ...
      R*beta_dot(:,9)).*cos(theta(:,9))*sin(gamma+delta).*...
      cos(beta(:,9))).^2 +  (-Utest(j)*cos(gamma) + (c_mean/2*...
      theta_dot(:,9) - R*beta_dot(:,9)).*sin(theta(:,9))*...
      cos(gamma+delta)).^2).^(1/2);
end

%--------------------------- STROUHAL NUMBER ------------------------------

% Calculate wing tip amplitude in Z direction and frequency values
for j = 1:length(freq)
```

```
    A(j) = max(TIP(marker_start(j):marker_stop(j),3)) - ...
                min(TIP(marker_start(j):marker_stop(j),3));
    f(j) = 1/(time(marker_stop(j))-time(marker_start(j)));
end

% Calculate Strouhal Number
St = zeros(length(Utest),length(f));
for j = 1:length(f)
    St(:,j) = f(j)*A(j)./Utest;
end

% Plot Strouhal Number
for j = 1:length(f)
    plot(Utest,St(:,j));
    hold on
end
plot([1 10],[0.2 0.2],[1 10],[0.4 0.4]);
title('Strouhal Number: Blue Ornithopter')
xlabel('U, m/s'), ylabel('Strouhal Number, St')
hold off
figure

%----------------------------- REYNOLDS NUMBER ----------------------------

% Reynolds number using test velocity and mean chord
Re_U = rho*c_mean*Utest/mu;

for j = 1:length(f)
    for i = 1:length(Utest)
        % Calculate min and max mean velocities
        V_mean_max(i,j) = max(V_mean(marker_start(j):marker_stop(j),i));
        V_mean_min(i,j) = min(V_mean(marker_start(j):marker_stop(j),i));
        Vmean(i,j) = (V_mean_max(i,j) + V_mean_min(i,j))/2;
        % Calculate Reynolds Numbers
        Re_mean_high(i,j) = rho*c_mean*V_mean_max(i,j)/mu;
        Re_mean_low(i,j) = rho*c_mean*V_mean_min(i,j)/mu;
        Re_mean(i,j) = (Re_mean_high(i,j) + Re_mean_low(i,j))/2;
        Re_root_high(i,j) = rho*c(1)*max(V_root(marker_start(j):...
            marker_stop(j),i))/mu;
        Re_root_low(i,j) = rho*c(1)*min(V_root(marker_start(j):...
            marker_stop(j),i))/mu;
        Re_tip_high(i,j) = rho*c(9)*max(V_tip(marker_start(j):...
            marker_stop(j),i))/mu;
        Re_tip_low(i,j) = rho*c(9)*min(V_tip(marker_start(j):...
            marker_stop(j),i))/mu;
    end
end

% Plot Re range for each for various U velocities
subplot(1,3,1);
plot(f,Re_mean_low(1,:),'k:',f,Re_mean_high(1,:),'k--',...
        f,Re_root_low(1,:),'r:',f,Re_root_high(1,:),'r--',...
        f,Re_tip_low(1,:),'b:',f,Re_tip_high(1,:),'b--');
xlabel('Flapping Frequency, Hz');
ylabel('Reynolds Number');
```

```
title('U = 2 m/s');
if bird == 'T'
   axis([f(end) f(1) 0 3e5]);
else
   axis([f(1) f(end) 0 3e5]);
end

subplot(1,3,2);
plot(f,Re_mean_low(4,:),'k:',f,Re_mean_high(4,:),'k--',...
      f,Re_root_low(4,:),'r:',f,Re_root_high(4,:),'r--',...
      f,Re_tip_low(4,:),'b:',f,Re_tip_high(4,:),'b--');
xlabel('Flapping Frequency, Hz');
ylabel('Reynolds Number');
title('U = 5 m/s');
if bird == 'T'
   axis([f(end) f(1) 0 3e5]);
else
   axis([f(1) f(end) 0 3e5]);
end

subplot(1,3,3);
plot(f,Re_mean_low(7,:),'k:',f,Re_mean_high(7,:),'k--',...
      f,Re_root_low(7,:),'r:',f,Re_root_high(7,:),'r--',...
      f,Re_tip_low(7,:),'b:',f,Re_tip_high(7,:),'b--');
xlabel('Flapping Frequency, Hz');
ylabel('Reynolds Number');
title('U = 8 m/s');
if bird == 'T'
   axis([f(end) f(1) 0 3e5]);
else
   axis([f(1) f(end) 0 3e5]);
end
legend('Mean: Low Boundary','Mean: High Boundary','Root: Low Boundary',...
   'Root: High Boundary','Tip: Low Boundary','Tip: High Boundary');
figure

%--------------------------- REDUCED FREQUENCY --------------------------

w = 2*pi*f; % angular velocity at frequency f

% Calculate mean, root and tip reduced frequency bounds
for j = 1:length(f)
   for i = 1:length(Utest)
      % Calculate Reynolds Number
      k_mean_low(i,j) = w(j)*c_mean/(max(V_mean(marker_start(j):...
         marker_stop(j),i))*2);
      k_mean_high(i,j) = w(j)*c_mean/(min(V_mean(marker_start(j):...
         marker_stop(j),i))*2);
      k_root_low(i,j) = w(j)*c(1)/(max(V_root(marker_start(j):...
         marker_stop(j),i))*2);
      k_root_high(i,j) = w(j)*c(1)/(min(V_root(marker_start(j):...
         marker_stop(j),i))*2);
      k_tip_low(i,j) = w(j)*c(9)/(max(V_tip(marker_start(j):...
         marker_stop(j),i))*2);
      k_tip_high(i,j) = w(j)*c(9)/(min(V_tip(marker_start(j):...
```

```
            marker_stop(j),i))*2);
    end
end

% Plot Re range for each for various U velocities
subplot(1,3,1);
plot(f,k_mean_low(1,:),'k:',f,k_mean_high(1,:),'k--',...
        f,k_root_low(1,:),'r:',f,k_root_high(1,:),'r--',...
        f,k_tip_low(1,:),'b:',f,k_tip_high(1,:),'b--');
xlabel('Flapping Frequency, Hz');
ylabel('Reduced Frequency');
title('U = 2 m/s');
if bird == 'T'
    axis([f(end) f(1) 0 2]);
else
    axis([f(1) f(end) 0 2]);
end

subplot(1,3,2);
plot(f,k_mean_low(4,:),'k:',f,k_mean_high(4,:),'k--',...
        f,k_root_low(4,:),'r:',f,k_root_high(4,:),'r--',...
        f,k_tip_low(4,:),'b:',f,k_tip_high(4,:),'b--');
xlabel('Flapping Frequency, Hz');
ylabel('Reduced Frequency');
title('U = 5 m/s');
if bird == 'T'
    axis([f(end) f(1) 0 2]);
else
    axis([f(1) f(end) 0 2]);
end

subplot(1,3,3);
plot(f,k_mean_low(7,:),'k:',f,k_mean_high(7,:),'k--',...
        f,k_root_low(7,:),'r:',f,k_root_high(7,:),'r--',...
        f,k_tip_low(7,:),'b:',f,k_tip_high(7,:),'b--');
xlabel('Flapping Frequency, Hz');
ylabel('Reduced Frequency');
title('U = 8 m/s');
if bird == 'T'
    axis([f(end) f(1) 0 2]);
else
    axis([f(1) f(end) 0 2]);
end
legend('Mean: Low Boundary','Mean: High Boundary','Root: Low Boundary',...
    'Root: High Boundary','Tip: Low Boundary','Tip: High Boundary');
figure

%-------------------- PARASITE & INDUCED DRAG & POWER ---------------------

% Induced drag estimation
Di_mean = 2*(weight*cos(gamma))^2./(rho*(Vmean.^2)*pi*e*B^2);
Di_U = 2*(weight*cos(gamma))^2./(rho*(Utest.^2)*pi*e*B^2);

% Flat plate parasite drag coefficient
Cf_fp_mean = 0.455*(log10(Re_mean)).^-2.58;
```

```
Cf_fp_U = 0.455*(log10(Re_U)).^-2.58;

% Bird parasite drag coefficient
CDp_mean = K*Cf_fp_mean;
CDp_U = K*Cf_fp_U;

% Parasite drag
Dp_mean = rho*(Vmean.^2)*Sw.*CDp_mean/2;
Dp_U = rho*(Utest.^2)*Sw.*CDp_U/2;

% Total Drag
D_mean = Di_mean + Dp_mean;
D_U = Di_U + Dp_U;

% Plot the drag
plot(Utest,Di_U,'r-.',Utest,Dp_U,'b-.',Utest,D_U,'k-.');
hold on
for j = 1:length(f)
   plot(Utest,Di_mean(:,j),'r:',Utest,Dp_mean,'b--',Utest,D_mean,'k');
end
legend('Induced Drag, U_r_e_f = U','Parasite Drag, U_r_e_f = U',...
        'Total Drag, U_r_e_f = U','Induced Drag, U_r_e_f = V_m_e_a_n',...
        'Parasite Drag, U_r_e_f = V_m_e_a_n');
title('Blue Ornithopter: Drag Curves')
xlabel('Flight Velocity U, m/s'), ylabel('Drag, N')
hold off
figure

% Compute the mean power requirements
Pi_mean = Di_mean.*Vmean;
Pp_mean = Dp_mean.*Vmean;
Pi_U = Di_U.*Utest;
Pp_U = Dp_U.*Utest;
P_U = Pi_U + Pp_U;
Ptot_mean = Pi_mean + Pp_mean;

% Plot the power curves
plot(Utest,Pi_U,'r-.',Utest,Pp_U,'b-.',Utest,P_U,'k-.');
hold on
for j = 1:length(f)
   plot(Utest,Pi_mean(:,j),'r:',Utest,Pp_mean,'b--',Utest,Ptot_mean,'k');
   hold on
end
legend('Induced Power, U_r_e_f = U','Parasite Power, U_r_e_f = U',...
        'Total Power, U_r_e_f = U','Induced Power, U_r_e_f = V_m_e_a_n',...
        'Parasite Power, U_r_e_f = V_m_e_a_n');
title('White Ornithopter: Power Curves')
xlabel('Flight Velocity U, m/s'), ylabel('Power Required, Watts')
hold off

%------------------- INDUCED VELOCITIES: Momentum Theory ------------------

% Equivalent actuator disk area
Ae = R^2*stroke_amp*cos(gamma);
```

```
% Induced velocity from momentum theory using weight, drag
u_theory = (D_U+weight*sin(gamma))./(2*rho*Ae*Utest*e);
v_theory = (weight*cos(gamma))./(2*rho*Ae*Utest*e);

% Initialize u,v matrices
u = zeros(rows,n_blades);
v = zeros(rows,n_blades);
q = normalize_z(beta_dot(start:stop),length(time(start:stop)));

question = input('Would method of induced velocities is used (1 or 2?) ');
for j = 1:n_blades
   if question == 1
      g = find(Utest==U);
      u(start:stop,j) = u_theory(g);
      v(start:stop,j) = v_theory(g)*q;
   elseif question == 2
      % Induced velocities from momentum theory using measured force values
      u(:,j) = sign(axial_interp).*(abs(axial_interp)/(2*rho*Ae)).^(1/2);
      v(:,j) = sign(normal_interp).*(abs(normal_interp)/(2*rho*Ae)).^(1/2);
   end
end

% Plot momentum theory induced velocity results
plot(Utest,u_theory,'b--',Utest,v_theory,'r:');
legend('u = horizontal','v = vertical');
xlabel('Flight Speed U, m/s'); ylabel('Induced Velocity, m/s');
title('Induced Velocity from Method 1: Steady Flight Condition');
figure

if bird == 'T'
   T = (time(marker_start(4):marker_stop(4))-time(marker_start(4)))/...
      (time(marker_stop(4))-time(marker_start(4)));
   plot(T,u(marker_start(4):marker_stop(4)),'b--',T,...
      v(marker_start(4):marker_stop(4)),'r:');
   title('Blue Ornithopter: Induced Velocity Method 2');
else
   T = (time(marker_start(9):marker_stop(9))-time(marker_start(9)))/...
      (time(marker_stop(9))-time(marker_start(9)));
   plot(T,u(marker_start(9):marker_stop(9)),'b--',T,...
      v(marker_start(9):marker_stop(9)),'r:');
   title('White Ornithopter: Induced Velocity Method 2');
end
xlabel('t/T for One Flapping Period at 4.5Hz to 5Hz')
ylabel('Induced Velocity, m/s')
legend('u = horizontal','v = vertical')


%
%                END OF PARAMETER ANALYSIS
%
%
%                BEGIN AERO MODEL ANALYSIS
%
%
```

```
%
%%%------------------------ VELOCITY and AOA ------------------------------


% Point of pitch rotation, 1/4 chord for luff region, LE for flap region
a = [-.5 -.5 -.5 -.5 -.5 -.5 -.5 -.5 -1 -1 -1 -1];

Vblade = zeros(rows,n_blades); % Blade velocity vertical to flapping axis
Hblade = zeros(rows,n_blades); % Blade velocity horizontal to flapping axis
Vtot = zeros(rows,n_blades);   % Total velocity vertical to flapping axis
Htot = zeros(rows,n_blades);   % Total velocity horizontal to flapping axis
Vrel = zeros(rows,n_blades);

% Vertical and axial velocities of blade element center points
for j = 1:n_blades
   % Leading edge blade elements, one through nine
   if 1 <= j <= 9
      Vblade(:,j) = U*sin(gamma) - r(j)*beta_dot(:,j).*cos(beta(:,j))...
         + theta_dot(:,j).*(-a(j)*b(:,j) + b(:,j)).*cos(theta(:,j))...
         .*cos(beta(:,j));
      Hblade(:,j) = U*cos(gamma) + theta_dot(:,j).*(-a(j)*b(:,j) + ...
         b(:,j)).*sin(theta(:,j));
   % Blade element ten
   elseif j == 10
      Vblade(:,j) = U*sin(mean(theta(:,1:3),2)) - r(j)*beta_dot(:,j)...
         .*cos(beta(:,j)) + theta_dot(:,j).*(-a(j)*b(:,j) + ...
         b(:,j)).*cos(theta(:,j)).*cos(beta(:,j));
      Hblade(:,j) = U*cos(mean(theta(:,1:3),2)) +  theta_dot(:,j).*...
         (-a(j)*b(:,j) + b(:,j)).*sin(theta(:,j));
   % Blade element eleven
   elseif j == 11
      Vblade(:,j) = U*sin(mean(theta(:,3:6),2)) - r(j)*beta_dot(:,j)...
         .*cos(beta(:,j)) + theta_dot(:,j).*(-a(j)*b(:,j) + ...
         b(:,j)).*cos(theta(:,j)).*cos(beta(:,j));
      Hblade(:,j) = U*cos(mean(theta(:,3:6),2)) +  theta_dot(:,j).*...
         (-a(j)*b(:,j) + b(:,j)).*sin(theta(:,j));
   % Blade element twelve
   elseif j==12
      Vblade(:,j) = U*sin(mean(theta(:,6:8),2)) - r(j)*beta_dot(:,j)...
         .*cos(beta(:,j)) + theta_dot(:,j).*(-a(j)*b(:,j) + ...
         b(:,j)).*cos(theta(:,j)).*cos(beta(:,j));
      Hblade(:,j) = U*cos(mean(theta(:,6:8),2)) +  theta_dot(:,j).*...
         (-a(j)*b(:,j) + b(:,j)).*sin(theta(:,j));
   end
   Vtot(:,j) = Vblade(:,j) + u(:,j)*sin(gamma+delta) - ...
      v(:,j)*cos(gamma+delta);
   Htot(:,j) = Hblade(:,j) + u(:,j)*cos(gamma+delta) + ...
      v(:,j)*sin(gamma+delta);
   Vrel(:,j) = (Vtot(:,j).^2 + Htot(:,j).^2).^(1/2);
end

% Estimate a_o based on membrane theory for luff region
a_o = zeros(rows,n_blades);
for j = 1:8
   a_o(:,j) = -0.636*sqrt(epsilon(:,j))/(2*pi).*sign(-beta_dot(:,j));
```

```
end

% Calculate inflow angle phi
phi = atan2(Vtot,Htot);

% Adjust pitch phase slightly (0.02 sec)
for i = 8:rows
   for j = 1:n_blades
         theta_new(i,j) = theta_adj(i-7,j);
   end
end

% Relative angle of attack at 3/4 chord
alpha = zeros(rows,n_blades);
alpha = theta_new - a_o + phi;

 % ---------------- REDUCED FREQUENCY & LIFT DEFICIENCY ------------------

% Calculate local reduced frequency at spanwise locations
for i = 1:n_blades
   if i < 10
      k_act(:,i) = 2*pi*frequency*c(i)./(2*Vrel(:,i));
   elseif i == 10
      k_act(:,i) = mean(k_act(:,1:3),2);
   elseif i == 11
      k_act(:,i) = mean(k_act(:,3:6),2);
   elseif i == 12
      k_act(:,i) = mean(k_act(:,6:8),2);
   end
end

% Determine Theodorsen lift deficiency function values @ k
load theodorsen.mat
for m = 1:n_blades
   for n = 1:length(time)
   Ck_real_interp(n,m) = interp1(k,Ck_real,k_act(n,m));
   Ck_imag_interp(n,m) = interp1(k,Ck_imag,k_act(n,m));
   Ck_mag(n,m) = sqrt(Ck_real_interp(n,m)^2 + Ck_imag_interp(n,m)^2);
   Ck_phase(n,m) = atan(Ck_imag_interp(n,m)/Ck_real_interp(n,m));
   end
end

% ------------------------ CIRCULATORY LIFT FORCE ------------------------

% Initialize circulatory lift coefficient matrix
CL_c = zeros(rows,n_blades);

% Quasi-Steady Lift Coeffient with addition of C(k) factor and sail theory
CL_c = 2*pi.*sin(alpha).*Ck_mag + 0.636*sqrt(epsilon);

dL_c = rho*(Vrel.^2)/2.*CL_c.*dc;    % Circulatory lift per unit span dr

% Calculate forces over blade spans
for j = 1:n_blades
```

```
    L_c(:,j) = dL_c(:,j)*dr(j);
end

% -------------------------- NON-CIRCULATORY FORCE -------------------------

% Non-circulatory lift
for j = 1:n_blades
    % Acceleration, 180 degrees opposite stroke angle curve
    accel(:,j) = r(j)*beta_ddot(:,j).*cos(theta(:,j))+theta_dot(:,j).*U ...
        + theta_ddot(:,j).*(-a(j)*b(:,j));
    N_nc(:,j) = pi*rho.*(Cmax(j)^2)/4.*(accel(:,j))*dr(j);
end

% --------------------------- TOTAL LIFT & DRAG ----------------------------

% Break circulation force into horizontal (H) and vertical (V) components
for j = 1:n_blades
    dV_c(:,j) = L_c(:,j).*cos(phi(:,j))*cos(gamma+delta);
    dH_c(:,j) = L_c(:,j).*sin(phi(:,j))*cos(gamma+delta);
    dV_nc(:,j) = N_nc(:,j).*cos(-theta(:,j)).*cos(beta(:,j))...
        *cos(gamma+delta);
    dH_nc(:,j) = N_nc(:,j).*sin(-theta(:,j))*cos(gamma+delta);
end

V_c_luff = sum(dV_c(:,1:8),2)*2;
H_c_luff = sum(dH_c(:,1:8),2)*2;
V_nc_luff = sum(dV_nc(:,1:8),2)*2;
H_nc_luff = sum(dH_nc(:,1:8),2)*2;

V_c_tip = dV_c(:,9)*2;
H_c_tip = dH_c(:,9)*2;
V_nc_tip = (dV_nc(:,9))*2;
H_nc_tip = (dH_nc(:,9))*2;

V_c_flap = sum(dV_c(:,10:12),2)*2;
H_c_flap = sum(dH_c(:,10:12),2)*2;
V_nc_flap = sum(dV_nc(:,10:12),2)*2;
H_nc_flap = sum(dH_nc(:,10:12),2)*2;

% Circulatory and Non-circulatory components
vert_c = V_c_luff + V_c_tip + V_c_flap;
vert_nc = V_nc_luff + V_nc_tip + V_nc_flap;

%------------------------ PARASITE & INDUCED DRAG -------------------------

Vrel_mean = Vrel(:,8)+(c_mean-c(8))*(Vrel(:,9)-Vrel(:,8))/(c(9)-c(8));
Di = 2*(weight*cos(gamma))^2./(rho*(Vrel_mean.^2)*2*S*pi*e*AR);
Re = rho*c_mean*Vrel_mean/mu;
Cf_fp = 0.455*(log10(Re)).^-2.58;
CDp = K*Cf_fp;
Dp = rho*(Vrel_mean.^2)*Sw.*CDp/2;

% Total drag
drag = Di + Dp;
```

```
V_induced = -Di.*sin(mean(phi,2))*cos(gamma+delta);
H_induced = -Di.*cos(mean(phi,2))*cos(gamma+delta);
V_parasite = -Dp.*sin(mean(phi,2))*cos(gamma+delta);
H_parasite = -Dp.*cos(mean(phi,2))*cos(gamma+delta);

%-----------------------------------------------------------------------


vert_drag = V_induced + V_parasite;
horiz_c = H_c_luff + H_c_tip + H_c_flap;
horiz_nc = H_nc_luff + H_nc_tip + H_nc_flap;
horiz_drag = H_induced + H_parasite;

% Add force components, final force values
vert = vert_c + vert_nc + vert_drag;
horiz = horiz_c + horiz_nc + horiz_drag;
```

```
% blades.m - Blade Element Formation for Ornithopter Analysis

function [Bx,By,Bz,dr,dl,pitch_smooth,bend] = blades(bird,n,file,f_high,dt)

% bird = 'T' for blue (Trinity) or 'O' for white (Odyssey)
% n = blade number
% file = the file containing the wing marker locations

load(file)  % load marker locations

% Form blade elements of wing in triangular/LE region
% Calculate blade width dr, length dl, and local stroke angle (bend)

% Blade camber points set by Bx, By, Bz containing the x, y, z coordinates
% for the markers along the camber line. First and last columns of Bx, By,
% Bz are the leading and trailing edge points that set the blade chord

% Blue and white ornithopter have same blade formation for n = 1-4
% other blade elements will be handled individually

if n == 1
   Bx = [LE2(:,1) M11(:,1) M12(:,1) M13(:,1) M14(:,1) ME2(:,1)];
   By = [LE2(:,2) M11(:,2) M12(:,2) M13(:,2) M14(:,2) ME2(:,2)];
   Bz = [LE2(:,3) M11(:,3) M12(:,3) M13(:,3) M14(:,3) ME2(:,3)];
   dr = mean((sum((LE3-LE2).^2,2).^0.5)/2 + (sum((LE2-LE1).^2,2).^0.5)/2);
   dl = (sum((LE2-ME2).^2,2)).^0.5;
   bend = local_stroke(LE1,LE3);
elseif n == 2
   Bx = [LE3(:,1) M21(:,1) M22(:,1) M23(:,1) M24(:,1) ME3(:,1)];
   By = [LE3(:,2) M21(:,2) M22(:,2) M23(:,2) M24(:,2) ME3(:,2)];
   Bz = [LE3(:,3) M21(:,3) M22(:,3) M23(:,3) M24(:,3) ME3(:,3)];
   dr = mean((sum((LE4-LE3).^2,2).^0.5)/2 + (sum((LE3-LE2).^2,2).^0.5)/2);
   dl = (sum((LE3-ME3).^2,2)).^0.5;
   bend = local_stroke(LE2,LE4);
elseif n == 3
   Bx = [LE4(:,1) M31(:,1) M32(:,1) M33(:,1) M34(:,1) ME4(:,1)];
   By = [LE4(:,2) M31(:,2) M32(:,2) M33(:,2) M34(:,2) ME4(:,2)];
   Bz = [LE4(:,3) M31(:,3) M32(:,3) M33(:,3) M34(:,3) ME4(:,3)];
   dr = mean((sum((LE5-LE4).^2,2).^0.5)/2 + (sum((LE4-LE3).^2,2).^0.5)/2);
   dl = (sum((LE4-ME4).^2,2)).^0.5;
   bend = local_stroke(LE3,LE5);
elseif n == 4
   Bx = [LE5(:,1) M41(:,1) M42(:,1) M43(:,1) M44(:,1) ME5(:,1)];
   By = [LE5(:,2) M41(:,2) M42(:,2) M43(:,2) M44(:,2) ME5(:,2)];
   Bz = [LE5(:,3) M41(:,3) M42(:,3) M43(:,3) M44(:,3) ME5(:,3)];
   dr = mean((sum((LE6-LE5).^2,2).^0.5)/2 + (sum((LE5-LE4).^2,2).^0.5)/2);
   dl = (sum((LE5-ME5).^2,2)).^0.5;
   bend = local_stroke(LE4,LE6);
elseif n == 5
   if bird == 'T'
      Bx = [LE6(:,1) M51(:,1) M52(:,1) M53(:,1) ME6(:,1)];
      By = [LE6(:,2) M51(:,2) M52(:,2) M53(:,2) ME6(:,2)];
      Bz = [LE6(:,3) M51(:,3) M52(:,3) M53(:,3) ME6(:,3)];
   elseif bird == 'O'
```

```
        Bx = [LE6(:,1) M51(:,1) M52(:,1) M53(:,1) M54(:,1) ME6(:,1)];
        By = [LE6(:,2) M51(:,2) M52(:,2) M53(:,2) M54(:,2) ME6(:,2)];
        Bz = [LE6(:,3) M51(:,3) M52(:,3) M53(:,3) M54(:,3) ME6(:,3)];
    end
    dr = mean((sum((LE7-LE6).^2,2).^0.5)/2 + (sum((LE6-LE5).^2,2).^0.5)/2);
    dl = (sum((LE6-ME6).^2,2)).^0.5;
    bend = local_stroke(LE5,LE7);
elseif n == 6
    if bird == 'T'
        Bx = [LE7(:,1) M61(:,1) M62(:,1) M63(:,1) ME7(:,1)];
        By = [LE7(:,2) M61(:,2) M62(:,2) M63(:,2) ME7(:,2)];
        Bz = [LE7(:,3) M61(:,3) M62(:,3) M63(:,3) ME7(:,3)];
    elseif bird == 'O'
        Bx = [LE7(:,1) M61(:,1) M62(:,1) M63(:,1) M64(:,1) ME7(:,1)];
        By = [LE7(:,2) M61(:,2) M62(:,2) M63(:,2) M64(:,2) ME7(:,2)];
        Bz = [LE7(:,3) M61(:,3) M62(:,3) M63(:,3) M64(:,3) ME7(:,3)];
    end
    dr = mean((sum((LE8-LE7).^2,2).^0.5)/2 + (sum((LE7-LE6).^2,2).^0.5)/2);
    dl = (sum((LE7-ME7).^2,2)).^0.5;
    bend = local_stroke(LE6,LE8);
elseif n == 7
    if bird == 'T'
        Bx = [LE8(:,1) M71(:,1) M72(:,1) M73(:,1) ME8(:,1)];
        By = [LE8(:,2) M71(:,2) M72(:,2) M73(:,2) ME8(:,2)];
        Bz = [LE8(:,3) M71(:,3) M72(:,3) M73(:,3) ME8(:,3)];
    elseif bird == 'O'
        Bx = [LE8(:,1) M71(:,1) M72(:,1) M73(:,1) M73(:,1) ME8(:,1)];
        By = [LE8(:,2) M71(:,2) M72(:,2) M73(:,2) M73(:,2) ME8(:,2)];
        Bz = [LE8(:,3) M71(:,3) M72(:,3) M73(:,3) M73(:,3) ME8(:,3)];
    end
    dr = mean((sum((LE9-LE8).^2,2).^0.5)/2 + (sum((LE8-LE7).^2,2).^0.5)/2);
    dl = (sum((LE8-ME8).^2,2)).^0.5;
    bend = local_stroke(LE7,LE9);
elseif n == 8
    if bird == 'T'
        Bx = [LE9(:,1) M81(:,1) M82(:,1) ME9(:,1)];
        By = [LE9(:,2) M81(:,2) M82(:,2) ME9(:,2)];
        Bz = [LE9(:,3) M81(:,3) M82(:,3) ME9(:,3)];
    elseif bird == 'O'
        Bx = [LE9(:,1) M81(:,1) M82(:,1) M83(:,1) ME9(:,1)];
        By = [LE9(:,2) M81(:,2) M82(:,2) M83(:,2) ME9(:,2)];
        Bz = [LE9(:,3) M81(:,3) M82(:,3) M83(:,3) ME9(:,3)];
    end
    dr = mean((sum((LE10-LE9).^2,2).^0.5) + (sum((LE9-LE8).^2,2).^0.5)/2);
    dl = (sum((LE9-ME9).^2,2)).^0.5;
    bend = local_stroke(LE8,LE10);
elseif n == 9
    if bird == 'T'
        Bx = [LE12(:,1) TE13(:,1)];
        By = [LE12(:,2) TE13(:,2)];
        Bz = [LE12(:,3) TE13(:,3)];
        dr = mean(2*(sum((LE13-LE11).^2,2).^0.5));
        dl = (sum((LE12-TE13).^2,2)).^0.5;
        bend = local_stroke(LE10,LE13);
    elseif bird == 'O'
        Bx = [LE14(:,1) F33(:,1)];
```

```
        By = [LE14(:,2) F33(:,2)];
        Bz = [LE14(:,3) F33(:,3)];
        dr = mean(2*(sum((LE14-LE11).^2,2).^0.5));
        dl = (sum((LE14-F33).^2,2)).^0.5;
        bend = local_stroke(LE11,LE14);
    end
end

% Perform simple linear interpolation on some points for rear flap
% Form rear blades with just LE and TE points, find pitch & yaw
if n == 10
    if bird == 'T'
        mid = (ME2+ME3)/2;
        Bx = [mid(:,1) TE3(:,1)];
        By = [mid(:,2) TE3(:,2)];
        Bz = [mid(:,3) TE3(:,3)];
        dr = mean((sum((ME4-ME1).^2,2).^0.5 + sum((TE5-TE1).^2,2).^0.5)/2);
        dl = min((sum((mid-TE3).^2,2)).^0.5,51);
        bend = local_stroke(ME1,ME4);
    elseif bird == 'O'
        Bx = [ME3(:,1) TE3(:,1)];
        By = [ME3(:,2) TE3(:,2)];
        Bz = [ME3(:,3) TE3(:,3)];
        dr = mean((sum((ME5-ME1).^2,2).^0.5 + sum((TE5-TE1).^2,2).^0.5)/2);
        dl = min((sum((ME3-TE3).^2,2)).^0.5,51);
        bend = local_stroke(ME1,ME5);
    end
elseif n == 11
    if bird == 'T'
        mid = (ME5+ME6)/2;
        Bx = [mid(:,1) TE7(:,1)];
        By = [mid(:,2) TE7(:,2)];
        Bz = [mid(:,3) TE7(:,3)];
        dr = mean((sum((ME7-ME4).^2,2).^0.5 + sum((TE9-TE5).^2,2).^0.5)/2);
        dl = min((sum((mid-TE7).^2,2)).^0.5,100);
        bend = local_stroke(ME4,ME7);
    elseif bird == 'O'
        mid = (ME6+ME7)/2;
        Bx = [mid(:,1) TE7(:,1)];
        By = [mid(:,2) TE7(:,2)];
        Bz = [mid(:,3) TE7(:,3)];
        dr = mean((sum((ME8-ME5).^2,2).^0.5 + sum((TE9-TE5).^2,2).^0.5)/2);
        dl = min((sum((mid-TE7).^2,2)).^0.5,100);
        bend = local_stroke(ME5,ME8);
    end
elseif n == 12
    if bird == 'T'
        mid = ME8 + (ME9-ME8)*2/3;
        Bx = [mid(:,1) TE11(:,1)];
        By = [mid(:,2) TE11(:,2)];
        Bz = [mid(:,3) TE11(:,3)];
        dr = mean((sum((ME10-ME7).^2,2).^0.5 + sum((TE13-TE9).^2,2).^0.5)/2);
        dl = min((sum((mid-TE11).^2,2)).^0.5,152);
        bend = local_stroke(ME7,ME10);
    elseif bird == 'O'
        Bx = [ME9(:,1) TE11(:,1)];
```

```
        By = [ME9(:,2) TE11(:,2)];
        Bz = [ME9(:,3) TE11(:,3)];
        dr = mean((sum((ME10-ME8).^2,2).^0.5 + sum((TE13-TE9).^2,2).^0.5)/2);
        dl = min((sum((ME9-TE11).^2,2)).^0.5,152);
        bend = local_stroke(ME8,ME10);
    end
end

[m,n] = size(Bx); % size of each matrix

% Calculate difference between X & Z at LE and TE of blade element
Zdiff = Bz(:,1)-Bz(:,n);  % positive if pitch up, negative if pitch down
Xdiff = Bx(:,1)-Bx(:,n);  % negative always if taking LE - TE
% Calculate blade pitch wrt flapping axis
pitch = atan(-Zdiff./Xdiff);
[pitch_smooth,H,f,h,t] = hsmoo(pitch,f_high,dt);
```

```
% Take derivative in time using Adams-Bashforth 3 for central points, and
% Euler-Explicit or Adams-Bashforth 2 near boundaries

function Dsmooth = take_deriv(t,x,f_high,dt)

% Take the derivative of x with respect to t, where x can be multiple
% columns of data whose derivatives will be averaged across rows to give
% one mean derviative value.

% Determine number of rows or iterations for derivative
rows = length(t);

D = zeros(rows,1);  % Initialize results vector

% First and last time step using Euler Explicit approximation
D(1) = mean(((x(2,:)-x(1,:))/(t(2)-t(1))),2);
D(rows) = mean(((x(rows,:)-x(rows-1,:))/(t(rows)-t(rows-1))),2);

% Second time step using AB2
D(2) = mean((((x(3,:)-x(2,:))*2/(t(3)-t(2))+D(1))/3),2);

% Remaining time steps using AB3
for k = 3:rows-1
    D(k) = mean((((x(k+1,:)-x(k,:))*12/(t(k+1)-t(k)) + ...
        16*D(k-1) - 5*D(k-2))/23),2);
end

[Dsmooth,H,f,h,t] = hsmoo(D,f_high,dt);
```

Bibliography

1. PBS, April 2008, http://www.pbs.org/wgbh/nova/spiesfly/uavs.html
2. NASA Report: " A Report Overview of the Civil UAV Capability Assesment."
3. Mueller, T.J., *Fixed and Flapping Wing Aerodynamics for Micro Air Vehicle Applications*. Reston, VA: AIAA, 2001.
4. Grauer, J., and Hubbard Jr., J.E. "Development of a Sensor Suite for a Flapping-Wing UAV Platform," AIAA Paper No. 2008-224, 46th AIAA Aerospace Sciences Meeting and Exhibit, Reno, NV January 7-10, 2008.
5. Hein, B., Chopra, I., "Hover Performance of Micro Air Vehicles: Rotors at Low Re," *American Helicopter Society International Specialists Meeting on Unmanned Rotorcraft*, Chandler, AZ, January 2005.
6. Bohorquez, F., Pines, D., "Rotor and Airfoil Design for Efficient Rotary Wing Micro Air Vehicles," *61st Annual American Helicopter Society Forum*, Grapevine, TX, June 2005.
7. Ornithopter Zone, Aprill 2008, www.ornithopter.org
8. Videler, J.V., *Avian Flight*. Oxford University Press, New York City, NY, 2005.
9. Shyy, W., Lian, Y., Tang, J., Viieru, D., Liu, H., *Aerodynamics of Low Reynolds Number Flyers*. Cambridge University Press, New York, NY, 2008.
10. Azuma, A. *The Biokinetics of Flying and Swimming (2nd Ed)*. Reston, VA: American Institute of Aeronautics and Astronautics.
11. Ward-Smith, A.J., *Biophysical Aerodynamics and the Natural Environment*. John Wiley & Sons, New York, 1984.

12. Dr. James E. Hubbard Jr., Morpheus Laboratory Director, National Institute of Aerospace, 100 Exploration Way, Hampton, VA, 23666. Ph: 757-325-6830.
13. Anders, J.B., "Biomimetic Flow Control," AIAA Paper No. 2000-2543, Fluids 2000 Conference and Exhibit, Denver, CO June 19-22, 2000.
14. Shyy, W., Berg, M., and Ljungqvist, D., "Flapping and flexible wings for biological and micro air vehicles," *Progress in Aerospace Sciences*, Vol. 35, 1999, pp. 455-505.
15. Lian, Y., Shyy, W., Viieru, D., Zhang, B., "Membrane wing aerodynamics for micro air vehicles," *Progress in Aerospace Sciences*, Vol. 39, 2003, pp. 425-465.
16. Smith, M.J.C., Wilkin P.J., Williams, M.H., "The advantages of an unsteady panel method in modeling the aerodynamic forces on rigid flapping wings," *The Journal of Experimental Biology*, Vol. 199, 1996, pp. 1073-1083.
17. DeLaurier, J.D., "An aerodynamic model for flapping wing flight," *The Aeronautical Journal of the Royal Aeronautical Society*, April 1993, pp. 125-130.
18. Singh, B., and Chopra, I., "Dynamics of Insect-Based Flapping Wings: Loads Validation," AIAA Paper No. 2006-1663, 14th AIAA Adapative Structures Conference, Newport, Rhode Island, May 1-4, 2006.
19. Betteridge, D.S., Archer, R.D., " A Study of the Mechanics of Flapping Wings," *Aeronaut Quarterly*, May 1974, pp. 129-142.
20. Theodorsen, T., "General Theory of Aerodynamic Instability and the Mechanism of Flutter," NACA Report No 496, 1949.
21. Garrick, I.E. "Propulsion of a Flapping and Oscillating Airfoil," NACA Report No 567, 1936.

22. Phlips P.J., East R.A., Pratt N.H., “An unsteady lifting-line theory of flapping wings with application to the forward flight of birds,” *Journal of Fluid Mechanics*, Vol. 112, 1981, pp. 97-125.

23. Rayner, J.M. ”A vortex theory of animal flight. Part 2: The forward flight of birds,” *Journal of Fluid Mechanics*, Vol 91, No. 4, 1978, pp 731-763.

24. Lighthill, Sir James, “Some Challenging new applications for basic mathematical methods in the mechanics of fluids that were originally pursued with aeronautical aims,” *Aeronautical Journal*, Vol. 94, Feb. 1990, pp. 41-52.

25. Azuma, A., Okamoto, M., “Theoretical study on two dimensional aerodynamic characteristics of unsteady wings,” *Journal of Theoretical Biology*, Vol. 234, 2005, pp. 67-78.

26. Gray, K. Finaish, F., ”Unsteady Separated Flowfields Surrounding a Flapping Airfoil: Applications to Micro-Air Vehicles,” AIAA Paper No. 2000-3924, 18th AIAA Applied Aerodynamics Conference, Denver, CO, August 14-17, 2000.

27. Thwaites, B., “The Aerodynamic Theory of Sails I: Two-Dimensional Sails,” *Proceedings of the Royal Society of London. Series A, Mathematical and Physical Sciences*, Vol. 261, No. 1306, May 1961, pp. 402-422.

28. Newman, B.G., “Aerodynamic theory for membranes and sails,” *Progress in Aerospace Science*, Vol. 24, pp. 1-27, 1987.

29. Jones, K.D., Castro, B.M., Mahmoud, O., Pollard, S.J. and Platzer, M.F., “A Collaborative Numerical and Experimental Investigation of Flapping-Wing Propulsion,” 40th AIAA Aerospace Sciences Meeting and Exhibit, Reno, NV January 14-17, 2002.

30. Neef, M.F., and Hummel, D., "Euler Solutions for a Finite-Span Flapping Wing," Conference on fixed, flapping and rotary wing vehicles at very low Reynolds numbers, University of Notre Dame, IN, June 5-7, 2000.
31. Vest, M.S., and Katz, J., "Unsteady Aerodynamic Model of Flapping Wings," *AIAA Journal*, Vol. 34, No. 7, July 1996.
32. Vest, M.S., and Katz, J., "Aerodynamic Study of a Flapping Wing Micro-UAV," 37th AIAA Aerospace Sciences Meeting and Exhibit, Reno, NV January 11-14, 1999.
33. Lian, Y., OL, M.V., and Shyy, W., "Comparative Study of Pitch-Plunge Airfoil Aerodynamics at Transitional Reynolds Number," AIAA Paper No. 2008-652, 46th AIAA Aerospace Sciences Meeting and Exhibit, Reno, NV January 7-10, 2008.
34. Willis, D.J., Persson, P., Israeli, E.R., Peraire, J., Swartz, S.M., and Breuer, K.S., "Multifidelity Approaches for the Computational Analysis and Design of Effective Flapping Wing Vehicles," AIAA Paper No. 2008-518, 46th AIAA Aerospace Sciences Meeting and Exhibit, Reno, NV January 7-10, 2008.
35. Smith R. and Shyy W., "A viscous flow based membrane wing model," AIAA Paper No. 93-2955, 24th AIAA Fluid Dynamics Conference, Orlando, FL July 6-9, 1993.
36. Smith R. and Shyy W., "Coupled computations of a flexible membrane wing and unsteady viscous flow," AIAA Paper No. 95-2261, 26th AIAA Fluid Dynamics Conference, San Diego, CA June 19-22, 1995.

37. Smith R. and Wright J.A., "Simulation of the viscous aeroelastic response of a membrane airfoil to a harmonically varying freestream," AIAA Paper No. 2001-857, 39th AIAA Aerospace Sciences Meeting and Exhibit, Reno, NV January 8-11, 2008.
38. Vanden-Broeck, J.M., "Nonlinear Two-Dimensional Sail Theory," *Physics of Fluids*, Vol. 25, No. 3, March 1982.
39. de Matteis, G., and de Socio, L, "Nonlinear Aerodynamics of a Two-Dimensional Membrane Airfoil with Separation," *Journal of Aircraft*, Vol. 23, No. 11, November, 1986.
40. DeLaurier, J.D., "The Development of an Efficient Ornithopter Wing," *Aeronautical Journal*, May 1993, pp. 153-162.
41. DeLaurier, J.D., "A Study of Mechanical Flapping-Wing Flight," *Aeronautical Journal*, October 1993, pp. 277- 286.
42. Raney, D.L., and Slominski, E.C., "Mechanization and Control Concepts for Biologically Inspired Micro Air Vehicles," *Journal of Aircraft*, Vol. 41, No.6, 2004, pp. 1257-1265.
43. Malolan, V., Dineshkumar, M., and Baskar, V., "Design and Development of Flapping Wing Micro Air Vehicle," AIAA Paper No. 2004-40, 42th AIAA Aerospace Sciences Meeting and Exhibit, Reno, NV January 5-8, 2004.
44. Muniappan, A., Baskar, V., Duriyanandhan, V., "Lift and Thrust Characterization of Flapping Wing Micro Air Vehicle," AIAA Paper No. 2005-1055, 43rd AIAA Aerospace Sciences Meeting and Exhibit, Reno, NV January 10-13, 2005.

45. Aditya, K., and Malolan, V., "Investigation of Strouhal Number Effect on Flapping Wing Micro Air Vehicle," AIAA Paper No. 2007-486, 45th AIAA Aerospace Sciences Meeting and Exhibit, Reno, NV January 8-11, 2007.
46. Unger, R., Haupt, M.C., Horst, P., and Windte, J., "Structural Design and Aeroelastic Analysis of an Oscillating Airfoil for Flapping Wing Propulsion," AIAA Paper No. 2008-306, 46th AIAA Aerospace Sciences Meeting and Exhibit, Reno, NV January 7-10, 2008.
47. DeLuca, A.M., Reeder, M.F., OL, M.V., Freeman, J., Bautista I., and Simonich, M., "Experimental Investigation into the Aerodynamic Properties of a Flexible and Rigid Wing Micro Air Vehicle," AIAA Paper No. 2004-2396, 24th AIAA Aerodynamic Measurement Technology and Ground Testing Conference, Portland, OR, June 28 – July 1, 2004.
48. Tamai M., Murphy J.T., Hu H., "An experimental study of flexible membrane airfoils at low Reynolds numbers," AIAA Paper No. 2008-580, 48th AIAA Aerospace Sciences Meeting and Exhibit, Reno, NV January 7-10, 2008.
49. Rojratsirikul, P., Wang, Z., and Gursul, I., "Unsteady Aerodynamics of Membrane Airfoils," AIAA Paper No. 2008-613, 46th AIAA Aerospace Sciences Meeting and Exhibit, Reno, NV January 7-10, 2008.
50. Song A., Ziaodong T., Israeli E., Galvao R., Bishop K., Swartz S., and Breuer K., "The aero-mechanics of low aspect ratio compliant membrane wings, with applications to animal flight," AIAA Paper No. 2008-517, 48th AIAA Aerospace Sciences Meeting and Exhibit, Reno, NV January 7-10, 2008.

51. Abdulrahim, M., Garcia, H., Ivey, G.F., and Lind, R., "Flight Testing a Micro Air Vehicle Using Morphing For Aeroservoelastic Control," AIAA Paper No. 2004-1674, 45th AIAA Structures, Structural Dynamics & Materials Conference, Palm Springs, CA, April 19-22, 2004.
52. Withers, P.C., "An Aerodynamic Analysis of Bird Wings as Fixed Aerofoils," *Journal of Experimental Biology*, Vol. 90, 1981, pp. 143-162.
53. Liu, T., Kuykendoll, K., Rhew, R., and Jones, S., "Avian Wing Geometry and Kinematics," *AIAA Journal*, Vol. 44, No. 5, May 2006, pp. 954-963.
54. Tucker, V.A., "Gliding Birds: Reduction of Induced Drag by Wing Tip Slots Between the Primary Feathers," *Journal of Experimental Biology*, Vol. 180, 1993, pp. 285-310.
55. Tian, X., Iriarte, J., Middleton, K., Galvao, R., Israeli, E., Roemer, A., Sullivan, A., Song, A., Swartz, S., and Breuer, K., "Direct Measurements of the Kinematics and Dynamics of Bat Flight," 36th AIAA Fluid Dynamics Conference, San Francisco, CA, June 5-8, 2006.
56. Warrick, D.R., and Dial, K.P., "Kinematic, Aerodynamic and Anatomical Mechanisms in the Slow Maneuvering Flight of Pigeons," *The Journal of Experimental Biology*, Vol. 201, 1998, pg. 655-672.
57. Norberg, U.M. and Rayner, J.M.V., "Ecological Morphology and Flight in Bats," *Philosophical Transactions of the Royal Society of London. Series B, Biological Sciences*, Vol. 316, No. 1179, September 16, 1987, pp. 335-427.

58. Taylor, G.K., Nudds, R.L., and Thomas, A.L.R., "Flying and swimming animals cruise at a Strouhal number tuned for high power efficiency," *Nature*, Vol. 425, October 16, 2003, pp. 707-711.
59. Pennycuick, C.J., "Mechanics of Flight", *Avian Biology*, ed. D.S. Farner & J.R. King. London: Academic Press. 1975, .vol. 5, pp. 1-75.
60. Pennycuick, C.J., "Towards an optimal strategy for bird flight research," *Journal of Avian Biology*, Vol. 29, No. 4, 1998, pp. 449-457.
61. Tucker, V.A., and Parrott, G.C., "Aerodynamics of Gliding Flight in a Falcon and Other Birds," *Journal of Experimental Biology*, 1970, Vol. 52, pp. 345-367.
62. Spedding, G.R., "The Wake of a Kestrel in Flapping Flight", *Journal of Experimental Biology*, 1987, Vol. 127, pp. 59-78.
63. Lighthill, M.J. "Aerodynamic aspects of animal flight", in *Flying and Swimming in Nature*, ed. T.Y.T. Wu, C.J. Brokaw & C. Brennan, vol. 2, pp. 423-491. New York: Plenum Press, 1975.
64. Anderson Jr., J.D. *Fundamentals of Aerodynamics (3rd Ed)*. Boston, MA: McGraw Hill, 2001.
65. Kuethe, A.M., and Chow, C.Y., *Foundations of Aerodynamics: Bases of Aerodynamic Design (4th Ed.)*. New York: John Wiley and Sons, 1986.
66. DeLaurier, J.D., "Drag of wings with cambered airfoils and partial leading-edge suction," *Journal of Aircraft*, Vol. 20, No. 10, pp 882-886.
67. Jackson, P.S., "A Simple Model for Elastic Two-Dimensional Sails," *AIAA Journal*, Vol. 21, No. 1, January 1983, pp. 153-155.

68. Greenhalgh, S., Curtiss Jr., H.C., and Smith B., "Aerodynamic Properties of a Two-Dimensional Inextensible Flexible Airfoil," *AIAA Journal*, Vol. 22, No.7, July 1984, pp. 865-870.

69. Lian, Y., Shyy, W., and Haftka, R., "Shape Optimization of a Membrane Wing for Micro Air Vehicles," AIAA Paper No. 2003-106, 41st AIAA Aerospace Sciences Meeting and Exhibit, Reno, NV January 6-9, 2003.

70. Levin, O., and Shyy, W., "Optimization of a Flexible Low Reynolds Number Airfoil," AIAA Paper No. A01-16055, 39th AIAA Aerospace Sciences Meeting and Exhibit, Reno, NV January 8-11, 2001.

71. Leishman, J. G., *Principles of Helicopter Aerodynamics*, New York: Cambridge University Press, 2000.

72. Hong, Y., and Altman, A., "An Experimental Study of Lift Force Generation Resulting from Spanwise Flow in Flapping Wings," AIAA Paper No. 2006-448, 44th AIAA Aerospace Sciences Meeting and Exhibit, Reno, NV January 8-12, 2006.

73. Hong, Y., and Altman, A., "Vortex Lift Contributions in the Spanwise Flow in Flapping Wings," AIAA Paper No. 2006-3002, 24th AIAA Applied Aerodynamics Conference, San Francisco, CA June 5-8, 2006.

74. Sitaraman, J. and Roget, B., "A Computational Study of Flexible Wing Ornithopter Flight," AIAA Paper No. 2008-6397, 26th AIAA Applied Aerodynamics Conference, Honolulu, HI, August 18-21, 2008.